



UNIVERSITY OF TRENTO - Italy

Department of Physics

Second order nonlinearities in silicon photonics

Doctoral dissertation

in fulfillment of the requirements
for the degree of *Doctor of Philosophy*
in the subject of Physics

Candidate:
Claudio Castellan

Supervisor:
Prof. Lorenzo Pavesi

March 2019

Claudio Castellan

Second order nonlinearities in silicon photonics

22 March 2019

Supervisor: Prof. Lorenzo Pavesi

Reviewers: Prof. Pablo Sanchis and Prof. Vittorio Passaro



This work is licensed under a [Creative Commons Attribution-NonCommercial-NoDerivatives 4.0 International License](https://creativecommons.org/licenses/by-nc-nd/4.0/).

University of Trento

Nanoscience Laboratory

Department of Physics

Via Sommarive 14

38123 Trento

Abstract

In this thesis, second order optical nonlinearities in silicon waveguides are studied. At the beginning, the strained silicon platform is investigated in detail. In recent years, second order nonlinearities have been demonstrated on this platform. However, the origin of these nonlinearities was not clear. This thesis offers a clear answer to this question, demonstrating that this nonlinearity does not originate on the applied strain, but on the presence of trapped charges that induce a static electric field inside the waveguide. Based on this outcome, a way to induce larger electric fields in silicon waveguide is studied. Using lateral p-n junctions, strong electric fields are introduced in the waveguides, demonstrating both electro-optic effects and second-harmonic generation. These results, together with a detailed modeling of the system, pave the way through the demonstration of spontaneous parametric down-conversion in silicon.

Contents

1	Introduction	1
1.1	Nonlinear optics	1
1.1.1	An historical perspective	1
1.1.2	Why <i>nonlinear</i> ?	5
1.1.3	Nonlinear phenomena	6
1.2	Nonlinear optics in integrated devices	11
1.2.1	Why integrated?	11
1.2.2	Fundamental elements of integrated optics	12
1.2.3	Third order nonlinear integrated platforms	17
1.2.4	Second order nonlinear integrated platforms	20
1.3	Second order nonlinear silicon photonics	24
1.3.1	Pockels effect in silicon waveguides	24
1.3.2	SHG in silicon waveguides	27
1.4	This work	29
I	Tunable mechanical load in waveguides	31
2	Strain effects on microresonators	33
2.1	General features	34
2.1.1	The experimental setup	34
2.1.2	The structures under test	34
2.2	Basics of the linear theory of elasticity	35
2.3	Macroscopic simulation of the device	38
2.3.1	Description of the model	38
2.3.2	Validation of the model	39
2.4	Effect of strain on the resonance wavelength	39
2.5	Estimation of the waveguide width	43
3	Modeling the effects of strain on microresonators	45
3.1	Theoretical model	46
3.2	Contribution of the perimeter variation	47
3.3	Contribution of the refractive index variation	49
3.3.1	Evaluation of strain inside the waveguide	49
3.3.2	Photoelastic variation of the effective refractive index	50
3.3.3	Contribution of the waveguide deformation	51

3.4	Comparison with experiments	53
3.5	Conclusion and perspectives	54
II	Second harmonic generation in strained silicon waveguides	55
4	Modeling SHG in silicon waveguides	57
4.1	Theoretical description of SHG in waveguides	58
4.1.1	Optical pulses in nonlinear waveguides	58
4.1.2	SHG and other effects in waveguides	59
4.1.3	The SH pulse equation	60
4.1.4	The pump pulse equation	62
4.1.5	The coupled equations	63
4.1.6	Undepleted pump and continuous wave	63
4.2	Waveguide engineering	64
4.2.1	Waveguide cross-section	64
4.2.2	Phase matching through waveguide engineering	65
4.2.3	Strength of the modal combinations	69
4.2.4	Quantification of the strain-induced nonlinear strength	70
4.3	Estimating the generation efficiency	72
4.3.1	The split-step method	72
4.3.2	Propagating optical pulses	73
4.3.3	From the experiment to the $\chi^{(2)}$ coefficient	80
5	Demonstration of SHG in strained silicon waveguides	83
5.1	Experimental setup	83
5.1.1	The source	84
5.1.2	The pulse-shaping stage	85
5.1.3	The coupling stage	86
5.1.4	The detection stage	87
5.2	Characterization of SHG in strained silicon waveguides	88
5.2.1	Dependence on the pump wavelength	88
5.2.2	Dependence on the waveguide	90
5.2.3	Dependence on the pump power	90
5.2.4	Spectrum of the SH signal	91
5.3	Estimation of the nonlinear coefficient	92
6	SHG under external load	95
6.1	Effect of external load on SHG	95
6.1.1	Experimental setup	95
6.1.2	SHG under the effect of strain	96
6.2	Modeling the effect of strain on SHG	98
6.2.1	Macroscopic modeling of the sample	98

6.2.2	Effect of strain on phase-matching	98
6.2.3	Effect of strain on $\chi^{(2)}$	100
7	The role of charged centers on second harmonic generation	103
7.1	The origin of dangling bonds	104
7.2	Passivation of dangling bonds with UV light	105
7.2.1	C-V measurements to estimate the charge density	105
7.2.2	Estimation of the charge density	106
7.2.3	Effect of charge removal on waveguides	107
7.3	Effect of charge passivation on second harmonic generation	108
7.4	Modeling the effect of charges on second harmonic generation	109
7.4.1	Carrier distribution inside the waveguide	110
7.4.2	Effect of charges on propagation losses	111
7.4.3	Electric field distribution inside the waveguide	111
7.4.4	Charge-induced second order nonlinearities	112
7.5	Conclusions and perspectives	115
III	Second order nonlinearities in waveguides with static fields	117
8	DC Kerr effect and plasma dispersion in silicon racetrack resonators	119
8.1	Lateral p-n junctions in microresonators	120
8.1.1	Effect on the material refractive index	120
8.1.2	Effect on the material absorption	121
8.2	Microresonator engineering	122
8.2.1	Single mode waveguides	122
8.2.2	Distance between the waveguide and metal	123
8.2.3	Curvature radius	125
8.2.4	Resonator coupling region	125
8.3	The realized devices	126
8.4	The effect of doping on waveguides	128
8.4.1	Modeling the system via transfer matrix methods	129
8.4.2	Characterization of devices without junctions	131
8.4.3	The effect of doping on microresonators	136
8.4.4	Modeling free-carrier absorption	136
8.5	Electrical characterization of waveguides	138
8.6	Electro-optic measurements	139
8.6.1	Modeling the electro-optic strength	140
8.6.2	Measurement of the electro-optic effect	142
8.7	Perspectives	145
9	SHG and SPDC in silicon waveguides with lateral doping	147
9.1	Description of nonlinearities in quasi-phase-matched waveguides	148

9.1.1	Second Harmonic Generation	148
9.1.2	Spontaneous Parametric Down Conversion	149
9.1.3	The shape of the poling function	150
9.2	Engineering poled waveguides	152
9.2.1	Setting the poling period	154
9.2.2	Estimating the generation efficiency	155
9.2.3	Coherence length of the process	156
9.2.4	Realized waveguide geometries	156
9.2.5	Tolerance to fabrication uncertainties	158
9.2.6	Geometry of the junction	160
9.3	Modeling the electric field in poled waveguides	162
9.3.1	Description of the FEM model	163
9.3.2	Field distribution and nonlinear strength	163
9.3.3	The poling function	168
9.3.4	The maximum achievable field	169
9.3.5	The maximum nonlinearity	171
9.4	Estimation of the SHG and SPDC efficiency	173
10	Demonstration of SHG in silicon waveguides with lateral doping	175
10.1	The realized devices	175
10.2	Electrical characterization	177
10.3	Experimental characterization of SHG	178
10.3.1	Dependence on the pump wavelength	178
10.3.2	Dependence on the pump power	179
10.3.3	Dependence on the waveguide length	179
10.3.4	Dependence on the applied voltage	181
10.4	Comparison between the experiment and simulations	182
10.4.1	Phase-matching wavelength	183
10.4.2	SH power	184
10.5	Conclusions and perspectives	186
11	SHG and SPDC in silicon oxynitride waveguides	191
11.1	Waveguide cross-section	191
11.2	The DC field inside the waveguide	193
11.3	The required poling period	194
11.4	Conversion efficiency	198
12	Conclusions	199
	Bibliography	203
	Publications	215
	Acknowledgements	223

Introduction

1.1	Nonlinear optics	1
1.1.1	An historical perspective	1
1.1.2	Why <i>nonlinear</i> ?	5
1.1.3	Nonlinear phenomena	6
1.2	Nonlinear optics in integrated devices	11
1.2.1	Why integrated?	11
1.2.2	Fundamental elements of integrated optics	12
1.2.3	Third order nonlinear integrated platforms	17
1.2.4	Second order nonlinear integrated platforms	20
1.3	Second order nonlinear silicon photonics	24
1.3.1	Pockels effect in silicon waveguides	24
1.3.2	SHG in silicon waveguides	27
1.4	This work	29

1.1 Nonlinear optics

1.1.1 An historical perspective

Nonlinear optics has a supercentenarian history [1]. It begun in **1875**, when the Scotsman **John Kerr** discovered the phenomenon that now bears his name. Applying a strong DC field to a variety of solids and liquids, he observed a slight modification of their refractive index [2]. A second nonlinear optics milestone was put by the German physicist **Friedrich Pockels** in **1890s**. He analyzed non-centrosymmetric crystalline materials and observed a similar effect. However, in his case, the refractive index varied linearly (and not quadratically) on the applied field [3].

The term **nonlinear optics** was introduced for the first time by the Sovietic physicist **Sergey Vavilov** in 1944. Some year before he had observed a reduction of the uranium-doped glass absorption for large light intensities. This phenomenon, known today as saturable absorption, was the first purely optical nonlinear effect ever shown [4]. A similar effect, the luminescence saturation, enabled the realization of the **Icaroscope**, the first practical application of nonlinear optics. It was developed by the Institute of Optics during the **World War II** [5]. This device aimed to protect the

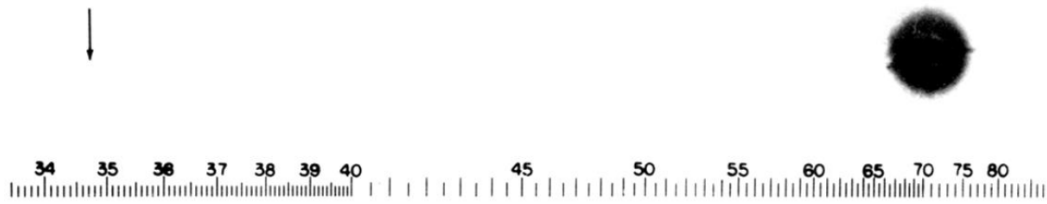


Fig. 1.1: Reproduction of the photographic plate where second harmonic signal was shown for the first time. The wavelength scale is in units of Å. The big spot represents the pump beam. The arrow should indicate the second harmonic signal, wrongly removed by the lithographer of the journal. Reprinted with permission from [9]. Copyright (1961) by the American Physical Society.

U.S. Navy during the bombing attacks by Japanese Air Force, which used to approach the ships from the sun direction in order to blind of the anti-aircraft gunners. The Icaroscope made use of phosphors, which possess a strong luminescence saturation. In this way, the sun appeared only 20 – 50 times brighter than the surrounding sky, while for the naked eye it is 10^4 times brighter [6, 7].

The **golden age** of nonlinear optics begun immediately after the invention of the laser by Theodore Maiman in May 1960 [8]. "If the laser was a solution, nonlinear optics was one of the problems it was seeking", comments Jeff Hecht in [5]. The laser provided intense, coherent and monochromatic light pulses, driving the disruptive development shown by nonlinear optics in successive years. The first nonlinear optics experiment with a laser was performed by **Peter Franken** at the University of Michigan in the middle of **1961**. A ruby laser beam at the wavelength of 694 nm was focused on crystalline quartz. The emergent beam was analyzed by a spectrograph, showing on a photographic plate the generation of a weak second harmonic signal at the halved wavelength of 347 nm [9]. For the first time, **second-harmonic generation** was shown. This was a disruptive result, despite of the extremely low conversion efficiency of about 1 part in 10^8 . As recalled by Franken in an interview in 1985, "the thought that you could have optical harmonics [...] in the 1959, '60 period [...] was a revolutionary thought". The efficiency was so low that, in the photographic plate reproduced in the 15 August 1961 issue of *Physical Review Letters* [9] and shown in Fig. 1.1, the second harmonic signal is not visible, eliminated by the lithographer of the journal that confused it with a flaw [5].

Starting from the seminal work of Franken, the study of nonlinear optics exploded. The successive milestone was put by Joe Giordmaine at the Bell Labs and by the group of Bob Terhune at the Ford Motor Co. Research Laboratory, who independently published their works on the same issue of *Physical Review Letters* in **January 1962** [10, 11]. They both worked on potassium dihydrogen phosphate (KDP) crystal, individuated as a particularly interesting nonlinear material. In their experiments, pump and second harmonic waves were orthogonally polarized. Exploiting the birefringence of KDP, they demonstrated extremely high generation efficiency when the waves propagated along directions ensuring the same refractive index for the



Fig. 1.2: Nicolaas Bloembergen, one of the scientists who derived the theory of nonlinear optics, in 1981, the year in which was awarded with the Nobel prize. "Nicolaas Bloembergen" by "... Vetter (Spaarnestad Photo)", licensed under BY-SA 3.0 nl (<https://creativecommons.org/licenses/by-sa/3.0/nl/deed.en>), via Wikimedia Commons.

pump and the second harmonic wave. This efficiency enhancement was attributed to the matching between the phases of the pump and of the generated waves. This technique, called **birefringent phase-matching**, later on in the years will be flanked by other phase-matching methods. In light of these results, the inefficiency of the Franken experiment was understood and ascribed to the lack of the phase-matching. Stimulated by recent observations, at Harvard Nicolaas Bloembergen started to develop the **theory of nonlinear optics**, which was published in September 1962 [12]. This work became soon a milestone, and fostered the new discoveries shown in the successive years. For this motivation, Bloembergen won the **Nobel Prize in Physics in 1981** [5]. In the first 1960s, many phenomena reported today in nonlinear optics textbooks were demonstrated, among which sum frequency generation [13], four-wave mixing [14], self focusing [15], self-phase modulation [16], stimulated Raman scattering [17] and stimulated Brillouin scattering [18].

On the other side of the cold war world, also Soviet institutions started to support nonlinear optics research. The first nonlinear optics laboratory was established at the Moscow State University in 1962, and gave rapidly respectable results [5]. Among the others, it is worth noting the first demonstration of an optical parametric oscillator, independently shown by Alexander Kovrigin in Moscow [19] and by Joe Giordmaine at the Bell Labs [20], which allowed to generate tunable outputs from fixed wavelength lasers.

According to Li in [21], the experiments described so far constitute the initial **foundation stage** of nonlinear optics, and cover the first years of 1960s. In the successive 20 years, nonlinear optics became mature. Many new and more sophisticated effects were demonstrated, among which optical bistability [22] and optical solitons [23]

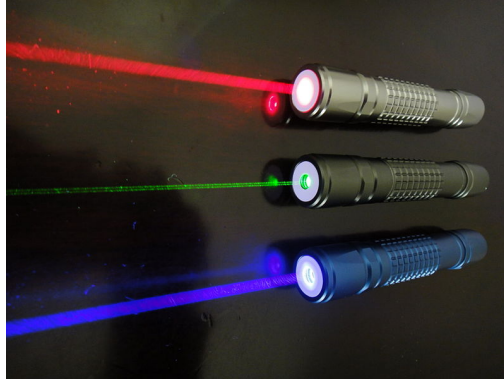


Fig. 1.3: Modern laser pointers, everyday objects enabled by nonlinear optics. "Q-LINE lasers" by Netweb01, licensed under CC BY-SA 3.0 (<https://creativecommons.org/licenses/by-sa/3.0>), from Wikimedia Commons.

Starting from the mid-1980s, the **application development stage** of nonlinear optics began. In this perspective, many researchers focused on the development of efficient and cost effective material platforms. Material science helped this progress, and made possible processes that before were only conceptually predicted. As an example, the quasi-phase-matching technique was proposed at first in the early 1960s by Bloembergen in his seminal work [12], but almost 30 years passed before its first demonstration due to technological limitations in the deposition techniques [24]. Nowadays, nonlinear optics finds lots of applications in many areas. One of these is the **laser technology**. As an example, the Q-switching and the mode-locking allow to generate ultrashort pulses down to attosecond [25]. Furthermore, frequency conversion makes fixed wavelength laser sources more flexible [26]. Widely diffused are also lasers where the fundamental frequency is doubled or tripled, like in most of the green laser pointers where neodymium lasers at 1064 nm are doubled to 532 nm [27]. Nonlinear optics is the key enabling technology for the field of **all-optical signal processing** [28]. It deeply penetrated also the **optical communications field**, to realize optical amplifiers and modulators, but also to prevent detrimental effects like phase modulation in long-distance fiber communications [29]. Other applications have been demonstrated in **material processing**, like the multiphoton lithography that allows to synthesize nanometer-scale materials [30].

The aim of this section was to offer an overview of the incredible advances made by nonlinear optics research in the last 60 years, emphasizing the large variety of applications that today are possible thanks to nonlinear optics. The list was surely not exhaustive, but this was not the intent of this introduction. For a more detailed overview, the reader can refer to [27].

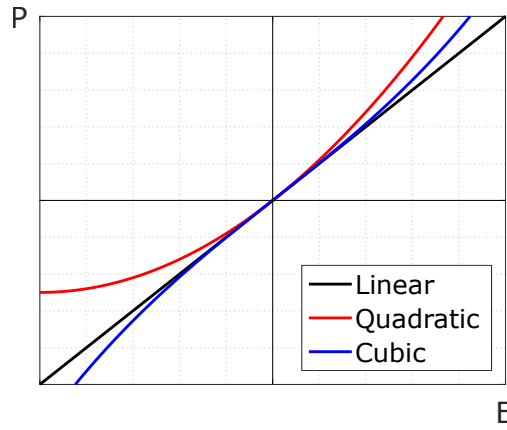


Fig. 1.4: Relationship between the polarization P and the applied field E for the case of a linear medium, quadratic nonlinear medium and cubic nonlinear medium.

1.1.2 Why nonlinear?

The phenomena described so far are said **nonlinear** because, to describe them, one has to assume that the material polarization \mathbf{P} responds in a nonlinear way to the applied optical field \mathbf{E} . These phenomena occur when the applied electric fields are strong enough to be comparable with the fields inside atoms and molecules. In this situation, the fields affect the electronic distribution inside the atoms, and the material changes its response [1]. If the applied fields are weaker, the electronic distribution is not affected and the **linear** optical description works well. This is the situation of most of the optical processes observed in the everyday life.

In a one-dimensional and linear optical framework, the polarization P and the applied field E are related by:

$$P = \alpha E, \quad (1.1)$$

where α is a proportionality constant. This behavior is sketched in Fig. 1.4. This has a mechanical analogy in the Hook's law, where the restoring force is proportional to the applied displacement. This analogy is at the basis of the Lorentz linear model of the atom, which treats the atom as a harmonic oscillator and describes well the linear optical properties in atomic vapors and nonmetallic solids [31].

When the fields start to affect the electronic distribution inside the atom, the material changes its response. Also this behavior is well described by the Lorentz atomic model, which shows that additional terms must be added in the relationship between the polarization vector and the applied field [31]. In this case, the dependence of the polarization P on the applied field E can be expanded in a Taylor series:

$$P = \alpha E + \beta E^2 + \gamma E^3 + \dots, \quad (1.2)$$

where α , β and γ are again proportionality constants. The phenomena enabled by the term proportional to E^2 are said **second-order** nonlinear effects, while the ones

proportional to E^3 are the so called **third-order** effects. Higher order effects are also possible, but they require larger applied fields. In Fig. 1.4 the relationship between P and E for second- and third-order nonlinearities is sketched. From the figure, it is clear that for the quadratic case the medium responds differently depending on the sign of the applied field: the response is larger than the linear case when $E > 0$, but it is weaker for $E < 0$. This does not happen for the cubic case, which shows a symmetric behavior with respect to the applied field. This suggests that quadratic nonlinearities can happen only in materials that are structurally different while moving in two opposite directions. In other words, only non-centrosymmetric crystals can possess second order nonlinearities [1]. This explains why, going back to the historical overview, Friedrich Pockels and Peter Franken measured Pockels effect and second-harmonic-generation in non-centrosymmetric materials. Both these effect can be included in the family of second order nonlinearities, and so they are possible only when crystal centrosymmetry is lacking. On the contrary, Kerr effect is a third order process, and so John Kerr was able to measure it in liquids.

1.1.3 Nonlinear phenomena

In this section, a complete description of the relationship between the polarization vector \mathbf{P} and the applied field \mathbf{E} is proposed. In this way, the main processes enabled by nonlinear optics will be introduced.

In the linear optical case, the linear polarization vector \mathbf{P}_0 and the applied field \mathbf{E} are related by [31]:

$$\mathbf{P}_0 = \varepsilon_0 \chi^{(1)} \cdot \mathbf{E} = \varepsilon_0 \sum_{ij} \chi_{ij}^{(1)} E_i \hat{\mathbf{u}}_j. \quad (1.3)$$

Here ε_0 is the vacuum permittivity, $\chi^{(1)}$ is the first order susceptibility tensor (whose elements are $\chi_{ij}^{(1)}$), E_i is the i -th component of the electric field and $\hat{\mathbf{u}}_j$ the unitary versor. The susceptibility tensor $\chi^{(1)}$ is related to the refractive index tensor n by $\chi_{ij}^{(1)} + 1 = n_{ij}^2$. When dealing with isotropic or amorphous materials both the susceptibility tensor and the refractive index can be considered as scalar quantities, while for crystals they must be generally considered as tensors.

In the general nonlinear optical case, the polarization vector \mathbf{P} can be expanded in a Taylor series:

$$\mathbf{P} = \mathbf{P}_0 + \mathbf{P}_{NL} = \mathbf{P}_0 + \mathbf{P}^{(2)} + \mathbf{P}^{(3)} + \dots, \quad (1.4)$$

being \mathbf{P}_{NL} the nonlinear polarization vector, while $\mathbf{P}^{(2)}$ and $\mathbf{P}^{(3)}$ are the second and third order nonlinear polarization vectors. They are given by [31]:

$$\mathbf{P}^{(2)} = \varepsilon_0 \sum_{ijk} \chi_{ijk}^{(2)} E_i E_j \hat{\mathbf{u}}_k, \quad (1.5a)$$

$$\mathbf{P}^{(3)} = \varepsilon_0 \sum_{ijkl} \chi_{ijkl}^{(3)} E_i E_j E_k \hat{\mathbf{u}}_l, \quad (1.5b)$$

where $\chi^{(2)}$ and $\chi^{(3)}$ are the second and the third order susceptibilities. Higher order nonlinear terms are weaker and weaker, they become important for large field intensities. In general for both second and third order nonlinearities the empirical Miller's rule is valid, stating that the nonlinear strength is proportional to the material refractive index [31].

Second order nonlinearities. To evaluate the main second order effects, the electric field in the material must be written as the superposition of two monochromatic waves¹:

$$\mathbf{E}(\mathbf{r}, t) = \text{Re} \left[\sum_{n=1}^2 \tilde{\mathbf{E}}_n(\mathbf{r}, \omega_n) e^{-i\omega_n t} \right] = \sum_{n=1}^2 \left[\mathbf{E}_n(\mathbf{r}, \omega_n) e^{-i\omega_n t} + c.c. \right], \quad (1.6)$$

where ω_n is the frequency of the n -th wave, while *c.c.* stands for "complex conjugate". From Eq. (1.5a), the second order nonlinear polarization vector can be derived [31]:

$$\mathbf{P}^{(2)}(\mathbf{r}, t) = \varepsilon_0 \chi^{(2)} : \left[\mathbf{E}_1^2(\mathbf{r}, \omega_1) e^{-i2\omega_1 t} + \mathbf{E}_2^2(\mathbf{r}, \omega_2) e^{-i2\omega_2 t} \right] \quad \text{SHG} \quad (1.7a)$$

$$+ \varepsilon_0 \chi^{(2)} : \left[2\mathbf{E}_1(\mathbf{r}, \omega_1) \mathbf{E}_2(\mathbf{r}, \omega_2) e^{-i(\omega_1 + \omega_2)t} \right] \quad \text{SFG} \quad (1.7b)$$

$$+ \varepsilon_0 \chi^{(2)} : \left[2\mathbf{E}_1(\mathbf{r}, \omega_1) \mathbf{E}_2^*(\mathbf{r}, \omega_2) e^{-i(\omega_1 - \omega_2)t} \right] \quad \text{DFG} \quad (1.7c)$$

$$+ \varepsilon_0 \chi^{(2)} : \left[\mathbf{E}_1(\mathbf{r}, \omega_1) \mathbf{E}_1^*(\mathbf{r}, \omega_1) + \mathbf{E}_2(\mathbf{r}, \omega_2) \mathbf{E}_2^*(\mathbf{r}, \omega_2) \right] \quad \text{OR} \quad (1.7d)$$

+ c.c.

Each line of Eq. (1.7) describes a different nonlinear phenomenon, whose acronym is used as a label in the equation.

Line (1.7a) describes a term of the nonlinear polarization vector at frequency $2\omega_1$ (resp. $2\omega_2$). This corresponds to **Second Harmonic Generation** (SHG), when a photon at frequency $2\omega_1$ (resp. $2\omega_2$) is generated from two photons at frequency ω_1 (resp. ω_2). This process is schematized in Fig. 1.5. As already introduced, this was the first nonlinear wavelength conversion process ever observed [9].

The term at line (1.7b) corresponds to **Sum Frequency Generation** (SFG), while line (1.7c) is related to **Difference Frequency Generation** (DFG). As shown in Fig. 1.5, photons are generated (respectively) at frequencies $\omega_1 + \omega_2$ and $\omega_1 - \omega_2$.

The term at line (1.7d) is **Optical Rectification** (OR), and generates a DC component of the polarization vector.

If one of the frequencies in Eq. (1.7) is much lower than the other (or is set to DC), the SFG and DFG terms become a polarization vector oscillating at the high

¹Note that in this definition, for simplicity, the term $\mathbf{E}_n(\mathbf{r}, \omega_n)$ is defined as $(1/2)\tilde{\mathbf{E}}_n(\mathbf{r}, \omega_n)$.

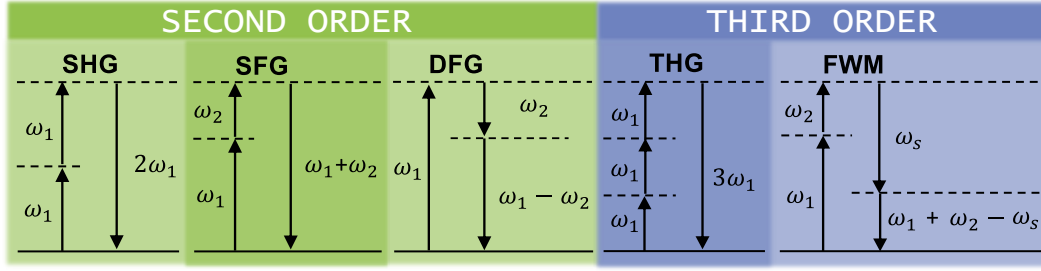


Fig. 1.5: Sketch of the main second- and third-order nonlinear processes.

frequency signal. This determines a material refractive index variation linearly dependent on the low-frequency wave amplitude. This is the **Pockels effect** (or linear electro-optic effect).

All the nonlinear phenomena described so far can be inserted in a classical scenario: once that a nonlinear perturbation of the polarization vector is introduced, Eq. (1.7) can be derived. However, there is a second order nonlinear phenomenon that cannot be derived from Eq. (1.7), namely the **Spontaneous Parametric Down Conversion** (SPDC) process. This process can be viewed as the fission of a photon in two photons with lower frequencies. SPDC is similar to DFG, but it happens without the coupling to a stimulating weak field because it is stimulated by random vacuum fluctuations. This process is particularly interesting because it generates couples of photons that are entangled in momentum, energy and time, and so it has lots of applications in the field of quantum photonics [32].

Third order nonlinearities. The third order nonlinear polarization vector $\mathbf{P}^{(3)}$ can be derived using the same procedure used for the second order one. The final result gives the following expression, where for simplicity all the permutations on the wave indices are omitted:

$$\mathbf{P}^{(3)}(\mathbf{r}, t) = \varepsilon_0 \chi^{(3)}: [\mathbf{E}_1^3(\mathbf{r}, \omega_1) e^{-i3\omega_1 t}] \quad \text{THG} \quad (1.8a)$$

$$+ \varepsilon_0 \chi^{(3)}: [3\mathbf{E}_1^2(\mathbf{r}, \omega_1) \mathbf{E}_2(\mathbf{r}, \omega_2) e^{-i(2\omega_1 + \omega_2)t}] \quad \text{FWM1} \quad (1.8b)$$

$$+ \varepsilon_0 \chi^{(3)}: [3\mathbf{E}_1^2(\mathbf{r}, \omega_1) \mathbf{E}_2^*(\mathbf{r}, \omega_2) e^{-i(2\omega_1 - \omega_2)t}] \quad \text{FWM2} \quad (1.8c)$$

$$+ \varepsilon_0 \chi^{(3)}: [6\mathbf{E}_1(\mathbf{r}, \omega_1) \mathbf{E}_2(\mathbf{r}, \omega_2) \mathbf{E}_3(\mathbf{r}, \omega_3) e^{-i(\omega_1 + \omega_2 + \omega_3)t}] \quad \text{FWM3} \quad (1.8d)$$

$$+ \varepsilon_0 \chi^{(3)}: [6\mathbf{E}_1(\mathbf{r}, \omega_1) \mathbf{E}_2(\mathbf{r}, \omega_2) \mathbf{E}_3^*(\mathbf{r}, \omega_3) e^{-i(\omega_1 + \omega_2 - \omega_3)t}] \quad \text{FWM4} \quad (1.8e)$$

$$+ \varepsilon_0 \chi^{(3)}: [3|\mathbf{E}_1(\mathbf{r}, \omega_1)|^2 \mathbf{E}_1(\mathbf{r}, \omega_1) e^{-i\omega_1 t}] \quad \text{SPM} \quad (1.8f)$$

$$+ \varepsilon_0 \chi^{(3)}: [6|\mathbf{E}_2(\mathbf{r}, \omega_2)|^2 \mathbf{E}_1(\mathbf{r}, \omega_1) e^{-i\omega_1 t}] \quad \text{XPM} \quad (1.8g)$$

+ *c.c.*

The term at line (1.8a) describes **Third Harmonic Generation** (THG). Similarly to SHG, here three photons with identical frequencies ω_1 sum up to generate a photon at triple frequency $3\omega_1$. This process is sketched in Fig. 1.5.

The elements at lines (1.8b)-(1.8e) describe **stimulated Four Wave Mixing** (FWM), where two pump waves interact with a weak wave, providing an amplification of the weak wave and the generation of a fourth wave. The generated waves are called signal (the one at lower frequency) and idler (the one at larger frequency). One of the FWM processes described by (1.8) is sketched in Fig. 1.5. The word *stimulated* is used to distinguish it from **spontaneous FWM**, a non-classical process that (similarly to SPDC) is stimulated by vacuum fluctuations. In this case, the signal and the idler photons are directly generated from the pump beam without the coupling with any weak signal beam [32].

The term at line (1.8f) describes both **Self Phase Modulation** (SPM) and **Two Photon Absorption** (TPA). SPM is linked to the real part of $\chi^{(3)}$, and is responsible of intensity-dependent perturbations of the refractive index. This is known also as **AC Kerr effect**. On the other hand, TPA is related to the imaginary part of $\chi^{(3)}$ and gives intensity-dependent variations of the absorption coefficient. It derives from the absorption of two photons which sum up to overcome the energy required to excite an electron from the valence to the conduction band. In this framework, the material refractive index n can be generally written as [33]:

$$n = n_0 + n_2 I + i \frac{\lambda}{4\pi} [\alpha_0 + \beta_{\text{TPA}} I], \quad (1.9)$$

where n_0 is the linear refractive index, α_0 is the linear loss coefficient, λ is wavelength, n_2 the Kerr coefficient, β_{TPA} the TPA coefficient and I the field intensity. The Kerr and TPA coefficients are related to an effective third order nonlinear coefficient $\chi_{\text{eff}}^{(3)}$ (that accounts for the independent terms of the tensor $\chi^{(3)}$) by the following expressions [33, 34]:

$$n_2 = \frac{3}{4\epsilon_0 c n_0^2} \text{Re} \left(\chi_{\text{eff}}^{(3)} \right) \quad \beta_{\text{TPA}} = \frac{3\omega}{2\epsilon_0 c^2 n_0^2} \text{Im} \left(\chi_{\text{eff}}^{(3)} \right), \quad (1.10)$$

where c is the speed of light in vacuum. The Kerr and TPA coefficients are usually compared by means of the **Figure Of Merit** $\text{FOM} = n_2 / (\lambda \beta_{\text{TPA}})$ [33]. Efficient third order nonlinear materials possess a high FOM, deriving from both a large Kerr coefficient and a small TPA coefficient.

The term at line (1.8g) describes **cross Phase Modulation** (XPM), where a signal at frequency ω_2 perturbs the propagation of a signal at frequency ω_1 .

Consider now the case when the frequency of one wave in Eq. (1.8) is much lower than the others, or is set to DC (for example $\omega_3 = 0$). In this situation, the nonlinear polarization vector $\mathbf{P}^{(3)}$ acquires terms at frequencies $2\omega_1$ and $2\omega_2$. These terms correspond to a SHG process. However, in this case SHG is enabled by $\chi^{(3)}$ through the application of the DC field. For this reason, this process is called **Electric Field**

Induced SHG (EFISH). When $\omega_3 = 0$, additional phase-modulation terms appear in Eq. (1.8). These terms introduce a perturbation of the material refractive index which is quadratically dependent on the low-frequency wave amplitude. This process is known as **DC Kerr effect** and, as already shown, has been the first nonlinear optical effect ever demonstrated.

Phase-matching. The nonlinear processes where the initial and the final quantum mechanical states of the system are the same [31] are called **parametric**. Parametric processes are described by the real part of the nonlinear susceptibility tensor, while non-parametric ones are described by the imaginary part. This means that photon energy conservation always occurs in parametric processes, while in non-parametric ones energy transfer with the medium can occur. In other words, parametric processes are the ones that involve frequency conversion, such as SHG, DFG, SFG, THG and FWM.

To be efficient, parametric processes require to satisfy the **phase-matching condition**, meaning that a given phase mismatch coefficient $\Delta\beta$ must be close to zero. This is because the conversion efficiency is generally proportional to a coefficient of the form $\text{sinc}^2[\Delta\beta L/2]$, where L is the length of the interaction region [31]. The phase mismatch coefficient is given by a combination of the propagation constants of the different waves. For example in SHG $\Delta\beta = 2\beta_p - \beta_{sh}$, where β_p and β_{sh} are the propagation constants of the pump and of the second harmonic waves. In other words, satisfying phase-matching requires that contributions generated in different regions of the nonlinear material add up constructively.

Due to material dispersion, phase-matching condition is hardly automatically satisfied and special countermeasures are required. The first phase-matching technique ever achieved is named **birefringent phase-matching**. It involves waves propagating with different polarizations, which feel different refractive indexes due to the material birefringence and that nullifies the phase-mismatch. This technique is the one adopted by Giordmaine and Terhune in their seminal experiments published in 1962 [10, 11]. Another similar technique exploits waves propagating in different modes of integrated waveguides. This technique, that is deeply investigated in this work, is named **intermodal phase-matching** [35]. Both the techniques described so far require the use of waves suitably chosen to achieve $\Delta\beta = 0$, and thus enter in the category of the **perfect phase-matching** techniques. These are distinguished from **Quasi Phase-Matching (QPM)** techniques, where phase-matching is introduced making use of spatial modulation of the material nonlinearity. In this case, if the material nonlinearity varies periodically in the propagation direction of the pulse with a period Γ , a new phase-mismatch parameter $\Delta\beta' = \Delta\beta - 2\pi/\Gamma$ must be considered [31]. The most common way to introduce QPM is to artificially introduce a periodic change of the sign of the nonlinear coefficient of the material [36]. This technique is commonly named **periodic poling**. However, also other QPM

techniques are possible, some of which exploit natural properties of the nonlinear materials. Among these for example the $\bar{4}$ symmetry phase-matching exploits the natural property of crystals like GaP, GaAs and ZnSe to shown crystallographic inversions when performing rotations of 90° about the $\bar{4}$ axis [37].

1.2 Nonlinear optics in integrated devices

1.2.1 Why integrated?

The efficiency of any nonlinear process strongly depends on the applied field intensity. In **bulk optics**, larger field intensities can be achieved by a tighter beam focusing. However, this causes a shortening of the interaction length, which sometimes can vanish the advantage resulting from the increased field intensity. A different approach to obtain large field intensities over long distances is to use waveguiding structures, and this motivated the growth of **nonlinear fiber optics** [29, 38]. Starting from early 1970s, many nonlinear phenomena were observed in optical fibers, including Raman and Brillouin scattering [39, 40], FWM [41, 42] and SPM [43]. In the 1980s more advanced nonlinear processes were studied, including optical solitons [23], pulse compression [44, 45] and optical switching [46]. Another step forward was done in the field of optical amplification. To overcome the limitations of rare-earth doped fibers, which could operate only in limited spectral regions, optical amplification was demonstrated in undoped fibers, making use of stimulated Raman scattering and FWM [29, 47, 48].

Another way to increase the nonlinear interaction is to act on the waveguide area, reducing it below the one of fibers typically used for telecommunications. This prompted the development of **sub-micron waveguides** (also referred as nanowires) [38]. Their development started in the early 2000s, and they have been produced using a variety of materials such as silica, high refractive index glasses, silicon, lithium niobate, and many others. The use of sub-micron waveguides does not influence only the interaction area of the optical field, but it also allows to control some other properties of the propagating modes. Regarding nonlinear processes, particularly important is the control of the Group Velocity Dispersion (**GVD**), which can be easily engineered in optical waveguides. Moreover, waveguides can also be used to form optical cavities, known also as **microresonators**. The use of cavities allows to increase the field strength, and thus the possibilities for nonlinear optical applications. Finally, one must also consider that optical waveguides are the fundamental elements of **integrated optical circuits**, whose development has become a hot topic in recent years [49]. Integrating nonlinear waveguides into integrated optical circuits offers an easy manipulation of the nonlinearly generated fields, and allows to reproduce in a mm^2 scale device the functionalities that are

typically performed on a laboratory optical bench. As an example, Fig. 1.6 shows a sketch of the circuit diagram recently reported in [50], where multidimensional entanglement is studied for dimension up to 15. This device, realized on the silicon platform, integrates 16 photon pair sources based on spontaneous FWM. The manipulation of the photon states is achieved thanks to 93 thermo-optical phase-shifters, 122 beamsplitters and 256 waveguide-crossings, integrating more than 550 photonic components on a single chip. This scenario has interesting implications for the deeper penetration of nonlinear optics in real life applications, thanks to the reduced fabrication cost and power consumption that characterizes in general integrated devices compared to traditional bulk optics [51].

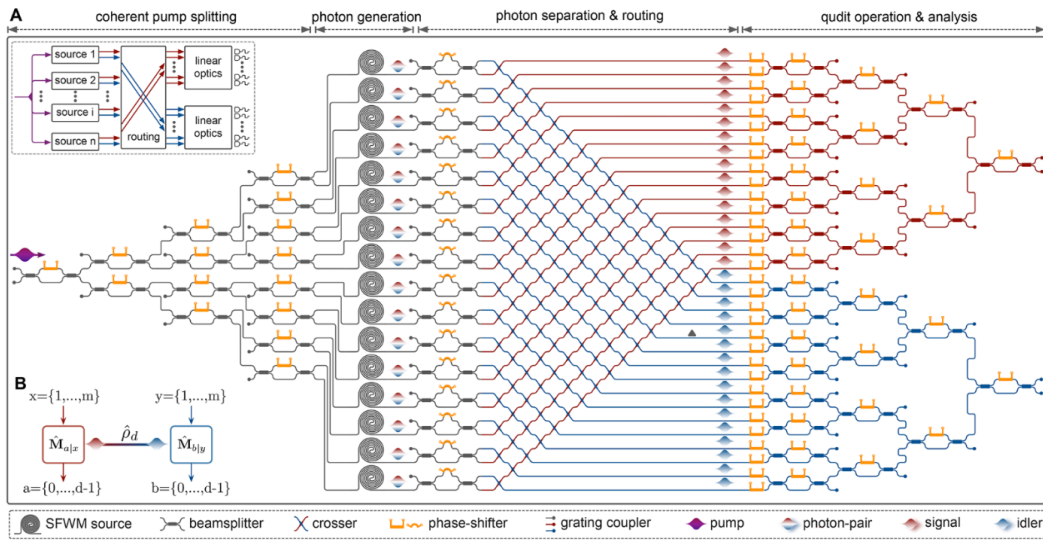


Fig. 1.6: Sketch of an integrated device where multidimensional entanglement is studied for dimension up to 15. From [50]. Reprinted with permission from AAAS.

1.2.2 Fundamental elements of integrated optics

Waveguides. Optical waveguides are devices engineered to guide light, inhibiting light propagation along some directions [52]. Different waveguiding platforms have been demonstrated, each based on a different physical mechanism including total internal reflection [52], photonic crystals [53] and plasmonic phenomena [54]. Here the most common platform is treated, where light is confined by **total internal reflection** in a high refractive index medium (the core) that is surrounded by a low refractive medium (the cladding). Waveguides with different shapes have been demonstrated, some of which are sketched in Fig. 1.7. The most common waveguide is the **optical fiber**, which has a cylindrical shape and a core formed by doped glass. In the **slab waveguide**, the core and the cladding materials extend infinitely in the plane, and light is confined in only one direction. In the **strip waveguide**, a strip of core material is embedded into the cladding, confining light in two directions.

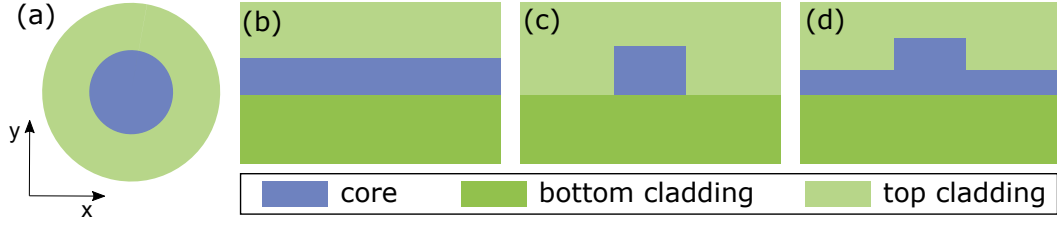


Fig. 1.7: Cross-section of some of the most common waveguide geometries. (a) Cylindrical geometry (typical geometry of optical fibers). (b) Slab waveguide. (c) Rectangular strip waveguide. (d) Rib waveguide.

Light is confined in two directions also in the **rib waveguide**, consisting of a slab waveguide superimposed by a strip waveguide. Strip and rib geometries are the most used in integrated optical circuits.

The optical field $\mathbf{E}(\mathbf{r}, \omega)$ propagating in a waveguide is generally written as $\mathbf{E}(\mathbf{r}, \omega) = \mathbf{e}(\mathbf{r}_\perp, \omega)e^{i\beta z}$, where z is the waveguide propagation direction, β the propagation constant, ω the frequency, $\mathbf{r}_\perp = (x, y)$ a vector in the plane orthogonal to z and $\mathbf{e}(\mathbf{r}_\perp, \omega)$ the electric field profile in the plane described by \mathbf{r}_\perp . The field distribution $\mathbf{e}(\mathbf{r}_\perp, \omega)$ satisfies the **Helmoltz equation** [52]:

$$\left(\frac{\omega^2}{c^2} n^2(\mathbf{r}_\perp) - \nabla_{\mathbf{r}_\perp}^2 \right) \mathbf{e}(\mathbf{r}_\perp, \omega) = \beta^2 \mathbf{e}(\mathbf{r}_\perp, \omega), \quad (1.11)$$

where $n(\mathbf{r}_\perp)$ is the refractive index distribution in the (x, y) plane. Equation (1.11) is an eigenvalue equation with a discrete number of solutions, called **modes**. Each mode is labeled by an index m , and is characterized by a field profile $\mathbf{e}_m(\mathbf{r}_\perp, \omega)$ and by a propagation constant β_m . For many geometries (such as the strip rectangular waveguide) analytic solutions of Eq. (1.11) do not exist, so they must be found numerically using for example Finite Element Method (FEM) simulations. Due to diffraction limit, a waveguide supports only a limited number of modes. To roughly estimate it, consider that light can be confined at sizes $> \lambda_0/2n$, being λ_0 the wavelength in vacuum. So, for a rectangular waveguide with dimensions $w \times h$, the maximum number of modes is $wh(\lambda_0/2n)^{-2}$ [55].

Figure 1.8 reports the modal profiles of the lowest order modes supported by a silicon strip rectangular waveguide with dimensions $1.5 \mu\text{m} \times 0.25 \mu\text{m}$. They are calculated using the COMSOL Multiphysics[®] FEM software [56]. The propagating

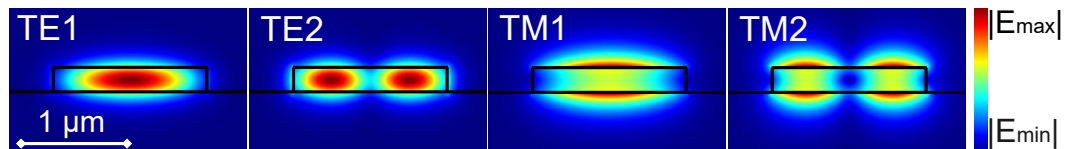


Fig. 1.8: Norm of the electric field amplitude of the two lowest order TE and TM modes of a $1.5 \mu\text{m} \times 0.25 \mu\text{m}$ silicon waveguide with a silica cladding at the wavelength of 1550 nm. These quantities are obtained from a FEM simulation using refractive indexes reported in [57, 58].

modes are distinguished in **Transverse Electric** (TE), when the electric field is directed along x direction, and **Transverse Magnetic** (TM), when the electric field is directed along y . Each solution is characterized by a number n_x (resp. n_y) of nodal points along the x (resp. y) direction, where the field is zero. From now on, in this work thin waveguides will be considered, such that $n_y = 0$. So, the mode order can be identified by a single label index ν , defined as $\nu = n_x + 1$. In this new notation, each supported mode can be labeled by an index m , which contains the mode polarization (TE or TM) and the modal order ν . For example, $m = \text{TE1}$ (resp. $m = \text{TM1}$) refers to the **fundamental** TE (resp. TM) mode.

As it is clear from Fig. 1.8, the field profile of the different modal orders have different extensions. The modal extension is evaluated by the **effective area** of the mode, defined as [59]:

$$A_{\text{eff},m} = \frac{\left(\int_{A_\infty} |\mathbf{e}_m(\mathbf{r}_\perp, \omega)|^2 dA \right)^2}{\int_{A_\infty} |\mathbf{e}_m(\mathbf{r}_\perp, \omega)|^4 dA}, \quad (1.12)$$

where the integral is taken on the whole transverse plane A_∞ described by \mathbf{r}_\perp . In nonlinear phenomena, small effective areas are preferred, to provide larger field intensities. Another feature to consider is the extension of the optical mode outside the waveguide core, known as **evanescent field**. A parameter accounting for that is the **confinement factor** Γ_m , which estimates the field fraction confined within the waveguide core area A_0 , and is defined as follows [59]:

$$\Gamma_m = \frac{\int_{A_0} n^2(\mathbf{r}_\perp) \mathbf{e}_m^2(\mathbf{r}_\perp, \omega) dA}{\int_{A_\infty} n^2(\mathbf{r}_\perp) \mathbf{e}_m^2(\mathbf{r}_\perp, \omega) dA}. \quad (1.13)$$

The **effective refractive index** of the mode m is defined as $n_{\text{eff},m} = (c/\omega)\beta_m$. The effective refractive index is a complex quantity, whose real part is related to propagation and whose imaginary part is related to absorption. In straight waveguides, absorption is due both to material absorption and to waveguide defects, which result from imperfections during the fabrication. Assuming an exponentially decreasing field intensity of the form $\exp(-\alpha_m z)$, the attenuation constant α_m is related to the imaginary part of the effective refractive by $\alpha_m = (2\omega/c) \text{Im}(n_{\text{eff},m})$. The propagation constant β_m depends on the frequency. Often it is expanded as a Taylor series around a central frequency ω_0 . The first expansion term $\beta_{1,m}$ is related to the **group velocity** of the mode $v_{G,m}$ and to the **group index** of the mode $n_{G,m}$ by: $v_{G,m} = 1/\beta_{1,m} = c/n_{G,m}$. The second term of the expansion $\beta_{2,m}$ is the **Group Velocity Dispersion** (GVD). The modal effective refractive index dispersion is said normal when $\beta_{2,m} > 0$ and anomalous when $\beta_{2,m} < 0$. GVD is of particular importance for nonlinear optics, especially when dealing with ultrashort pulses. In fact, GVD controls the pulse broadening and influences the phase-matching in frequency conversion processes. Moreover, large GVD determines **temporal walkoff**, consisting in the lose of the temporal overlap between pulses with different

frequencies. If the pulses are involved in nonlinear conversion phenomena, temporal walkoff limits conversion efficiency and modifies the pulse shape. As it has been already introduced, in small waveguides GVD can be easily tailored by properly engineering the waveguide dimensions, and this makes integrated waveguides particularly interesting for nonlinear phenomena [60].

Micro-resonators. Resonators have plenty of applications in the field of nonlinear optics, due to the strong field enhancement obtained within optical cavities [61]. The simplest optical cavity is the Fabry-Perot interferometer, constituted by a couple of parallel reflecting mirrors. Despite of its simple geometry, the Fabry-Perot scheme can be hardly integrated due to the difficulty to realize high quality integrated mirrors. Conversely, in the planar architecture of integrated circuits the use of **microring resonators** results particularly favorable [62]. Microring resonators consist of curved waveguides closed on themselves to form a loop. A microring resonator works also in the absence of the inner dielectric boundary, as it is confirmed by the existence of microdisk and microsphere resonator. Some examples of the micro-resonators that have been proposed are shown in Fig. 1.9. When

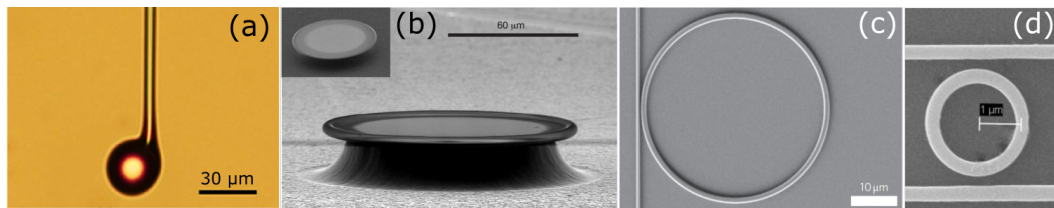


Fig. 1.9: Some examples of the micro-resonators that have been demonstrated. (a) Silica microsphere. Adapted from [63], CC BY-NC-SA 3.0. (b) Silica microtoroid. Reprinted by permission from Macmillan Publishers Ltd: Nature Photonics [64], Copyright 2003. (c) Silicon nitride microring resonator in the all-pass configuration. Reprinted by permission from Macmillan Publishers Ltd: Nature Photonics [65], Copyright 2010. (d) Silicon microring resonator in the add-drop configuration. Adapted with permission from [66]. Note the size difference between the different devices, due to the different refractive index of the different material platforms.

dealing with microdisks or with microrings with large waveguides, the propagating modes are said **Whispering Gallery Modes (WGM)**, recalling the original discovery of this kind of structure for sound waves in the whispering gallery of the Saint Paul's Cathedral in London. Typically, light is coupled within the resonator by placing a waveguide (the bus waveguide) close to it. In this way, the evanescent field of the mode propagating in the bus waveguide feels the resonator, and light coupling occurs. When only one bus waveguide is present, the micro-resonator is said in the **all-pass configuration**. This is the configuration of the resonator presented in Fig. 1.9 (c). Another common configuration is the **add-drop configuration**, which has a second coupling waveguide and is equivalent to the Fabry-Perot interferometer [62]. An example is presented in Fig. 1.9 (d).

A micro-resonator supports only a discrete set of wavelengths that coherently-reinforce themselves after successive roundtrips and provide high energy storage inside the cavity. In other words, the supported wavelengths are those that accumulate a phase multiple integer of 2π in a complete roundtrip. This sets a **resonance condition**, which relates the M -th order resonant wavelength λ_M to the cavity length L and to the effective refractive index of the propagating mode n_{eff} [67, 68]:

$$\lambda_M = \frac{n_{\text{eff}}L}{M}, \quad M \in \mathbb{N}. \quad (1.14)$$

The typical transmission spectrum of a micro-resonator in the all-pass configuration is sketched in Fig. 1.10(a). The spectral distance between adjacent resonances

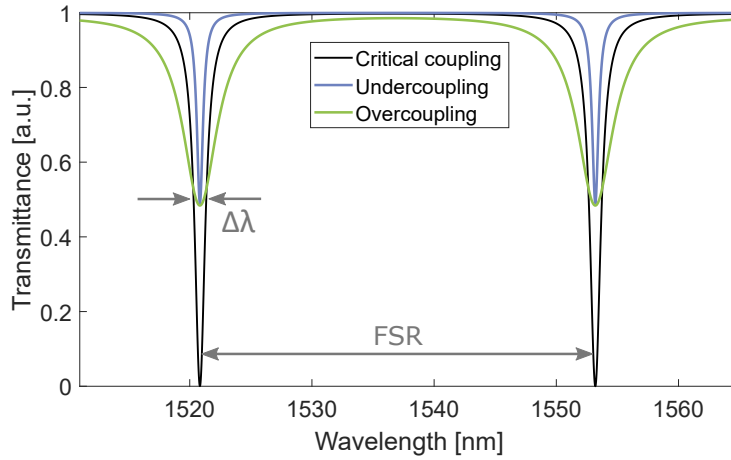


Fig. 1.10: Typical transmission spectra of resonators in the all-pass configuration. The different colors refer to different regimes of the resonator, respectively critical coupling (black), undercoupling (blue) and overcoupling (green).

is called **Free Spectral Range** (FSR). It is related to the group index of the cavity mode n_G by [68]:

$$\text{FSR}_M = \frac{\lambda_M^2}{n_G(\lambda_M)L}. \quad (1.15)$$

The finite linewidth of each resonance is described by the **Full Width at Half Maximum** (FWHM) $\Delta\lambda_M$, which in turn defines the resonance **quality factor** Q_M as [59]:

$$Q_M = \frac{\lambda_M}{\Delta\lambda_M}. \quad (1.16)$$

The quality factor is related to the attenuation rate in the cavity α by [59]:

$$Q_M = \frac{2\pi c}{\lambda_M} \frac{1}{\alpha(\lambda_M)}. \quad (1.17)$$

The attenuation rate in the resonator can be due to intrinsic losses α_i (which consist of material absorption, bending losses, scattering losses, surface absorption) and to

extrinsic losses α_e (due to the coupling to the bus waveguide). From this definition, intrinsic and extrinsic quality factors are defined:

$$Q_{M,i} = \frac{2\pi c}{\lambda_M} \frac{1}{\alpha_i(\lambda_M)} \quad Q_{M,e} = \frac{2\pi c}{\lambda_M} \frac{1}{\alpha_e(\lambda_M)}, \quad (1.18)$$

which are related to the total quality factor by $Q_M^{-1} = Q_{M,i}^{-1} + Q_{M,e}^{-1}$. Comparing the intrinsic and the extrinsic quality factor allows determining the operating regime of the resonator. If $Q_{M,i}/Q_{M,e} > 1$, coupling losses exceed the intrinsic losses, and the resonator is in the **overcoupling** regime. When $Q_{M,i}/Q_{M,e} < 1$, the resonator is in the **undercoupling** regime. When $Q_{M,i} = Q_{M,e}$ (and so $\alpha_i = \alpha_e$) the resonator is **critically coupled**. It can be shown that the resonator operating regime strongly affects also the resonator spectrum. In Fig. 1.10 the transmission spectra of a resonator in the all-pass configuration are shown in all the possible regimes. In the critical coupling regime, the spectrum shows a dip going to zero transmission. In the overcoupling regime, the resonance is wider and does not go to zero. In the undercoupling regime, the resonance is narrower and still does not approach zero.

1.2.3 Third order nonlinear integrated platforms

In this section, the most common material platforms investigated to study third order nonlinear effects are introduced. Third order nonlinearities have been largely investigated because they are possible in all the materials, even in the centrosymmetric ones. Table 1.1 shows the nonlinear coefficients of the nonlinear materials treated in this section. Instead of showing the third order nonlinear susceptibility $\chi^{(3)}$, the Kerr coefficient n_2 and the TPA coefficient β_{TPA} are shown, since they are the values usually reported in literature. The corresponding susceptibilities can be derived using Eq. (1.10).

When dealing with third order nonlinear optics, an important parameter is the so-called nonlinear coefficient $\gamma_m^{(3)}$, which is defined by [59]:

$$\gamma_m^{(3)} = \frac{2\pi}{\lambda} \frac{n_2}{A_{\text{eff},m}}. \quad (1.19)$$

This coefficient considers that a strong nonlinearity can result from both high material nonlinearity n_2 as well as small effective area $A_{\text{eff},m}$ (and so large modal confinement).

Optical fibers. Optical fibers are the first integrated structures where nonlinear optics was studied. The original intent was to reduce nonlinear effects, to limit pulse degradation in long-distance communications. Afterwards, nonlinear fiber optics was developed to exploit the high field confinement achievable in integrated structures. However, the diameters of single-mode optical fibers developed for

Tab. 1.1: Nonlinear parameters of some platforms used in integrated nonlinear optics evaluated at wavelengths around 1550 nm.

Material	n_2 [$10^{-20} \text{ m}^2/\text{W}$]	β_{TPA} [$10^{-15} \text{ m}/\text{W}$]	FOM
Silica glass [69]	2.6	Negligible	$\gg 1$
Silicon Oxynitride [70]	7	Negligible	$\gg 1$
Silicon Nitride [71]	24	Negligible	$\gg 1$
Hydex®[69]	13	Negligible	$\gg 1$
AsS [72]	300	6.2	> 200
GeSbS [73]	93	100	6
Crystalline silicon [72]	600	5×10^3	0.8
AlGaAs [72]	1430	4×10^3	2.3

telecom applications typically exceed $10 \mu\text{m}$, therefore nonlinear interaction requires very long fibers. To increase the interaction strength, processes able to fabricate low loss optical fibers with small core diameters have been developed. Nowadays, the most common fabrication technique consists of heating a standard fiber fixed on translational stages that stretch it and reduce the fiber diameter down to tens of nanometers [74].

Nonlinear effects in fibers have been widely investigated in last years. Recent advances demonstrated THG on a conversion bandwidth exceeding 36 nm in tapered fibers [75], as well as parametric amplification of more than 25 dB thanks to FWM [76]. Thanks to the easy tailoring of the GVD, a broad supercontinuum ranging from 780 to 1890 nm was shown [77]. Great results have been obtained also by using photonic crystal fibers, which introduce more degrees of freedom in the engineering process and allow to investigate a large variety of phenomena [78].

Hence, optical fibers shows remarkable nonlinear characteristics, on a platform that possess high flexibility and can be connected with low losses to other optical fibers. However, as reported in Tab. 1.1, silica glass does not possess such a large nonlinearity if compared to other nonlinear platforms. Moreover, according to current fabrication techniques, optical fibers are not suitable for mass production, and they cannot be easily combined with other optical components in a low footprint integrated device. All these characteristics make optical fibers of great interest, but their development is limited to situations where the integration of a high number of optical components is not required.

High index glasses. Miller’s rule predicts a proportionality between the nonlinear parameter and the material refractive index. So, high refractive index glasses have been investigated for the realization of integrated nonlinear optical devices. These include **silicon oxynitride** (SiON), **silicon nitride** (SiN) and a doped glass called **Hydex®** [69, 70]. These platforms are compatible with the extremely developed Complementary Metal–Oxide–Semiconductor (CMOS) infrastructure, the fabrication process dominating integrated electronics. Therefore, devices based on these

technology could rapidly enter in the mass production, due to the presence of a well established infrastructure. As it can be seen from Tab. 1.1, all these platforms possess a nonlinear refractive index larger than the one of silica glass. Moreover, due to the larger refractive index contrast between the core and the cladding materials, a smaller effective area is possible, which in turn determines a larger nonlinear parameter $\gamma^{(3)}$. Furthermore, high index glass platforms possess negligible TPA, which on the contrary compromises the performances of semiconductor material platforms like silicon. Therefore, even if nonlinearity is not as strong as in semiconductors, the pump power can be increased at will, without introducing nonlinear losses. For this reason, these platforms are interesting for integrated nonlinear photonics, and allowed observing complex nonlinear phenomena like frequency combs at telecom wavelengths [65, 79].

Another class of glasses showing interesting properties are **chalcogenide glasses**. They consist of alloys formed by chalcogen elements (like sulfur, selenium, or tellurium) and by network forming elements (like arsenic, antimony, or germanium). Chalcogenide glasses show nonlinear refractive indices comparable with the ones of silicon while keeping low TPA [72, 73]. As it is visible from Tab. 1.1, this determines an interestingly high FOM. However, chalcogenides are characterized by challenging fabrication issues incompatible with CMOS technology, and suffer of limited stability [80]. Therefore, it is difficult to take advantage from this platform for the mass production of nonlinear integrated circuits.

Semiconductors. Semiconductors like **silicon** and **AlGaAs** are the most commonly investigated nonlinear materials. This is mainly motivated by their large nonlinear coefficient at telecom wavelengths. Moreover, due to their large refractive index, they are used to realize high index contrast waveguides, reducing the mode effective area and so increasing the nonlinear parameter. As an example, in silicon waveguides nonlinear parameters $\gamma^{(3)}$ as large as $2 \times 10^5 \text{ W}^{-1}\text{km}^{-1}$ can be obtained, orders of magnitude larger than $1 \text{ W}^{-1}\text{km}^{-1}$, typically available in single mode optical fibers [80].

The biggest limitation of these platforms results from multiphoton absorption processes, the most common of which is TPA. This process causes a saturation of the transmitted power and creates free-carriers, which in turn introduce losses by means of free-carrier absorption [67]. This fact is evidenced by the low FOM shown by semiconductor platforms. A possibility to prevent this process is to move at larger wavelengths, where multiphoton processes become negligible. As an example, in silicon TPA becomes negligible above $2.2 \mu\text{m}$, and this is one of the motivations of the recent interest for **mid-infrared** silicon photonics [81]. Another technique developed to prevent free-carrier absorption relies on the embedding of the waveguide into lateral p-n junction using rib geometries [82]. In this way, by applying a reverse bias to the junction, it is possible to reduce the carrier density and so the effect of

free carrier-absorption.

Among the others, silicon proved as the most attractive semiconductor for nonlinear applications [67]. This is due to both its low cost and the compatibility with CMOS technology, which allows to realize high quality integrated structures. **Nonlinear silicon photonics** showed a rapid development in the last decade. Lots of processes were demonstrated, which include parametric mixing [35, 83, 84], THG [85], parametric amplification [86, 87] and supercontinuum generation [88]. This fostered the development of many fields, among which integrated quantum photonics can be recalled. In the field of integrated quantum photonics, spontaneous FWM in integrated silicon waveguides has been widely used for the generation of quantum states of light [67, 89].

1.2.4 Second order nonlinear integrated platforms

Research in the field of integrated nonlinear optics has been mainly focused on third order nonlinear processes, due to the exiguous number of non centrosymmetric materials where second order nonlinearities are available. However, the use of second order nonlinearities could give interesting outcomes for different reasons. On the one hand, being a lower order effect, smaller powers are required to enable the nonlinear processes. On the other hand, second order nonlinearities can enable nonlinear processes that have interesting features for plenty of applications. As an example, consider the generation of entangled photons, a prominent requirement in quantum photonics. Currently, it is performed in integrated devices using spontaneous FWM. However, an extremely difficult task is to separate the entangled photon pairs from the strong pump peak, since they are spectrally close. By using the second order process SPDC, entangled photon pairs would be produced very far from the pump wavelength, simplifying considerably the filtering process.

In this framework, this section shows a brief overview of the integrated platforms where second order nonlinear processes have been investigated. An overview of the $\chi^{(2)}$ strengths for the main second-order nonlinear materials is shown in Tab 1.2.

Lithium niobate. Lithium niobate (LiNbO_3) is called the *silicon of photonics*, due to its interesting properties and ease of fabrication that make it the ideal candidate for plenty of optical applications [92]. The most interesting property is its strong $\chi^{(2)}$ coefficient, as it is reported in Tab. 1.2. Thanks to it, electro-optic modulators based on Pockels effect have been realized and can be found on the market. Moreover, lithium niobate is a ferroelectric crystal, meaning that its crystalline unit cell possesses a dipole moment. When an intense electric field is applied to the crystal, the structure of the unit cell is inverted, flipping the dipole orientation and so flipping the sign of $\chi^{(2)}$ [36]. The inversion of the $\chi^{(2)}$ sign of can be applied in a periodic way along the crystal, forming the so called periodic poling. This method is commonly used

Tab. 1.2: Comparison between the $\chi^{(2)}$ strengths of the main second order nonlinear materials. For simplicity, the value reported in the table is the largest element of the $\chi^{(2)}$ tensor. Refer to each reference to recover the tensor element which provides the value reported in the table. The reported values have been measured via SHG experiments, using the pump wavelength λ_p reported in the third column of the table, which is close to $1.550\ \mu\text{m}$. Due to Miller's rule, even larger values can be obtained for shorter wavelengths (where the refractive index is larger).

Material	$\chi^{(2)}$ [pm/V]	λ_p [μm]
LiNbO ₃ [90]	39	1.313
LiTaO ₃ [90]	21.4	1.313
KTP [90]	22.2	1.313
AlN [91]	4.7	1.550
GaAs [90]	238	1.533
GaP [90]	73.6	1.313

to introduce phase-matching in frequency conversion processes, and thanks to that efficient generation of entangled photons is possible via SPDC process [93].

The processes described so far can be performed by bulk lithium niobate crystals that can be found on the market. Recently, great effort has been devoted to the realization of lithium niobate waveguides to perform efficient nonlinear processes on an integrated platform. In this framework, the generation and the manipulation of entangled photons on a reconfigurable lithium niobate circuit has been demonstrated [92]. The sketch of this device is shown in Fig. 1.11. Photons are generated by means of an integrated periodically poled waveguide, and reconfigurable manipulation is enabled by integrated electro-optic modulators. However, this circuit is based on conventional bulky structures, and has dimensions of $50\ \text{mm} \times 5\ \text{mm} \times 0.5\ \text{mm}$.

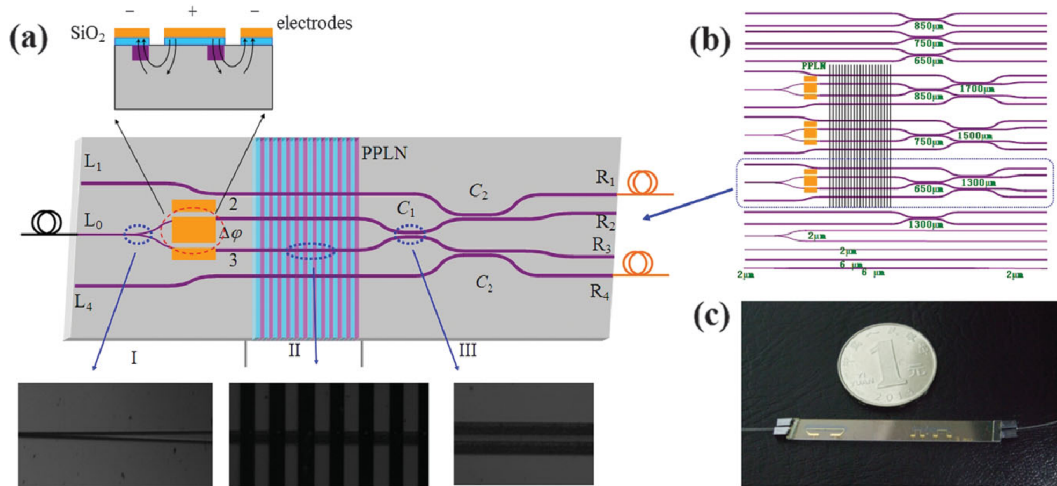


Fig. 1.11: (a) Sketch of the photonic circuit demonstrated in [92]. (b) Sketch of the whole chip. (c) Real picture of the chip with the optical fiber connections to inject and extract light. Reprinted with permission from [92]. Copyright (2014) by the American Physical Society.

More recently, a lot of effort has been put towards the realization of more compact

structures, based on the deposition of lithium niobate layers of thickness in the range 200 nm to 600 nm [94]. On the one hand, this allowed to demonstrate high-performance small-dimension electro-optic modulators: the most recent advances in this field are reviewed in [95]. On the other hand, the SHG process has been studied. Conversion processes based on periodic-poling [96] as well as poling-free mechanisms [97, 98] have been demonstrated. Preliminary results on the generation of entangled photon pairs by SPDC in these structures have been also very recently reported [99].

Plenty of nonlinear processes can be enabled in lithium niobate, and this makes it as one of the most promising material platforms. One of the biggest limitations is its cost, which makes difficult to really conceive it as the new silicon for integrated photonics.

Other nonlinear crystals. In bulk optics, also other materials have been investigated for second order nonlinear processes, like lithium tantalate (LiTaO_3) and potassium titanyl phosphate (KTP). Table 1.2 shows that their nonlinear strength is comparable with the one of lithium niobate. However, to the best of our knowledge, results on the integration of these platforms have been never reported so far.

Aluminum nitride. Another interesting material for the realization of integrated second order nonlinear devices is aluminum nitride (AlN). SHG has been demonstrated both in straight waveguides and in resonators [91], measuring a $\chi^{(2)}$ of 4.7 pm/V. More recently, also SPDC has been demonstrated in a microring resonator [100]. The authors demonstrated also the potential of this process as a source of heralded photons for quantum information, measuring the second-order correlation function of the down-converted photons. A scheme of the device used in this work is sketched in Fig. 1.12.

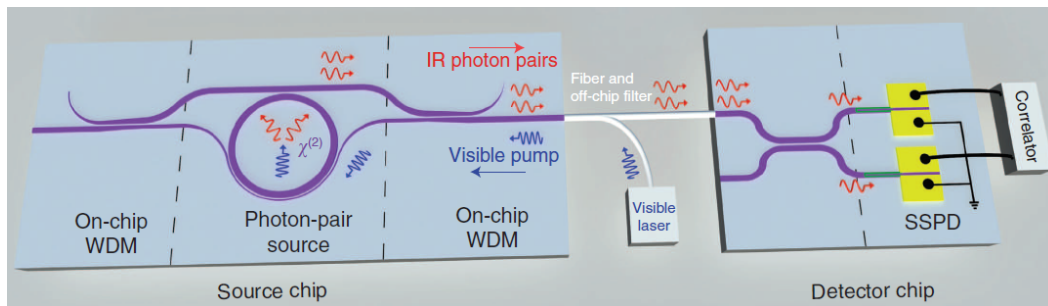


Fig. 1.12: Scheme of the AlN source of photon pairs described in [100]. Infrared photon pairs are generated in a AlN microring resonator from a visible pump. On a second chip, photon pairs are split and detected by Superconducting Single-Photon Detectors (SSPDs). A correlator is used to perform coincidence measurements. Adapted from [100], CC BY-NC-ND 4.0.

(Aluminum) gallium arsenide. Another interesting platform for second order nonlinear photonics is gallium arsenide (GaAs) and all its alloys like aluminum-gallium-arsenide (AlGaAs). Depending on the alloy concentration the nonlinear strength of these materials can strongly differ. In any case, very large nonlinear coefficients can be obtained, like it is reported in Tab. 1.2. In this framework, an efficient SHG process has been recently demonstrated in GaAs waveguides [101]. In this case, an intermodal phase-matching mechanism has been adopted, studying the conversion between the fundamental TE mode and the fundamental TM mode.

This platform can admit another phase-matching mechanism, based on the fact that its crystalline structure possesses the $\bar{4}$ symmetry. For materials with this symmetry, rotations of 90° about the $\bar{4}$ axis are equivalent to crystallographic inversions. So, in curved geometries like microresonators, the propagating field feels 4 crystallographic inversions per round-trip. This method can be used to introduce phase-matching in frequency conversion processes. Based on this concept, SHG has been demonstrated in GaAs microdisks [102] as well as in snake-shaped waveguides [103].

Gallium phosphide. Also gallium phosphide (GaP) can be considered for its nonlinear properties, as indicated by the strength of the nonlinear parameter reported in Tab. 1.2. SHG in an integrated GaP microresonator has been very recently demonstrated [104]. Since also GaP possesses a $\bar{4}$ symmetry, the possibility of realizing SHG using $\bar{4}$ phase-matching techniques has been also proposed [105].

Centrosymmetric materials. The material platforms described in this section possess a nonzero $\chi^{(2)}$ because they have a non-centrosymmetric crystal structure. On the contrary, in centrosymmetric crystals $\chi^{(2)} = 0$. This is the case of all the material platforms described in Sec. 1.2.3, and that is why third order nonlinearities have been mainly studied in that case.

However, many attempts have been done to introduce second order nonlinearities also in centrosymmetric materials. Most of these attempts deal with the centrosymmetry breaking. For example, recent experiments showed SHG in fiber nanowires, caused by the molecular anisotropy at the glass-air boundary [106].

Some attempts have been done also for the study of second order nonlinearities in high index glasses. For example, in SiN waveguides the inversion symmetry at the waveguide boundary has been studied, resulting however in a very limited second order nonlinear susceptibility [107, 108].

The possibility to introduce second order nonlinearities has been strongly investigated also in silicon. This mainly deals with the compatibility with the CMOS technology, which could provide a rapid entrance in the mass production of silicon-based devices, differently from the other platforms treated in this section. The mainly investigated approach to introduce $\chi^{(2)}$ in silicon considered the application of straining layers on the top of silicon waveguides, aimed at breaking its centrosym-

metric crystal structure. This led to the demonstration of Pockels effect and SHG in silicon waveguide strained by SiN cladding, opening the research field of **strained silicon photonics** [67]. However, some ambiguities in the reported results have been recently shown, opening a debate in the scientific community on their real interpretation. The work of this thesis fits within this field. So, this topic will be introduced in detail in the next section.

1.3 Second order nonlinear silicon photonics

As recalled many times in this chapter, the attractive photonic properties of silicon lack of an usable $\chi^{(2)}$. To overcome this limit, it is required to perturb its centrosymmetric structure. To achieve this goal, many efforts have been done in recent years. Most of them are based on the use of strain layers deposited on the top of waveguides, and will be treated in this section. All the studies reported so far deal with Pockels effect and SHG. So, these effects are treated here separately. This gives the chance to introduce also the strong debate that recently opened on the interpretation of the measured effects. The work developed in this thesis really fits within this topic, and is also introduced in detail in this section.

1.3.1 Pockels effect in silicon waveguides

The pioneers of Pockels effect in silicon. The first study on second order nonlinearities in silicon goes back to 2006, when the demonstration of Pockels effect was claimed for the first time [109]. In this work, the authors investigated a silicon photonic crystal waveguide with a SiN stressing layer. A Mach-Zehnder interferometer (MZI) was used to detect the refractive index variation induced by a DC field applied to one of the two MZI arms. This effect was ascribed to Pockels effect, enabled by an effective $\chi^{(2)} \simeq 15 \text{ pm/V}$ introduced by the straining overlayer. A sketch of the waveguide used in this work is shown in Fig. 1.13(a).

The outcomes resulting from this work were extremely promising for the realization of silicon-based electro-optic modulators based on Pockels effect. Such a goal was desirable for many reasons, and offered many advantages if compared to modulation techniques based on thermo-optic or carrier dispersion effects. These advantages are mostly based on the fact that a Pockels electro-optic modulator does not involve the physical movement of carriers. This can enable ultrafast modulation speed beyond 1 GHz, but also a reduced power consumption in the application of the driving voltage. All these aspects, together with the strong measured $\chi^{(2)}$ (not so far from the value of lithium niobate, see Tab. 1.2), officially opened the strained silicon photonics research field, and motivated plenty of studies in the following years. Optimizing the waveguide geometry and the cladding deposition techniques, the

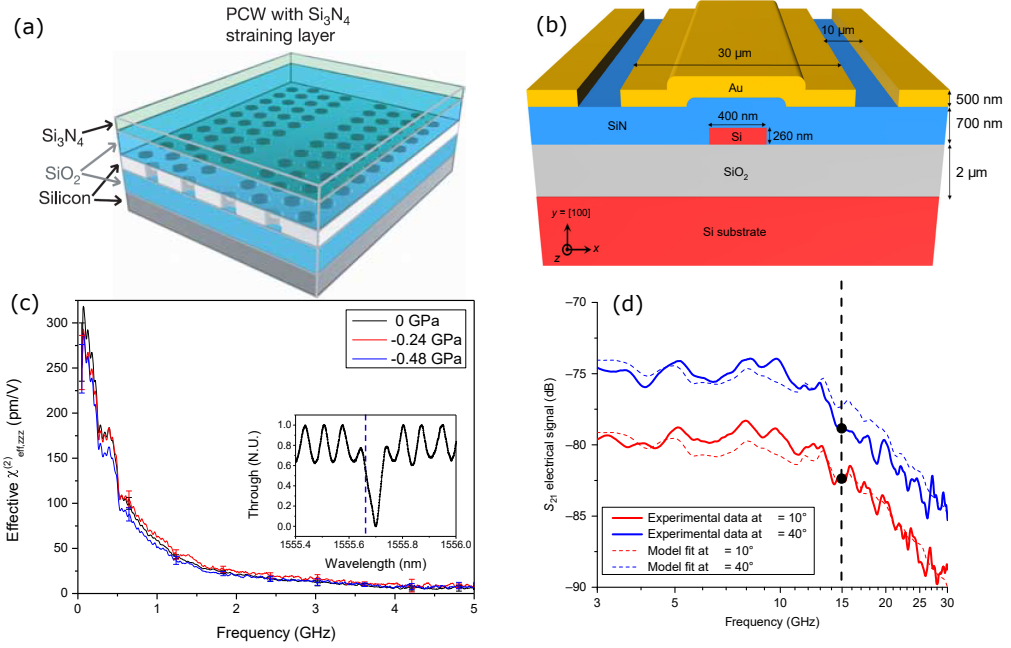


Fig. 1.13: (a) Sketch of the photonic crystal waveguide used in [109]. Reprinted by permission from Macmillan Publishers Ltd: Nature [109], Copyright 2006. (b) Sketch of the strained waveguide used in [110]. Reprinted from [110], CC BY 4.0. (c) $\chi^{(2)}$ strength as a function of the electrical modulation frequency. For high frequency modulations, the nonlinear strength is below noise. Reproduced from [111]. (d) High frequency electro-optic effect measured on waveguides with different crystallographic orientations. Reprinted from [110], CC BY 4.0.

various elements of the $\chi^{(2)}$ tensor were reported, and a $\chi^{(2)} \simeq 190$ pm/V was demonstrated [112, 113]. The spectral dependence of $\chi^{(2)}$ was also measured, showing an increasing behavior with wavelength. A value of $\chi^{(2)} \simeq 340$ pm/V was measured at the wavelength of $1.63 \mu\text{m}$ [114]. Table 1.3 reports an overview of the different $\chi^{(2)}$ values measured from Pockels effect in strained silicon waveguides. A sketch of the typical waveguides used in these works is shown in Fig. 1.13(b).

Tab. 1.3: Overview of the different $\chi^{(2)}$ values measured from Pockels effect in strained silicon waveguides and reported in literature.

Reference	Year	$\chi^{(2)}$ [pm/V]
[109]	2006	15
[112]	2011	122
[113]	2013	190
[114]	2014	340
[111]	2015	< 8
[110]	2018	1.8

Theoretical description of Pockels effect in silicon. Many efforts were devoted to the derivation of a theoretical model able to describe the measured effects.

In the first work on this topic the authors develop a simple model, which relates $\chi^{(2)}$ to the **strain gradient** inside the material [115]. This strain gradient determines a charge redistribution, which in turn induces a net electric field E_{net} . The model developed in [115] shows that one can write $\chi^{(2)} \sim \chi^{(3)} E_{\text{net}}$. The authors use Coulomb's law to estimate E_{net} , and with a stress value of 1 GPa they estimate $\chi^{(2)} \sim 0.02 \text{ pm/V}$, much lower than the values reported in the experiments. In a more recent work the authors confirm that, while this model works properly for materials with intrinsic $\chi^{(2)}$ like GaAs, it underestimates $\chi^{(2)}$ in strained silicon structures [116]. The authors try to clarify this discrepancy, and they attribute it to the SiN cladding, which possesses a large nonlinear polarizability. Due to this last, when a strain gradient is applied, the bonds suffer a small reorientation, which can generate a large $\chi^{(2)}$.

Also other theoretical works have been reported. One of these suggests to write the $\chi^{(2)}$ tensor elements as a linear combination of the components of the strain gradient tensor, using fifteen independent coefficients [117]. However, these coefficient can not be theoretically derived, but need to be fitted to experimental measurements. Another model was based on the sp³ bond-orbital theory [118]. In this model, the relationship between the $\chi^{(2)}$ tensor and the strain gradient only depends on two parameters, which can be theoretically estimated. This model succeeded in the estimation of the photoelastic effect, but the predicted value of $\chi^{(2)}$ varies between 0.1 pm/V and 0.3 pm/V, much smaller than the experimental values reported so far. Recent studies raised many doubts about the interpretation of the $\chi^{(2)}$ measurements described so far, and, consequently, on the theoretical estimations that are in turn based on these questionable measurements.

Ambiguities of the reported results. In [119] the authors show that the phase-shift measured in all the previous experiments could be attributed to the free-carrier accumulation inside the waveguide. The accumulation is induced by the applied DC field, but also depends on the surface charged layer present at the waveguide interface. This charged layer is due to the creation of dangling bonds during the deposition of the SiN cladding, which determine the presence of a positively charged layer at the interface between silicon and the SiN cladding.

In order to disentangle Pockels effect from free-carrier induced effects, an AC field in the GHz range has been applied instead of the usual DC field. In this frequency range, only the contribution due to $\chi^{(2)}$ is expected, since the free-carrier modulation speed limits to hundreds of MHz [111]. The experiment was performed on a racetrack resonator. As reproduced in Fig. 1.13(c), no evidence of Pockels effect was shown. The noise level of the measurement allowed to set an upper limit to

the strain-induced $\chi^{(2)}$ at (8 ± 3) pm/V. More recent works offered new proofs of this interpretation, based on experimental observations that are confirmed by simulations [120, 121].

Recent advances on Pockels effect in silicon. Very recently, a new contribution in the field of Pockels effect in strained silicon waveguides has been reported [110]. This shows a high-speed electro-optic measurement, which allows disentangling the fast nonlinear effect from the slow free carrier dispersion effect. Based on this, the authors report a strain-induced $\chi^{(2)}$ of about 1.8 pm/V. The authors show also a dependence of the measured effect on the waveguide orientation, and they attribute this to occurrence of the Pockels effect, whose strength depends on the silicon crystal direction. Figure 1.13(d) reproduces the high frequency measurement reported in [110] for two different waveguide orientations. The coefficients connecting strain gradients to the strain-induced $\chi^{(2)}$ are fitted from the experiment according to the theoretical model proposed in [118]. Even if the order of magnitude is the same, the coefficients estimated from the experimental fit are at least 2 – 3 times larger than the ones resulting from the ab-initio calculations shown in [118]. Moreover, to definitely attribute this result to Pockels effect, the occurrence of the DC Kerr effect should be excluded.

In other works, different methods to induce $\chi^{(2)}$ have been proposed. As an example, in [122] the authors show the surface activation of $\chi^{(2)}$ induced by means of an HBr dry etching process, which is fully compatible with the CMOS technology. The authors report a $\chi^{(2)} \sim 9$ pm/V. More recently, another work reported on the possibility to integrate on silicon barium titanate (BaTiO_3 , or BTO) [123]. This ferroelectric material possess a very large nonlinearity, and allowed to measure Pockels effect with $\chi^{(2)} \sim 1800$ pm/V.

1.3.2 SHG in silicon waveguides

SHG in strained silicon. Strained silicon waveguides have been also investigated as a platform to study SHG. In the first report on SHG in strained silicon, a $\chi^{(2)}$ of (40 ± 30) pm/V has been demonstrated [124]. A SEM image of the waveguide used in this experiment is shown in Fig. 1.14(a). The experiment was performed using pump wavelengths above $2\mu\text{m}$ in highly multimodal waveguides, without considering any phase-matching technique. Figure 1.14(b) reproduces the measured spectrum, showing both the pump and the SH pulses.

However, more recent experiments showed that not only strain can cause the measured SHG. Like for Pockels effect, also in this case charged defects trapped in the SiN cladding can contribute. In this case, charges introduce a DC field E_{DC} in the waveguide. This DC field couples to the pump wave through $\chi^{(3)}$, generating

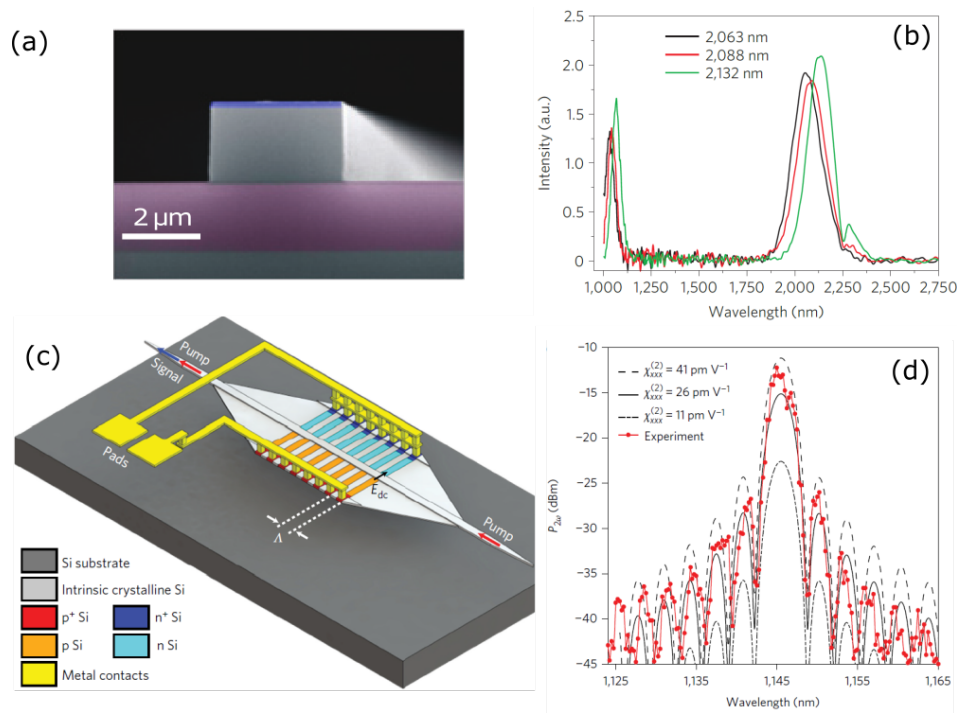


Fig. 1.14: (a) SEM image of the input facet of the waveguide studied in [124]. (b) Spectrum showing the pump and the SHG signal, as it is reported in [124]. (c) Sketch of the device proposed in [125] to exploit EFISH using lateral p-n junctions. (d) Comparison between the measured SH spectrum and calculations done using different values of $\chi^{(2)}$. Panels (a-b) are reprinted by permission from Macmillan Publishers Ltd: Nature Materials [124], Copyright 2012. Panels (c-d) are reprinted by permission from Macmillan Publishers Ltd: Nature Photonics [125], Copyright 2017.

an effective $\chi_{\text{EFISH}}^{(2)} = 3\chi^{(3)}E_{DC}$ known as the Electric-Field-Induced SHG (EFISH) [126]. Both strain and EFISH contribute providing the same final effect. A clear disentanglement between their respective contributions is still lacking. A complete knowledge of the contributions of strain and charged defects could offer a milestone in the future development of this field.

In this thesis, this topic is treated deeply, trying to offer a clear picture on the relative strength between strain and EFISH.

Field-induced SHG in silicon. EFISH is a nonlinear process with a $\chi^{(3)}$ origin, but its outcome is the same as a bulk $\chi^{(2)}$ process. So, this process can be directly exploited to realize second order nonlinear processes. In strained silicon waveguides, EFISH is a passive process that originates from the presence of trapped charges accumulated during SiN deposition. However, waveguides where EFISH is actively introduced have been also demonstrated.

In [125], the authors proposed to use rib waveguides, inducing the DC field by lateral p-i-n junctions. The periodic separation of the junctions along the waveguide propagation direction allowed to introduce a periodically varying DC field, able to

quasi-phase-match the pump and the generated signals. The sketch of this waveguide is shown in Fig. 1.14(c). Using this approach, a $\chi_{\text{EFISH}}^{(2)} \sim 41 \text{ pm/V}$ has been estimated. Even if requiring to actively apply the DC field, this method allows to introduce a larger effective $\chi^{(2)}$ if compared to the strained silicon approach. Moreover, the quasi-phase-matching technique allows to study the conversion between fundamental optical modes, providing in this way a larger conversion efficiency. The spectrum of the measured SH signal is shown in Fig. 1.14(d).

Due to these aspects, this method is acquiring more and more interest. As an example, in [127] the authors propose to use the same approach to investigate SHG in silicon microresonators.

Also in this thesis this method is investigated in detail. Compared to [125], additional waveguide geometries are proposed. Furthermore, the possibility to investigate also the opposite process (namely, SPDC) is also studied.

1.4 This work

This thesis work was performed within two projects. SIQURO project studied silicon-based integrated quantum photonic circuits for different applications, ranging from quantum computing to secure communications [128]. Nemo project investigates optical frequency combs in quadratic media, with particular attention to the silicon integrated platform [129]. The manuscript is organized in three parts.

Part I studies the effect of strain on integrated optical structures. The study carried on in this part aims both at characterizing a device able to introduce mechanical load in integrated optical structures, as well as at developing a simulation tool able to describe the effect of strain in integrated structures. In **Chapter 2** the experimental characterization of a set of silicon racetrack resonators is shown. A mechanical load is applied, and the effect on the resonator transmission spectrum is measured. Then, in **Chapter 3**, the effect of the mechanical load is modeled. These simulations take into account the possible effects that affect the optical properties of the resonator, mainly the waveguide deformation and the photoelastic effect. Good agreement is found between the simulation and the experiment, proving that this simulation tool can be used to model the effect of strain on integrated optical structures.

Part II is dedicated to the study of SHG in strained silicon waveguides. **Chapter 4** introduces the theoretical framework of SHG in waveguides. Then, the waveguide engineering procedure used to design the waveguides is described. The technical details of the SHG experiment are then described in **Chapter 5**, showing also the characterization of the SHG process. The two successive chapters are dedicated to the study of the origin of this process. **Chapter 6** investigates the role of strain on the measured effect. The SHG process is studied under the effect of an external mechanical load, and experimental results are interpreted also by the comparison

with simulations. **Chapter 7** studies the effects on SHG of the charges trapped at the waveguide borders, which introduce a static electric field in the waveguide that enables the EFISH process. UV treatment is applied to remove these charges, and the effect on SHG is studied. The complete suppression of the SHG signal after the UV treatment, together with the independence of the SHG efficiency on the applied strain, demonstrates the main role of charges on the measured SHG.

The main outcome of the study shown in Part II is that, even if the waveguides are designed to introduce a mechanical strain that can break the crystal centrosymmetry, the origin of the measured SHG has to be attributed to charges trapped at the interface, which introduce a static field within the waveguide. Clearly, this is not the most efficient way to introduce static fields in the waveguide. In **Part III** a more efficient way to introduce static fields inside waveguides is studied. The first approach consists of using silicon rib waveguides with lateral p-n junctions. By polarizing the junctions, a static field is introduced. In **Chapter 8** this kind of geometry is characterized both theoretically and experimentally by considering silicon racetrack resonators with lateral junctions, and studying the effect of the junction polarization on the resonator transmission spectra. **Chapter 9** applies this configuration to SHG. First, SHG theory is adapted to the new waveguide geometry, which also introduces the periodic poling as a method to satisfy phase-matching. Then, the waveguide engineering procedure is shown. This chapter considers also the possibility to perform the opposite process, namely the SPDC process. The experimental characterization of SHG is then shown in **Chapter 10**. Using a similar approach, **Chapter 11** studies the possibility to perform SHG and SPDC in silicon oxynitride waveguides. In this case, being silicon oxynitride a dielectric, the static field is applied by means of metallic pads. This platform, even if less efficient in terms of the nonlinear strength, can offer advantages for the experimental measurement of these effects.

Finally, **Chapter 12** draws conclusions and shows perspectives of this work.

The results described in this work have been obtained thanks to the collaboration with different people, most of which are or have been part of the NanoScience Laboratory. At the beginning of each chapter, I specify the role of everyone. In general, I mainly dealt with the design and the modeling of the integrated optical structures described in this work, as well as with their experimental characterization.

Part I

Tunable mechanical load in waveguides

In this part, the effect of strain on integrated optical structures is studied. This study aims both at characterizing a device able to introduce mechanical load in integrated optical structures, as well as at developing a simulation tool able to describe the effect of strain in integrated structures.

In **Chapter 2** the experimental characterization of a set of silicon racetrack resonators is shown. A mechanical load is applied, and the effect on the resonator transmission spectrum is measured.

In **Chapter 3**, the effect of the mechanical load is modeled. Good agreement is found between the simulation and the experiment, proving that this simulation tool can be used to model the effect of strain on integrated optical structures.

Strain effects on microresonators

2.1	General features	34
2.1.1	The experimental setup	34
2.1.2	The structures under test	34
2.2	Basics of the linear theory of elasticity	35
2.3	Macroscopic simulation of the device	38
2.3.1	Description of the model	38
2.3.2	Validation of the model	39
2.4	Effect of strain on the resonance wavelength	39
2.5	Estimation of the waveguide width	43

In silicon photonics, the role of strain has been investigated for many applications. The most recent and attractive one is related to the possibility of transferring silicon photonic devices to polymeric flexible substrates [130], which offers interesting features for the realization of **complex flexible integrated devices**. Silicon-based strain sensors have been realized on standard Silicon-On-Insulator (SOI) substrates [131], on polymeric flexible substrates [132] and on silicon oxide membranes [133]. Straining layers have been also deposited to control the photoelastic variation of the waveguide refractive index, balancing the geometric birefringence and realizing **polarization insensitive devices** [134]. More interestingly for the purpose of this work, straining layers have been used to **break the centrosymmetry** of silicon, introducing second order nonlinear optical effects [67].

This chapter analyzes the role of strain in integrated devices. The strain is applied in a controlled way by using a micrometric screw, which causes the sample to bend. The experimental setup and the analyzed devices are described in Sec. 2.1. In Sec. 2.2, the basic principles of the linear theory of elasticity are introduced. Section 2.3 shows the macroscopic simulation describing the sample bending. In Sec. 2.4 the experimental results on the strain-induced resonance shift are presented. Finally, Sec. 2.5 analyzes the waveguide deformation and the actual dimension of the device.

The experiments described in this chapter have been performed together with Miss A. Chalyan. The samples used in the experiments have been designed by Dr. M. Borghi and Dr. M. Mancinelli. The samples have been fabricated by Dr. M. Bernard and Dr. M. Ghulinyan at Fondazione Bruno Kessler.

The experiment described in this chapter is also described in [135].

2.1 General features

2.1.1 The experimental setup

The experimental setup used during this work is sketched in Fig. 2.1. The input and the output channels of the analyzed structures are accessed via edge coupling using tapered lensed fibers, passing in a polarization stage before entering into the input waveguide. The sample is mounted on a screw-equipped sample holder, magnified in Fig. 2.2. The source is a continuous-wave laser, tunable around the wavelength of 1600 nm. The detection is performed using an InGaAs amplified detector coupled to a multimeter. Using the screw, a displacement is applied to the central point of the sample along the direction orthogonal to its main plane (z direction), while the displacement on the sides is inhibited along z , causing the bending of the sample. The point load generates a 2-D strain field in the sample, whose components are principally directed along the longest dimension of the chip. A more complete description of the screw-equipped sample holder can be found in [111].

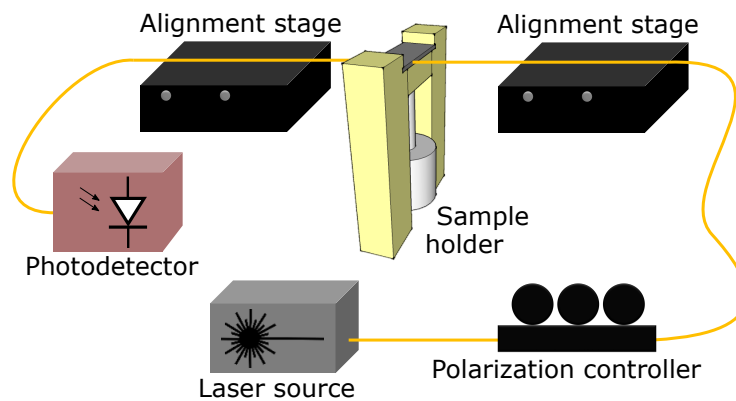


Fig. 2.1: Sketch of the experimental setup. It is formed by a tunable laser source, a fiber polarization controller, an input-output alignment stage, a screw-equipped sample holder and an InGaAs photodetector.

2.1.2 The structures under test

Figure 2.2 shows the top-view of the typical test structure. This was designed to study the strain-induced electro-optic effect in silicon (see more in [111]). The device consists of a racetrack resonator in an add-drop filter configuration designed to work in the Transverse-Magnetic (TM) polarization. It is realized with a 365 nm UV lithography on a 6' SOI wafer, whose cross-section is sketched in Fig. 2.3. Over a 600 μm thick silicon substrate, a 3 μm thick Buried Oxide (BOX) layer forms the lower cladding. All the resonator waveguides have a 243 nm \times 400 nm cross-section,

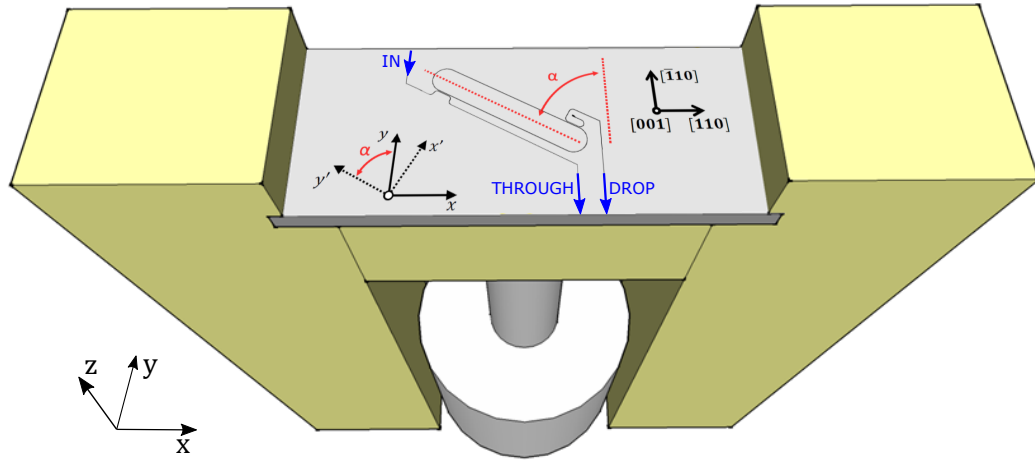


Fig. 2.2: Zoom-in picture of the screw-equipped sample holder. On the sample it is depicted a resonator whose main axis is rotated of an angle α with respect to the y direction. The resonator dimensions are deliberately out of scale.

guaranteeing the single mode operation at wavelengths around 1600 nm^1 . On the waveguide top, a 140 nm thick SiN layer is conformally deposited via Low-Pressure Chemical Vapor Deposition (LPCVD). A 900 nm thick Plasma-Enhanced Chemical Vapor Deposition (PECVD) silica layer forms the upper cladding. The resonators perimeter is $416 \mu\text{m}$, with a straight coupling region length of $12.91 \mu\text{m}$, a curvature radius of $15 \mu\text{m}$ and a 400 nm gap between the resonator and the bus waveguide. The resonators are fabricated with five different orientations with respect to the silicon crystallographic axes, expressed by the angle α indicated in Fig. 2.2. For $\alpha = 0^\circ$ the resonator longest dimension is oriented along the $[\bar{1}10]$ crystallographic direction. The maximum angle is $\alpha = 90^\circ$, corresponding to a resonator oriented along the $[110]$ direction. Other resonators oriented at angles of $\alpha = 30^\circ$, 45° and 60° are present on the sample.

2.2 Basics of the linear theory of elasticity

Consider a material undergoing a small deformation. This deformation can be described by a displacement vector \mathbf{u} , which relates the original position of a point \mathbf{r} with its position \mathbf{r}' after the effect of deformation [117, 136, 137]:

$$\mathbf{u} = \mathbf{r}' - \mathbf{r}. \quad (2.1)$$

¹The waveguide height is evaluated from interferometric measurements. Clearly, this value is affected by fabrication uncertainty. Variations on height and width produce the same outcome, which is a modification of the mode effective index, and it is not possible to disentangle them. However, fabrication uncertainties affect mainly the width rather than the height. So, in the following the waveguide height is always set to its nominal value, considering only variations on the width.

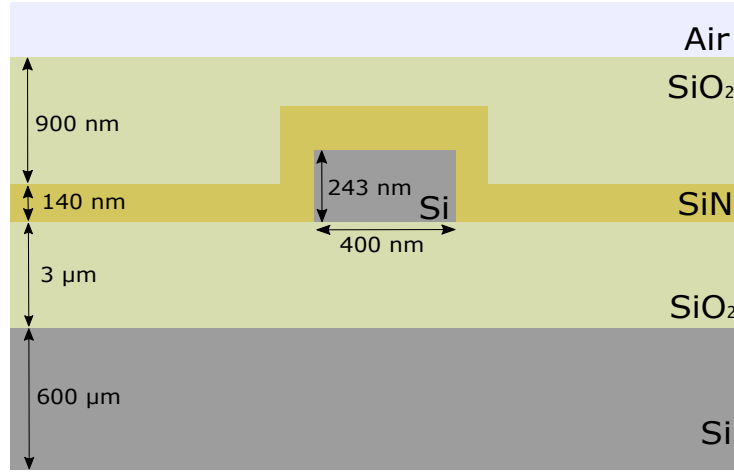


Fig. 2.3: Off-scale picture of the waveguide cross section with nominal dimensions.

In the linear theory of elasticity, this deformation is described by the symmetric **strain tensor** ε , whose elements ε_{ij} are defined by:

$$\varepsilon_{ij} = \frac{1}{2} \left(\frac{\partial u_i}{\partial x_j} + \frac{\partial u_j}{\partial x_i} \right). \quad (2.2)$$

The **volumetric strain** ε_v is defined as the trace of the strain tensor ε . It is often referred as dilatation, since it can be physically interpreted as the local the relative variation of volume ($\Delta V/V$). The volumetric strain is an important quantity, because it is invariant with respect to rotations of the reference system [137].

A deformed material is subject to internal forces, which tend to bring the material back to its undeformed state. The i -th component of the local force F_i is related to the **stress tensor** σ , which is defined by [136]:

$$F_i = \sum_j \frac{\partial \sigma_{ij}}{\partial x_j}. \quad (2.3)$$

The relationship between stress and strain is described by the **generalized Hook's law**, which relates how a material is deformed as a consequence of an applied stress (and vice versa) [138]:

$$\sigma = \mathcal{C}\varepsilon \quad \varepsilon = \mathcal{S}\sigma, \quad (2.4)$$

where \mathcal{C} and \mathcal{S} are called (respectively) stiffness and compliance tensors. In anisotropic materials, these tensors have in general $3^4 = 81$ elements. However, the number of elements can be reduced by considering the material symmetries. In particular, if a material has at least two orthogonal planes of symmetry, the

orthotropic representation can be used. In this case, the relationship between stress and strain can be written as [138]:

$$\begin{pmatrix} \varepsilon_{xx} \\ \varepsilon_{yy} \\ \varepsilon_{zz} \\ \varepsilon_{yz} \\ \varepsilon_{zx} \\ \varepsilon_{xy} \end{pmatrix} = \begin{pmatrix} \frac{1}{E_x} & \frac{-\nu_{yx}}{E_y} & \frac{-\nu_{zx}}{E_z} & 0 & 0 & 0 \\ \frac{-\nu_{xy}}{E_x} & \frac{1}{E_y} & \frac{-\nu_{zy}}{E_z} & 0 & 0 & 0 \\ \frac{-\nu_{xz}}{E_x} & \frac{-\nu_{yz}}{E_y} & \frac{1}{E_z} & 0 & 0 & 0 \\ 0 & 0 & 0 & \frac{1}{G_{yz}} & 0 & 0 \\ 0 & 0 & 0 & 0 & \frac{1}{G_{zx}} & 0 \\ 0 & 0 & 0 & 0 & 0 & \frac{1}{G_{xy}} \end{pmatrix} \begin{pmatrix} \sigma_{xx} \\ \sigma_{yy} \\ \sigma_{zz} \\ \sigma_{yz} \\ \sigma_{zx} \\ \sigma_{xy} \end{pmatrix}, \quad (2.5)$$

where E_i is the i -th component of the **Young's modulus**, ν_{ij} is the ij -th component of the **Poisson's ratio** and G_{ij} is the ij -th component of the **shear modulus**.

Regarding silicon, if cartesian coordinates are aligned with the crystal axes [100], [010] and [001] one can demonstrate that all the E_i , ν_{ij} and G_{ij} are equal [138]. These quantities are reported in Tab. 2.1. If the cartesian coordinates are directed along different axes, the stiffness matrix must be properly rotated [138, 139].

In the case of isotropic crystals, all the E_i , ν_{ij} and G_{ij} are equal [138]. Moreover, in this case the shear modulus is not independent on the other quantities, and it is given by $G = E/[2(1 + \nu)]$ [140]. Furthermore, as expected, rotations along any axis do not affect the stiffness matrix. The isotropic materials analyzed in this work are silicon oxide and silicon nitride, and their elastic parameters are reported in Tab. 2.1.

When affected by deformation, also the refractive index of a material is affected. This effect is known as **photoelastic effect**. In the presence of photoelasticity, the different components of the refractive index can be rewritten as [140]:

$$\begin{pmatrix} n_{xx} \\ n_{yy} \\ n_{zz} \\ n_{yz} \\ n_{zx} \\ n_{xy} \end{pmatrix} = \begin{pmatrix} n_0 \\ n_0 \\ n_0 \\ 0 \\ 0 \\ 0 \end{pmatrix} - \begin{pmatrix} C_1 & C_2 & C_2 & 0 & 0 & 0 \\ C_2 & C_1 & C_2 & 0 & 0 & 0 \\ C_2 & C_2 & C_1 & 0 & 0 & 0 \\ 0 & 0 & 0 & C_3 & 0 & 0 \\ 0 & 0 & 0 & 0 & C_3 & 0 \\ 0 & 0 & 0 & 0 & 0 & C_3 \end{pmatrix} \begin{pmatrix} \sigma_{xx} \\ \sigma_{yy} \\ \sigma_{zz} \\ \sigma_{yz} \\ \sigma_{zx} \\ \sigma_{xy} \end{pmatrix}, \quad (2.6)$$

where n_0 is the refractive index of the unstrained material. The coefficients C_1 , C_2 and C_3 are the so called stress-optic constants, which are related to the mostly used photoelastic coefficients p_{11} , p_{12} and p_{44} by [140]:

$$C_1 = \frac{n_0^3(p_{11} - 2\nu p_{12})}{2E} \quad C_2 = \frac{n_0^3[p_{12} - \nu(p_{11} + p_{12})]}{2E} \quad C_3 = \frac{n_0^3 p_{44}}{2G}. \quad (2.7)$$

Also in this case, for isotropic materials only two coefficients are independent, being $p_{44} = (p_{11} - p_{12})/2$ [140]. The coefficients for the different materials analyzed in this work are reported in Tab. 2.1.

Tab. 2.1: Material parameters used in this work.

	Silicon	Silicon Oxide	Silicon Nitride
Refractive index n (@ 1600 nm)	3.474 ^a	1.443 ^a	1.995 ^a
Young modulus E (GPa)	130 [138] ^b	76.7 [141]	255 [142]
Poisson ratio ν	0.28 [138] ^b	0.186 [141]	0.23 [142]
Shear modulus G (GPa)	79.6 [138] ^b	32.3 ^c	118.6 ^c
Photoelastic coefficient p_{11}	-0.0997 ^d	0.19 ^e	- ^f
Photoelastic coefficient p_{12}	0.0107 ^d	0.27 ^e	- ^f
Photoelastic coefficient p_{44}	-0.051 ^g	-0.04 ^h	- ^f

^a Measured with ellipsometry technique.

^b Referred to the reference system with the axes directions [100], [010], [001]. In [139] and [138] the method used to derive the stiffness matrix along arbitrarily directed axes is shown.

^c Evaluated using $G = E/[2(1 + \nu)]$ (valid for isotropic crystals) [140].

^d Interpolated from measurements taken at $\lambda = 1.15 \mu\text{m}$ and $\lambda = 3.39 \mu\text{m}$ [140].

^e Interpolated from measurements taken at $\lambda = 0.633 \mu\text{m}$ [140] and $\lambda = 1.15 \mu\text{m}$ [141].

^f No data in literature. Since SiN forms a thin cladding, no relevant effective index variations can be obtained varying its photoelastic coefficients. So, the same values as silica are used.

^g Evaluated from [140].

^h Calculated using the relationship $p_{44} = (p_{11} - p_{12})/2$, that is valid for isotropic crystals [140].

2.3 Macroscopic simulation of the device

2.3.1 Description of the model

To compare numerical and experimental results, it is necessary to correctly estimate local strains in the structures due to the sample bending. This estimation is performed with a 3D FEM simulation of the entire sample subjected to a point load using the Structural Mechanics module of COMSOL Multiphysics® software [56]. The waveguides, BOX and cladding layers are 200 times thinner than the $600 \mu\text{m}$ thick silicon substrate, so that the latter is mainly responsible for the overall mechanical behavior of the whole sample. As a consequence, in order to reduce the computational burden, the simulation is limited to the silicon substrate. The simulation boundary conditions are represented in Fig. 2.4. The effect of the screw is considered as a prescribed displacement along z applied to the center of the sample, while the two supports are modeled by a fixed line constraint and by a prescribed zero z displacement line, which prevents the sample being blocked.

Figure 2.4 reports the volumetric strain relative to a mechanical displacement of $150 \mu\text{m}$ applied by the screw. This strain is larger in the center, while approaching the boundaries it decreases and vanishes. The use of the volumetric strain is legitimized by the fact that, from the simulation, it results that the shear components of the stress tensor are at least one order of magnitude smaller than the principal components. The elastic parameters of silicon needed for this simulation, as well as the other material parameters used in this work, are the ones reported in Tab. 2.1.

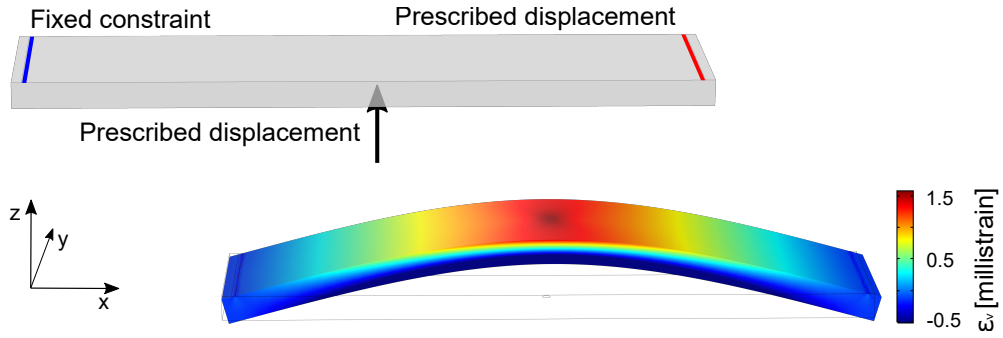


Fig. 2.4: On the top: 3D simulation boundary conditions for beam bending. The prescribed displacement and the fixed constraint on the top represent the supports, while the arrow describes the screw displacement. On the bottom: volumetric strain ε_v superimposed in color scale over the beam deformation evaluated applying a displacement of $150\ \mu\text{m}$ to the sample center. Displacements are emphasized by a factor of 10.

2.3.2 Validation of the model

The degree of accuracy of the 3D macroscopic simulation is validated via experimental measurements. The sample curvature (as a function of the z -displacement) is experimentally measured as illustrated in Fig. 2.5. Similarly to the method proposed in [143], a HeNe laser impinges on the sample surface and is reflected on a screen. Using the micrometer screw, the sample curvature is modified, causing a movement of the spot position on the screen. The reflected beam is deflected by an angle δ . By using simple geometric considerations, it can be shown that $\delta = 2\theta$, where θ is the rotation of the normal to the sample surface. The angle δ is determined as $\delta \sim \Delta H/L$, being ΔH the spot displacement on the screen and L the distance between the mirror M2 and the screen².

Figure 2.6 shows the bending angle as a function of the position on the sample surface for three different applied displacement values. The position x on the sample surface is referred to the center of the sample. The experimental results and the simulation show a good agreement, varying both the position on the sample and the displacement applied by the screw.

2.4 Effect of strain on the resonance wavelength

The output spectrum recorded on the drop port of an analyzed resonator is shown in Fig. 2.7. The FSR is about 1.5 nm. The quality factor varies from resonator to

²This estimation is approximated because the spot displacement is determined not only by the sample deflection, but also by the variation of the beam position on mirror M2. This is caused both by the sample movement Δz in the z direction, and by the distance z_0 between the sample surface and the mirror M2. Since $L = 3.73\ \text{m}$, $L \gg z_0 = 0.1\ \text{m}$. Moreover $\Delta H \gg \Delta z$, being $\Delta H \sim \text{cm}$ and $\Delta z < 150\ \mu\text{m}$. Thus, the approximation $\delta \sim \Delta H/L$ is valid.

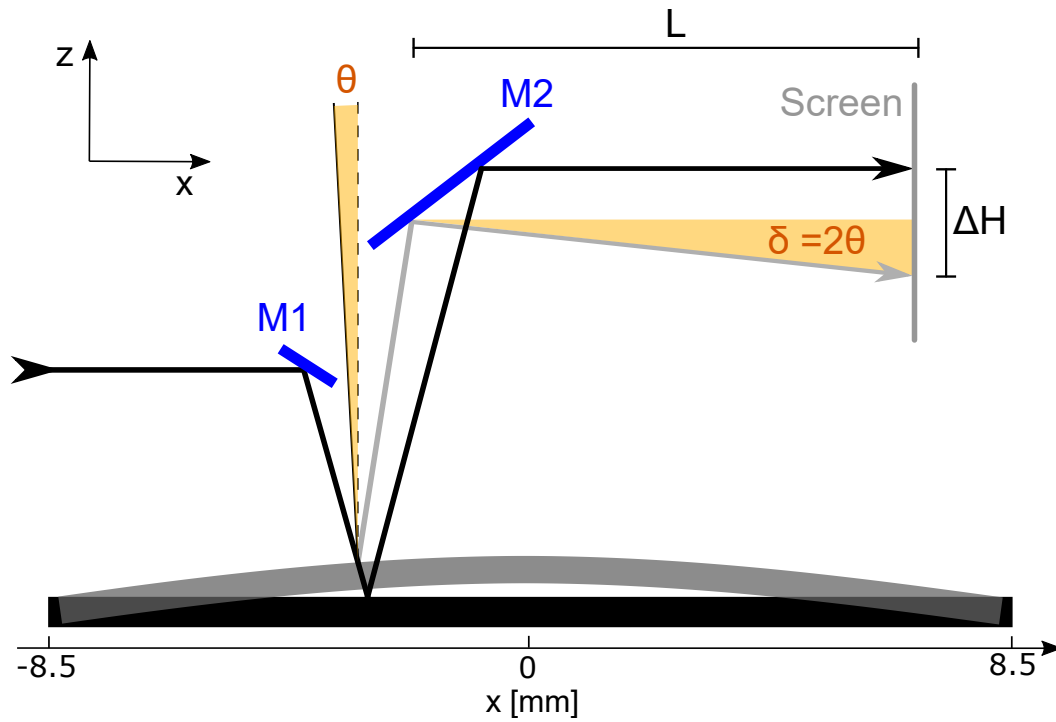


Fig. 2.5: Setup used to measure the sample curvature. The black line describes the HeNe laser path when the sample is undeformed, while the gray path corresponds to the deformed sample.

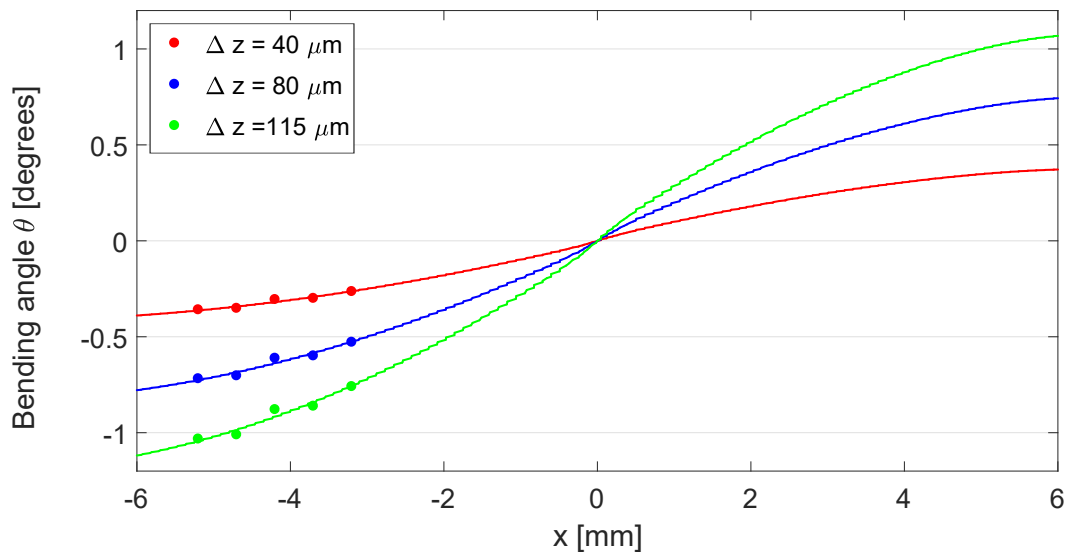


Fig. 2.6: Rotation of the normal to the surface θ as a function of the position on the sample surface for three different screw displacements Δz . The experimental data (points) are compared with simulations (straight lines). Errorbars are smaller than data symbols. The zero reference position along x direction refers to the central point of the sample.

resonator in the range 5000 to 10 000 due to fabrication variations.

In Fig. 2.8 the transmission spectra of two resonators with different orientation angles α are shown as a function of the displacement Δz applied by the screw in the sample center. In the case of $\alpha = 0^\circ$ the strain induces a blue-shift of the resonance,

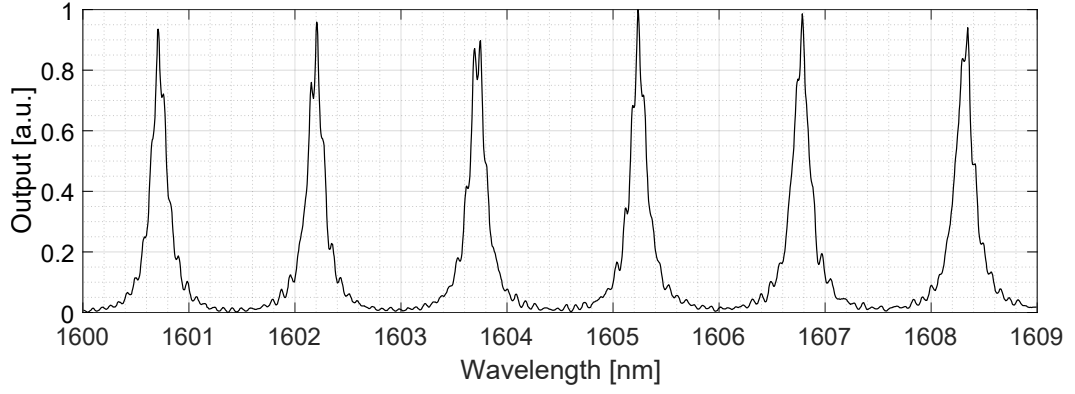


Fig. 2.7: Drop port spectrum of one analyzed resonator.

while it is red-shifted when $\alpha = 90^\circ$.

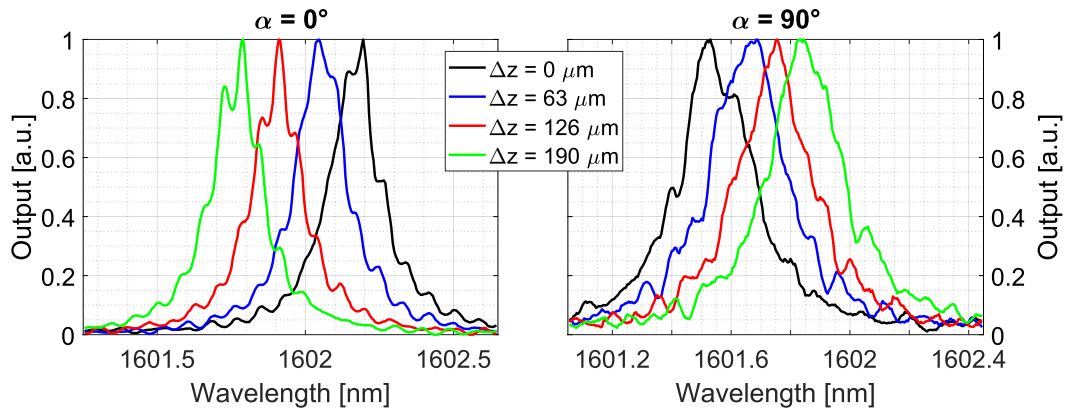


Fig. 2.8: Drop port spectra of two resonators oriented with different angles α . The different colors refer to measurements taken with different Δz .

The same fact can be observed from Fig. 2.9, where the resonance wavelength dependence on Δz is shown. However, the difference between the two measurements is not only the orientation of the resonator, but also its position on the sample. As it can be seen from Fig. 2.4, even if the displacement applied by the screw at the center of the sample is the same, the strain varies considerably in the sample. Therefore, the local strain level experienced by each resonator can be different. For this reason, the resonance shift must be normalized with respect to the local strain acting on each resonator. The local strain is quantified using the 3D FEM simulation described previously and evaluating the volumetric strain ε_v at the location of the resonator. The top axes of Fig. 2.9 show the volumetric strains corresponding to the displacements Δz reported on the bottom axes. The slope of the linear fit curve represents the resonance shift per unit strain. Once this normalization is applied, comparable results can be found from identically oriented resonators located in different positions on the sample (for example, -0.39 ± 0.09 pm/microstrain and -0.32 ± 0.05 pm/microstrain for two identical resonators oriented with $\alpha = 0^\circ$ situated at about 4.2 mm and 1.9 mm from the center of the sample).

In Fig. 2.10 the resonance shift per unit strain is analyzed as a function of α . The

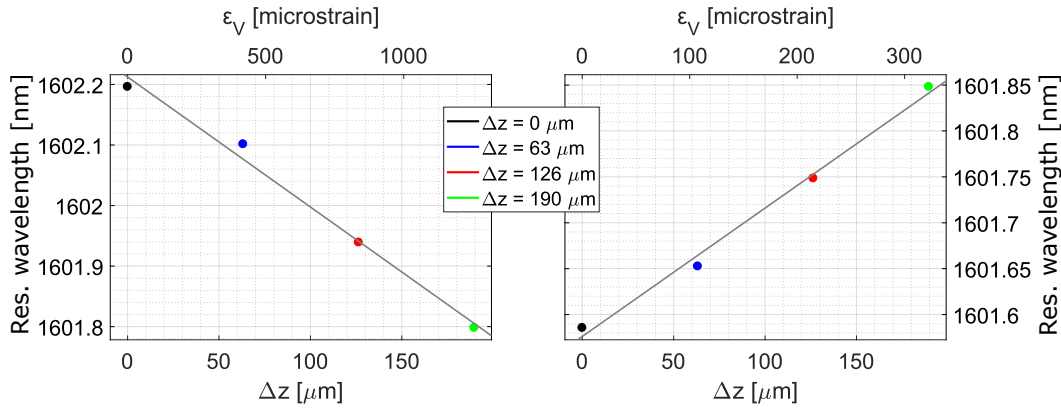


Fig. 2.9: Dependence on Δz of the resonance wavelength evaluated from a Lorentian fit of the spectra. The top axes report the corresponding volumetric strain evaluated from the 3D macroscopic simulation. The gray lines are linear fits of the experimental data.

normalized shift increases monotonically with α , demonstrating that, changing the resonator orientation, it is possible to tune the resonance shift from negative to positive values, as well as to design a strain insensitive resonator.

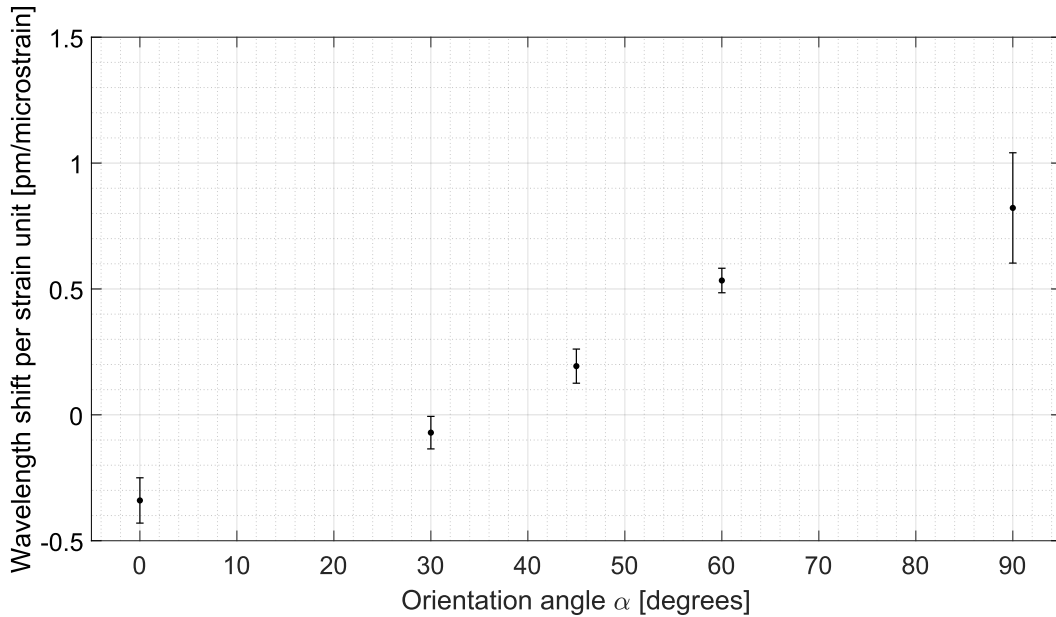


Fig. 2.10: Resonance shift per strain unit for resonators oriented with different angles α . Errorbars represent 95% confidence bounds resulting from the linear fits.

The difference in the errorbars of the measurements reported in Fig. 2.10 derives from two reasons. On the one hand, the error made in the determination of the resonance wavelength is related to the shape of each resonance, that differ from resonator to resonator due to the quality factor difference and to the Fabry-Perot interference caused by the bus waveguide facets, which differ from resonator to resonator. On the other hand, the different errors are determined by the different location of the resonators on the sample. Resonators located close to the sample

border feel a smaller strain and a smaller resonance shift compared to the case if they were located in the center of the sample, determining a larger error in the estimation of the wavelength shift per unit strain. As an example, resonators oriented with angles 0° and 90° are located more closely to the sample border than the other resonators, and so the errorbar on these measurements is larger.

2.5 Estimation of the waveguide width

The left hand side of Fig. 2.11 shows the wavelength dependence of the group index n_g for one analyzed resonator. The experimental values are evaluated from the experimental FSR using Eq. (1.15). The group index is evaluated for different strain levels applied by the screw. The group index variation induced by the applied strain is below the experimental error level, revealing that in this way it is not possible to detect any deformation of the waveguide cross section caused by strain. A similar observation derives from the right hand side of Fig. 2.11, where the experimental wavelength dependence of the quality factor is reported. Any variation of the quality factor caused by strain (such as the variation of the gap between the resonator and the bus waveguide) is below the experimental error.

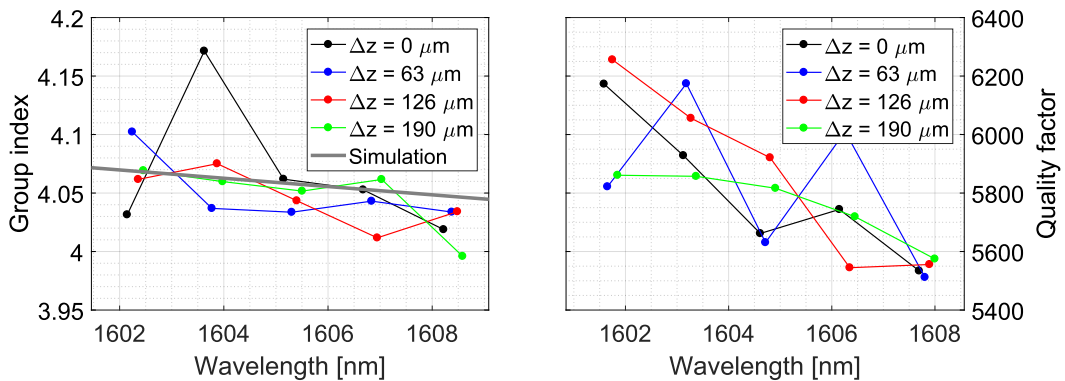


Fig. 2.11: On the left hand side: wavelength dependence of the resonator group index with an orientation angle $\alpha = 60^\circ$. The experimental value is evaluated from the FSR, while the simulated result derives from a FEM simulation of a waveguide with a cross section of $390 \text{ nm} \times 243 \text{ nm}$. On the right hand side: wavelength dependence of the quality factor of the same resonator.

The comparison between the experimental group index and the simulation can provide an estimation of the actual dimensions of the analyzed resonator waveguide. As already remarked, fabrication uncertainties affect mainly the waveguide width rather than the height. Therefore, the waveguide height is set to its nominal value of 243 nm (evaluated from interferometric measurements). The group index dependence on the waveguide width is calculated with a 2D mode solver from the effective refractive index dispersion, and is shown in red in Fig. 2.12. The blue line represents the experimental value of the group index, estimated from the data shown

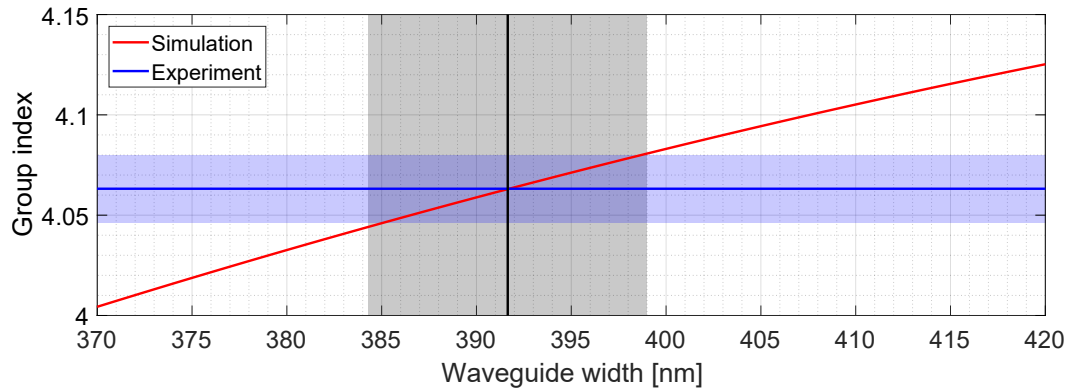


Fig. 2.12: Comparison between the simulated dependence of the group index on the waveguide width (red) and the experimental value (blue), from which the actual width of the waveguide is determined (black). The light colors represent the errorbars.

in Fig. 2.11. From the intercept between the experimental and the theoretical group index the actual waveguide width of the resonator is estimated to be 391 ± 7 nm, slightly smaller than the nominal value of 400 nm. Any variation of the waveguide width caused by strain is below the error of this estimation.

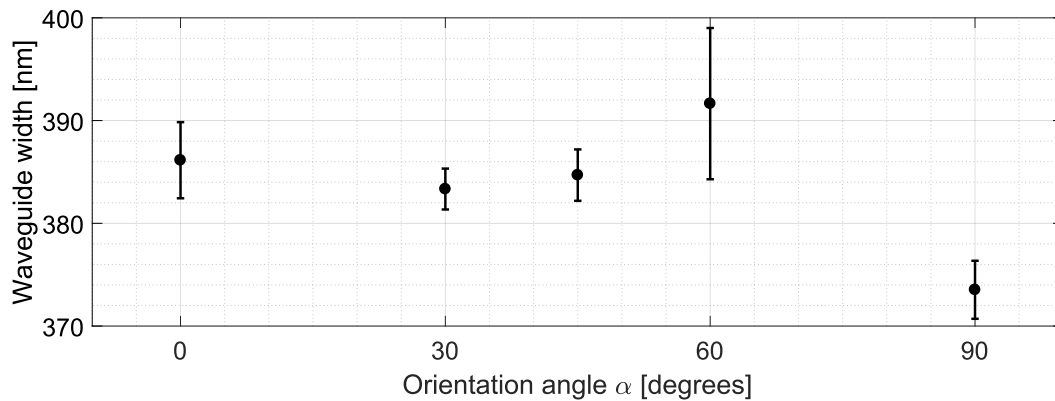


Fig. 2.13: Waveguide width evaluated from the experimental group index for the resonators analyzed in this work.

Figure 2.13 shows the waveguide width evaluated for all the resonators analyzed in this work, providing a mean width of 384 ± 2 nm.

All the simulations reported in the next chapter use the mean experimental group index value ($n_g = 4.08$) and the mean waveguide width ($w = 384$ nm) determined here. This has been done essentially for saving computational time, while it would have been more accurate using the proper waveguide width for each orientation angle. However, such a small variation of the waveguide geometry does not affect the final results reported in the next chapter, which are mainly affected by the variation of the waveguide orientation and so by the variation of the elastic properties of the material.

Modeling the effects of strain on microresonators

3.1	Theoretical model	46
3.2	Contribution of the perimeter variation	47
3.3	Contribution of the refractive index variation	49
3.3.1	Evaluation of strain inside the waveguide	49
3.3.2	Photoelastic variation of the effective refractive index . .	50
3.3.3	Contribution of the waveguide deformation	51
3.4	Comparison with experiments	53
3.5	Conclusion and perspectives	54

In the previous chapter, the experimental characterization of silicon racetrack resonators under the effect of mechanical load has been shown. In this chapter, extending the study proposed in [131] and [143], the origin of the strain-induced resonance shift is analyzed. In this framework, the different effects responsible for the resonance shift are taken into account. The model developed in this chapter considers both mechanical deformation of the device, which affects the resonator perimeter and the waveguide cross-section, and the strain-induced refractive index variation, due to the photoelastic effect.

In Sec. 3.1, the model proposed in [131] is generalized to consider all the effects that can play a role in the strain-induced resonance wavelength shift. Then, Sec. 3.2 and Sec. 3.3 consider separately the effect of mechanical deformation and the effect of the strain-induced refractive index variation. Finally all these effects are put together and compared with the experimental results in Sec. 3.4. In Sec. 3.5 the main conclusions of this work are given, offering also some interesting perspectives. The simulation procedure described in this chapter has been performed thanks to the discussions with Dr. P. Guilleme and Dr. F. Bosia.

The model described in this chapter is also described in [135].

3.1 Theoretical model

The model proposed in [131] is generalized considering also the role of strain in the curved ones parts of the resonator. The resonator resonance condition states that:

$$M\lambda_M = 2Ln_s + 2\pi R\bar{n}_c, \quad (3.1)$$

where M is an integer number, λ_M the M -th resonant wavelength, n_s the effective index of the straight waveguide, L the length of the straight part of the resonator and R the radius (see Fig. 3.1). \bar{n}_c is the mean effective index in the curved section, related to the effective index $n_c(\gamma)$ at a generic angle γ on the curve by:

$$\bar{n}_c = \frac{1}{\pi} \int_0^\pi n_c(\gamma) d\gamma. \quad (3.2)$$

Dealing with photoelasticity this dependence is important because the refractive index components in the different directions depend on strain in different directions.

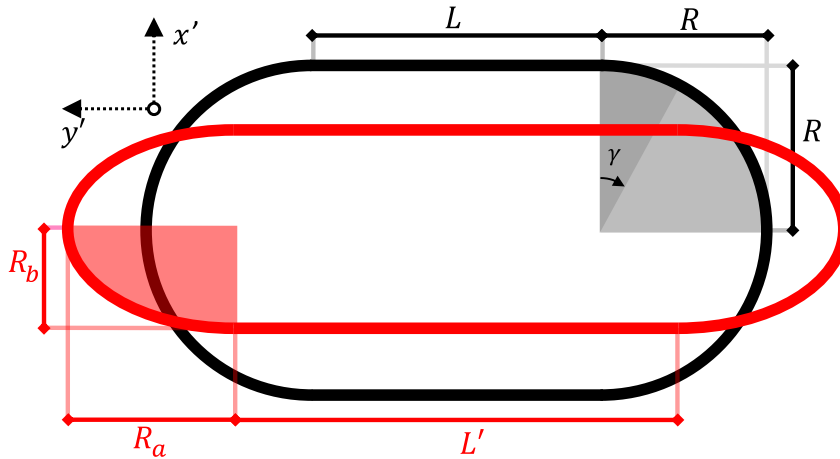


Fig. 3.1: Out of scale model showing the effect of strain on the resonator. The unstrained resonator shape (in black) is modified by strain into the red shape.

Resonance condition (3.1) can be derived with respect to the volumetric strain ε_v . The value of M can be replaced using again Eq. (3.1). Doing this, one must consider that the effective indices depend both on strain and wavelength. So:

$$\frac{d}{d\varepsilon_v} n_s(\varepsilon_v, \lambda) = \frac{\partial n_s}{\partial \varepsilon_v} + \frac{\partial n_s}{\partial \lambda} \frac{\partial \lambda}{\partial \varepsilon_v} \quad \frac{d}{d\varepsilon_v} \bar{n}_c(\varepsilon_v, \lambda) = \frac{\partial \bar{n}_c}{\partial \varepsilon_v} + \frac{\partial \bar{n}_c}{\partial \lambda} \frac{\partial \lambda}{\partial \varepsilon_v} \quad (3.3)$$

Strain has two effects on the effective refractive index: on the one hand it modifies the material refractive index due to the photoelastic effect, on the other hand it deforms the waveguide cross-section. These contributions are separated as follows:

$$\frac{\partial n_s}{\partial \varepsilon_v} = \left. \frac{\partial n_s}{\partial \varepsilon_v} \right|_{\text{ph}} + \left. \frac{\partial n_s}{\partial \varepsilon_v} \right|_{\text{def}} \quad \frac{\partial \bar{n}_c}{\partial \varepsilon_v} = \left. \frac{\partial \bar{n}_c}{\partial \varepsilon_v} \right|_{\text{ph}} + \left. \frac{\partial \bar{n}_c}{\partial \varepsilon_v} \right|_{\text{def}}, \quad (3.4)$$

where the subscripts "ph" and "def" refer respectively to the photoelastic and to the deformation contributions. Finally, the following equation is derived:

$$\frac{\partial \lambda_m}{\partial \varepsilon_v} = \frac{\partial \lambda_m^{\text{per}}}{\partial \varepsilon_v} + \frac{\partial \lambda_m^{\text{ph}}}{\partial \varepsilon_v} + \frac{\partial \lambda_m^{\text{def}}}{\partial \varepsilon_v}, \quad (3.5)$$

where $\partial \lambda_m^{\text{per}}/\partial \varepsilon_v$ is the resonance shift due to perimeter variation, $\partial \lambda_m^{\text{ph}}/\partial \varepsilon_v$ is the resonance shift due to photoelastic refractive index variation and $\partial \lambda_m^{\text{def}}/\partial \varepsilon_v$ is the resonance shift due to waveguide deformation. These quantities are given by:

$$\frac{\partial \lambda_m^{\text{per}}}{\partial \varepsilon_v} = \frac{\lambda_m n_s}{P n_g} \frac{\partial P}{\partial \varepsilon_v}, \quad (3.6a)$$

$$\frac{\partial \lambda_m^{\text{ph}}}{\partial \varepsilon_v} = \frac{\lambda_m}{P n_g} \left(2L \left. \frac{\partial n_s}{\partial \varepsilon_v} \right|_{\text{ph}} + 2\pi R \left. \frac{\partial \bar{n}_c}{\partial \varepsilon_v} \right|_{\text{ph}} \right), \quad (3.6b)$$

$$\frac{\partial \lambda_m^{\text{def}}}{\partial \varepsilon_v} = \frac{\lambda_m}{P n_g} \left(2L \left. \frac{\partial n_s}{\partial \varepsilon_v} \right|_{\text{def}} + 2\pi R \left. \frac{\partial \bar{n}_c}{\partial \varepsilon_v} \right|_{\text{def}} \right). \quad (3.6c)$$

Here, $P = 2L + 2\pi R$ is the racetrack resonator perimeter and n_g is the straight waveguide group index. Deriving this, the curved and the straight group indexes are considered equal, based on the fact that the radii of the resonators analyzed in this work ($R = 15 \mu\text{m}$) are much larger than wavelength. For the same reason, also the curved effective refractive index is considered equal to the one of the straight waveguide ($\bar{n}_c = n_s$). On the other hand, the applied strain can act differently on the straight and on the curved waveguides, and therefore $\partial n_s/\partial \varepsilon_v \neq \partial \bar{n}_c/\partial \varepsilon_v$.

3.2 Contribution of the perimeter variation

Equation (3.6a) shows that the resonance shift induced by the resonator perimeter variation $\partial \lambda_m^{\text{per}}/\partial \varepsilon_v$ depends on the effective index n_s (evaluated by a 2D FEM mode solver) and on the perimeter dependence on the local volumetric strain $\partial P/\partial \varepsilon_v$ (calculated from the macroscopic 3D simulation of Sec. 2.3).

The strain felt by each resonator is evaluated from the sample macroscopic simulation. For a resonator oriented at an angle α , the strain tensor components along the main resonator axes ($\varepsilon_{x'x'}$ and $\varepsilon_{y'y'}$) are evaluated from the strain components along original axes (ε_{xx} and ε_{yy}) and from the shear strain element (ε_{xy}) using [144]:

$$\varepsilon_{x'x'} = \varepsilon_{xx} \cos^2 \alpha + \varepsilon_{yy} \sin^2 \alpha + 2\varepsilon_{xy} \sin \alpha \cos \alpha, \quad (3.7a)$$

$$\varepsilon_{y'y'} = \varepsilon_{xx} \sin^2 \alpha + \varepsilon_{yy} \cos^2 \alpha - 2\varepsilon_{xy} \sin \alpha \cos \alpha. \quad (3.7b)$$

From the sketch of Fig. 3.1, the new length of the resonator straight part L' is:

$$L' = L(1 + \varepsilon_{y'y'}), \quad (3.8)$$

while the resonator curve becomes an ellipse whose semi-axes R_a and R_b are:

$$R_a = R(1 + \varepsilon_{y'y'}) \quad R_b = R(1 + \varepsilon_{x'x'}). \quad (3.9)$$

The new perimeter P' of the resonator is then:

$$P' = 2L' + 2\pi\sqrt{\frac{R_a^2 + R_b^2}{2}}. \quad (3.10)$$

Equations (3.8) and (3.9) show that the local volumetric strain is the relevant parameter to calculate the perimeter variation. As a consequence, the results shown in the following are independent on the position on the macroscopic simulation surface since the resonance shift is normalized to the local volumetric strain. This fact agrees with the experimental observation that the resonance shift per strain unit does not depend on the location on the sample but only on α .

The top panel of Fig. 3.2 shows the simulated perimeter variation dependence on the local volumetric strain ε_v for different α . Increasing strain, perimeter increases. This effect is maximized when the resonator is oriented along the main axis of the sample ($\alpha = 90^\circ$), where the elongation of the straight part of the resonator is maximum.

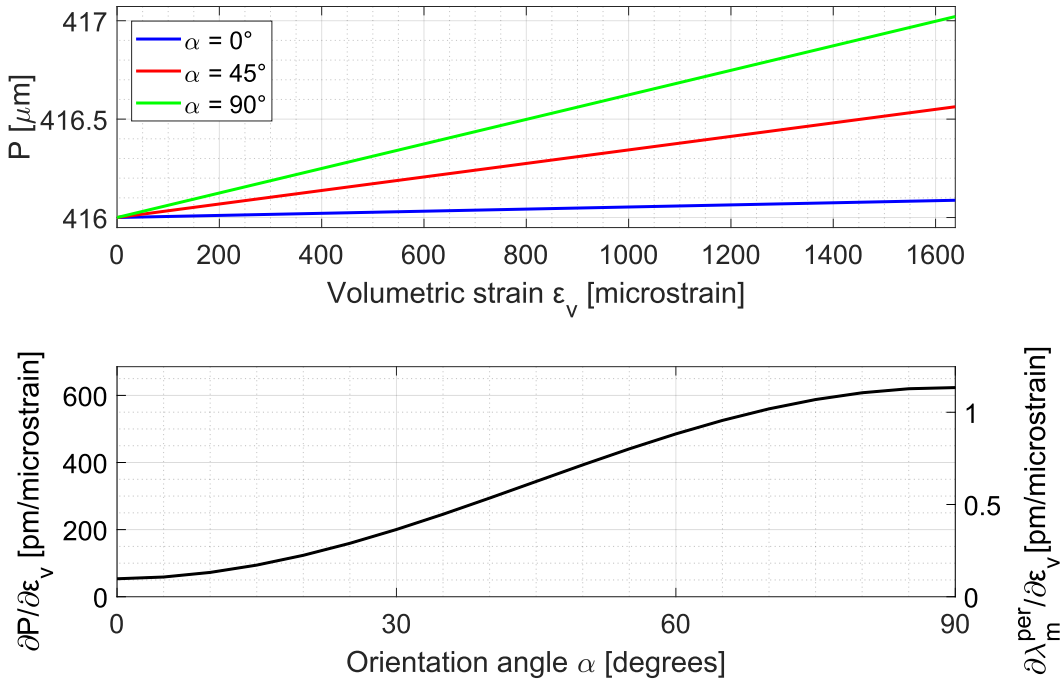


Fig. 3.2: On the top: simulated dependence of the resonator perimeter P on the volumetric strain ε_v for different α . On the bottom: dependence of the perimeter variation per strain unit on α . The corresponding resonance shift is shown on the right axis.

The bottom panel of Fig. 3.2 shows the perimeter variation per unit of volumetric strain ($\partial P/\partial \varepsilon_v$) as a function of α . This quantity is calculated from a linear fit of the results shown on the top panel of Fig. 3.2. The resonance shift due to the perimeter variation $\partial \lambda_m^{\text{per}}/\partial \varepsilon_v$ is calculated from Eq. (3.6a) and is shown on the right axis of the bottom panel of Fig. 3.2. A positive variation of the volumetric strain ε_V induces a resonance red-shift, whose magnitude increases with α .

3.3 Contribution of the refractive index variation

The evaluation of the strain effect on the effective refractive index requires to know the strain distribution inside the resonator waveguides. Then, the photoelastic matrix is used to connect the stress map to the refractive index variation map, from which the new effective refractive index of the propagating mode is calculated. Similarly, the waveguide deformation is determined from the strain distribution inside the waveguide, determining then the effective index in the deformed waveguide.

3.3.1 Evaluation of strain inside the waveguide

Since there are three orders of magnitude difference between the size of the waveguide and that of the sample, it is impossible to use the global 3D simulation of Sec. 2.3 to determine the strain distribution inside the waveguide. So, only a limited area is modeled, constituted by the oxide substrate, the waveguide and the cladding layers (as it is sketched in Fig. 3.3). Nevertheless, the global strain induced by the screw is taken from the macroscopic simulation, properly rotated in the xy -plane using Eq. (3.7) and applied in terms of prescribed displacements at the oxide substrate. The size of the reduced simulation is chosen to avoid unwanted boundary effects in the waveguide core. Apart from silicon, all the materials are amorphous, so their elastic properties are orientation independent. On the contrary, for silicon it is important to consider the crystallographic direction along which the structure is grown, and its stiffness matrix is accordingly rotated [138, 139]. As an example, the inset of Fig. 3.3 reports the normal x' component of the strain tensor in the waveguide cross-section plane for resonator oriented at $\alpha = 0^\circ$ with $\Delta z = 150 \mu\text{m}$. This method can also be used to evaluate the strain distribution in the resonator curve. In this case, the strain distribution in the waveguide curve at an angle γ is evaluated applying a rotation of $\alpha + \gamma$. In principle, the evaluation of this quantity should consider that the waveguide is curved. However, since the radius of curvature is large ($15 \mu\text{m}$), the strain distribution in the waveguide is well approximated without accounting for curvature.

In this framework, one should also take into account the residual stresses introduced during the deposition of the cladding materials, which must be considered in the

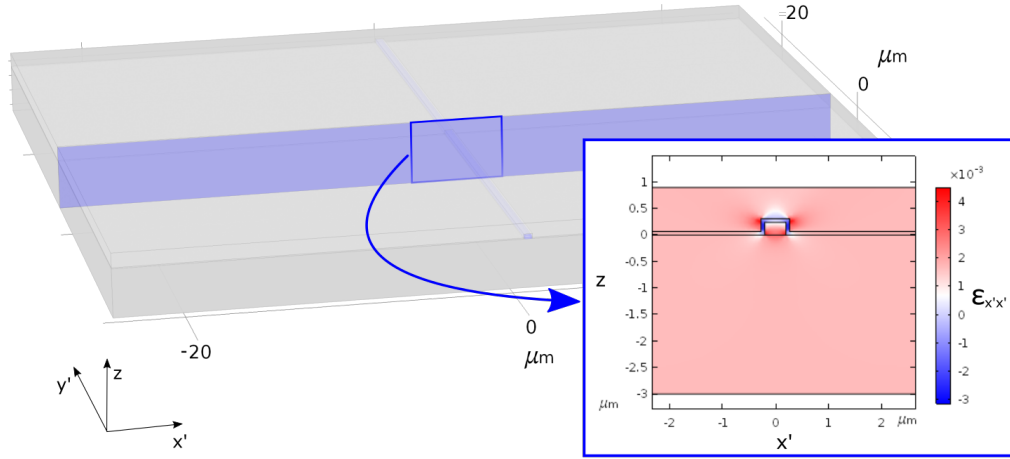


Fig. 3.3: Simulation domain of the local 3D strain simulation of the waveguide. The inset reports the color scale strain distribution in the waveguide cross-section in the simulation domain center, referred to $\alpha = 0^\circ$ and $\Delta z = 150 \mu\text{m}$.

simulation as initial stress conditions. However, the interest of this work is devoted to the study of the strain-induced refractive index variation, which is a differential quantity related to the strain variation rather than to the absolute strain inside the waveguide. Therefore, since this model is linear, the presence of residual stresses can be omitted. To verify the validity of the approximation, all the simulations described in the following have been performed with and without considering residual stresses, finding negligible differences in terms of the predicted resonance wavelength shift.

3.3.2 Photoelastic variation of the effective refractive index

Once the stress distribution inside the waveguide cross-section is evaluated as described in the previous point, the photoelastic matrix can be used to calculate the strain-induced refractive index variation [140]. It is worth noting that this matrix also needs to be rotated according to silicon crystallographic directions. Once the new refractive indexes of all the involved materials are evaluated, the new effective refractive index is evaluated using a FEM mode solver [141]. While doing this in the straight part of the resonator is straightforward, in the evaluation of the curved index $n_c(\gamma)$ one should consider that the cross-section plane in the curve rotates with an angle described point-by-point by γ . However, as a further approximation, it is assumed that the effective refractive index varies continuously from the straight index n_s to the effective refractive index evaluated in the halfway point of the curved section n_\perp (corresponding to the angle $\gamma = 90^\circ$). Thus, $n_c(\gamma)$ is given by:

$$n_c(\gamma) = n_s \cos^2(\gamma) + n_\perp \sin^2(\gamma), \quad (3.11)$$

from which the mean index in the curved \bar{n}_c is calculated using Eq. (3.2). Through this approach, for a given resonator orientation and for a given applied strain, the

effective refractive index is evaluated in the straight part (n_s) and in the halfway point of the curve (n_\perp). The top panel of Fig. 3.4 shows the simulated effective refractive index variation per strain unit for both n_s and \bar{n}_c . Equation (3.6b) allows then to evaluate the photoelastic contribution to the resonance wavelength shift $\partial\lambda_m^{\text{ph}}/\partial\varepsilon_v$, that is shown in the bottom panel of Fig. 3.4. This plot shows that the shift increases with α moving from negative to positive values.

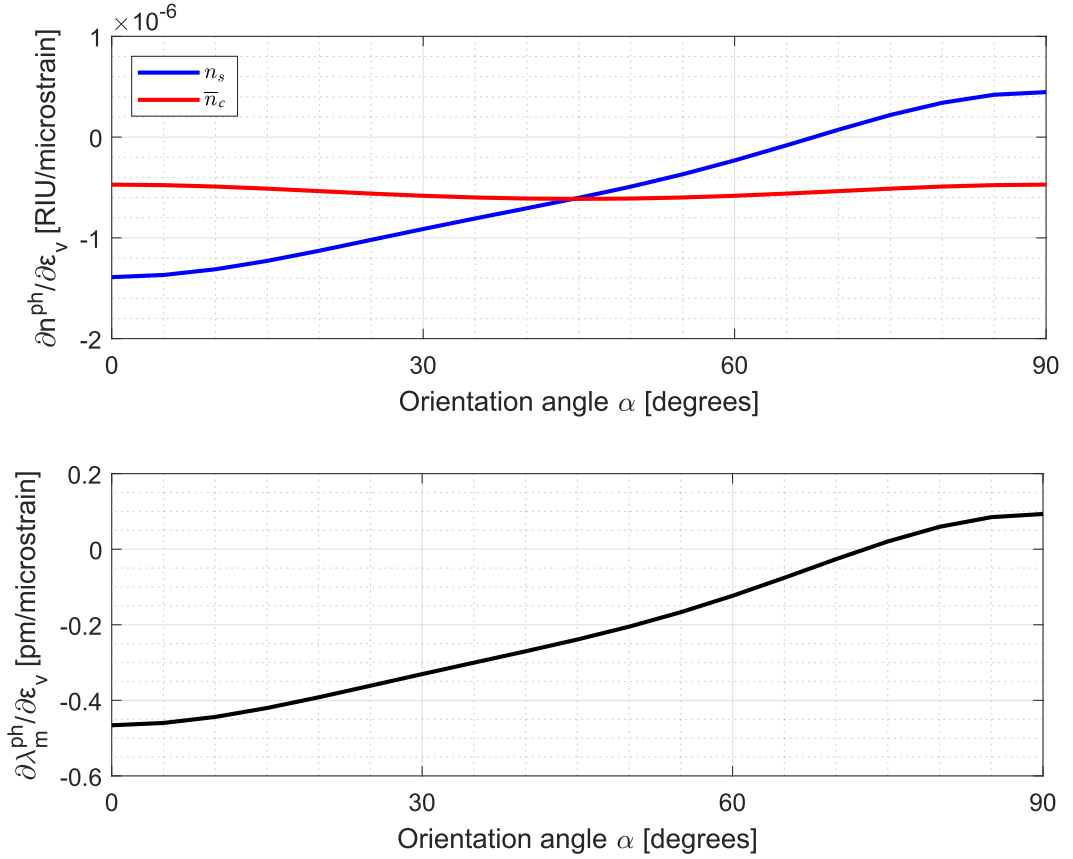


Fig. 3.4: On the top: photoelastic variation of the effective refractive index in the straight and in the curved part of the resonator as a function of the resonator orientation. On the bottom: photoelastic contribution to the resonance wavelength shift.

3.3.3 Contribution of the waveguide deformation

The deformation-induced effective index variation is evaluated using the same approach used for photoelastic effect. For the straight part of the resonator, the new effective index is determined once that the deformed waveguide cross-section is known. Similarly, once the effective refractive index of the deformed waveguide is evaluated in the middle of the curve, the index at a generic angle γ of the curve is calculated using Eq. (3.11). Both in the straight part and in the middle of the curve, the waveguide deformation is estimated calculating the mean strain values in the waveguide cross-section ($\bar{\varepsilon}_{x'x'}$ and $\bar{\varepsilon}_{zz}$) from the 3D simulation of the waveguide.

Assuming that the deformed waveguide maintains its rectangular cross-section, its new height h' and width w' are related to the unstrained parameters h and w by:

$$h' = h(1 + \bar{\varepsilon}_{zz}) \quad w' = w(1 + \bar{\varepsilon}_{x'x'}). \quad (3.12)$$

The dependence on the applied volumetric strain of the waveguide height and width in the straight part of the resonator are shown in Fig. 3.5. First, one notes that the waveguide width variation is below the typical errorbars of the estimation given in Sec. 2.5. Moreover, for all the resonator orientations, the waveguide height decreases as the volumetric strain increases, showing a larger effect on the resonators oriented along the main direction of the sample ($\alpha = 90^\circ$). On the other hand, an increase of the volumetric strain causes an increase of the waveguide width, whose magnitude progressively reduces from $\alpha = 0^\circ$ to $\alpha = 90^\circ$. Due to this fact, for the resonator oriented at $\alpha = 0^\circ$ the effect of the height reduction is balanced by the increase of the waveguide width, determining a small effective refractive index variation. On the contrary, the waveguide of the resonator oriented at $\alpha = 90^\circ$ is mainly influenced by the height reduction and by only a small width increase, thus displaying a larger effective refractive index variation.

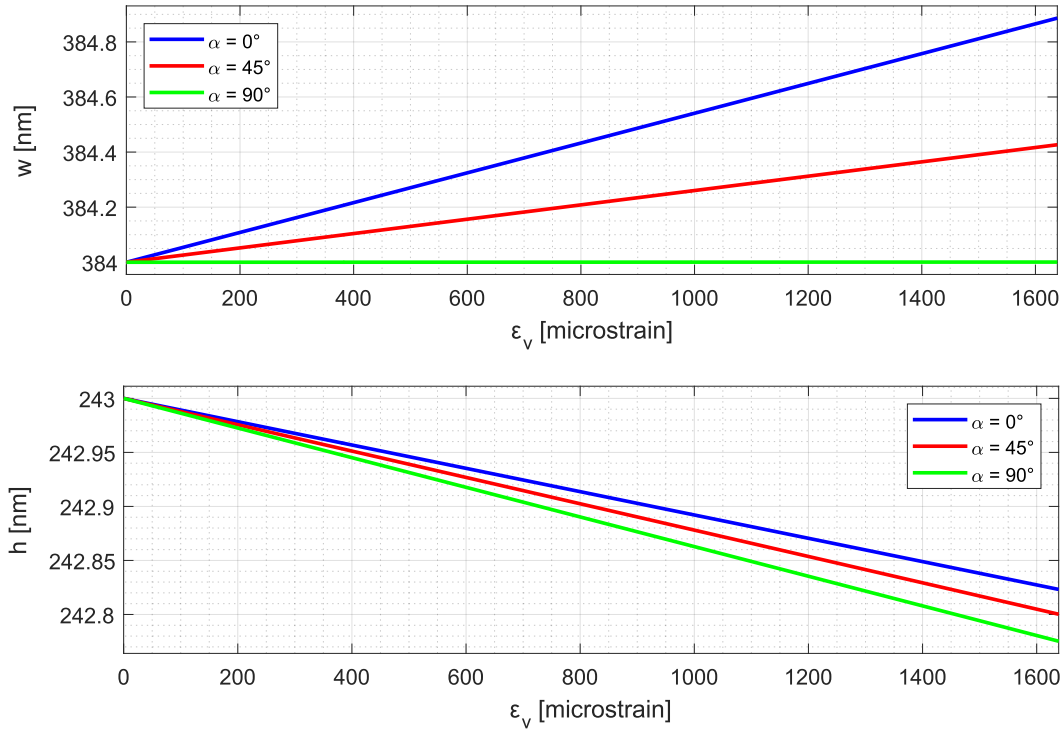


Fig. 3.5: Waveguide width and height in the straight part of the resonator as a function of the applied strain and for different orientations.

This can be seen in the top panel of Fig. 3.6, showing the effective index variation caused by waveguide deformation. The bottom panel of Fig. 3.6 shows the deformation contribution to the resonance shift $\partial\lambda_m^{\text{def}}/\partial\varepsilon_v$ evaluated using Eq. (3.6c).

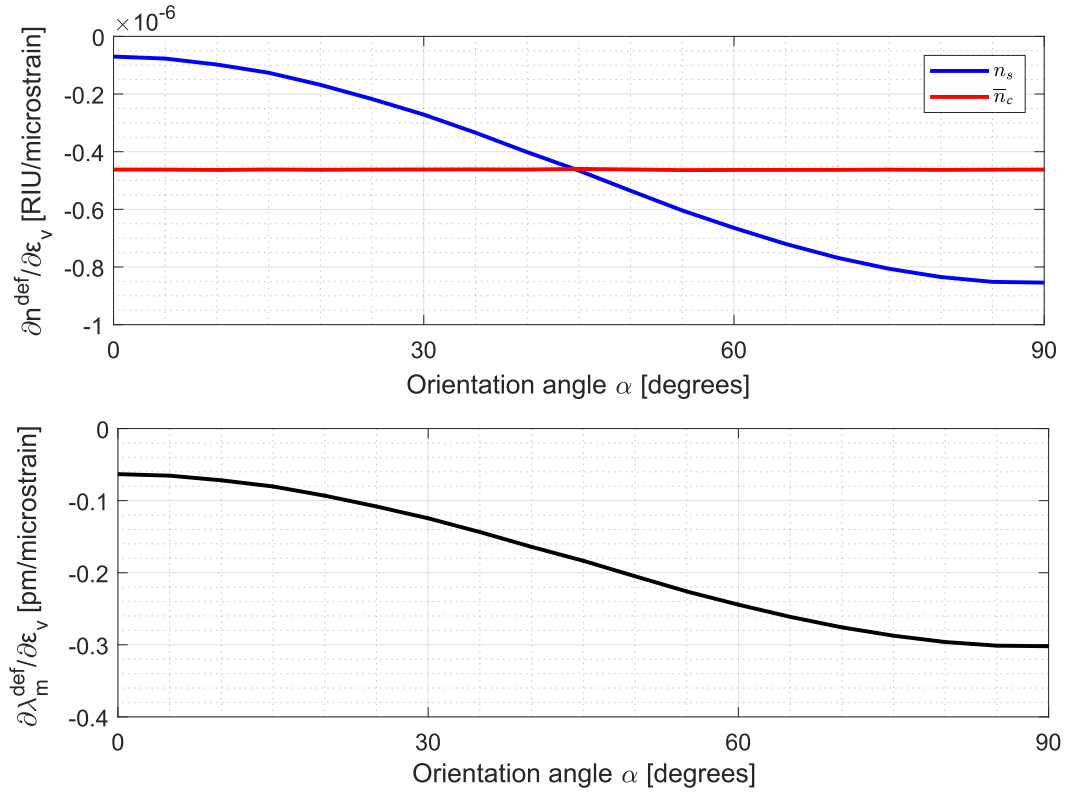


Fig. 3.6: On the top: waveguide deformation effect on the effective refractive index in the straight and in the curved part of the resonator. On the bottom: contribution of the waveguide deformation to the resonance wavelength shift.

3.4 Comparison with experiments

Figure 3.7 shows, as a function of the resonator orientation, the contributions to the resonance shift calculated so far: the one from the perimeter variation, the photoelastic effect and the waveguide deformation. According to Eq. (3.5), the sum of these terms gives the global shift. Finally, the experimental points from Fig. 2.10 are added. The good agreement legitimizes the approximations of the model.

For small angles, i.e. when the resonator is perpendicular to the direction of the elongation imposed to the sample, the photoelastic effect is the main contribution. The contributions related to the mechanical deformation of the device, such as the one due to the perimeter variation and the one related to the transverse waveguide deformation, are smaller and balance themselves. On the contrary, for large angles, the perimeter variation plays the dominant role. Moreover, this contribution is the one that has the largest variation amplitude with respect to the sample orientation, roughly twice the ones of the two others.

Varying the orientation angle, the global resonance wavelength shift changes sign, passing from negative to positive. The angle where the shift approaches 0 is about 34.5° , where all the contributions balance giving rise to a strain insensitive resonator.

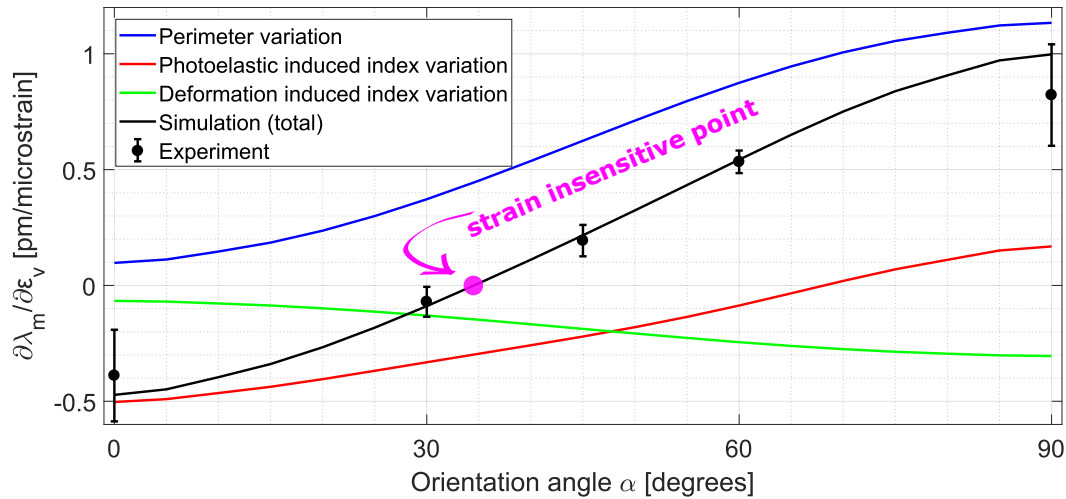


Fig. 3.7: Resonance shift as a function of the resonator orientation angle. The experimental data are shown as black dots. The simulated contributions to the resonance shift of perimeter variation (blue), photoelastic effect (red) and waveguide deformation (green) add up providing the total simulated resonance shift (black).

3.5 Conclusion and perspectives

In this part, the role of strain on a set of elongated SOI racetrack resonators with different orientation angles has been analyzed. Using a 3D simulation of the whole deformed chip, the resonance wavelength shift was normalized to the local strain value experienced by each resonator. Moreover, a macroscopic simulation is used to model all the effects causing the resonance wavelength shift. The strain-induced perimeter variation was considered, as well as the strain-induced variation of the material refractive index and the deformation of the waveguide cross-section. The simulated results are in good agreement with the experiment, which vary from positive to negative values when changing the resonator orientation angle. The possibility of tuning the resonance shift with the resonator orientation offers interesting perspectives for strain sensors, since the presence of many resonators with different orientations on the same sample can provide information on the strain direction. Moreover, the resonator orientation angle can be tuned to realize strain-insensitive resonators, offering interesting applications in flexible photonics. An interesting property is that the applied strain has not a permanent effect: when the strain is removed, the resonance shifts back to its original position.

Regarding the interests of this thesis, the results of this chapter show that the simulation procedure provides good agreement with the experiment. Therefore, in the following chapters, the same tool is used to describe the effect of strain in waveguides engineered to achieve second order nonlinearities.

Part II

Second harmonic generation in strained silicon waveguides

This part is dedicated to the study of SHG in strained silicon waveguides.

Chapter 4 introduces the theoretical framework of SHG in waveguides. Then, the waveguide engineering procedure used to design the waveguides is described.

The technical details of the SHG experiment are described in **Chapter 5**, showing also the characterization of the SHG process.

Chapter 6 investigates the role of strain on the measured effect. The SHG process is studied under the effect of an external mechanical load, and the experimental results are interpreted also by the comparison with simulations.

Chapter 7 studies the effects on SHG of the charges trapped at the waveguide borders, which introduce a static electric field in the waveguide that enables the EFISH process. UV treatment is applied in order to remove these charges, and the effect on SHG is studied.

Modeling SHG in silicon waveguides

4.1	Theoretical description of SHG in waveguides	58
4.1.1	Optical pulses in nonlinear waveguides	58
4.1.2	SHG and other effects in waveguides	59
4.1.3	The SH pulse equation	60
4.1.4	The pump pulse equation	62
4.1.5	The coupled equations	63
4.1.6	Undepleted pump and continuous wave	63
4.2	Waveguide engineering	64
4.2.1	Waveguide cross-section	64
4.2.2	Phase matching through waveguide engineering	65
4.2.3	Strength of the modal combinations	69
4.2.4	Quantification of the strain-induced nonlinear strength	70
4.3	Estimating the generation efficiency	72
4.3.1	The split-step method	72
4.3.2	Propagating optical pulses	73
4.3.3	From the experiment to the $\chi^{(2)}$ coefficient	80

In Sec. 1.3.2, the ambiguities of the previous experiments studying SHG in strained silicon waveguides have been pointed out. One of these ambiguities was related to the origin of the measured effect, which could not be unambiguously attributed to strain. Also other effects could have had a role, like the EFISH process due to the trapped charges, as well as the generation in the SiN cladding via the evanescent field. The other ambiguity was related to the method used to estimate the $\chi^{(2)}$ coefficient. First, the estimation was performed in highly multimodal waveguides, without taking into account any phase-matching mechanism. Moreover, even though a pulsed source was used, the estimation of $\chi^{(2)}$ was performed considering a continuous-wave approach. Both these facts could have introduced plenty of errors in the determination of $\chi^{(2)}$.

The first requirement to clarify these points is to possess a reliable method to control the process and unambiguously determine $\chi^{(2)}$. For this purpose, in this chapter an analytic model to describe the propagation of ultra-short optical pulses in waveguides is proposed. The model is theoretically presented in Sec. 4.1. Based on this,

waveguides to demonstrate an efficient and controlled SHG process are engineered. The engineering procedure is described in Sec. 4.2. In Sec. 4.3, a method to solve numerically the equations proposed by the model is presented. In the end, it is shown how this model can be used to reconstruct the $\chi^{(2)}$ value from the experimental SH signal.

The model and the simulations described in this chapter benefited from the discussions with Dr. M. Mancinelli, Dr. C. Manganelli, Dr. C. Bonati and Dr. P. Pintus. Part of the model described here is also described in [67, 145].

4.1 Theoretical description of SHG in waveguides

In this section, a theoretical model to study SHG in waveguides is proposed. First, a general method to study optical pulses in nonlinear waveguides is introduced. Then, this method is applied to SHG, taking into account also other nonlinear effects that affect the pulse propagation. Finally, an analytic solution for SHG efficiency is derived in a simplified approximation.

4.1.1 Optical pulses in nonlinear waveguides

The aim of this part is to describe the propagation of optical pulses in waveguides. Consider first the unperturbed waveguide, when only linear optical effects occur. In this situation, the propagating pulse is described by the electromagnetic field $(\mathbf{E}_0, \mathbf{H}_0)$. Equation (1.4) shows that optical nonlinearities induce a perturbation $\delta\mathbf{P} = \mathbf{P}_{NL} \neq 0$ of the polarization vector. This determines a modification of the electromagnetic field, that is altered to $(\mathbf{E}_1, \mathbf{H}_1)$. **Lorentz's reciprocity theorem** relates the perturbed and the unperturbed fields via the following relationship [34, 67]:

$$\frac{\partial}{\partial z} \int_{A_\infty} (\mathbf{E}_0^* \times \mathbf{H}_1 + \mathbf{E}_1 \times \mathbf{H}_0^*) \cdot \hat{\mathbf{z}} \, dA = i\omega \int_{A_\infty} \mathbf{E}_0^* \cdot \delta\mathbf{P} \, dA. \quad (4.1)$$

All the integrals are taken on the plane A_∞ , orthogonal to the field propagation direction $\hat{\mathbf{z}}$, while ω is the pulse frequency.

From now on, consider fields linearly polarized in the A_∞ plane. Assume also the unperturbed pulse spectral width $\Delta\omega$ much smaller than its central frequency ω_0 ($\Delta\omega \ll \omega_0$). For near infrared wavelengths $\omega_0 \sim 1 \times 10^{15} \text{ s}^{-1}$. So, this approximation is valid for pulse temporal widths $\gg 1 \text{ fs}$. In this situation, the unperturbed fields can be written as:

$$\mathbf{E}_0(\mathbf{r}, \omega_0) = \frac{1}{2} \mathbf{e}(\mathbf{r}_\perp, \omega_0) e^{i\beta_0 z} \quad \mathbf{H}_0(\mathbf{r}, \omega_0) = \frac{1}{2} \mathbf{h}(\mathbf{r}_\perp, \omega_0) e^{i\beta_0 z}, \quad (4.2)$$

being $\beta_0 = \beta(\omega_0)$, \mathbf{r}_\perp a vector in the A_∞ plane, while $\mathbf{e}(\mathbf{r}_\perp, \omega_0)$ and $\mathbf{h}(\mathbf{r}_\perp, \omega_0)$ are the profiles of the electromagnetic field in the A_∞ plane at frequency ω_0 . With this notation, the total power P_0 carried by the unperturbed electromagnetic field is:

$$P_0 = \frac{1}{4} \int_{A_\infty} [\mathbf{e}(\mathbf{r}_\perp, \omega_0) \times \mathbf{h}^*(\mathbf{r}_\perp, \omega_0) + \mathbf{e}^*(\mathbf{r}_\perp, \omega_0) \times \mathbf{h}(\mathbf{r}_\perp, \omega_0)] \cdot \hat{\mathbf{z}} \, dA. \quad (4.3)$$

On the other hand, a general expression for the perturbed solution is:

$$\mathbf{E}(\mathbf{r}, \omega) = \frac{1}{2} u(z, \omega) \mathbf{e}(\mathbf{r}_\perp, \omega) e^{i\beta(\omega)z} \quad \mathbf{H}(\mathbf{r}, \omega) = \frac{1}{2} u(z, \omega) \mathbf{h}(\mathbf{r}_\perp, \omega) e^{i\beta(\omega)z}, \quad (4.4)$$

where it is assumed that the perturbation introduces a modulation of the field amplitude described by the **slowly varying envelope** $u(z, \omega)$. Assume now that the field profiles in the A_∞ plane are not modified by the perturbation, so:

$$\mathbf{e}(\mathbf{r}_\perp, \omega) \sim \mathbf{e}(\mathbf{r}_\perp, \omega_0) \quad \mathbf{h}(\mathbf{r}_\perp, \omega) \sim \mathbf{h}(\mathbf{r}_\perp, \omega_0). \quad (4.5)$$

In this case, the optical power carried by the perturbed field is $P = P_0 |u(z, \omega)|^2$.

Using Eq. (4.2) and Eq. (4.4) in Eq. (4.1), the following equation is derived:

$$\frac{du(z, \omega)}{dz} + i(\beta - \beta_0)u(z, \omega) = \frac{i\omega}{2P_0} e^{-i\beta z} \int_{A_\infty} \mathbf{e}^*(\mathbf{r}_\perp, \omega_0) \cdot \delta\mathbf{P}(\mathbf{r}, \omega) \, dA. \quad (4.6)$$

Concluding, Eq. (4.6) can be used to describe the propagation of optical pulses in waveguides under the effect of a polarization vector perturbation $\delta\mathbf{P}(\mathbf{r}, \omega)$. If multiple pulses propagate in the same waveguide and their spectra do not overlap, each of them can be described by an independent equation in the form of Eq. (4.6).

4.1.2 SHG and other effects in waveguides

In the case of the SHG, two optical pulses propagate in the optical waveguide: the pump pulse at frequency ω_p and the SH pulse at frequency $\omega_{sh} = 2\omega_p$. Since the pump and the SH spectra do not overlap, an independent equation must be written for each pulse, using the proper $\delta\mathbf{P}(\mathbf{r}, \omega)$ in Eq. (4.6).

However, not only SHG occurs while the pulses propagate. For example, this work deals mainly with waveguides made by silicon, which possesses a strong $\chi^{(3)}$. So, third order **pulse distortion effects** such as SPM and XPM must be considered. Moreover, fabrication imperfections introduce in the waveguides a **linear absorption** term, which determines a perturbation of the polarization vector as well. So, the polarization vector perturbation can be generally written as:

$$\delta\mathbf{P}(\mathbf{r}, \omega) = \mathbf{P}^{(2)}(\mathbf{r}, \omega) + \mathbf{P}^{(3)}(\mathbf{r}, \omega) + \mathbf{P}_L(\mathbf{r}, \omega), \quad (4.7)$$

being $\mathbf{P}^{(2)}(\mathbf{r}, \omega)$ the polarization vector term due to $\chi^{(2)}$, $\mathbf{P}^{(3)}(\mathbf{r}, \omega)$ the polarization vector term due to $\chi^{(3)}$ and $\mathbf{P}_L(\mathbf{r}, \omega)$ a linear perturbation of the polarization vector, due for example to propagation losses.

The equation describing the propagation of the SH pulse is derived in Sec. 4.1.3, while the equation describing the pump pulse is derived in Sec. 4.1.4. Finally, in Sec. 4.1.5 the results are summarized in a system of coupled equations describing the propagation of both the pulses. In the following, the subscript p is used to refer to the pump pulse, while the subscript sh is used to refer to the SH pulse.

4.1.3 The SH pulse equation

In this section, the equation describing the propagation of the SH pulse is derived. Doing that, the three terms expressed in Eq. (4.7) are considered separately. In the end, all the terms are grouped in the global equation describing the propagation of the SH pulse.

Contribution of SHG. According to Eq. (1.7) the term $\mathbf{P}^{(2)}(\mathbf{r}, \omega_{sh})$ is given by:

$$\begin{aligned}\mathbf{P}^{(2)}(\mathbf{r}, \omega_{sh}) &= \varepsilon_0 \chi^{(2)} : \mathbf{E}_p^2(\mathbf{r}, \omega_p) \\ &= \frac{\varepsilon_0}{4} \chi^{(2)} : \mathbf{e}^2(\mathbf{r}_\perp, \omega_p) u_p^2 e^{i2\beta_p z}.\end{aligned}\quad (4.8)$$

In the last equation the definition of Eq. (4.4) has been used. Moreover, the spatial and the spectral dependence of $u_p(z, \omega)$ have been omitted, while $\beta_p = \beta(\omega_p)$.

By taking $\delta\mathbf{P} = \mathbf{P}^{(2)}$ and replacing it in Eq. (4.6), it is possible to derive the equation describing the propagation of the SH pulse when only SHG effect is considered:

$$\frac{du_{sh}}{dz} + i(\beta_{sh} - \beta_{0,sh})u_{sh} = i\gamma_{sh}^{(2)} \frac{P_{0,p}}{\sqrt{P_{0,sh}}} u_p^2 e^{i\Delta\beta z}.\quad (4.9)$$

The coefficient $\Delta\beta = (2\beta_p - \beta_{sh})$ is named **phase-mismatch**, while the nonlinear coefficient $\gamma_i^{(2)}$ is defined by:

$$\gamma_i^{(2)} = \omega_i \frac{n_{G,p} \sqrt{n_{G,sh}}}{\sqrt{8A_0 \varepsilon_0 c^3}} \Gamma^{(2)}.\quad (4.10)$$

The coefficient $n_{G,i}$ is the group index of the pulse at frequency ω_i and A_0 is the waveguide area. The term $\Gamma^{(2)}$ is defined by:

$$\Gamma^{(2)} = \frac{\sqrt{A_0} \int \mathbf{e}(\mathbf{r}_\perp, \omega_p) \chi^{(2)} : \mathbf{e}^*(\mathbf{r}_\perp, \omega_{sh}) \mathbf{e}(\mathbf{r}_\perp, \omega_p) \, dA}{\left(\int n^2(\mathbf{r}_\perp, \omega_p) |\mathbf{e}(\mathbf{r}_\perp, \omega_p)|^2 \, dA \right) \left(\int n^2(\mathbf{r}_\perp, \omega_{sh}) |\mathbf{e}(\mathbf{r}_\perp, \omega_{sh})|^2 \, dA \right)^{1/2}},\quad (4.11)$$

where all the integrals are taken over all the A_∞ plane, while $n(\mathbf{r}_\perp, \omega_i)$ is the refractive index distribution at frequency ω_i in the A_∞ plane.

Contribution of third order nonlinearities. The term $\mathbf{P}^{(3)}(\mathbf{r}, \omega_{sh})$ can be derived from Eq. (1.8). Consider that, while propagating, the SH pulse feels the effect of SPM and XPM. However, the pump pulse is often much stronger than the SH pulse. In this situation, the SPM term can be neglected, considering only the XPM term. In this case, $\mathbf{P}^{(3)}(\mathbf{r}, \omega_{sh})$ is given by:

$$\begin{aligned}\mathbf{P}^{(3)}(\mathbf{r}, \omega_{sh}) &= 6\varepsilon_0\chi^{(3)}:|\mathbf{E}_p(\mathbf{r}, \omega_p)|^2\mathbf{E}_{sh}(\mathbf{r}, \omega_{sh}) \\ &= \frac{3\varepsilon_0}{4}\chi^{(3)}:|\mathbf{e}(\mathbf{r}_\perp, \omega_p)|^2\mathbf{e}(\mathbf{r}_\perp, \omega_{sh})|u_p|^2u_{sh}e^{i\beta_{sh}z}.\end{aligned}\quad (4.12)$$

Considering $\delta\mathbf{P} = \mathbf{P}^{(3)}$, Eq. (4.6) becomes:

$$\frac{du_{sh}}{dz} + i(\beta_{sh} - \beta_{0,sh})u_{sh} = 2i\gamma_{sh,p}^{(3)}P_{0,p}|u_p|^2u_{sh}.\quad (4.13)$$

The coefficient $\gamma_{i,j}^{(3)}$ is defined by:

$$\gamma_{i,j}^{(3)} = \frac{3\omega_i n_{G,i} n_{G,j}}{4\varepsilon_0 A_0 c^2} \Gamma_{i,j}^{(3)},\quad (4.14)$$

while $\Gamma_{i,j}^{(3)}$ is given by:

$$\Gamma_{i,j}^{(3)} = \frac{A_0 \int \mathbf{e}^*(\mathbf{r}_\perp, \omega_j) \chi^{(3)}: \mathbf{e}(\mathbf{r}_\perp, \omega_i) \mathbf{e}^*(\mathbf{r}_\perp, \omega_i) \mathbf{e}(\mathbf{r}_\perp, \omega_j) dA}{\left(\int n^2(\mathbf{r}_\perp, \omega_i) |\mathbf{e}(\mathbf{r}_\perp, \omega_i)|^2 dA \right) \left(\int n^2(\mathbf{r}_\perp, \omega_j) |\mathbf{e}(\mathbf{r}_\perp, \omega_j)|^2 dA \right)}.\quad (4.15)$$

Also here all the integrals are taken over all the A_∞ plane.

Contribution of losses. The term $\mathbf{P}_L(\mathbf{r}, \omega_{sh})$ describes the linear perturbation of the polarization vector induced by propagation losses in the waveguide. It is given by:

$$\begin{aligned}\mathbf{P}_L(\mathbf{r}, \omega_{sh}) &= \varepsilon_0 \delta\chi^{(1)} \mathbf{E}_{sh}(\mathbf{r}, \omega_p) \\ &= \frac{\varepsilon_0}{2} \delta\chi^{(1)} u_{sh} \mathbf{e}(\mathbf{r}_\perp, \omega_{sh}) e^{i\beta_{sh}z},\end{aligned}\quad (4.16)$$

where $\delta\chi^{(1)}$ describes the perturbation of the first order susceptibility due to losses. Substituting this into Eq. (4.6) it becomes:

$$\frac{du_{sh}}{dz} + i(\beta_{sh} - \beta_{0,sh})u_{sh} = -\frac{\alpha_{sh}}{2}u_{sh}.\quad (4.17)$$

The term α_i is the loss coefficient of the mode at frequency ω_i , defined as:

$$\alpha_i = -\frac{i\omega_i\varepsilon_0}{2P_{0,i}} \int_{A_\infty} \delta\chi^{(1)}(\mathbf{r}_\perp, \omega_i) |\mathbf{e}^*(\mathbf{r}_\perp, \omega_i)|^2 dA.\quad (4.18)$$

It is related to the spatial distribution $\delta\chi^{(1)}$ inside the waveguide, which, in turn, is related to the spatial distribution of the absorption coefficient determined by losses¹. However, the loss coefficient inside the waveguide depends mainly on the fabrication imperfections, which cannot be quantified analytically. So, α_i is typically determined from experimental measurements of the attenuation inside the waveguide.

General equation for the SH pulse. The equation describing the propagation of the SH pulse is determined by assembling Eq. (4.9), (4.13) and (4.17):

$$\begin{aligned} \frac{du_{sh}}{dz} + i(\beta_{sh} - \beta_{0,sh})u_{sh} &= \\ &= i\gamma_{sh}^{(2)} \frac{P_{0,p}}{\sqrt{P_{0,sh}}} u_p^2 e^{i\Delta\beta z} + 2i\gamma_{sh,p}^{(3)} P_{0,p} |u_p|^2 u_{sh} - \frac{\alpha_{sh}}{2} u_{sh}. \end{aligned} \quad (4.19)$$

4.1.4 The pump pulse equation

This section considers the propagation of the pump pulse. Analogously to the SH pulse, the three terms expressed in Eq. (4.7) are considered separately. In the end, all the terms are grouped in the global equation.

Contribution of SHG. According to Eq. (1.7) the term $\mathbf{P}^{(2)}(\mathbf{r}, \omega_p)$ is given by:

$$\begin{aligned} \mathbf{P}^{(2)}(\mathbf{r}, \omega_p) &= 2\varepsilon_0\chi^{(2)} : \mathbf{E}_{sh}(\mathbf{r}, \omega_{sh})\mathbf{E}_p^*(\mathbf{r}, \omega_p) \\ &= \frac{\varepsilon_0}{4}\chi^{(2)} : \mathbf{e}(\mathbf{r}_\perp, \omega_{sh})\mathbf{e}^*(\mathbf{r}_\perp, \omega_p)u_{sh}u_p^* e^{i(\beta_{sh}-\beta_p)z}. \end{aligned} \quad (4.20)$$

Considering $\delta\mathbf{P} = \mathbf{P}^{(2)}$ in Eq. (4.6), the equation describing the propagation of the pump pulse under the effect of only SHG can be derived:

$$\frac{du_p}{dz} + i(\beta_p - \beta_{0,p})u_p = 2i\gamma_p^{(2)} \sqrt{P_{0,sh}u_{sh}} u_p^* e^{-i\Delta\beta z}. \quad (4.21)$$

Contribution of third order nonlinearities. The term $\mathbf{P}^{(3)}(\mathbf{r}, \omega_p)$ can be derived from Eq. (1.8). If the pump pulse is much stronger than the SH pulse, the SPM term dominates over XPM term caused by the SH pulse, and it is given by:

$$\begin{aligned} \mathbf{P}^{(3)}(\mathbf{r}, \omega_p) &= 3\varepsilon_0\chi^{(3)} : |\mathbf{E}_p(\mathbf{r}, \omega_p)|^2 \mathbf{E}_p(\mathbf{r}, \omega_p) \\ &= \frac{3\varepsilon_0}{8}\chi^{(3)} : |\mathbf{e}(\mathbf{r}_\perp, \omega_p)|^2 \mathbf{e}(\mathbf{r}_\perp, \omega_p) |u_p|^2 u_p e^{i\beta_p z}. \end{aligned} \quad (4.22)$$

¹According to Eq. (1.9), in presence of losses $\delta\chi^{(1)} \simeq 2n_0\delta n = in_0c\alpha_0/\omega_i$, where n_0 is the linear refractive index in absence of losses, δn is the refractive index perturbation due to losses and α_0 is the material loss coefficient. Since $\alpha_0 > 0$, it results that also $\alpha_i > 0$. So, according to Eq. (4.17), the signal is attenuated during propagation in presence of losses.

Considering $\delta\mathbf{P} = \mathbf{P}^{(3)}$, Eq. (4.6) becomes:

$$\frac{du_p}{dz} + i(\beta_p - \beta_{0,p})u_p = i\gamma_{p,p}^{(3)}P_{0,p}|u_p|^2 u_p. \quad (4.23)$$

Contribution of losses. Similarly to the SH pulse, the pump pulse is affected by propagation losses in the following way:

$$\frac{du_p}{dz} + i(\beta_p - \beta_{0,p})u_p = -\frac{\alpha_p}{2}u_p. \quad (4.24)$$

General equation for the pump pulse. By assembling Eq. (4.21), (4.23) and (4.24), the equation describing the pump pulse is given by:

$$\frac{du_{sh}}{dz} + i(\beta_p - \beta_{0,p})u_p = 2i\gamma_p^{(2)*}\sqrt{P_{0,sh}u_{sh}u_p^*}e^{-i\Delta\beta z} + i\gamma_{p,p}^{(3)}P_{0,p}|u_p|^2 u_p - \frac{\alpha_p}{2}u_p. \quad (4.25)$$

4.1.5 The coupled equations

Sections 4.1.3 and 4.1.4 show that the pump and the SH pulses propagate in a waveguide according to Eq. (4.19) and Eq. (4.25). By Fourier-transforming them, a system of coupled equations describing the spatial and the temporal evolution of the pump and of the SH amplitudes $u_p(z, t)$ and $u_{sh}(z, t)$ can be derived:

$$\left\{ \begin{array}{l} \frac{du_{sh}}{dz} + \sum_{m \geq 1} \frac{(i)^{m-1} \beta_{sh,m}}{m!} \frac{\partial^m u_{sh}}{\partial t^m} = \\ \quad = i\gamma_{sh}^{(2)} \frac{P_{0,p}}{\sqrt{P_{0,sh}}} u_p^2 e^{i\Delta\beta z} + 2i\gamma_{sh,p}^{(3)} P_{0,p} |u_p|^2 u_{sh} - \frac{\alpha_{sh}}{2} u_{sh}, \\ \frac{du_p}{dz} + \sum_{m \geq 1} \frac{(i)^{m-1} \beta_{p,m}}{m!} \frac{\partial^m u_p}{\partial t^m} = \\ \quad = 2i\gamma_p^{(2)*} \sqrt{P_{0,sh}u_{sh}u_p^*} e^{-i\Delta\beta z} + i\gamma_{p,p}^{(3)} P_{0,p} |u_p|^2 u_p - \frac{\alpha_p}{2} u_p. \end{array} \right. \quad (4.26)$$

From this formulation, it is clear that the terms on the left hand side of the equations describe the spatial and the temporal evolution of the pulses. In the meanwhile, the terms on the right hand side of the equations describe SHG, third order phase-modulations and losses.

4.1.6 Undepleted pump and continuous wave

Equations (4.26) describe the propagation of optical pulses considering SHG, but also temporal dispersion, third order nonlinear phase modulations (SPM and XPM) and losses. This system of equations can be simplified by neglecting third-order

nonlinearities and the effect of losses. Moreover, in the **continuous-wave approximation** the term with time derivatives can be also neglected. In this scenario, the equation describing the propagation of the SH pulse is simplified as follows:

$$\frac{du_{sh}}{dz} = i\gamma_{sh}^{(2)} \frac{P_{0,p}}{\sqrt{P_{0,sh}}} u_p^2 e^{i\Delta\beta z}. \quad (4.27)$$

Consider a small generation efficiency. So, the pump power is not affected by the generation of the SH pulse, and $u_p(z) \sim \text{const}$. This condition is often referred as **undepleted pump approximation** [31]. Moreover, assume that $\gamma_{sh}^{(2)}$ is constant along z (this is typically valid, except the situation where periodically poling is used to quasi-phase-match the pump and the SH pulses). In this case, on the right-hand side of Eq. (4.27) only the exponential term depends on z , and the equation can be easily integrated over all the waveguide length L . In this case, the total SH power is:

$$P_{sh} = P_{0,sh} |u_{sh}|^2 = P_p^2 |\gamma_{sh}^{(2)}|^2 L^2 \text{sinc}^2 \left(\frac{\Delta\beta L}{2} \right). \quad (4.28)$$

This is the most common way to express the SH power in the continuous-wave and in the undepleted pump approximations. It shows that the SH power quadratically depends on both the pump power P_p and the waveguide length L . Moreover, the SH power depends quadratically on the second order nonlinear coefficient $\gamma_{sh}^{(2)}$. In the simple situation when SHG is mediated by a single element of the $\chi^{(2)}$ tensor, and if $\chi^{(2)}$ is constant in the waveguide cross-section, Eq. (4.10) and Eq. (4.11) show that $\gamma_{sh}^{(2)} \propto \chi^{(2)}$. So, SH power depends quadratically also on $\chi^{(2)}$. Equation (4.28) shows that the SH power depends also on the squared cardinal sine of $\Delta\beta L/2$. This term expresses phase-matching. If $\Delta\beta = 0$, perfect phase-matching is satisfied. As $\Delta\beta$ increases, the generation efficiency lowers. The coherence length $L_{coh} = \pi/\Delta\beta$ describes the length over which the SHG process is still efficient [1].

4.2 Waveguide engineering

This section describes the engineering procedure performed to define the geometry of the waveguides designed for SHG. Here, the selected waveguide geometry and the adopted phase-matching mechanism are introduced, providing then a comparison between the efficiency strength of the selected structures.

4.2.1 Waveguide cross-section

The devices are designed to be fabricated on a 6' SOI wafer, with a 243 nm thick silicon layer and a $3\mu\text{m}$ thick BOX. Such a thin layer is used to minimize the effective area of the propagating modes, and so to increase the nonlinear interaction

strength. Moreover, a stressing cladding is expected to introduce a larger strain if the waveguide is thin². A 365 nm UV lithography is used to define the waveguides, which are realized by reactive ion etching in the Bruno Kessler Foundation clean room. On the waveguide top, a 140 nm thick SiN cladding layer is conformally deposited via LPCVD. This introduces a tensile stress in the silicon layer, estimated around 1.25 GPa via wafer bow measurement. The height of the SiN layer corresponds to the maximum value before cracking the wafer. In this way, the achievable stress in the silicon layer is maximized. The waveguide width varies between the different devices: it is properly selected to introduce phase-matching. A sketch of a typical waveguide cross-section is shown in Fig. 4.1.

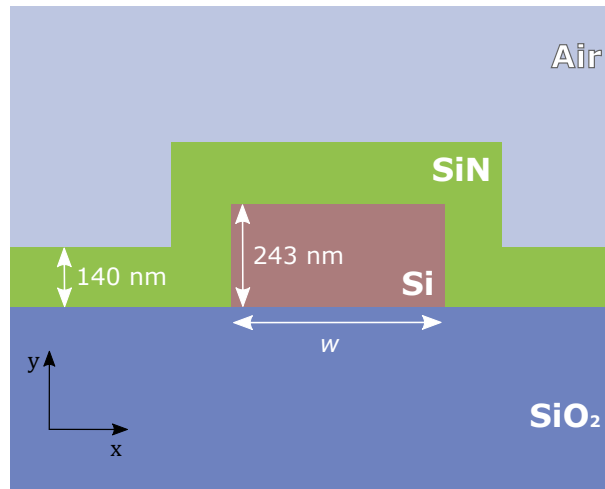


Fig. 4.1: Cross section of the waveguides described in this chapter. The width w is independently selected for each combination to have intermodal phase-matching.

4.2.2 Phase matching through waveguide engineering

In the SHG process, phase-matching requires that $\Delta\beta = 2\beta_p - \beta_{sh} = 0$. Considering that $\beta = 2\pi n_{\text{eff}}/\lambda$ and $\lambda_p = 2\lambda_{sh}$, the phase-matching condition becomes [146]:

$$n_{\text{eff},p} = n_{\text{eff},sh}. \quad (4.29)$$

This condition is hard to satisfy between pump and SH signals propagating on the same modal order because, due to their distant wavelengths, the effective refractive index dispersion impedes to satisfy it.

The most common technique to overcome this problem is to introduce a periodic

²The waveguide height is evaluated from interferometric measurements of the realized devices. Clearly, this value can be affected by fabrication uncertainty. However, fabrication uncertainties affect mainly the waveguide width rather than the height. Variations on height and width both produce a modification of the mode effective index, and it is not possible to disentangle them. Therefore, in the following the waveguide height is always set to its nominal value, considering only width variations.

modulation of the second-order nonlinear coefficient along the waveguide propagation direction. This technique, known as periodically poling, introduces an additional term in the phase-mismatch coefficient to achieve quasi-phase-matching. The use of this technique in nonlinear crystals like lithium niobate has been already presented in the introduction of this work. The ferromagnetic properties of lithium niobate can be exploited to change the $\chi^{(2)}$ sign by applying a strong DC field. However, in this work the physical mechanism providing $\chi^{(2)}$ is not clear. It can be due to strain, EFISH or generation in the SiN cladding, and it is the aim of this work trying to give an answer to this point. So, since the physical mechanism providing $\chi^{(2)}$ is unknown, it is not possible to investigate a method able to provide a change in the sign of $\chi^{(2)}$. Therefore, the problem is overcome by using pump and SH waves propagating on different modal orders. This method is commonly referred as **intermodal phase-matching** [35]. Using the intermodal approach, the waveguide width w is chosen to satisfy the phase-matching condition for a given combination of pump and SH modes.

The modal combinations analyzed in this work aim at phase-matching pump wavelengths above $2.2\mu\text{m}$. This is due to two main reasons. First, at these wavelengths TPA is negligible, so the pump power in the waveguide can be increased without enhancing free-carrier-induced losses [81]. Second, pump wavelengths above $2.2\mu\text{m}$ generate SH signals above $1.1\mu\text{m}$, in the transparent spectral region of silicon.

In Fig. 4.2 an example of the waveguide engineering procedure is shown. In red, the effective refractive index dispersion of the TE1 mode at the pump wavelength λ_p in a $1\mu\text{m}$ wide waveguide is shown. This value is obtained using the Electromagnetic Module of the COMSOL Multiphysics[®] FEM software [56], using refractive index dispersion measured with ellipsometry technique for all the materials. As expected, the effective refractive index decreases with wavelength, since the mode area increases and becomes less localized in the core. Moreover, also the material refractive index decreases with wavelength. Figure 4.2 reports also in blue the effective refractive index dispersion of the TM3 mode at the SH wavelength λ_{sh} for the same waveguide geometry. The pump and the SH dispersion curves cross at $\lambda_p \sim 2378\text{ nm}$, where $n_{\text{eff},p} = n_{\text{eff},sh}$ and **phase-matching condition is satisfied**. The insets of the figure show the simulated profiles of the pump and SH mode.

Equation (4.28) shows that the SHG efficiency is proportional to $\text{sinc}^2(\Delta\beta L/2)$. In Fig. 4.3 the normalized SHG efficiency is evaluated as $\text{sinc}^2(\Delta\beta L/2)$, and is reported in dB scale as a function of λ_p . The figure refers to a waveguide length of $L = 2\text{ mm}$, and to different values of waveguide width w . This result refers again to the conversion between the TE1 pump mode and the TM3 SH mode (TE1-TM3 combination). The figure shows that the phase-matching wavelength strongly depends on w .

The simulations reported so far refer to the TE1-TM3 combination. This is not the uniquely investigated combination. However, in all the investigated combinations the pump wave is on the fundamental TE1 mode. This is due to the fact that, in the pump spectral range, TM modes are not supported. Moreover, compared to higher

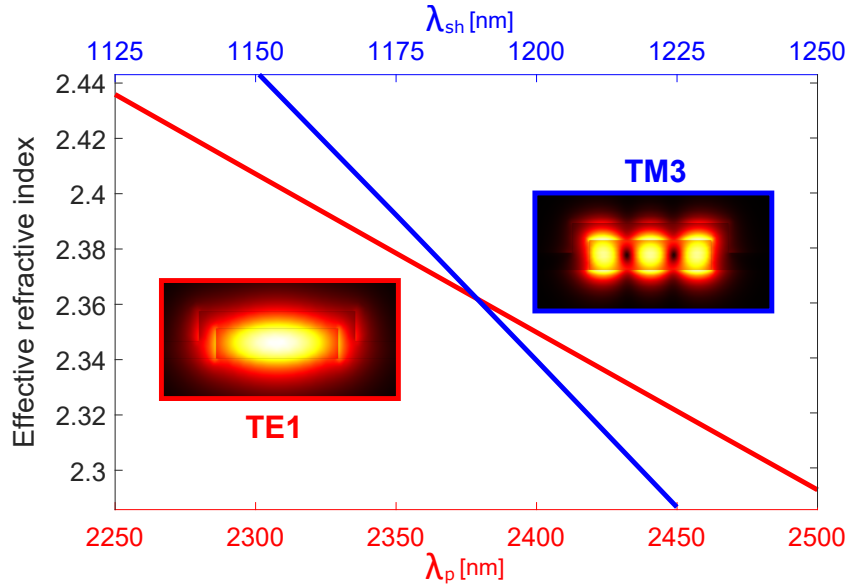


Fig. 4.2: Effective refractive index dispersion of the TE1 mode at pump wavelengths (in red) and of the TM3 mode at SH wavelengths (in blue) for a $1\ \mu\text{m}$ wide waveguide. The profiles of the two modes are shown in the insets.

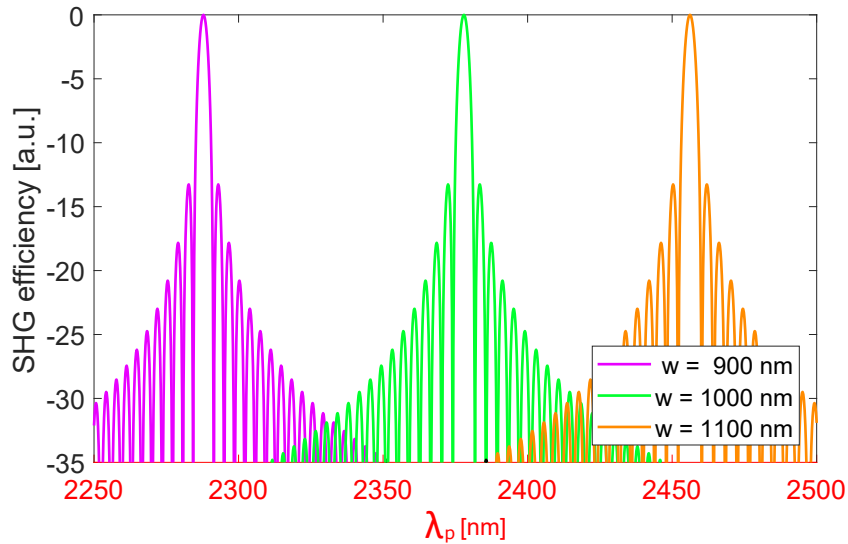


Fig. 4.3: Normalized SHG efficiency dependence on the pump wavelength λ_p . The SHG efficiency is evaluated as $\text{sinc}^2(\Delta\beta L/2)$ for $L = 2\ \text{mm}$. The simulations refer to the TE1-TM3 combination and to three different w .

order modes, the fundamental mode is the simpler to couple into the waveguide. In Fig. 4.4 λ_p is fixed at $2.3\ \mu\text{m}$ (and consequently λ_{sh} is fixed at $1.15\ \mu\text{m}$). In both the panels, the effective refractive index of the TE1 pump mode is reported in black against w . As expected, the effective refractive index increases with w , saturating at the slab waveguide value. The left hand side panel shows also the waveguide width dependence of the effective refractive index of all the TE modes supported by the waveguide at SH wavelengths. The three lowest order SH modes show effective refractive index values always larger than the pump mode. However, starting from

Tab. 4.1: Waveguide width w where phase-matching is achieved for the main modal combinations, considering $\lambda_p = 2.3\ \mu\text{m}$ and $\lambda_{sh} = 1.15\ \mu\text{m}$. For each combination, also the overlap coefficient K is reported.

Combination	w [μm]	K
TE1-TE4	1.08	~ 0
TE1-TE5	1.44	4.3×10^{-4}
TE1-TE6	1.79	~ 0
TE1-TE7	2.13	1.6×10^{-4}
TE1-TE8	2.46	~ 0
TE1-TM3	0.91	3.7×10^{-3}
TE1-TM4	1.54	~ 0
TE1-TM5	2.10	5.7×10^{-4}

the TE4 mode, the SH and the pump effective refractive indexes cross. This means that, for that modal combination, phase-matching is satisfied at the crossing w . The right hand side panel of Fig. 4.4 shows the same quantities referred to the TM SH modes. In this case, the two lowest order SH modes never cross the pump mode, while phase-matching is achieved starting from the TM3 mode.

To summarize, Tab. 4.1 shows w values where phase-matching is achieved for the main modal combinations for $\lambda_p = 2.3\ \mu\text{m}$ and $\lambda_{sh} = 1.15\ \mu\text{m}$.

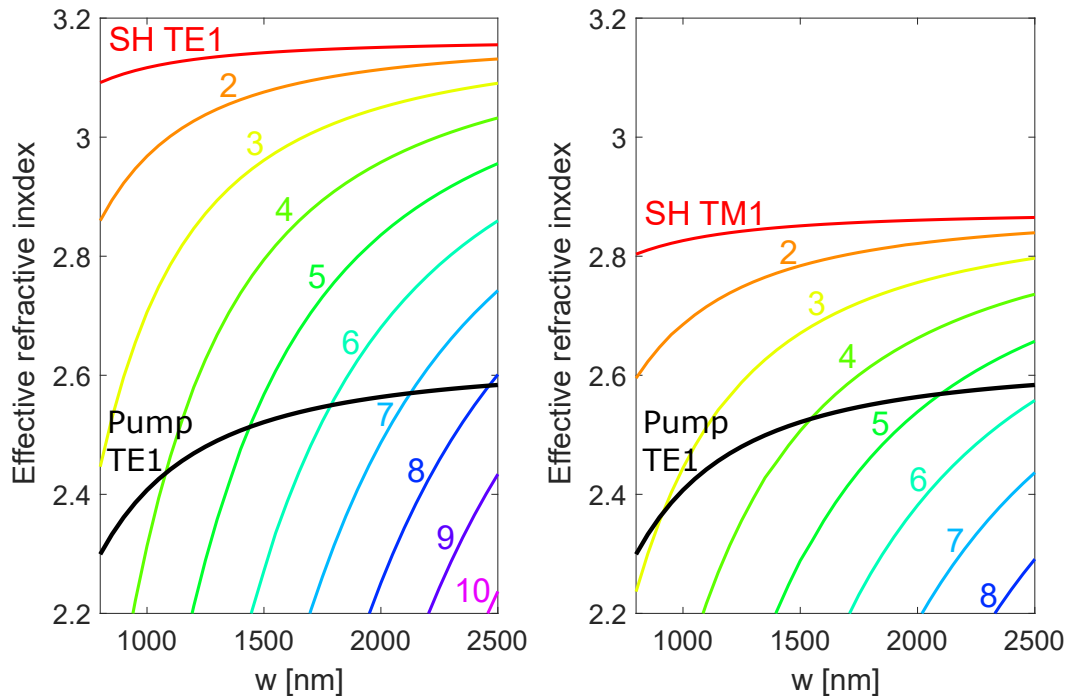


Fig. 4.4: Left: waveguide width dependence of the effective refractive index of the fundamental TE pump mode (black) and of all the SH TE modes (color). Right: waveguide width dependence of the effective refractive index of the fundamental TE pump mode (black) and of all the SH TM modes (color). In both the situations, $\lambda_p = 2.3\ \mu\text{m}$ and $\lambda_{sh} = 1.15\ \mu\text{m}$.

4.2.3 Strength of the modal combinations

Equation (4.28) shows that the generation efficiency is proportional to $|\gamma^{(2)}|^2$. The definition of $\gamma^{(2)}$ given in Eq. (4.10) shows that, in turn, the generation efficiency is proportional to $|\Gamma^{(2)}|^2$. However, $\Gamma^{(2)}$ cannot be determined, because it requires to know the spatial distribution of the unknown tensor $\chi^{(2)}$. However, it would be interesting to define a parameter quantifying the SHG strength independently on $\chi^{(2)}$, accounting only the overlap between the pump and the SH modes.

To this purpose, consider the case of a spatially constant $\chi^{(2)}$. Moreover, consider that only one element of the $\chi^{(2)}$ tensor is nonzero. In this case, $\Gamma^{(2)}$ becomes:

$$\Gamma^{(2)} = \chi^{(2)} K \quad (4.30)$$

where the dimensionless parameter K is defined by:

$$K = \frac{\sqrt{A_0} \int e_x(\mathbf{r}_\perp, \omega_p) e_k^*(\mathbf{r}_\perp, \omega_{sh}) e_x(\mathbf{r}_\perp, \omega_p) dA}{\left(\int n^2(\mathbf{r}_\perp, \omega_p) |e_x(\mathbf{r}_\perp, \omega_p)|^2 dA \right) \left(\int n^2(\mathbf{r}_\perp, \omega_{sh}) |e_k(\mathbf{r}_\perp, \omega_{sh})|^2 dA \right)^{1/2}}. \quad (4.31)$$

This equation considers a TE polarized pump field (directed along x) and a SH field TE or TM polarized (the electric field is directed along a generic direction $k = x, y$ depending on the polarization). The coefficient K is related to the **overlap between the pump and the SH modes**. For a spatially constant $\chi^{(2)}$, the SHG conversion efficiency is proportional to K . A large K determines a good overlap between the modes and so a strong conversion efficiency, while a small K means a bad mode overlap and so a bad conversion efficiency.

The far is $\chi^{(2)}$ from being spatially constant, the less is SHG efficiency related to K . However, it is possible to define (in general) an **effective second order susceptibility** $\chi_{\text{eff}}^{(2)}$ as follows:

$$\chi_{\text{eff}}^{(2)} = \left| \frac{\Gamma^{(2)}}{K} \right|. \quad (4.32)$$

This quantity can be interpreted as the equivalent spatially constant $\chi^{(2)}$ that would have given the same SHG efficiency.

In Tab. 4.1, the K value is reported for each of the analyzed modal combinations. It can be noted that SHG efficiency is smaller if the SH signals generated on larger order modes. Moreover, $K \sim 0$ when the SH signal is generated on a even parity mode. This is due to the symmetry of the modes, which nullifies the integral at the numerator of the definition of K . So, if $\chi^{(2)}$ is spatially constant, modal combinations with SH signal generated on a even parity mode are not admitted. In principle, this is not true if $\chi^{(2)}$ is not constant. However, Eq. (4.11) shows that in general $\Gamma^{(2)} = 0$ if $\chi^{(2)}$ is symmetric along the x direction with respect to the center of the waveguide.

Therefore, SHG is admitted for even parity SH modes only if $\chi^{(2)}$ is not symmetric along the x direction with respect to the center of the waveguide.

4.2.4 Quantification of the strain-induced nonlinear strength

So far, the strength of the modal combinations have been evaluated using the parameter K , which is related to the overlap between the pump and the SH modes. If $\chi^{(2)}$ is constant within the waveguide, the coefficient $\Gamma^{(2)}$ can be evaluated from K using Eq. (4.30). If $\chi^{(2)}$ is not constant within the waveguide, one should directly use the definition of $\Gamma^{(2)}$ given in Eq. (4.11).

As already mentioned, the real origin of SHG is not clear, and it is the aim of this thesis trying to understand it. However, suppose for a while that it can be entirely attributed to strain. How strong would be SHG in this case? So far, no convincing models showing connections between strain and $\chi^{(2)}$ have been reported in literature, especially for SHG. However, very recently in [110] the authors measured an electro-optic effect in a strained waveguide, ascribing it to Pockels effect. Using the theoretical model reported in [118], they fitted the experimental data with parameters connecting strain gradient and $\chi^{(2)}$. Assume now that the parameters reported in that work can be used also for SHG (indeed, this is not the case, because the frequencies of the fields involved in the Pockels effect are very different from the ones involved in SHG). In this case, the $\chi^{(2)}$ distribution inside the waveguide can be estimated using the coefficients reported in [110] and the strain gradient distribution calculated with a FEM simulation. This can be used in turn to determine the $\Gamma^{(2)}$ coefficient and, so, the SHG efficiency.

Doing so, as an example, the conversion between the TE1 pump mode and the TM3 SH mode are considered. The tensor element involved in this conversion process is $\chi_{\text{strain},xy}^{(2)}$. According to [118], this element is given by:

$$\chi_{\text{strain},xy}^{(2)}(\phi) = \Gamma_{xy,xy}\eta_{xy}(\phi) + \Gamma_{xy,yyy}\eta_{yyy}(\phi), \quad (4.33)$$

where ϕ defines the crystallographic axis along which the waveguide is oriented, $\eta_{mnl} = d\varepsilon_{mn}/dx_l$ are the strain gradient components and $\Gamma_{ijk,mnl}$ are coefficients that depend on the semiconductor. In the case of this work, $\phi = 0^\circ$. So, from [110] it is possible to derive $\Gamma_{xy,xy} = -4 \times 10^{-16} \text{ m}^2/\text{V}$ and $\Gamma_{xy,yyy} = -5.1 \times 10^{-16} \text{ m}^2/\text{V}$. These values can then be used to connect the strain gradient map within the waveguide to the strain-induced $\chi_{\text{strain}}^{(2)}$, and, in turn, the coefficient $\Gamma^{(2)}$ can be evaluated according to Eq. (4.11).

To do so, one has first to evaluate the strain gradient distribution inside the waveguide. This is done by using the Structural Mechanics Module of COMSOL Multiphysics[®] software [56]. The system is modeled using a 2D simulation domain, based on the simulation procedure described in chapter 3. A tensile stress of

1.25 GPa is included in the SiN cladding as an initial condition. This value corresponds to the one measured by wafer bow in the actual system. Using this simulation, the strain and the strain gradient components can be evaluated. As an example, Fig. 4.5 reports on a color map the strain components ε_{xx} and ε_{yy} , as well as the strain gradient components η_{xxy} and η_{yyy} , which are the components present in Eq. (4.33). The elastic parameters of the various materials are the same already reported in chapter 3. The solution refers to a waveguide width $w = 900$ nm, which should provide phase-matching between the TE1-TM3 modal combinations.

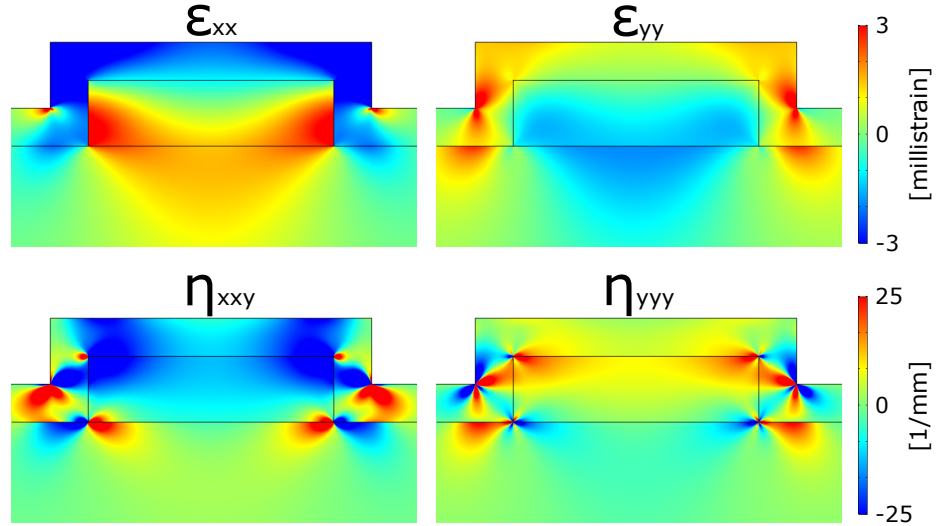


Fig. 4.5: Color map representing the strain components ε_{xx} and ε_{yy} , as well as the strain gradient components η_{xxy} and η_{yyy} , in a 900 nm wide waveguide.

By using these values, the $\chi_{\text{strain},xxy}^{(2)}$ map inside the waveguide is calculated according to Eq. (4.33), and it is shown in Fig. 4.6.

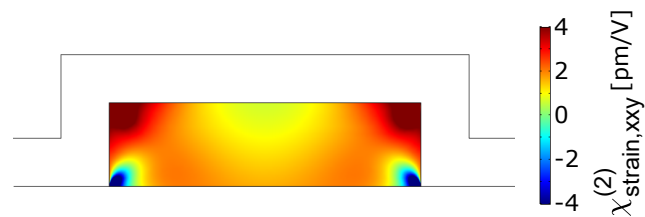


Fig. 4.6: Color map representing the $\chi_{\text{strain},xxy}^{(2)}$ distribution, evaluated according to Eq. (4.33) in a 900 nm wide waveguide.

The average value of $\chi_{\text{strain},xxy}^{(2)}$ inside the waveguide is 1.75 pm/V. Using this map, it is possible to evaluate the coefficient $\Gamma^{(2)}$ according to Eq. (4.11). Considering the modal combination TE1-TM3, one estimates $|\Gamma^{(2)}| = 0.47$ fm/V. Thanks to (4.32), this corresponds to an effective second order nonlinearity $\chi_{\text{eff}}^{(2)} = 0.13$ pm/V. In other words, this is the constant $\chi^{(2)}$ value that would give the same $\Gamma^{(2)}$ provided by the simulated strain gradient distribution and by the model of [110, 118]. Note

that $\chi_{\text{eff}}^{(2)}$ is much weaker than the average $\chi_{\text{strain},xy}^{(2)}$, because of the mismatched overlap with the optical modes determined by Eq. (4.11).

4.3 Estimating the generation efficiency

In the previous section, the methods adopted to engineer the waveguide geometry to enable SHG through intermodal phase-matching have been shown. In this way, the proper waveguide width for each modal combination has been calculated, estimating also the expected efficiency assuming a spatially constant $\chi^{(2)}$. All these parameters are reported in Tab. 4.1. However, to fully describe SHG also dispersive and third-order nonlinear effects must be considered. In other words, Eq. (4.26) must be solved. To this purpose, in this section a method to solve Eq. (4.26) is shown. This allows to individuate some detrimental effects that can occur, which are used to properly fix some details in the experiments described in the following chapters. Moreover, the method described here can be used to estimate $\chi^{(2)}$ from the experiment.

4.3.1 The split-step method

To solve Eq. (4.26), the split-step method is used [29]. Using this technique, the spatial domain z is divided in small segments. The initial condition at $z = 0$ is given by the temporal profile of the SH pulse, that is null, and of the pump pulse, that is described by a **Gaussian shape**:

$$u_p(z = 0, t) \sim e^{t^2/2\sigma_t^2}. \quad (4.34)$$

The quantity σ_t describes the temporal width of the pulse. It is related to the FWHM Δt by $\Delta t = 2\sqrt{2\ln 2}\sigma_t$. The temporal FWHM is related to the spectral width of the pulse $\Delta\omega$ by the time-bandwidth product. For a transform-limited (no frequency chirp) Gaussian pulse, it is given by [147]:

$$\Delta t \Delta\omega = 4\ln 2. \quad (4.35)$$

In each spatial domain, the solution resulting from the previous step is used as initial condition. In each segment, the solution is evaluated with the following steps.

1. Equation (4.26) is solved considering only the **temporal dispersion**. In other words, all the terms on the right hand side of the equations are neglected. This simplified equation is solved in the Fourier domain.

Tab. 4.2: Parameters used for the simulation described in this section, referred to the conversion between the TE1 pump mode at $\lambda_p = 2295$ nm and the TM3 SH mode $\lambda_{sh} = \lambda_p/2$ in a 900 nm wide waveguide.

Parameter	Pump TE1	SH TM3
n_{eff}	2.363	2.363
β_1 [ps/ μm]	0.0126	0.0165
β_2 [ps ² / μm]	4.1×10^{-7}	-2.2×10^{-6}
$\Gamma_{p,p}^{(3)}$ [$\mu\text{m}^2/\text{V}^2$] ^a		2.1×10^{-9}
$\Gamma_{p,sh}^{(3)}$ [$\mu\text{m}^2/\text{V}^2$] ^b		1.2×10^{-9}

^a $\Gamma_{p,p}^{(3)}$ is evaluated according to Eq. (4.15), using the $\chi_{xxxx}^{(3)}(\omega_p, \omega_p, \omega_p, \omega_p)$ tensor element evaluated at 2200 nm ($\chi_{xxxx}^{(3)} = 3.4 \times 10^{-7} \mu\text{m}^2/\text{V}^2$) [81].

^b $\Gamma_{p,sh}^{(3)}$ is evaluated according to Eq. (4.15). In this case, the $\chi_{xyyy}^{(3)}(\omega_p, \omega_p, \omega_{sh}, \omega_{sh})$ tensor element must be considered, recalling that in the range between 1200 nm and 2400 nm $\chi_{xyyy}^{(3)} = \chi_{xxxx}^{(3)}/2.36$ [148]. However, that tensor element is not available in literature. To this purpose, it is taken the mean value between the values at pump and SH wavelengths ($\chi_{xxxx}^{(3)} = 2.5 \times 10^{-7} \mu\text{m}^2/\text{V}^2$) [81].

2. The first step solutions are used as initial conditions to solve a simplified version of the Eq. (4.26), which considers only **SPM, XPM and losses**.
3. Up to now, the two equations in Eq. (4.26) are solved independently. In this step, they are finally coupled. The solutions resulting from the previous step are used to solve Eq. (4.26) where only the **SHG term** is considered.

This iterative procedure is computed till the end of the waveguide. So, at each step of the iteration, the temporal shape of the pulse is evaluated. Moreover, by taking the Fourier transform, also the pulse spectrum evolution can be easily determined.

4.3.2 Propagating optical pulses

In the following, Eq. (4.26) is solved using the split step method just described. To evidence the role of each term of Eq. (4.26), the system is solved taking into account only some of the effects. Then, a global solution of the equation is finally proposed. The aim of this study is to characterize the evolution of the pulses in the waveguide, as well as to determine the best conditions to use in the experiment.

The solution proposed here is evaluated for the TE1-TM3 combination. According to Tab. 4.1, this solution is the most efficient for a spatially constant $\chi^{(2)}$. The solution refers to a waveguide width $w = 900$ nm, where phase-matching occurs at a pump wavelength $\lambda_p = 2295$ nm. The parameters used for this simulation are shown in Tab. 4.2.

The temporal and the spectral shape of the optical pulse are the ones of the laser system used to experimentally characterize them, which is described in the next chapter. This laser system has a peak power of ~ 17 GW, a temporal width $\sigma_t \sim 35$ fs, and a 1 kHz repetition rate. The laser peak power is too large to directly couple

it into the waveguide, because it causes a damage of the waveguide input facet. For this purpose, the peak power must be reduced. This can be done in two ways. The simplest one is to attenuate it, maintaining the pulse shape. The other possibility is to re-shape the pulse, enlarging it temporally and so reducing its peak power. So, in the following different simulations are proposed where the pulse temporal width is changed. When not differently specified, the peak power is fixed at 5 W. Considering the typical setup described in the following, this value can prevent facet damage during coupling.

Since the $\chi^{(2)}$ tensor distribution within the waveguide is unknown, in the following simulation it is assumed for simplicity constant. In this way, according to Eq. (4.30), $\Gamma^{(2)} = \chi^{(2)}K$. The value of K is given in Tab. 4.1. Regarding $\chi^{(2)}$, when not differently specified, it is taken as 0.1 pm/V. This is an arbitrary value, that is taken in order to test the simulation code. As it is specified in the next section, this model is used then to reconstruct the $\chi^{(2)}$ value starting from the experiment. However, this value is of the same order of magnitude of that estimated in Sec. 4.2.4, evaluated assuming that $\chi^{(2)}$ is due to strain with the coefficients of [110].

In the following, it is often needed to pass from the peak power of a pulse P to its average power $\langle P \rangle$. In general, this can be done as:

$$\langle P \rangle = r \int P |u(t)|^2 dt, \quad (4.36)$$

where r is the pulse repetition rate (here $r = 1$ kHz), while the integral is taken over all the pulse duration. This expression is often approximated as:

$$\langle P \rangle = rP\Delta t, \quad (4.37)$$

SHG alone. To demonstrate the correct operation of the solution method based on the split-step method, Eq. (4.26) is solved first by considering only the SHG terms (so, neglecting time evolution, phase-modulation and losses). While solving Eq. (4.26), phase-matching is considered satisfied, so $\Delta\beta = 0$.

Figure 4.7 (a) reports on the left hand side axis the SH average power $\langle P_{sh} \rangle$ as a function of the waveguide length L . The result shows a quadratic dependence on the waveguide length L . The same quadratic dependence is shown when considering the peak SH power P_{sh} , reported on the right hand axis of Fig. 4.7(a). This is in agreement with the expectation resulting from Eq. (4.28). In Fig. 4.7(a) the SH power is reported for three different pump powers, showing the quadratic proportionality on the pump power predicted by Eq. (4.28).

When showing a polynomial dependence between two quantities, it is useful to report them in a log-log scale. For example, Eq. (4.28) shows that $P_{sh} = kL^2$, being k a proportionality constant. By taking the logarithm, it is possible to write $\log(P_{sh}) = 2 \log(L) + \log(k)$. Thus, reporting P_{sh} versus L in a log-log scale, a linear

behavior is expected, with a slope equal to 2. So, the quantities reported in Fig. 4.7(a) are shown in log-log scale in Fig. 4.7(b). All the curves show a slope equal to 2, reproducing the expected quadratic dependence. Moreover, it can be noted that a variation in the pump power produces a shift in the plot. Also this fact is understandable, since a pump power variation is described by a variation of the proportionality constant k , which corresponds to a shift in the log-log plot.

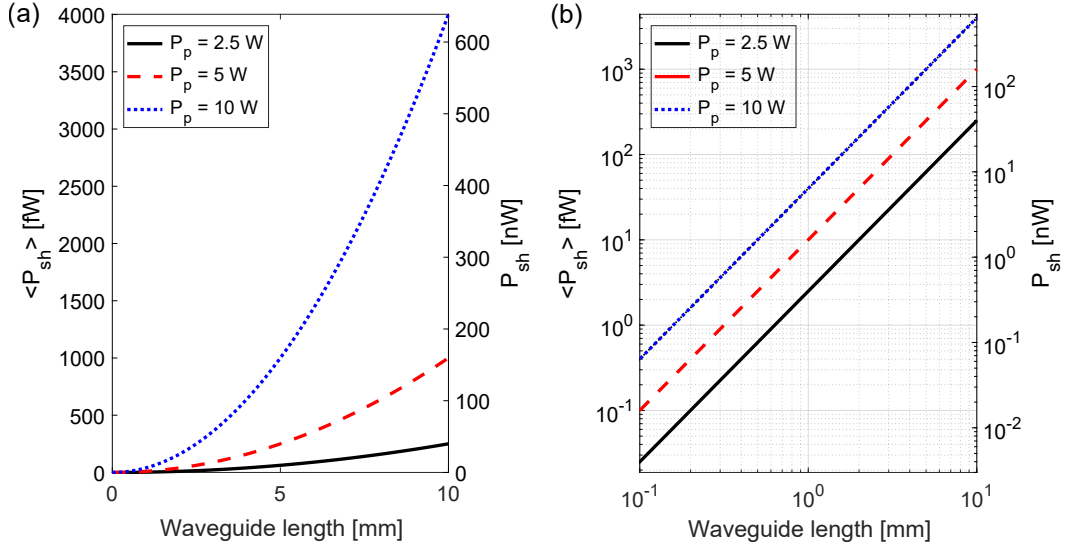


Fig. 4.7: (a) Simulated SH average power (left side) and peak SH power (right side) as a function of the waveguide length. This quantity is reported for three different pump powers. In the simulation only SHG is considered, neglecting temporal dispersion, phase-modulation and propagation losses. (b) Same quantity of panel (a) reported in log-log scale.

Equation (4.28) shows that P_{sh} grows quadratically also with the pump power P_p . This is well reproduced by the numeric solution proposed here, shown in Fig. 4.8(a) and referred to a 1 cm long waveguide. The same happens when reporting the dependence on the second order nonlinear coefficient $\chi^{(2)}$, shown in Fig. 4.8(b) and referred again to a 1 cm long waveguide.

Figure 4.9(a) shows the SH peak power as a function of the waveguide length L for different temporal extensions of the pulses. In the three simulations, the pump peak power is kept constant. The plot shows that the SH peak power does not depend on the pulse temporal duration. This is not surprising. In fact, peak SH power does not depend on the temporal shape of the pulse and remains constant once the pump peak power is fixed. On the other hand, Fig. 4.9(b) reports the average SH power as a function of the waveguide length L for different temporal extensions of the pulses. The figure shows that, increasing the temporal extension of the pump pulse, the SH power increases. This is because a temporally longer pump pulse generates a longer SH pulse with the same peak power, so its average power is larger. Therefore, given a certain pump peak power, a longer pulse is preferable because it allows to increase the SH power. Moreover, due to Fourier relation, a temporally longer pulse has a thinner spectrum. This is preferable, because it can match better the spectral

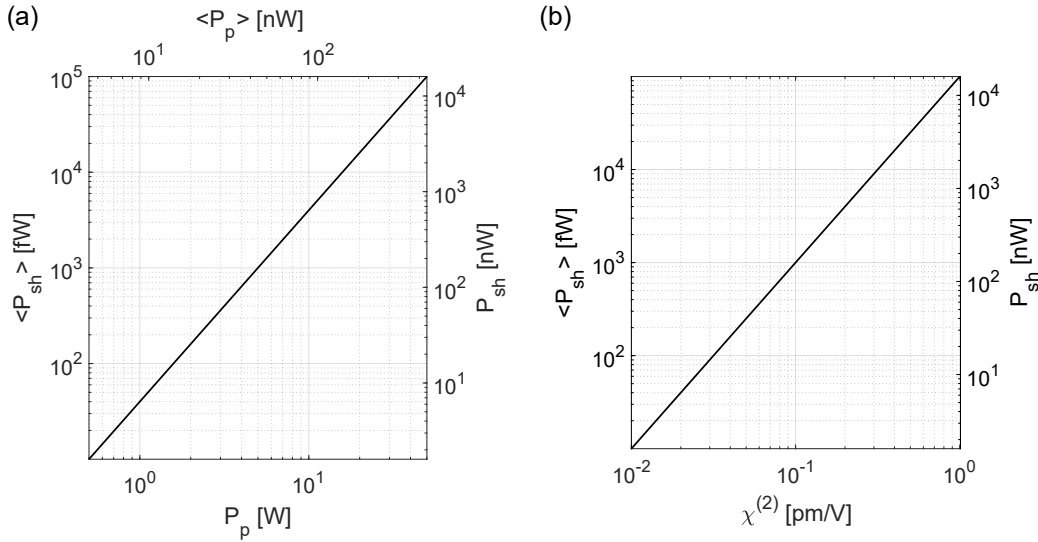


Fig. 4.8: (a) Average (left axis) and peak (right axis) SH power as a function of the average (top axis) and peak (bottom axis) pump power in a 1 cm long waveguide. (b) SH average power (left axis) and peak SH power (right axis) as a function of the second order nonlinear coefficient $\chi^{(2)}$ in a 1 cm long waveguide. In these simulations, only SHG is considered.

bandwidth over which the phase-matching condition $\Delta\beta \sim 0$ can be considered valid.

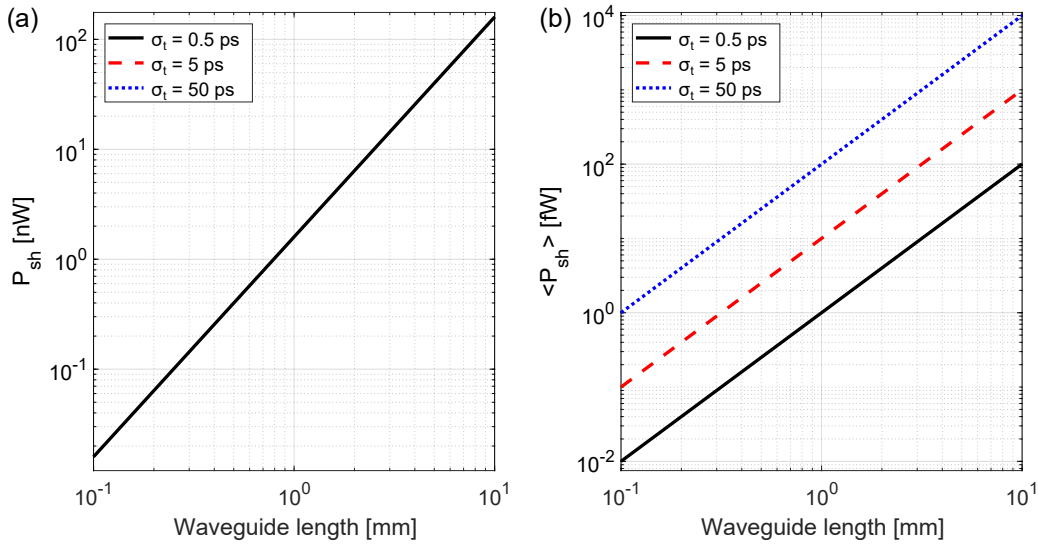


Fig. 4.9: (a) Simulated SH peak power as a function of the waveguide length for three temporal widths of the pulse. The pulse peak power is 5 W. In the three cases, the curves perfectly overlap. (b) SH average power as a function of the waveguide length in the same situation of panel (a). Here, only SHG is considered.

SHG and temporal dispersion. Here, Eq. (4.26) is numerically solved via split-step method considering both SHG and time evolution terms. Figure 4.10 shows the temporal shape of both the pump (dotted curve) and the SH pulses (solid curve) in

different positions within the waveguide. The three panels refer each to a different temporal width of the pump pulse (respectively, 0.5 ps, 5 ps and 50 ps). In all the situations, the pump pulse is centered at time $t = 0$ at the beginning of the sample. Looking in other positions of the sample, the pump pulse is present at different time positions, showing that it is evolving in time. Regarding the SH pulse, it is not present at the beginning of the waveguide (in fact, at the initial point only the pump mode is excited). Then, in other positions along the waveguide propagation direction, the SH pulse appears. However, the temporal shape of the SH pulse is strongly dependent on the pump pulse shape. For long pump pulses, like the one referred to $\sigma_t = 50$ ps, the SH pulse grows along the waveguide, maintaining its Gaussian shape. This is not true for shorter pulses. In these cases, the SH peak power grows in the first part of the waveguide. Then, it saturates, and the pulse starts to broaden in time. To this purpose, note the difference in the values of β_1 reported in Tab. 4.2. Since the group velocity v_g is given by $1/\beta_1$, the SH pulse propagates more slowly than the pump pulse, so they lose their temporal overlap. Therefore, the part of SH signal generated close to the end of the waveguide is already out of the sample when the signal generated at the beginning is still propagating in the waveguide. This phenomenon is called **temporal walkoff**, and determines a distortion of the temporal shape of the SH pulse. The same phenomenon can be understood by looking at Fig. 4.11(a), where the SH peak pump power is shown as a function of the sample length for three different time durations. Only for long pulses the peak power grows quadratically, while it reaches a saturation for shorter pulses. The shorter the pulse, the stronger the effect of walkoff. This result is of particular interest if compared with the result of Fig. 4.9, when temporal evolution was not considered. The same effect can be seen by looking at the average SH power, shown in Fig. 4.11(b). Also the average power shows a quadratic dependence up to a certain waveguide length, after which the growth is less than quadratic.

Phase-modulation terms. The contribution of phase-modulation is mainly related to the spectral distortion of the pulses. Figure 4.12 shows the spectral broadening of the pump pulse while propagating in the waveguide. The three panels of Fig. 4.12 refer to different temporal widths of the pump pulse, which clearly correspond to three different spectral widths. The longer the pulse in time, the narrower its spectrum. The three situations refer to three pulses having different temporal width but the same peak power. So, when considering the spectrum, the narrower pulse possesses larger peak power. Figure 4.12 shows that, while evolving, the pump pulse broadens due to phase-modulation. The figure shows that the effect is stronger for pulses with a broader spectrum (and so, with a shorter time extension). The spectral broadening of the pulse is detrimental because of the limited bandwidth of the phase-matching condition. So, an efficient SHG process requires a spectrally narrow pulse, which correspond to a long pulse in time.

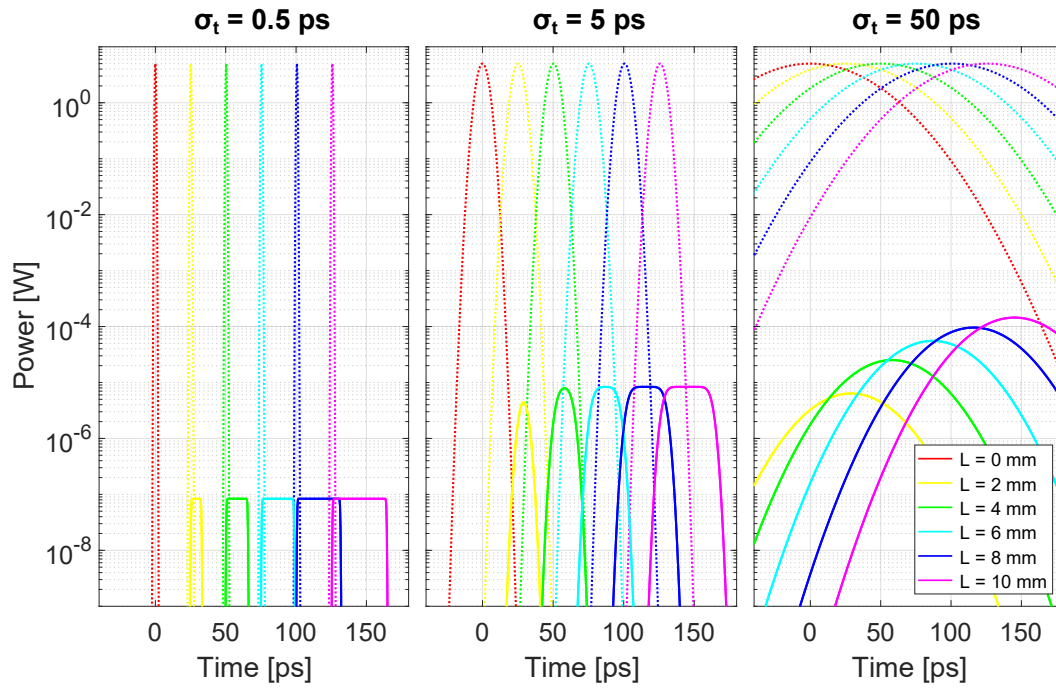


Fig. 4.10: Pump (dotted) and SH (solid) temporal profiles in different position along a 1 cm long waveguide. The positions where the profiles are taken are specified in the legend. The three panels refer to three different temporal durations of the pulse. The simulations have been performed considering SHG and time evolution terms.

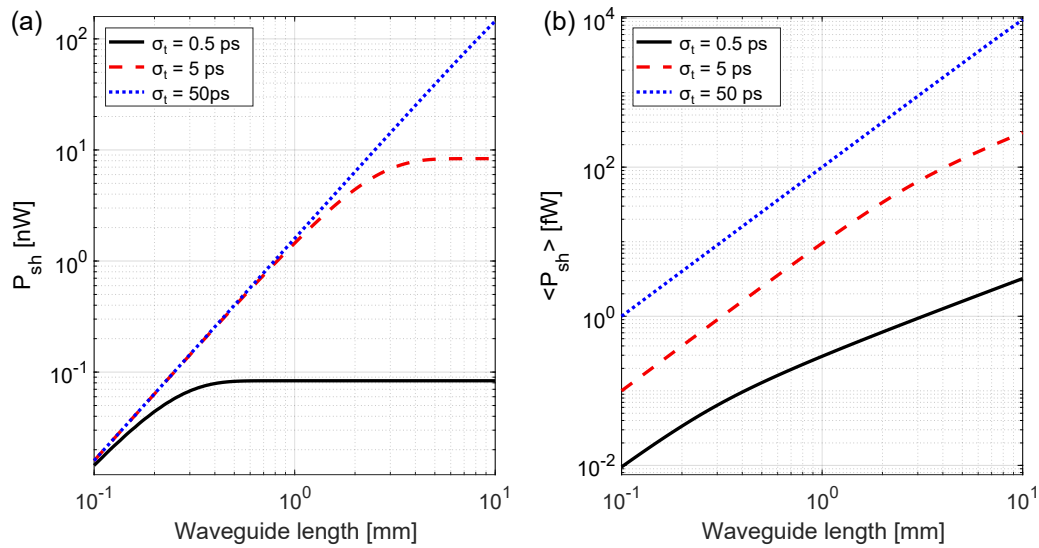


Fig. 4.11: (a) SH peak power as a function of the waveguide length when both SHG and temporal evolution are considered. The result refers to three different durations of the pump pulse. (b) SH average power as a function of the waveguide length.

Global solution. Figure 4.13 shows the evolution of pump and SH pulses in a waveguide when SHG, time evolution and phase-modulation terms are considered. The result is similar to the one shown in Fig. 4.10, when no phase-modulation terms was considered. However, from a comparison between the figures it can be noted that phase-modulation introduce a further distortion of the pulse shape.

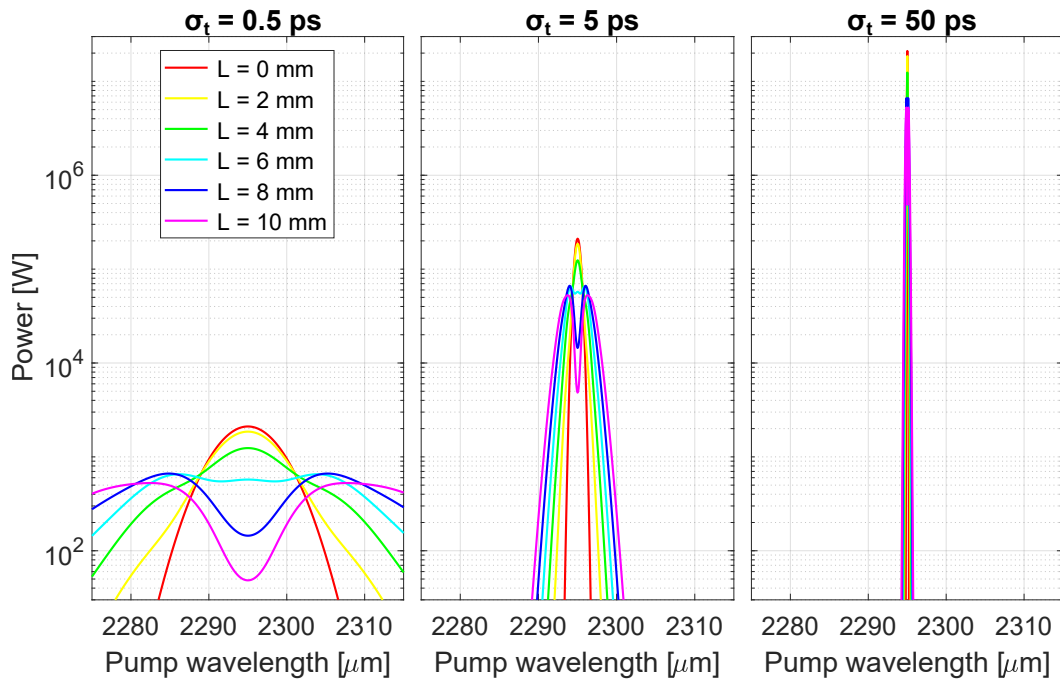


Fig. 4.12: Spectral profile of the pump pulse while propagating in the waveguide. The three panels refer to three different pulse temporal durations.

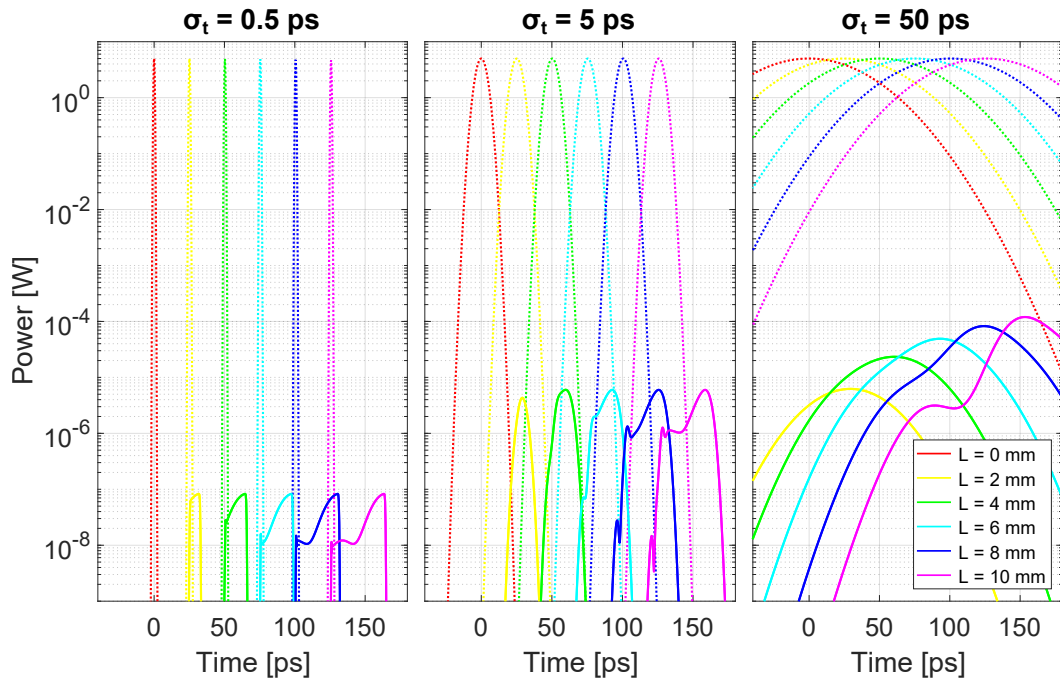


Fig. 4.13: Pump (dotted) and SH (solid) temporal profiles in different position along a 1 cm long waveguide. The three panels refer to different temporal durations of the pump pulse. The simulation panels considers SHG, time evolution and phase-modulation.

The result changes a lot when also propagation losses are considered. Figure 4.14 shows the same quantity of Fig. 4.13, but it takes into account also losses. For simplicity, the pump and SH losses are assumed equal and correspond to 8 dB/cm.

The losses affect the pump pulse, which weakens while propagating in the waveguide. Also the SH pulse is affected by losses. In fact, on the one hand the SH pulse itself is weakened. Moreover, due to the weakening of the pump pulse, also the power generated by means of SHG is reduced. Due to this, after a certain length of the sample, the SH power reduces. So, in some cases, shorter waveguides provide a larger conversion efficiency. The shorter the pulse, and the larger is this effect. So, also for this motivation, temporally longer pulses are preferable.

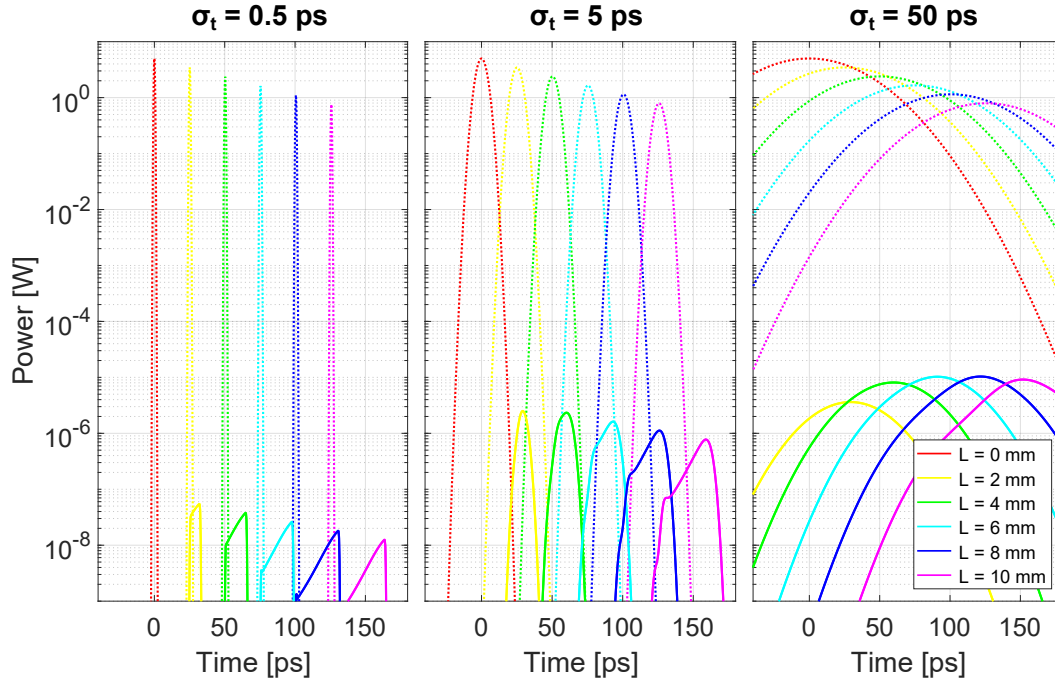


Fig. 4.14: Pump (dotted) and SH (solid) temporal profiles in different position along a 1 cm long waveguide. The three panels refer to different temporal durations of the pump pulse. The simulation considers SHG, time evolution, phase-modulation terms and propagation losses of 8 dB/cm for both the pulses.

To underline the effect of propagation losses, Fig. 4.15 shows the peak SH power (panel a) and the average SH power (panel b) as a function of the waveguide length for three different values of propagation losses (0.08 dB/cm, 0.8 dB/cm and 8 dB/cm). In this case, the pulse temporal width is 5 ps. It can be noted that propagation losses strongly affect the SHG efficiency. If propagation losses are below 1 dB/cm, a longer waveguide provides a larger efficiency. However, if losses are larger, the SH power can be increased by reducing the waveguide length.

4.3.3 From the experiment to the $\chi^{(2)}$ coefficient

In previous sections, a method to solve Eq. (4.26) has been introduced. Using this method, the SH power can be determined once that some parameters are known. These include the pump power, some waveguide parameters (like the ones reported

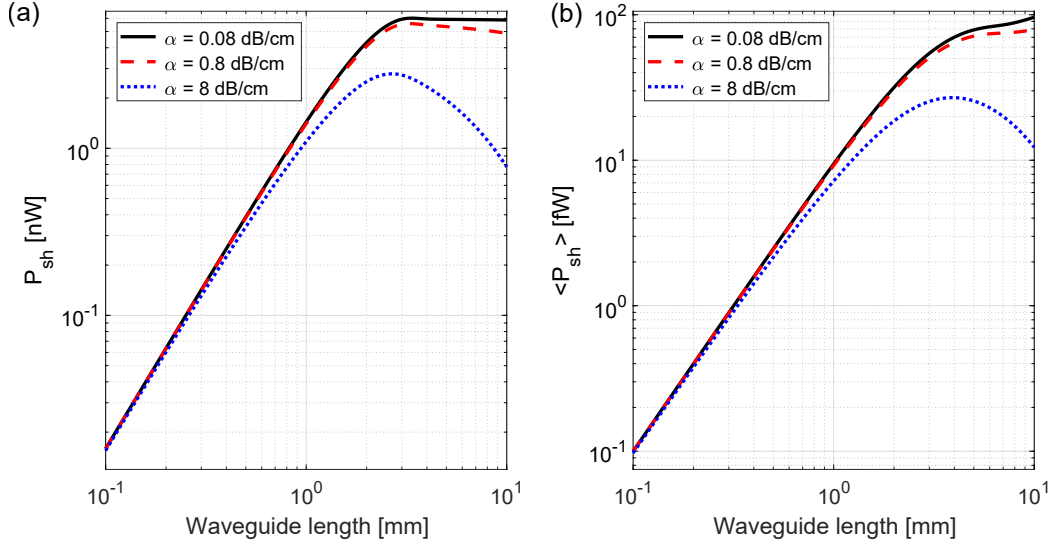


Fig. 4.15: Peak SH power (a) and average SH power (b) as a function of the waveguide length. The simulation solves all the terms of Eq. (4.26) and considers three different values of propagation losses.

in Tab. 4.2), the waveguide length, the pulse temporal duration, the propagation losses, and the second order nonlinear coefficient $\chi^{(2)}$.

In the previous sections, a uniform $\chi^{(2)}$ distribution within the waveguide has been assumed. In this situation, according to Eq. (4.30), $\Gamma^{(2)} = \chi^{(2)}K$. However, this is not the most general case: if the nonlinear susceptibility is not uniform, $\chi^{(2)}$ cannot be factorized out of the integral which defines $\Gamma^{(2)}$. So, in general, the SHG efficiency depends on $\Gamma^{(2)}$, which encodes in its integral definition the overlap between the distribution of $\chi^{(2)}$ and of the propagating modes.

The coefficient $\Gamma^{(2)}$ is, in general, complex. However, for a small $\Gamma^{(2)}$, the SH pulse does not much affect the pump pulse. Neglecting dispersion and phase-modulation, the SHG equation in Eq. (4.26) has a simple solution of the form $u_{sh} \propto \Gamma^{(2)}$. The quantity measured in the experiment is $P_{sh} = P_{0,sh}|u_{sh}|^2$, and so it depends only on the modulus of $\Gamma^{(2)}$ and not on its phase. This fact is confirmed by the numeric solution of Eq. (4.26). So, considering the typical powers of the experiment shown in the following, $|\Gamma^{(2)}|$ can be considered an input parameter of the numerical model.

As an example, in Fig. 4.16 the average SH power is reported in a color map as a function of both the pump average power and the second order nonlinear coefficient $|\Gamma^{(2)}|$. The simulation refers to the TE1-TM3 combination in a 900 nm wide and 5 mm long waveguide, for a pulse duration of 5 ps and assumes propagation losses of 8 dB/cm for both the pump and the SH pulses. On the right hand side axis of the plot, it is also reported the coefficient $\chi_{\text{eff}}^{(2)}$ which is related to the term $|\Gamma^{(2)}|$ according to Eq. (4.32). In the simple situation of a spatially constant $\chi^{(2)}$, one has $\chi_{\text{eff}}^{(2)} = \chi^{(2)}$.

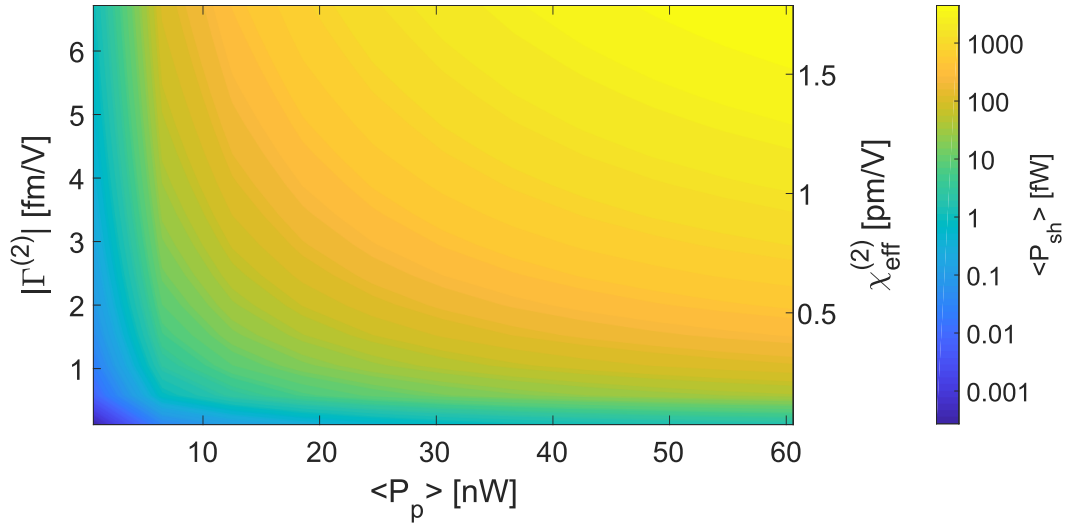


Fig. 4.16: Average SH power as a function of the pump average power and both the second order nonlinear coefficient $|\Gamma^{(2)}|$ and $\chi_{eff}^{(2)}$. The simulation refers to the TE1-TM3 combination in a 900 nm wide and 5 mm long waveguide, with a pulse duration of 5 ps and propagation losses of 8 dB/cm for both the pump and the SH pulses.

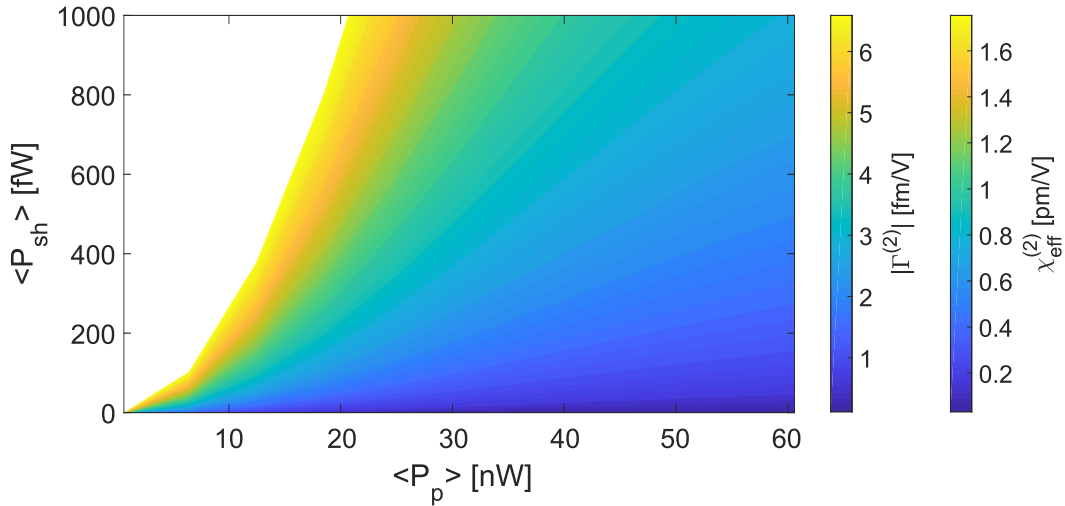


Fig. 4.17: Second order nonlinear coefficients as a function of the pump average power and the SH average power. This figure is obtained by inverting the curve of Fig. 4.16.

While performing the experiment, all the parameters used in this model can be estimated, except $|\Gamma^{(2)}|$. Typically, during the experiment one measures the pump power and the SH power, and wants to estimate the coefficient $|\Gamma^{(2)}|$ (or, analogously, $\chi_{eff}^{(2)}$). So, it can be useful to invert the plot shown in Fig. 4.16, reporting the coefficients $|\Gamma^{(2)}|$ and $\chi_{eff}^{(2)}$ as a function of the pump and the SH powers. This is shown in Fig. 4.17. Fitting this curve, $|\Gamma^{(2)}|$ and $\chi_{eff}^{(2)}$ can be determined from the pump and the SH powers. In the experiments shown in the following, the nonlinear coefficient is estimated in this way.

Demonstration of SHG in strained silicon waveguides

5.1	Experimental setup	83
5.1.1	The source	84
5.1.2	The pulse-shaping stage	85
5.1.3	The coupling stage	86
5.1.4	The detection stage	87
5.2	Characterization of SHG in strained silicon waveguides	88
5.2.1	Dependence on the pump wavelength	88
5.2.2	Dependence on the waveguide	90
5.2.3	Dependence on the pump power	90
5.2.4	Spectrum of the SH signal	91
5.3	Estimation of the nonlinear coefficient	92

This chapter describes the experimental characterization of SHG in strained silicon waveguides. The waveguides analyzed in this part result from the engineering procedure described in Sec. 4.2. Section 5.1 offers an introduction to the experimental setup. Then, in Sec. 5.2 the experimental characterization of the SHG process is shown. Finally, in Sec. 5.3 the nonlinear coefficient $\chi^{(2)}$ providing the detected signal is estimated.

The experimental setup described in this work was assembled by Mr. A. Marchesini, Dr. A. Trenti and Dr. M. Mancinelli. The experiments have been realized together with Miss C. Vecchi, Dr. A. Trenti and Mr. A. Marchesini. The samples have been fabricated by Dr. M. Ghulinyan at Fondazione Bruno Kessler.

Part of the experiment described here is also described in [145, 146, 149].

5.1 Experimental setup

In this section, the experimental setup used to demonstrate the SHG is described. The setup is sketched in Fig. 5.1, and is similar to the one described in [146, 150]. It is formed by the four following parts.

1. The source.

2. The pulse-shaping stage.
3. The coupling stage.
4. The detection stage.

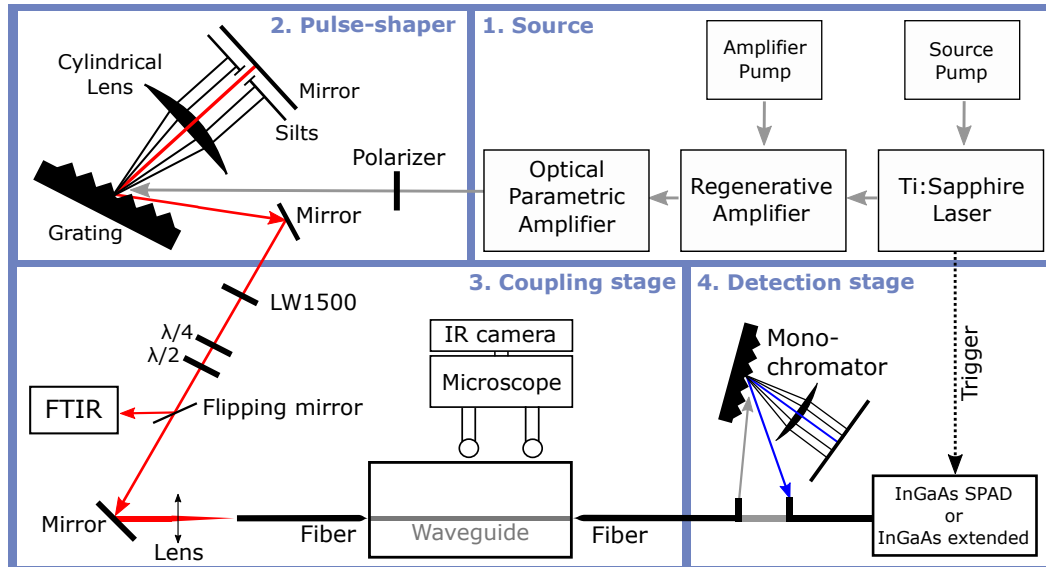


Fig. 5.1: Experimental setup described in this section.

5.1.1 The source

The source is, in turn, constituted by three stages.

The first stage is a solid-state **Ti:sapphire laser** (Spectra-Physics Tsunami®). It is optically pumped by a 4 W laser at a wavelength of 532 nm (Spectra-Physics Millennia®). The Ti:sapphire laser can operate both in the quasi Continuous-Wave (CW) condition, as well as in mode-locked condition that is achieved using an acousto-optic modulator. For the purpose of this experiment, the laser operates in the mode-locked condition at a central wavelength of 800 nm. Its bandwidth is 70 nm, with $\sigma_t = 35$ fs and a 82 MHz repetition rate. The average power is around 500 mW.

The Ti:sapphire laser is amplified by a **regenerative amplifier** (Spectra-Physics Spitfire®). The regenerative amplifier is formed by another Ti:sapphire laser cavity pumped by a 20 W laser at 527 nm, with a repetition rate of 1 kHz (Spectra-Physics Empower®). The optical pulses coming from the Tsunami laser are overlapped with the ones of the regenerative amplifier through a timing control unit. To reduce the peak power within the cavity, the Tsunami pulse is temporally stretched before being amplified. Then, at the output of the amplifier, the pulse is compressed. At the output of the amplifier, an average power above 3 W is measured, with 1 kHz repetition rate.

The last part of the pump system is a nonlinear stage formed by an **optical para-**

metric amplifier (Light Conversion TOPAS-C®). Within this stage, the amplified beam at 800 nm is split in two arms. One of these arms impinges on a sapphire plate. It generates a supercontinuum signal in the range from 1.14 μm to 1.6 μm . The supercontinuum is then mixed in a nonlinear crystal with the other arm of the amplified beam at 800 nm. Through DFG process, two beams are generated. The wavelength of these beams can be tuned by changing the orientation angle of the nonlinear crystal. The first beam (named signal beam) can be tuned in the range from 1.14 μm to 1.6 μm , while the second beam (the idler beam) is tunable in the range from 1.6 μm to 2.6 μm . The signal and the idler beams are generated on linear orthogonal polarizations, which can be separated using a polarizer. Therefore, considering only the idler, this stage can act as a tunable mid-infrared light source. In the next sections, the idler beam will be referred as the **pump beam**.

The spectrum of the pulse emitted by the TOPAS-C® is shown in Fig. 5.2. It is measured using a Fourier Transform Infrared (FTIR Brucker Vertex-70v®) spectrometer, which is provided by an InSb detector that allows a sensitivity in the range from 1 μm to 5.5 μm . The spectrum shown in Fig. 5.2 is performed when the OPA signal is set at 1200 nm, with the corresponding idler centered at 2400 nm. Changing the OPA settings, the two peaks can be spectrally shifted. The total average power emitted by the OPA is $\langle P_p \rangle \sim 600$ mW. Using Eq. (4.37), this corresponds to a peak power $P_p \sim 7$ GW (considering $r = 1$ kHz and $\Delta t = 82.4$ fs, calculated assuming a Gaussian pulse with $\sigma_t = 35$ fs). As already remarked in the previous chapter, a direct coupling of such a huge power within the waveguide is not possible, because it determines the input waveguide facet burning. This motivates the necessity of a pulse shaping-stage, which is described in the next section. Using this additional stage, the pump pulse is spectrally cut, determining a temporal enlargement of the pulse width and a reduction of the peak power. Moreover, a reduction of the spectral width of the pump pulse allows to match better the wavelength range over which the phase-matching condition is satisfied.

5.1.2 The pulse-shaping stage

The time-bandwidth product shown in Eq. (4.35) indicates that a pulse can be temporally tailored by shaping its spectrum. The pulse-shaper assembled for this experiment works in the 4f reflection configuration [151]. First, a diffraction grating separates the spectral components of the pulse. Then, a cylindrical lens is used to transform the grating angular dispersion into a spatial dispersion. Tunable slits modulate the intensity of the various frequency components. A mirror reflects back the selected frequencies, which are then focused by the lens on the grating and create again a reshaped collimated beam. On the one hand, this system can be reconfigured by modifying the aperture of the slits, setting the width of the pulse at the output of the pulse-shaping stage. On the other hand, an automatic rotation system placed

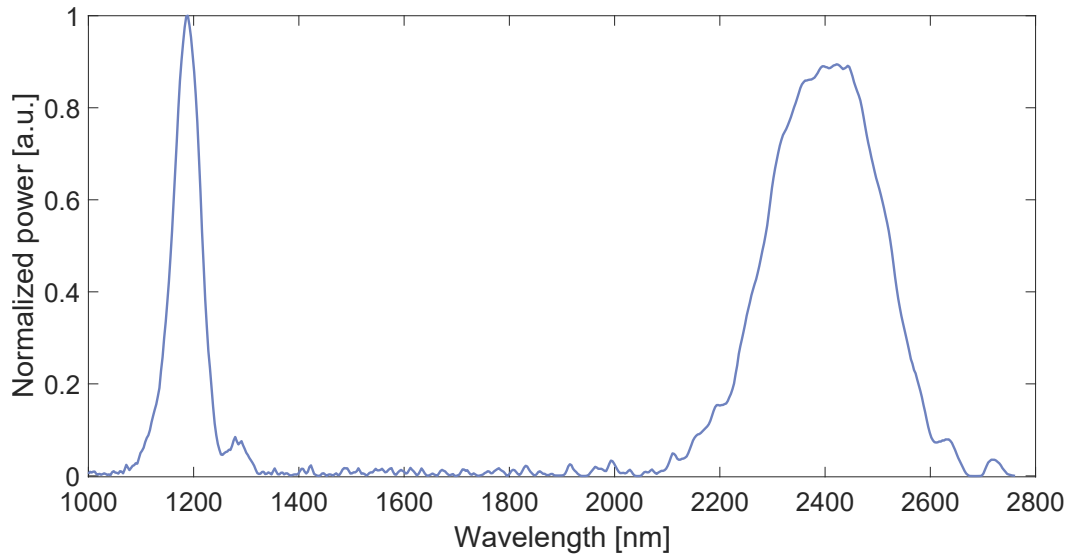


Fig. 5.2: Spectrum of the pulse emitted by the TOPAS-C®. The measurement is performed by a FTIR spectrometer.

below the diffraction grating can be used to tune the central wavelength of the output pulse.

In Fig. 5.3, a normalized spectrum of the pulse before and after the pulse-shaping stage is shown. Using this configuration, the pulse spectrum is cut from 253 nm to 14 nm. A further reduction of the slit aperture allows to tailor the pulse width to 0.5 nm. Clearly, this shaping mechanism is inherently lossy. However, for the purposes of this experiment, an additional stage of filters is used to further reduce the power.

For the purpose of this experiment, it is particularly important to filter out any other component of the OPA signal pulse. In fact, the pulse-shaper does not transmit only the selected wavelength, but also its halved wavelength thanks to the second order diffraction of the grating. This is particularly detrimental in a SHG experiment, when the SH signal is generated at the halved wavelength of the pump signal. To this purpose, a polarizer is placed at the output of the OPA system, able to select the idler beam that is orthogonally polarized with respect to the signal beam. Moreover, after the pulse-shaping stage, the signal is filtered by a 1500 nm long-wave pass filter with a > 50 dB extinction ratio.

From now on, the beam exiting the pulse-shaper is named **pump pulse**.

5.1.3 The coupling stage

The pulse exiting the pulse-shaper is ready for being coupled into the waveguide. After two mirrors, a collimator couples light into a tapered lensed optical fiber. This fiber is used to couple light into the waveguide via butt coupling. A second fiber at the waveguide output collects the transmitted power. Both the fibers are

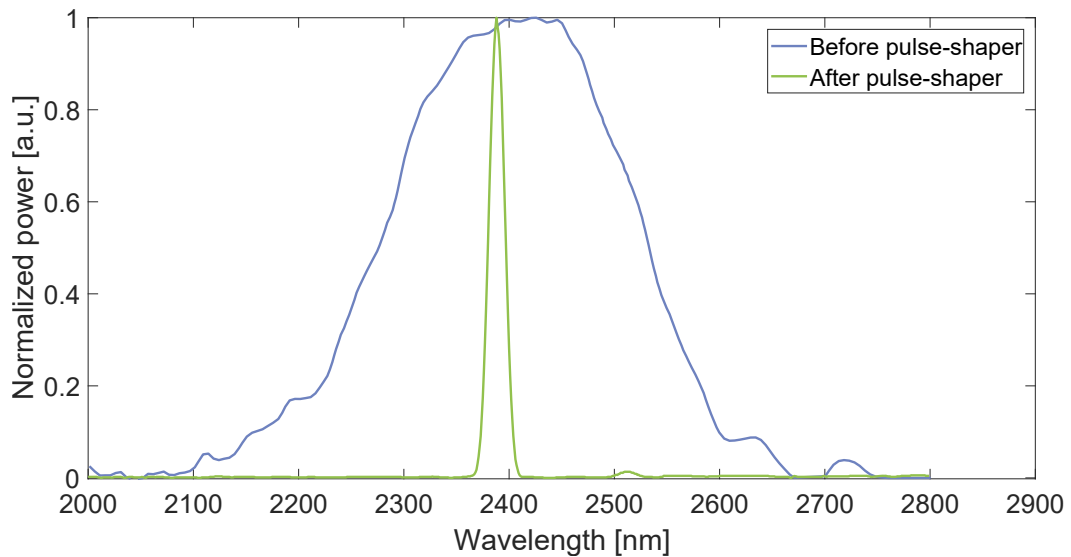


Fig. 5.3: Normalized spectra of the idler pulse emitted by the TOPAS-C@before (blue) and after (green) the pulse-shaper.

mounted on piezoelectric controlled flexure stages. A polarizing stage constituted by a half waveplate and a quarter waveplate is placed before the collimator. They allow to select the proper polarization coupled into the waveguide, correcting any polarization distortion introduced by the coupling fiber. They are properly set by maximizing the pump signal transmitted by the waveguide, considering that for the MIR wavelengths used in this experiment the waveguides under analysis support only the TE polarization. The wavelength of the beam exiting the pulse shaper can be monitored by performing a scan with the FTIR spectrometer.

Two reasons prevent from a proper alignment of the system using directly the pump beam. First, the pump average power coming out from the pulse-shaper is below $1\ \mu\text{W}$, so it is not possible to trace it using standard viewing cards. Moreover, the NIR-VIS camera (FIND-R-SCOPE-85700®) used for the alignment is not sensitive to MIR wavelengths, so it is not possible to look at any scattering from the sample during the alignment. So, a telecom wavelength beam generated by an Amplified Stimulated Emission (ASE) source is made collinear with the pump pulse. This auxiliary beam is used for a rough alignment to the waveguide. The collinearity of the ASE beam with the pump beam guarantees a rough coupling of the pump pulse, which is then maximized using an extended InGaAs photodiode (Thorlabs FD05D®), whose responsivity extends in the range 800 nm to 2600 nm.

5.1.4 The detection stage

The pump power transmitted by the waveguide is checked by the extended InGaAs photodiode. A lock-in amplifier triggered by the pump signal allows to improve the signal sensitivity, which can be set to about 200 pW.

The detection of the SHG signal is more challenging. In fact, the simulations reported in Fig. 4.15 show that the average SHG power is at the fW level for a $\chi^{(2)}$ of the order of 0.1 pm/V. Therefore, a photon counting technique is necessary to detect it. The detection is performed using an InGaAs Single Photon Avalanche Diode (SPAD ID-Quantique-ID201®). This detector possesses a detection efficiency in the range 10 % to 25 % at wavelengths around 1150 nm to 1200 nm, where the SH signal is expected. To reduce the SPAD dark counts, a triggered configuration is used. When triggered by the pump signal, the detector opens a 2.5 ns detection window. The SPAD gating time is tuned using a side effect caused by the pump pulse, which is detected by the SPAD through TPA process. Once that the SPAD gating time is properly set, the pump signal is filtered out. The filtering is performed by bending the collecting tapered lensed fiber, exploiting the fact that the fiber does not guide well the MIR wavelengths. So, bending losses extinguish the pump without affecting the SH signal, whose wavelength is well guided by the fiber. The average SH power $\langle P_{sh} \rangle$ collected by the SPAD is calculated from the counting rate C measured by the SPAD using the following relationship:

$$\langle P_{sh} \rangle = \frac{hc}{\lambda_{sh}} \frac{C - C_{dc}}{DE}, \quad (5.1)$$

being h the Planck constant, C_{dc} the dark-count rate and DE the detector detection efficiency.

When required, the SHG signal can be spectrally analyzed by using a scanning monochromator. This is realized with a diffraction grating in a double-pass configuration. This monochromator is placed between the collecting fiber and the detector.

5.2 Characterization of SHG in strained silicon waveguides

In this section, the experimental characterization of the SHG process in strained silicon waveguides is shown.

5.2.1 Dependence on the pump wavelength

Figure 5.4 shows the experimental dependence of the SH power on the pump wavelength λ_p . The measurement is performed using the technique sketched in the inset of the figure. The pump wavelength is modified by changing the orientation angle of the diffraction grating of the pulse-shaper. Simultaneously, the SHG signal is detected by the SPAD detector. The pump signal is filtered by bending the output

fiber. The plot in Fig. 5.4 refers to a 1050 nm wide 4 mm long waveguide, that is expected to phase-match the TE1-TM3 modal combination. The measurement shows a strong dependence of the SH power on λ_p , with a clear peak for $\lambda_p \sim 2391$ nm. This is a first demonstration of the SHG occurrence, since it is expected that SHG occurs only for certain wavelengths where phase-matching is satisfied.

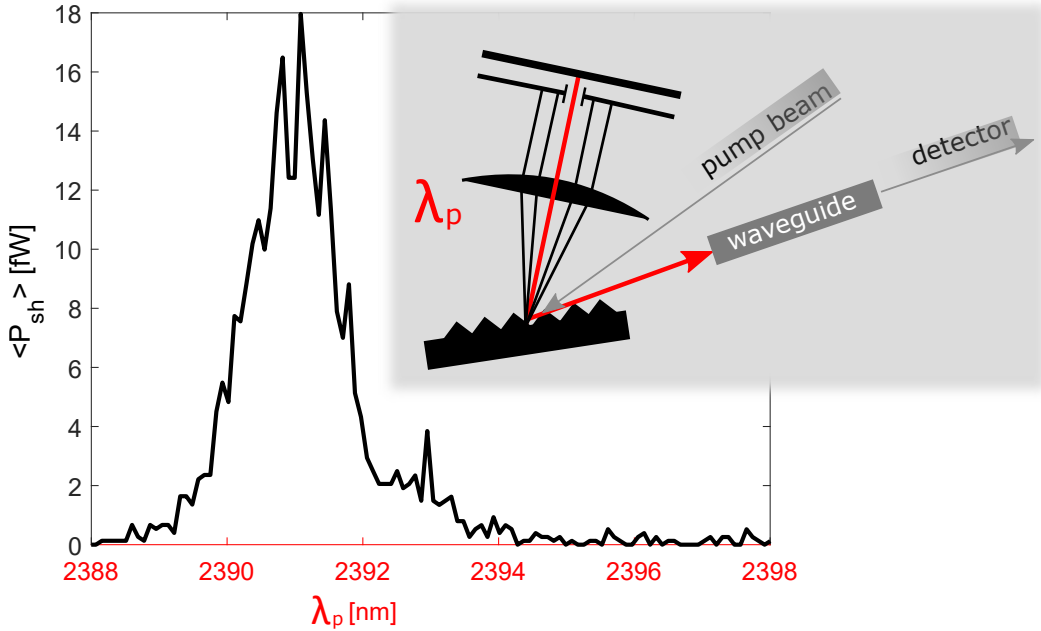


Fig. 5.4: On-chip average SH power as a function of the pump wavelength λ_p . In the inset, the technique used to perform this measurement is sketched. The measurement refers to a 1050 nm wide 4 mm long waveguide.

The value reported in Fig. 5.4, as well as all the results reported in the following, is the on-chip SH power. It is evaluated from the SH power measured by the SPAD detector and from an analytic estimation of the coupling efficiency κ , that is calculated as follows [35]:

$$\kappa = \frac{\int \psi_k(\mathbf{r}_\perp, \omega_{sh}) e_k^*(\mathbf{r}_\perp, \omega_{sh}) dA \int \psi_k^*(\mathbf{r}_\perp, \omega_{sh}) e_k(\mathbf{r}_\perp, \omega_{sh}) dA}{\int |\psi_k(\mathbf{r}_\perp, \omega_{sh})|^2 dA \int |e_k(\mathbf{r}_\perp, \omega_{sh})|^2 dA} \quad (5.2)$$

where $e_k(\mathbf{r}_\perp, \omega_{sh})$ is the profile of the optical mode to be coupled in the waveguide cross-section plane defined by \mathbf{r}_\perp at the SH frequency ω_{sh} , and $\psi_k(\mathbf{r}_\perp, \omega_{sh})$ indicates the coupling fiber profile. The label k indicates the polarization of the mode to be coupled ($k = x$ for TE polarization, $k = y$ for TM polarization). The integrals are taken over the whole plane defined by \mathbf{r}_\perp . The field profile of the fiber is experimentally measured by using a laser at SH wavelengths in the tip-to-tip configuration, detecting the transmitted power as a function of the relative position of the two fibers. In this way, a Gaussian profile with a $2.55 \mu\text{m}$ diameter is estimated. On the other hand, the field profile of the waveguide mode is calculated from FEM simulations. Using Eq. (5.2), $\kappa = 15.5$ dB is estimated for the collection of the TM3

mode for a waveguide width $w = 1 \mu\text{m}$. The other mode described in this chapter is the TM5 mode in a waveguide $2.3 \mu\text{m}$ wide, where $\kappa = 21.3 \text{ dB}$.

5.2.2 Dependence on the waveguide

Another proof that the measured signal is due to SHG results from the study of the phase-matching pump wavelength dependence on w . This quantity is shown in Fig. 5.5(a), referring again to the TE1-TM3 modal combination. The measured values are shown by the colored points in the figure. Blue points refer to measurements performed on waveguides of one chip, while green points refer to measurements performed on waveguides of another chip located in a different position on the wafer. The trend expected by simulations is shown as a straight line. The experimental trend agrees with simulations, even if it shows an offset. This offset can be attributed to variations of w in different positions of the wafer. To evidence this fact, Fig. 5.5(a) shows also a gray area. This corresponds to simulations performed assuming 5% variations on w , which is the typical fabrication uncertainty. The fact that the experimental results fall in the gray area confirms this reasoning. Furthermore, Fig. 5.5(a) shows also that waveguides belonging to the same chip possess almost the same shift with respect to simulations. This demonstrates that the waveguide geometry is uniform on the short-scale distance on the chip.

In Fig. 5.5(b) the same result is shown for larger waveguides ($w \sim 2.3 \mu\text{m}$). In this case, SHG can be attributed to the TE1-TM5 combination. The same reasoning presented for the previous combination can be extended to this case, showing short-scale uniformity of the waveguide geometry and good agreement with the trend predicted by simulations.

The TE1-TM3 and the TE1-TM5 modal combinations are the ones experimentally demonstrated, and will be also discussed in the following. The other combinations shown in Tab. 4.1 (e.g. TE1-TM7, TE1-TE5, TE1-TE7) did not show any detectable SH power in the experiment. The combinations providing generation on even parity modes (e.g. TE1-TM4, TE1-TM6, TE1-TE4, TE1-TE6) have been not realized because, as it is reported in Tab. 4.1, they are expected to be totally inefficient for a symmetric $\chi^{(2)}$.

5.2.3 Dependence on the pump power

Theory predicts a quadratic dependence of the SH power on the pump power. This fact is confirmed experimentally, as it is shown in Fig. 5.6, where the on-chip average SH power $\langle P_{sh} \rangle$ is reported in log-log scale as a function of the average pump power $\langle P_p \rangle$. A slope of 1.81 ± 0.12 is determined. This almost matches the value of 2 predicted by theory. The measurement refers to the same waveguide used for the

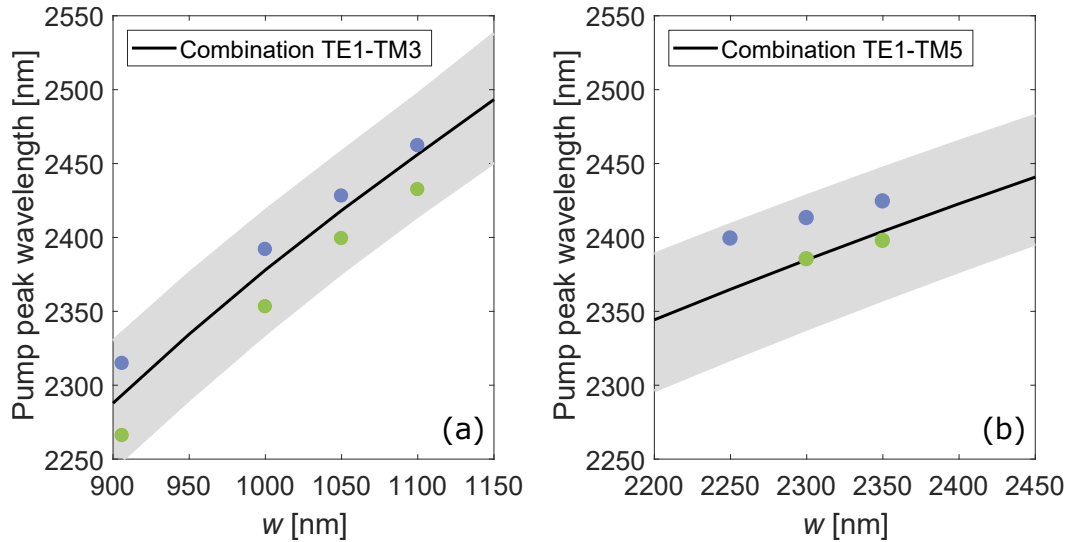


Fig. 5.5: Phase-matching pump wavelength dependence on waveguide width w . Panel (a) refers to the TE1-TM3 combination, while panel (b) refers to the TE1-TM5 combination. The points refer to experimental measurements, and points with the same color refer to waveguides on the same chip. The straight line shows the theoretical expectation, while the gray area refers to 5% variations on w .

measurement of Fig. 5.4.

The method used to estimate the on-chip SH power has already been introduced, based on the overlap integral between the fiber and the waveguide modal profiles. On the other hand, the on-chip pump power is estimated using an experimental technique, based on the measurement of the power incident on the waveguide facet and on the measurement of the in-coupling losses. In-coupling losses are determined via cut-back method, measuring the power transmitted by waveguides of different lengths [152]. In the case of the TE1-TM3 combination ($w \sim 1 \mu\text{m}$) in-coupling losses are about 9 dB, while they are about 4 dB in the case of the TE1-TM5 combination ($w \sim 2.3 \mu\text{m}$).

5.2.4 Spectrum of the SH signal

To finally prove the SHG occurrence, the spectrum of the generated signal is measured. This measurement is performed using the scanning monochromator placed between the collecting fiber and the SPAD detector. The result of this measurement is shown in Fig. 5.7. In this case, both the pump wavelength λ_p and the SHG wavelength λ_{sh} are scanned. The technique used for this measurement is summarized in the inset of Fig. 5.7. The detected SHG power is centered at $\lambda_{sh} \sim \lambda_p/2$, offering a further confirmation of the SHG occurrence.

Figure 5.8 shows the spectra of the SH signals measured on waveguides with different w , where the proper pump wavelength is set to provide phase-matching. The

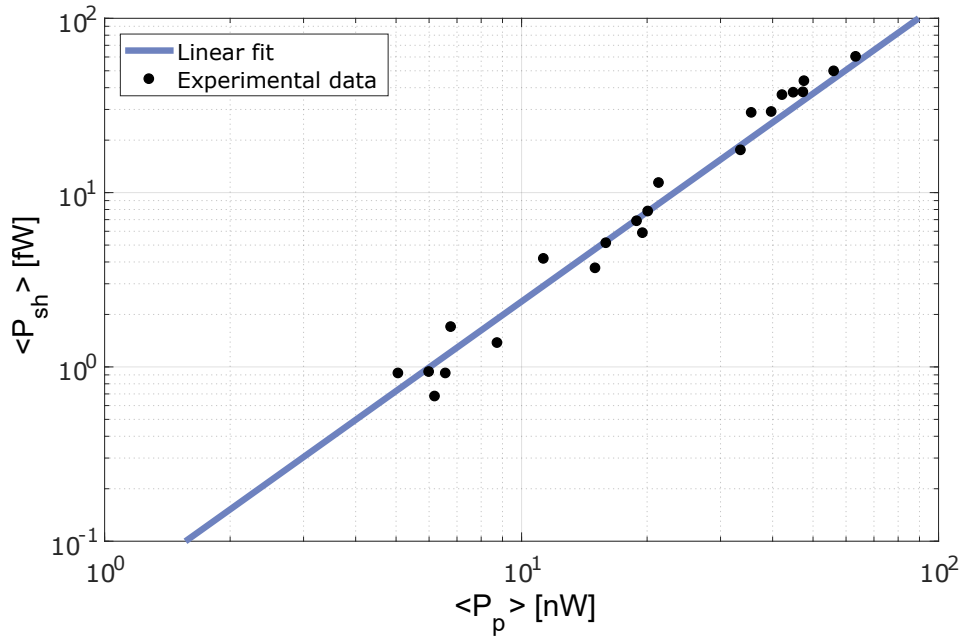


Fig. 5.6: On-chip SH power as a function of the on-chip pump power. Results are reported in a log-log plot and are fitted by a straight line, showing a slope of 1.81 ± 0.12 . The measurement refers to a 1050 nm wide 4 mm long waveguide, referred to the TE1-TM3 combination.

figure shows that, like for pump wavelength, also the SH wavelength increases with the waveguide width.

5.3 Estimation of the nonlinear coefficient

In Sec. 4.3.3 a method to estimate the nonlinear coefficients $|\Gamma^{(2)}|$ and $\chi_{\text{eff}}^{(2)}$ from the experimental measurement has been shown. For each experimental configuration, a conversion curve like the one sketched in Fig. 4.17 can be calculated. Doing that, one must use the proper experimental parameters (like the pulse wavelength and temporal duration), the proper waveguide geometry (length and width) and the proper modal combination. Using this conversion curve, once that the on-chip pump and SH power are calculated from the experiment, it is possible to estimate the corresponding nonlinear coefficients $|\Gamma^{(2)}|$ and $\chi_{\text{eff}}^{(2)}$.

The model used to calculate the conversion curve uses parameters that come both from FEM simulations (propagation constants, group indices, modal profiles) and from experimental measurements (refractive indexes, propagation losses). The pump loss coefficient is estimated by cut-back method. It is $\alpha_P \sim 8$ dB/cm for the TE1-TM3 modal combination ($w \sim 1 \mu\text{m}$) and 5 dB/cm for the TE1-TM5 modal combination ($w \sim 2.3 \mu\text{m}$). On the other hand, the SH loss coefficient α_{sh} has not been experimentally evaluated due to the fact that it propagates on high order modes. So it has been approximated $\alpha_{sh} \sim \alpha_p$. Since the waveguides considered

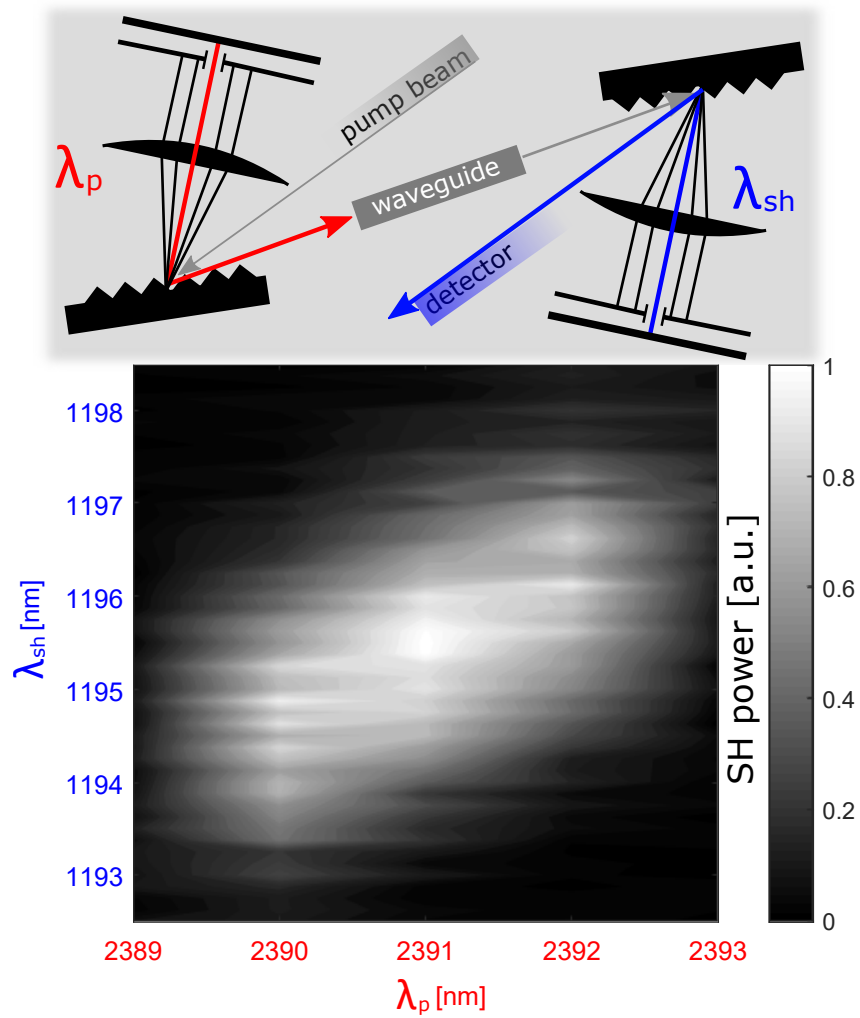


Fig. 5.7: Spectral analysis of the SH power. This measurement is performed using the technique sketched on the top. The measurement refers to a 1050 nm wide 4 mm long waveguide, providing phase-matching on the TE1-TM3 combination.

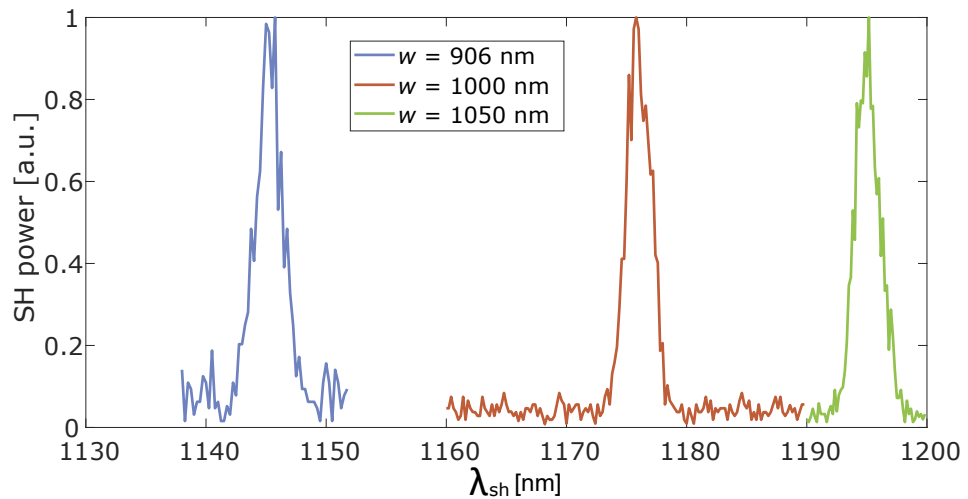


Fig. 5.8: Spectral analysis of the SH pulse, once that the proper pump pulse wavelength is set. The three measurements refer to three different waveguide widths w .

Tab. 5.1: Estimation of the nonlinear coefficients $|\Gamma^{(2)}|$ and $\chi_{\text{eff}}^{(2)}$, evaluated from the experimental measurements with the method described in Sec. 4.3.3. The error bars result from statistical analysis and represent one standard deviation. The coefficients $\chi_{\text{eff}}^{(2)}$ are related to $|\Gamma^{(2)}|$ according to Eq. (4.32).

Combination	$ \Gamma^{(2)} $ [fm/V]	$\chi_{\text{eff}}^{(2)}$ [pm/V]
TE1-TM3	1.7 ± 0.2	0.46 ± 0.06
TE1-TM5	0.39 ± 0.06	0.6 ± 0.1

here are very short (in the range 2 mm to 6 mm), the role of α_{sh} not crucial.

Table 5.1 shows these values calculated from the experimental measurements, referred to the TE1-TM3 and to the TE1-TM5 combinations. The results are calculated from measurements on waveguides of different L and different w . For the TE1-TM3 combination, each value reported in Tab. 5.1 is an average of 64 measurements, while for the TE1-TM5 combination it refers to 11 measurements.

The results reported in the table show that the combination TE1-TM3 has a $|\Gamma^{(2)}|$ value around 4 times larger than the TE1-TM5 combination. This fact is connected to the experimental observation that, given a certain pump power, the generated SH signal is much stronger in the TE1-TM3 combination than in the TE1-TM5 combination. On the other hand, $\chi_{\text{eff}}^{(2)}$ values are comparable within the error bars. This is connected to the fact the TE1-TM3 combination has a stronger K value with respect to the TE1-TM5 combination, as reported in Tab. 4.1. So, even if the values of $|\Gamma^{(2)}|$ are different, the values of $\chi_{\text{eff}}^{(2)}$ evaluated according to Eq. (4.32) are comparable. Recalling that K is related to the mode overlap between the pump and the SH modes and not to the value of $\chi^{(2)}$, it means that the strong difference between the $|\Gamma^{(2)}|$ shown by the two combinations has to be ascribed mainly to a difference in the overlap of the optical modes, and not to a different distribution of $\chi^{(2)}$ inside the waveguide.

SHG under external load

6.1	Effect of external load on SHG	95
6.1.1	Experimental setup	95
6.1.2	SHG under the effect of strain	96
6.2	Modeling the effect of strain on SHG	98
6.2.1	Macroscopic modeling of the sample	98
6.2.2	Effect of strain on phase-matching	98
6.2.3	Effect of strain on $\chi^{(2)}$	100

The results presented in the previous chapter offer a proof that SHG can be measured in a silicon waveguide with a SiN cladding. However, the experiment does not clarify the origin of this process, which can be generated by strain, charges trapped in the cladding and generation by the evanescent field overlapping the cladding. In this section, the role of strain is investigated in detail. Section 6.1 reports the results of a SHG experiment where an external load is applied to the sample. In Sec. 6.2 these results are investigated more in detail by modeling the strained waveguide.

The experiments have been realized together with Miss C. Vecchi and Dr. A. Trenti. Part of the work described in this chapter is also described in [145].

6.1 Effect of external load on SHG

6.1.1 Experimental setup

The SHG experiment described in the previous chapter is replied using a screw-equipped sample holder like the one sketched in Fig. 6.1 and described in Chapter 2 and in [111, 135]. Using this sample holder the edges of the sample are fixed, while the screw introduces a vertical displacement ΔH in the center of the sample. This load, applied orthogonally to the main plane of the sample, bends it and allows to set a tunable strain inside the waveguide. When no external load is applied, only the stress introduced by the SiN cladding is present. Wafer bow measurements set this stress level to 1.25 GPa. Applying the external load, strain can be increased up to the sample rupture.

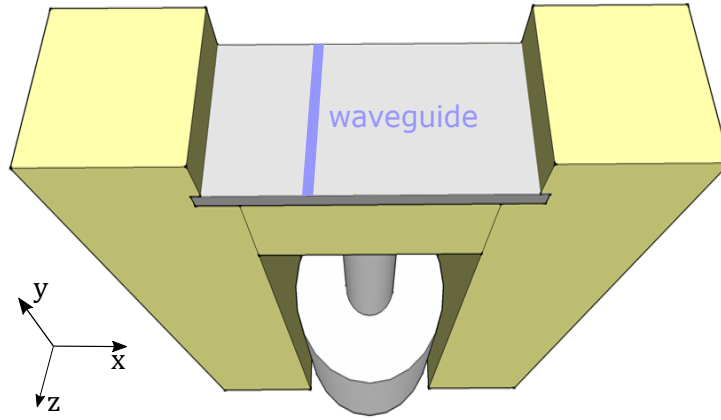


Fig. 6.1: Sketch of the screw-equipped sample holder used in this experiment. By rotating the screw, a vertical displacement ΔH can be applied in the center of the sample, while the edges of the sample are fixed.

6.1.2 SHG under the effect of strain

Figure 6.2 shows the dependence of the on-chip SHG power on the pump wavelength λ_p for different values of ΔH applied by the screw. The measurement is performed on a 906 nm wide and 4 mm long waveguide, which shows phase-matching on the TE1-TM3 modal combination. SHG is observed for all the applied values of ΔH . Moreover, while increasing the strain level, the SHG peak is moved towards shorter wavelengths, demonstrating a blue-shift of the phase-matching wavelength. However, the SHG magnitude does not vary significantly with strain.

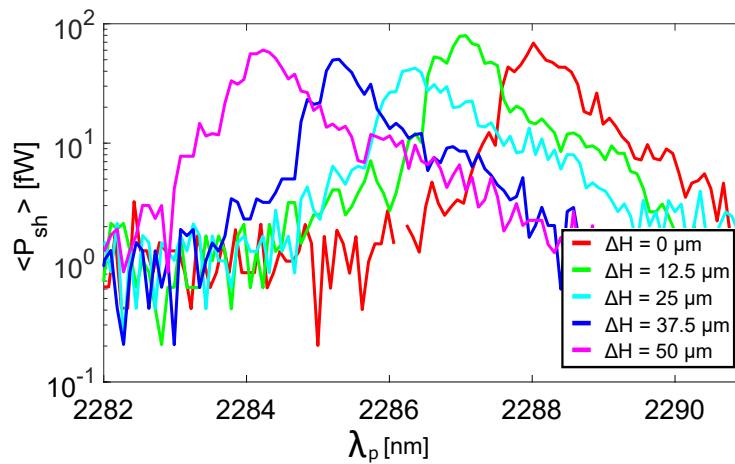


Fig. 6.2: On-chip SH power as a function of the pump wavelength λ_p for different loads ΔH applied by the screw.

To emphasize the shift induced by strain, in Fig. 6.3 the pump phase-matching wavelength is reported as a function of ΔH . The phase-matching wavelength shifts linearly, showing a maximum shift of about 3.8 nm for $\Delta H = 50 \mu\text{m}$. The phase-matching wavelength variation proves that the strain inside the waveguide is actually varied by the applied load. The shift can be ascribed to a strain-induced effective

refractive index variation in the waveguide, determined both by the photoelastic effect and by the waveguide deformation [135]. In fact, if the pump and the SH modes undergo to effective refractive index changes δn_p and δn_{sh} , the phase-matching condition is changed to $n_{p,0} + \delta n_p = n_{sh,0} + \delta n_{sh}$, being $n_{p,0}$ and $n_{sh,0}$ the effective refractive indexes unaffected by strain. If $\delta n_p \neq \delta n_{sh}$, the phase-matching wavelength is changed.

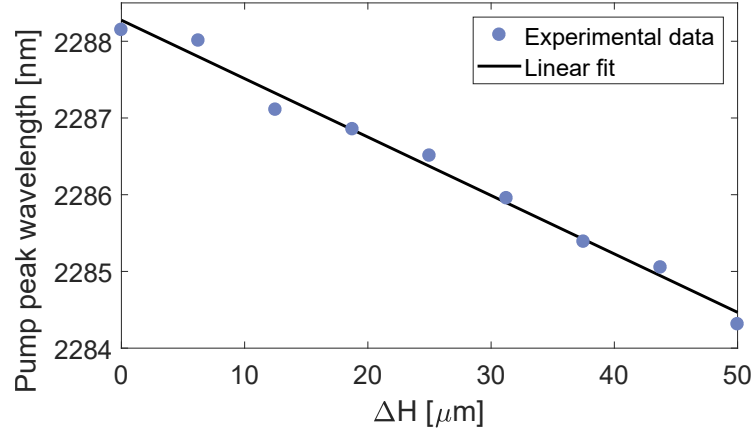


Fig. 6.3: Pump phase-matching wavelength as a function of the applied load ΔH .

Figure 6.4 reports the dependence of $\chi_{\text{eff}}^{(2)}$ on the applied load ΔH . Surprisingly, the load increase does not affect significantly $\chi_{\text{eff}}^{(2)}$. This fact seems to contradict the interpretation of strain as the main cause of SHG.

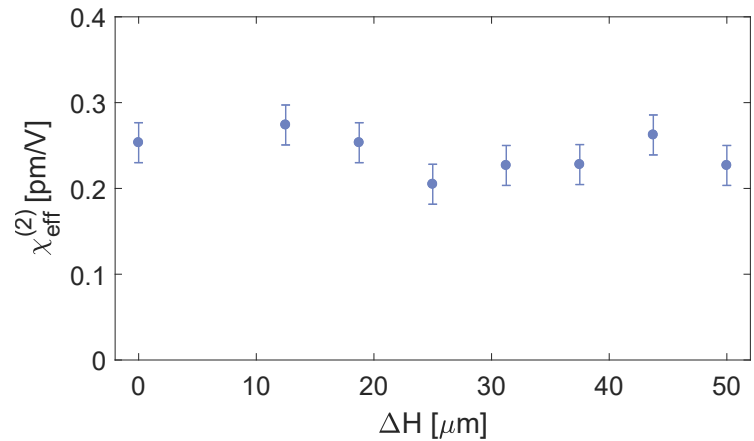


Fig. 6.4: Dependence of $\chi_{\text{eff}}^{(2)}$ on the applied load ΔH . The error bars are estimated from repeated measurements. Note that the $\chi_{\text{eff}}^{(2)}$ value reported here is lower than the result of Tab. 5.1. This fact derives from the large variability of $\chi_{\text{eff}}^{(2)}$ between the different samples, considered by the statistical analysis shown in Tab. 5.1.

6.2 Modeling the effect of strain on SHG

To confirm the interpretation of the strain-induced shift of the phase-matching wavelength, the system is modeled using a procedure similar to the one described in Chapter 3 and in [135].

6.2.1 Macroscopic modeling of the sample

Using this procedure, as a first step, the silicon substrate is modeled using a 3D FEM simulation. The simulation domain used in this part is sketched on the top in Fig. 6.5. The screw introduces a displacement ΔH along the y direction, shown in the figure by the arrow. On the top, the fixed supports are modeled by a prescribed displacement and a fixed constraint applied to lines directed along the x direction. To properly model the screw effect, a crucial parameter is the contact area between the screw and the sample. Here, good agreement with the experiment is obtained by using a screw contact diameter of $7\ \mu\text{m}$. The bottom of Fig. 6.5 reports the result of a 3D simulation for $\Delta H = 50\ \mu\text{m}$. In the figure, displacements are emphasized by a factor 10. Superimposed to the deformed sample, the volumetric strain ε_v is shown in color scale.

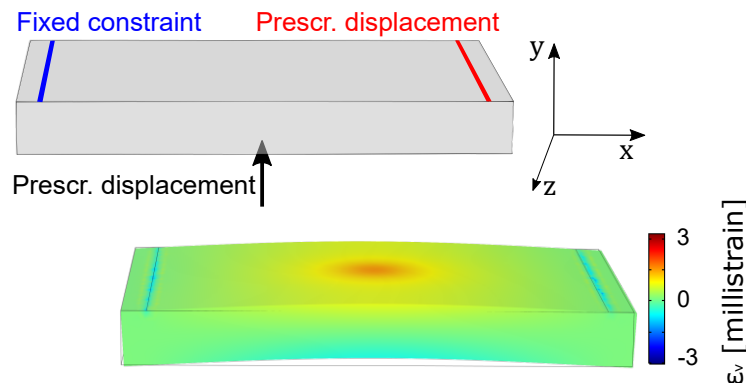


Fig. 6.5: Top: sketch of the 3D FEM simulation modeling the silicon substrate deformed by the load applied by the screw. The lines on the top of the sample model the supports, described by a prescribed displacement and a fixed constraint. The screw displacement is sketched by the arrow on the bottom of the sample. Bottom: results of the simulation for a load $\Delta H = 50\ \mu\text{m}$. Displacements are emphasized by a factor 10. The color map reproduces the volumetric strain ε_v superimposed to the deformed sample.

6.2.2 Effect of strain on phase-matching

The results of the simulation described so far are then used to estimate the strain inside the waveguide. Doing that, the results of the 3D model are used as prescribed

displacements in a 2D model of the waveguide cross-section. Using this approach, the strain distribution inside the waveguide can be evaluated. As an example, Fig. 6.6 shows the strain tensor element ε_{xx} inside the waveguide, evaluated for $\Delta H = 0 \mu\text{m}$ (left) and $\Delta H = 50 \mu\text{m}$ (right). In the situation $\Delta H = 0 \mu\text{m}$, when no load is applied, the strain inside the waveguide is entirely due to the stress applied by the SiN cladding. This is introduced as an initial condition in the 2D simulation. On the contrary, the case $\Delta H = 50 \mu\text{m}$ corresponds to the maximum displacement introduced in the experiment before breaking the sample. Comparing the result at $\Delta H = 50 \mu\text{m}$ with the one at $\Delta H = 0 \mu\text{m}$, the average strain inside the waveguide is increased of about 50%.

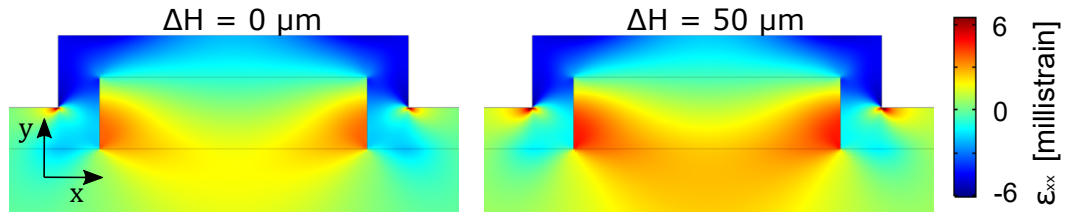


Fig. 6.6: Strain tensor element ε_{xx} inside a 906 nm wide waveguide, corresponding to $\Delta H = 0 \mu\text{m}$ (left) and to $\Delta H = 50 \mu\text{m}$ (right). The 2D simulation is performed using the results of the 3D model shown in Fig. 6.5 as prescribed displacements.

The results of the simulations reported in Fig. 6.6 are used to determine two quantities.

1. Given the average strain inside the waveguide along the x and the y directions, the size of the deformed waveguide is estimated. This is used to evaluate the effective refractive index variations induced by deformation $\delta n_{p|def}$ and $\delta n_{sh|def}$. These quantities are shown in Fig. 6.7(a) as a function of the applied displacement ΔH . They refer to a 906 nm wide waveguide, considering the TE1 mode for the pump and the TM3 mode for the SH signal. Deformation causes a positive variation of the effective refractive index for both the modes.
2. Given the strain distribution inside the waveguide, the photoelastic coefficients are used to compute a map of the photoelastic variation of the refractive index. This is used in turn to determine the photoelastic-induced effective refractive index variations $\delta n_{p|ph}$ and $\delta n_{sh|ph}$. These quantities are shown in Fig. 6.7(b) as a function of ΔH . The photoelastic effective index variation of the two modes, due to their different polarizations, has opposite sign. Moreover, comparing this effect with the effect of deformation reported in Fig. 6.7(a), it results that photoelastic effect is one order of magnitude stronger.

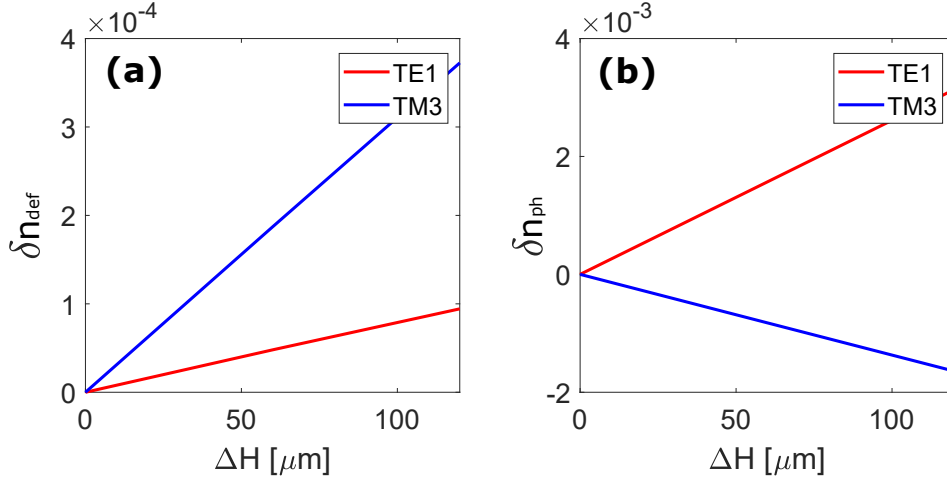


Fig. 6.7: Effective refractive index variations induced by deformation (a) and by the photoelastic effect (b) as a function of the applied displacement ΔH . The results are reported for the pump TE1 mode at the wavelength of 2293.8 nm (red lines) and the SH TM3 mode at the corresponding halved wavelength (blue lines). The simulations refer to a 906 nm wide waveguide.

Once that the effective refractive index variation induced by deformation and photoelasticity are known, the new pump and SH effective indexes are calculated as:

$$\begin{aligned} n_p &= n_{p,0} + \delta n_p = n_{p,0} + \delta n_{p|def} + \delta n_{p|ph}, \\ n_{sh} &= n_{sh,0} + \delta n_{sh} = n_{sh,0} + \delta n_{sh|def} + \delta n_{sh|ph}. \end{aligned} \quad (6.1)$$

In Fig. 6.8 the pump and SH effective refractive indices are shown as a function of pump and SH wavelengths, referred to both the cases $\Delta H = 0 \mu\text{m}$ (solid lines, no strain is applied) and to $\Delta H = 50 \mu\text{m}$ (dashed line, maximum strain is applied). Due to the fact that photoelasticity has a much stronger effect than deformation, the pump effective index increases, while the SH index lowers. This causes a shift of the pump phase-matching wavelength of almost 4 nm, comparably with the experiment. One can note that the phase-matching wavelength shown here is 2293.8 nm at $\Delta H = 0 \mu\text{m}$, slightly different from the value of 2288 nm shown in the experimental measurement of Fig. 6.2. This fact depends on the local variations of the waveguide geometry. However, what matters is a comparison between the phase-matching shift and not its absolute value.

6.2.3 Effect of strain on $\chi^{(2)}$

In [110, 118] a model connecting the strain gradient to the strain-induced second order nonlinear coefficient $\chi_{\text{strain}}^{(2)}$ is proposed. Using this model, the $\chi_{\text{strain}}^{(2)}$ map in the waveguide has been calculated in Sec. 4.2.4. Here, the same is done in Fig. 6.9, which reports the distribution of $\chi_{\text{strain},xy}^{(2)}$ in a 906 nm wide waveguide in the situations $\Delta H = 0 \mu\text{m}$ and $\Delta H = 50 \mu\text{m}$. The average value of $\chi_{\text{strain},xy}^{(2)}$ is

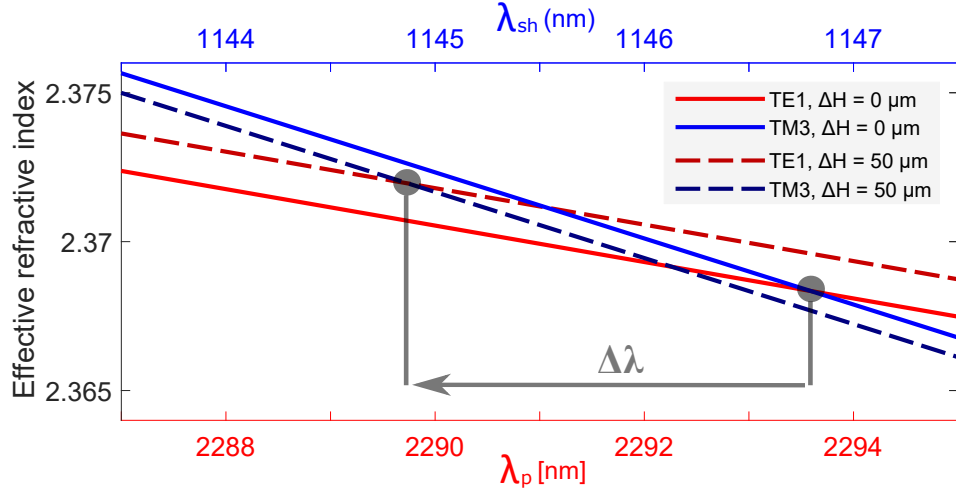


Fig. 6.8: Effective refractive index of the pump TE1 mode (blue) and of the SHG TM5 mode (red) as a function of the pump and of the SHG wavelengths. Solid lines refer to simulations realized with no applied load ($\Delta H = 0 \mu\text{m}$), while dashed lines refer to $\Delta H = 50 \mu\text{m}$. The applied strain determines the phase-matching shift $\Delta\lambda$.

around 1.75 pm/V in the case $\Delta H = 0 \mu\text{m}$, while it reaches about 2 pm/V in the situation $\Delta H = 50 \mu\text{m}$, with an increase of about 14%. However, these quantities cannot be directly compared with the experimental $\chi_{\text{eff}}^{(2)}$. In fact, the generation efficiency is not directly linked to $\chi_{\text{strain},xy}^{(2)}$, but to its overlap with the optical modes. So, the value of $|\Gamma^{(2)}|$ is evaluated according to Eq. (4.11) and the $\chi^{(2)}$ map of Fig. 6.9. A variation from 0.47 fm/V to 0.72 fm/V is estimated while passing from $\Delta H = 0 \mu\text{m}$ to $\Delta H = 50 \mu\text{m}$. This corresponds to a variation of $\chi_{\text{eff}}^{(2)}$ from 0.13 pm/V to 0.20 pm/V , with an increase of almost 50%

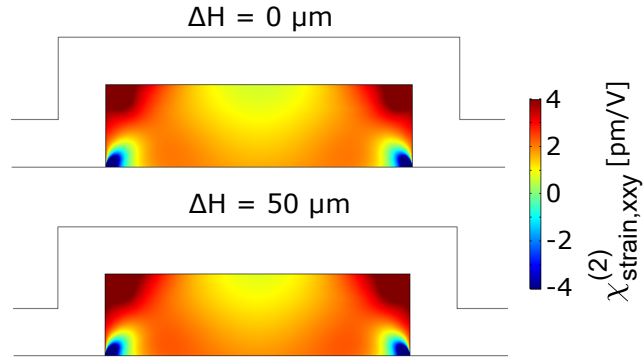


Fig. 6.9: Distribution of $\chi_{\text{strain},xy}^{(2)}$ in a 906 nm wide waveguide, evaluated according to the model shown in [110, 118] and corresponding to $\Delta H = 0 \mu\text{m}$ and $\Delta H = 50 \mu\text{m}$.

This allows concluding that, even if the model shown in [110, 118] predicts a $\chi_{\text{eff}}^{(2)}$ variation of 50%, the experimental SHG efficiency does not change significantly. This is a first proof that strain is not the main origin of the measured SHG.

The role of charged centers on second harmonic generation

7.1	The origin of dangling bonds	104
7.2	Passivation of dangling bonds with UV light	105
7.2.1	C-V measurements to estimate the charge density	105
7.2.2	Estimation of the charge density	106
7.2.3	Effect of charge removal on waveguides	107
7.3	Effect of charge passivation on second harmonic generation	108
7.4	Modeling the effect of charges on second harmonic generation	109
7.4.1	Carrier distribution inside the waveguide	110
7.4.2	Effect of charges on propagation losses	111
7.4.3	Electric field distribution inside the waveguide	111
7.4.4	Charge-induced second order nonlinearities	112
7.5	Conclusions and perspectives	115

The results shown in the previous chapter demonstrate that strain has a marginal role in the SHG process. Therefore, SHG is due to other processes, such as the charges trapped in the SiN cladding, as well as the generation in the cladding through the evanescent field. In this chapter, the role of trapped charges is analyzed. First, their origin is recalled in Sec. 7.1. Then, in Sec. 7.2, it is shown how ultraviolet radiation can annihilate them. In Sec. 7.3 the same treatment is applied to waveguides, in order to analyze the effect on the SHG process. The experiment shows a complete suppression of the SHG signal after UV treatment, demonstrating in this way the crucial role of trapped charges. In Sec. 7.4 the system is modeled, finding good agreement with the experiment. Finally, Sec. 7.5 shows the main conclusions and perspectives of this work on SHG in strained waveguides.

The experiments described in this chapter has been realized together with Miss C. Vecchi and Dr. A. Trenti. The UV exposure of the samples, as well as the C-V measurements used to estimate the density of the trapped charges, have been realized by Dr. M. Ghulinyan at Fondazione Bruno Kessler.

Part of the work described in this chapter is also described in [145].

7.1 The origin of dangling bonds

In the ideal bonding topology of SiN, silicon has four nitrogen atoms as neighbors, while nitrogen is bounded to three silicon atoms. This situation is sketched on the left side of Fig. 7.1. However, **defects** are often formed during the deposition of the material. They consist of local variations of the atomic network with respect to the ordered chemical structure of the material. The most important defects in SiN are the *K* centers and the *N* centers, which are also sketched in Fig. 7.1 [153, 154]. The *K* defect can be considered both as a silicon atom with three bonds or as a nitrogen atom with four bonds. On the other hand, the *N* defect consists of a silicon atom with five bonds or a nitrogen atom with two bonds. The bonds sketched in white in Fig. 7.1 are commonly referred as dangling bonds.

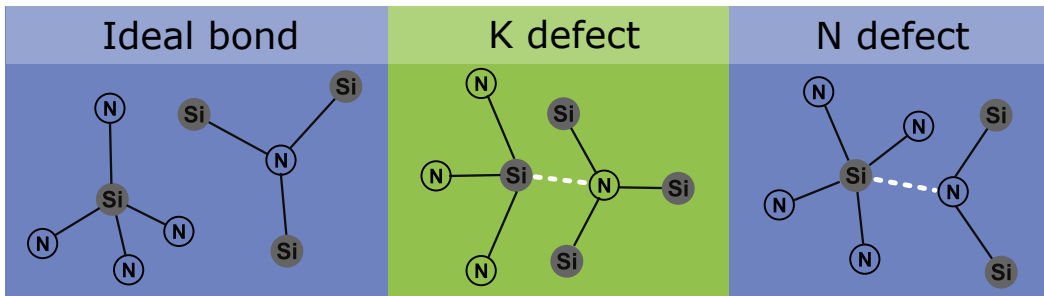


Fig. 7.1: Atomic bonding topologies in SiN: ideal topology (left), *K* center (center) and *N* center (right).

The *K* defect is particularly diffused and important. The *K* center can exist in three different charge states. In the positive state of the *K* center (named K^+ center) no electrons are present in the dangling bond. In the neutral state (named K^0 center) one electron is present in the dangling bond. In the negative state (K^- center) two electrons occupy the dangling bond [155]. The first is the most thermodynamically favorable defect, and creates a positively charged layer at the interface between silicon and SiN [136].

The existence of charged defects strongly affects the system studied in this work, where a SiN cladding is deposited on the top of a silicon waveguide. In fact, the presence of positively charged defects in the cladding results in a static field E_{DC} inside the waveguide. This static field adds up to the optical waves that propagate in the waveguide, and causes the **EFISH process**. As already introduced in Sec. 1.1.3, EFISH process is described by Eq. (1.8) when (for example) $\omega_3 = 0$. In this case, the nonlinear polarization vector $\mathbf{P}^{(3)}$ acquires terms at frequencies $2\omega_1$ and $2\omega_2$, corresponding to a SHG process. Comparing this case with Eq. (1.7), which describes second order processes, an effective second order nonlinear coefficient $\chi_{\text{EFISH}}^{(2)}$ can be introduced according to [126]

$$\chi_{\text{EFISH}}^{(2)} = 3\chi^{(3)}E_{DC}. \quad (7.1)$$

7.2 Passivation of dangling bonds with UV light

Removing the dangling bonds from the SiN cladding can be useful to understand the effect of EFISH on the measurements described so far. This can be done by irradiating the sample with **UV light**. This process annihilates the positive centers K^+ , neutralizing them to the state K^0 [155].

7.2.1 C-V measurements to estimate the charge density

The effect of UV irradiation on such a system is preliminarily measured on a simpler system, constituted by a 140 nm thick SiN layer deposited on the top of 600 μm thick p-doped silicon substrate. This constitutes a simplified version of the device where waveguides are defined. In the cross-section of this system, only one interface is present, specifically the Si/SiN interface that is of interest for this study. On the contrary, waveguides are defined on a SOI wafer, which possesses a SiO₂ layer between the waveguide level and the substrate. Therefore, in this device three interfaces are present, among which the two Si/SiO₂ interfaces are not interesting for the purposes of this study. Moreover, the lithographic definition of the waveguides can introduce problems in the measurement that is going to be presented. In the simple situation constituted by only two layers, C-V measurements in the MOS configuration can be used to estimate the areal charge density σ [156].

The left hand side of Fig. 7.2 shows the cross section of the device used for the **C-V measurements**. The test structure is contacted by an aluminum back contact and a 787 μm diameter Hg droplet as a gate contact.

The right hand side of Fig. 7.2 shows the typical low-frequency C-V curve measured in this kind of structures. For simplicity, it is assumed that the metal contact has the same work function of the semiconductor. It shows three regimes, represented with three different colors on the plot. These regimes can be described also in terms of the energy-band diagram shown in Fig. 7.3 [157].

- The **accumulation regime** results when negative voltages are applied to the metal in contact with the insulator ($V < 0$). This causes the bending of the bands close to the surface between semiconductor and the insulator. In this device no current flows, so the Fermi level does not change in the semiconductor. Therefore, close to the surface the valence band becomes closer to the Fermi level. Since the hole density is exponentially dependent on the energy difference between the valence band and the Fermi level, holes accumulate close to the interface. In other words, when a negative potential is applied to the metal in contact with the insulator, positive charges are attracted close to the interface. This situation is depicted on the left panel of Fig. 7.3.

- The condition when $V = 0$ is called the **flat-band** condition. In this case, bands become flat and the carrier distribution close to the interface is the same of the bulk silicon. In the C-V curve, in the flat-band condition the capacitance C_{fb} is related to the maximum capacitance in the accumulation regime C_{max} by [156]:

$$C_{fb} = C_{max} \frac{\varepsilon_0 \varepsilon_s A / L_D}{C_{max} + \varepsilon_0 \varepsilon_s A / L_D}, \quad (7.2)$$

being ε_s the semiconductor permittivity, A the Hg droplet area and L_D the Debye length of the semiconductor.

- If $V > 0$, the system approaches the **depletion region**. In this case, close to the interface the bands bend downward, and the distance from the Fermi level of conduction and of the valence bands becomes almost the same. In this case, sketched in the central panel of Fig. 7.3, holes are depleted.
- If $V \gg 0$, the bands are bent more and more. So, close to the interface, the distance between the Fermi level and the conduction band becomes smaller than the distance with the valence band. In this is situation, named **inversion region** and sketched in the right hand panel of Fig. 7.3, electrons accumulate close to the interface.

The situation depicted so far refers to the situation where difference between the metal contact and the semiconductor work functions is zero ($\phi_{ms} = 0$). In the general case when $\phi_{ms} \neq 0$, the flat-band voltage V_{fb} is equal to ϕ_{ms} . This situation is still different if fixed charges are accumulated at the insulator-semiconductor interface. If Q is the total accumulated charge, the flat-band voltage becomes [126]

$$V_{fb} = \phi_{ms} - \frac{Q}{C_{max}}. \quad (7.3)$$

So, the flat-band capacitance C_{fb} can be estimated using (7.2). Once that it is known, the flat-band voltage V_{fb} can be graphically estimated from the measured C-V curve. Finally, knowing ϕ_{ms} and using (7.3), the total accumulated charge Q can be determined. Assuming a uniform distribution of the accumulated charge, an areal charge density of $\sigma = Q/A$ can be determined.

7.2.2 Estimation of the charge density

Figure 7.4 shows the measured C-V curve before and after different UV exposure times. In the as-deposited structure, a flat-band voltage of around -8 V is shown. After the UV exposure, the curve is shifted towards larger voltages, saturating at $V_{fb} \sim -0.5$ V. This quantity corresponds to ϕ_{ms} for the situation analyzed in this work. In terms of charges, an areal charge density of $\sigma \sim 1.7 \times 10^{12} \text{ cm}^{-2}$ can be

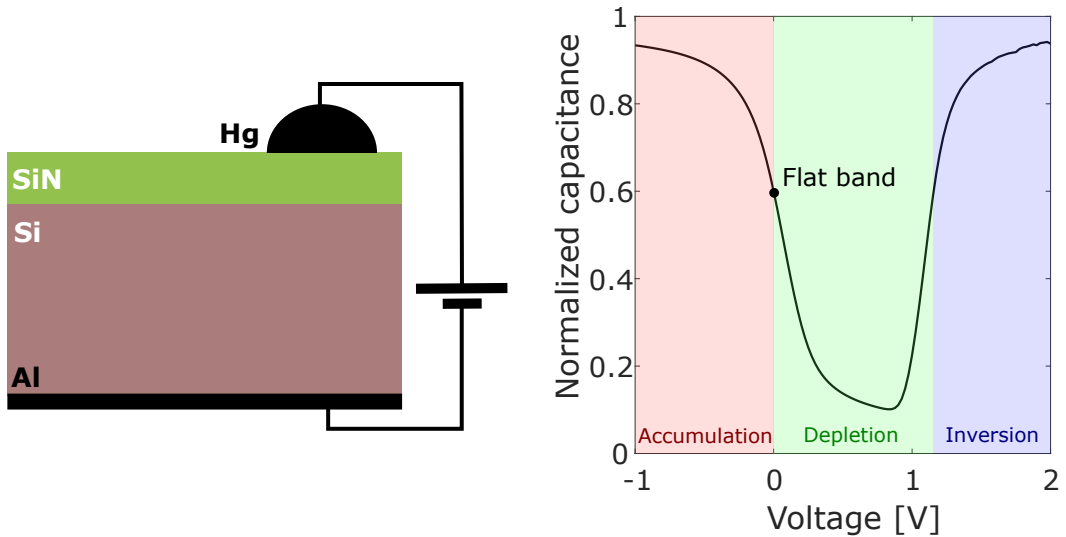


Fig. 7.2: Left: cross section of the device used for the C-V measurements, constituted by a 140 nm thick SiN layer deposited on the top of a 600 μm thick p-doped silicon substrate, and contacted by an aluminum back contact and a 787 μm diameter Hg droplet as a gate contact. Right: typical low frequency C-V curve of the structure shown on the left and referred to a p-type semiconductor.

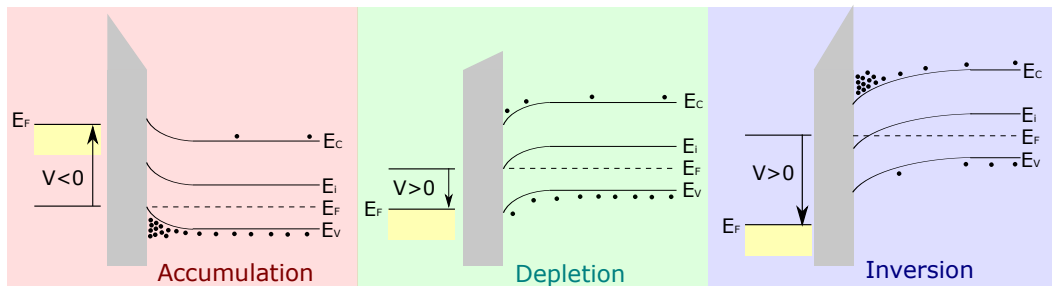


Fig. 7.3: Band diagrams for metal-insulator-semiconductor structures. The three panels refer to the three different regimes: accumulation (left), depletion (center) and inversion (right).

estimated for the as-deposited situation. After 23 hours of exposure to a 254 nm UV light, a reduction to $\sigma \sim 3.1 \times 10^9 \text{ cm}^{-2}$ is estimated, due to the neutralization of the charged K centers.

7.2.3 Effect of charge removal on waveguides

The same UV treatment is applied to the chip where the waveguides are defined. The UV treatment is expected to reduce propagation losses. In fact, the neutralization of dangling bonds in the SiN cladding causes a reduction of the carrier concentration in the silicon waveguide, which in turn reduces the effect of free carrier absorption. This effect was shown in a strip-loaded waveguide formed by a 27 nm thick silicon layer patterned by a SiN cladding, demonstrating a loss reduction from 5.1 dB/cm to 0.9 dB/cm [156]. This loss reduction is confirmed also in the case of this study,

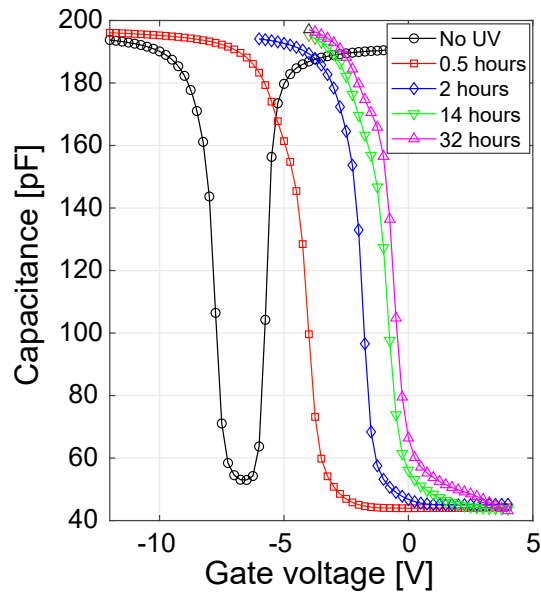


Fig. 7.4: 10 kHz C-V curves measured before and after different UV exposure times. Figure adapted with permissions from [156].

passing from 8 dB/cm to 4 dB/cm in a $1\ \mu\text{m}$ wide waveguide at wavelengths around 2300 nm after 23 hours of UV irradiation.

7.3 Effect of charge passivation on second harmonic generation

The SHG power measured before and after 23 hours of UV exposure are compared in Fig. 7.5(a). Remarkably, the measurement shows that the SHG signal is completely suppressed after the UV treatment. This result offers the clearest answer to the question on the origin of the detected signal, showing that SHG disappears when dangling bonds are passivated. This indicates that the detected SHG signal has to be entirely attributed to EFISH. Any other effect that can introduce $\chi^{(2)}$ in the material, such as strain or to the generation in the SiN cladding, is below the sensitivity of the experiment. The noise level of 0.5 fW allows to set an upper limit of 0.05 pm/V to the $\chi^{(2)}$ due to strain or generation in the cladding.

At this point, it can be interesting to apply again an external load to the sample using the screw equipped sample holder. This aims to investigate if the strain induced by the screw is enough to increase the strain-induced $\chi^{(2)}$ to have a measurable SHG power. In Fig. 7.5(b) the SHG power measured after applying a screw displacement $\Delta H = 25\ \mu\text{m}$ is shown in blue. The measurement shows a SHG peak. This peak is measured for a pump wavelength that is blue-shifted with respect to the one measured in the original waveguide. This shift can be attributed to the strain-induced variation of the effective refractive index, which induces a blue-shift of

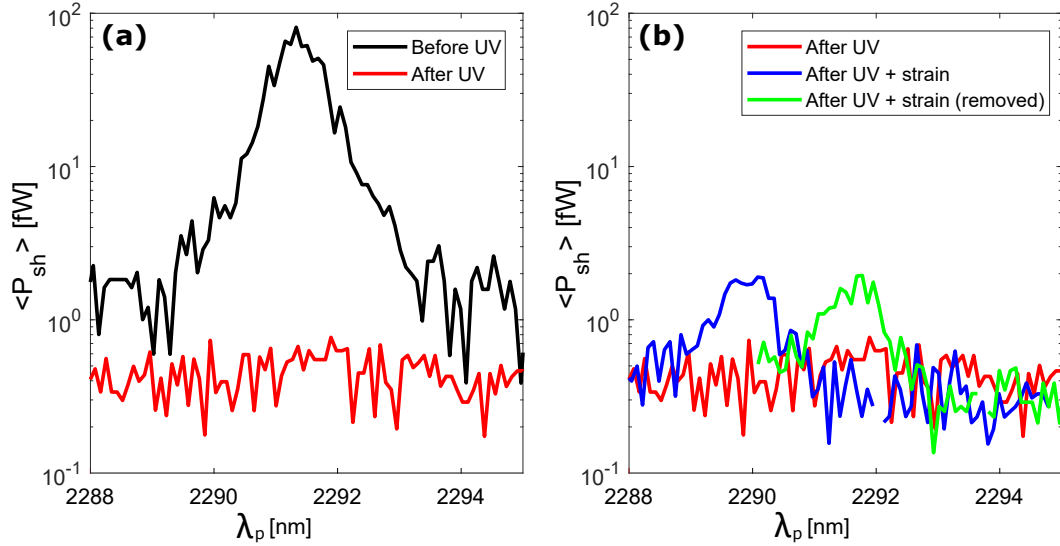


Fig. 7.5: (a) Dependence of the SHG power on the pump wavelength λ_p before (black) and after (red) a UV treatment of 23 hours. The measurement is performed on a 906 nm wide waveguide. (b) Dependence of the SHG power on λ_p after a UV treatment of 23 hours (red, the same as panel a), after the UV exposure and applying a screw displacement $\Delta H = 25 \mu\text{m}$ (blue) and after removing the screw displacement (green).

the peak wavelength as remarked by previous measurements shown in Sec. 6.1. If this SHG signal is due to strain, it is expected to disappear when the strain is removed. However, this does not happen, as it is shown by the green curve in Fig. 7.5(b). The SHG peak is shifted back to its original position, as expected since the strain is removed and so the strain-induced refractive index change vanishes. However, the SHG magnitude remains the same. Therefore, the peak appeared after the application of strain cannot be attributed to a strain-induced $\chi^{(2)}$. A possible interpretation of this fact can be the re-activation of some K centers consequently to the applied load [158]. This fact is confirmed by the experimental observation that the SHG peak is suppressed by a further exposition to the UV light.

7.4 Modeling the effect of charges on second harmonic generation

The experiment shown in the previous section demonstrates that, when dangling bonds are passivated, the SHG signal is suppressed. This offers a clear proof on the origin of the measured signal. To confirm this hypothesis, the charge-induced electric field distribution inside the waveguide E_{DC} is estimated using FEM simulations. In this way, using Eq. (7.1), the distribution of $\chi_{\text{EFISH}}^{(2)}$ inside the waveguide can be determined. Once that this quantity is known, the parameter $|\Gamma^{(2)}|$ (or, alternatively, $\chi_{\text{eff}}^{(2)}$) can be estimated and compared to the one calculated from the experiment.

7.4.1 Carrier distribution inside the waveguide

The simulation considers a p-doped silicon with a concentration of 10^{15} cm^{-3} , as declared by the SOI wafer supplier. On the top and on the sidewalls of the waveguide, a positive surface charge density $\sigma \sim 1.7 \times 10^{12} \text{ cm}^{-2}$ is applied, as estimated by C-V measurements. In the simulation, the extension of the charged defects in the cladding is neglected, considering a uniform distribution at the interface. Simulations confirm that this is a good approximation, showing that the electric field distribution inside the waveguide mostly depends on the total charge in the cladding rather than on its distribution.

Figure 7.6 reports the distribution of holes (panel a) and electrons (panel b) inside the waveguide. The simulation refers to a 906 nm wide waveguide. The carrier population inside the waveguide is inverted with respect to the situation without charges at the interface, showing a hole concentration below 10^5 cm^{-3} and an electron concentration in the range 10^{15} cm^{-3} to 10^{19} cm^{-3} . This agrees with results reported for similar geometries, which showed population inversion induced by charges [156, 158, 159]. As expected, the largest electron concentration extends close to the cladding interface. On the contrary, holes accumulate close to the uncharged interface at the bottom.

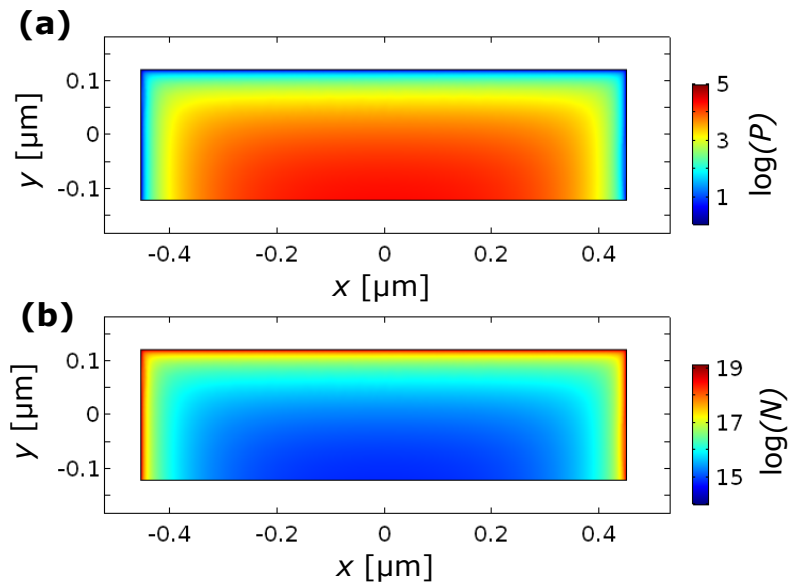


Fig. 7.6: Logarithm of hole (a) and electron (b) concentration inside a 906 nm wide waveguide caused by a surface charge density $1.7 \times 10^{12} \text{ cm}^{-2}$ applied to the top and to the lateral interfaces of the waveguide.

7.4.2 Effect of charges on propagation losses

Figure 7.6 shows the carrier distribution inside the waveguide due to the deposited charged defects. It is known that free carriers induce absorption in the material where they are generated. The carrier-induced absorption is described by the well known semi-empirical equation [160]. Considering the carrier distribution shown in Fig. 7.6, the distribution of the absorption coefficient can be evaluated and used in an optical simulation to estimate the propagation losses of the propagating mode. Considering a TE1 mode at the wavelength of $2.3\mu\text{m}$ in a 906 nm wide waveguide, a loss coefficient of about 4 dB/cm is estimated for a positive surface charge density $\sigma = 1.7 \times 10^{12}\text{ cm}^{-2}$. Using the charge density measured after 23 hours of UV exposure ($\sigma = 3.1 \times 10^9\text{ cm}^{-2}$), the loss coefficient essentially vanishes. The results of these simulation agree with the ones resulting from the experiment, which showed a loss reduction of 4 dB/cm after the UV treatment (passing from 8 dB/cm to 4 dB/cm). The residual loss coefficient of 4 dB/cm measured in the experiment after the UV treatment can be ascribed to sidewall roughness, which is not taken into account by the simulation.

7.4.3 Electric field distribution inside the waveguide

Using the model described previously, also the electric field distribution inside the waveguide can be estimated. In Fig. 7.7 both the components x and y of E_{DC} are reported. It is not surprising that the maximum value of E_{DC} is obtained close to the charged surface, with a rapid decrease while moving through the waveguide.

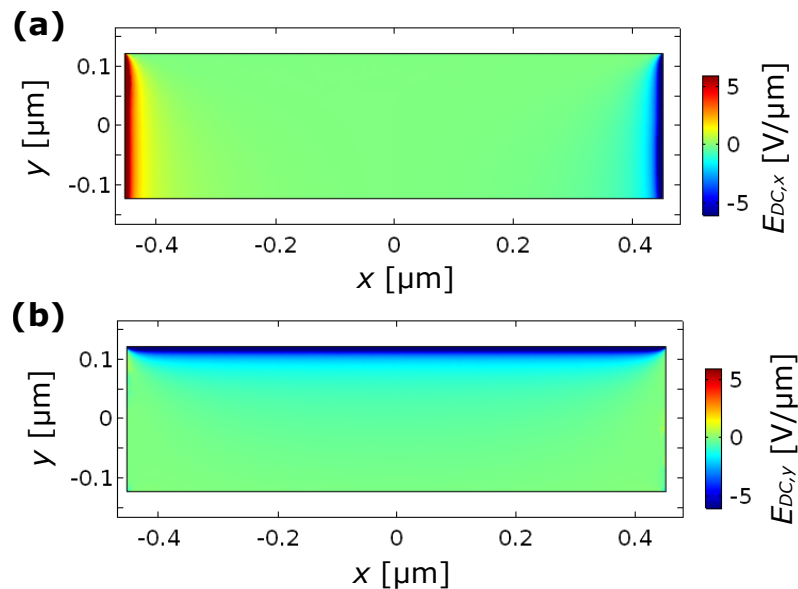


Fig. 7.7: Components x (a) and y (b) of the electric field E_{DC} determined by a surface charge density $1.7 \times 10^{12}\text{ cm}^{-2}$ on the top and on the sidewalls of a 906 nm wide waveguide.

7.4.4 Charge-induced second order nonlinearities

Once that the distribution of E_{DC} is known, the distribution of $\chi_{\text{EFISH}}^{(2)}$ inside the waveguide can be determined using Eq. (7.1). Doing that, the proper $\chi^{(3)}$ coefficient must be used.

Since the process under analysis relates the pump mode at frequency ω_p , the SH mode at frequency ω_{sh} and the DC field at frequency $\omega = 0$, the tensor $\chi^{(3)}(\omega_p, \omega_p, \omega_{sh}, 0)$ must be used. However, no estimations of this coefficient are reported in literature. Thus, as a first approximation, the term $\chi^{(3)}(\omega_p, \omega_p, \omega_p, \omega_p)$ is considered here.

SH signal on the TM mode. In the modal combinations where SHG has been experimentally evaluated, the pump mode is TE polarized (the electric field is directed along x), while the SH mode is TM polarized (the electric field is along y). So, the tensor elements that origin SHG are $\chi_{xxyy}^{(3)}$ (related to $E_{DC,x}$) and $\chi_{xyyy}^{(3)}$ (related to $E_{DC,y}$). However, in silicon $\chi_{xxyy}^{(3)} = 0$ for symmetry [148]. So, $\chi_{\text{EFISH}}^{(2)} = 3\chi_{xyyy}^{(3)}E_{DC,y}$.

Considering the spectral range from $1.2\mu\text{m}$ to $2.4\mu\text{m}$, the simple empirical relationship $\chi_{xxyy}^{(3)} = \chi_{xxxx}^{(3)}/2.36$ holds [161]. However, the measurements of $\chi_{xxxx}^{(3)}$ at pump wavelengths is ambiguous, and values in the range from $0.94 \times 10^{-19} \text{ m}^2/\text{V}^2$ to $4.24 \times 10^{-19} \text{ m}^2/\text{V}^2$ have been reported [81, 162, 163]. Therefore, an average of these values is used in this work.

Figure 7.8 shows $\chi_{\text{EFISH}}^{(2)} = 3\chi_{xyyy}^{(3)}E_{DC,y}$ in a 906 nm wide waveguide, where phase-matching is expected between the TE1 and the TM3 modes. The average value of $\chi_{\text{EFISH}}^{(2)}$ in the waveguide is -0.3 pm/V .

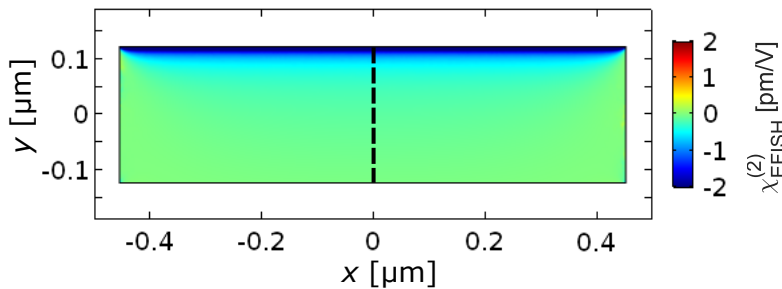


Fig. 7.8: $\chi_{\text{EFISH}}^{(2)}$ distribution in a 906 nm wide waveguide, where phase-matching on the TE1-TM3 modal combination is expected.

In Fig. 7.9 $\chi_{\text{EFISH}}^{(2)}$ is evaluated on a cutline directed in the y direction and passing through the center of the waveguide, showing a rapid decrease while moving from the charged to the neutral interface.

Table 7.1 shows the average of the absolute value of $\chi_{\text{EFISH}}^{(2)}$ in the waveguide for the combinations shown in Tab. 4.1. It can be noted that, higher is the modal order where the SH signal is generated, and larger is the $\chi_{\text{EFISH}}^{(2)}$ value. This is due to the fact that, higher the order where the SH signal is generated, and larger is the

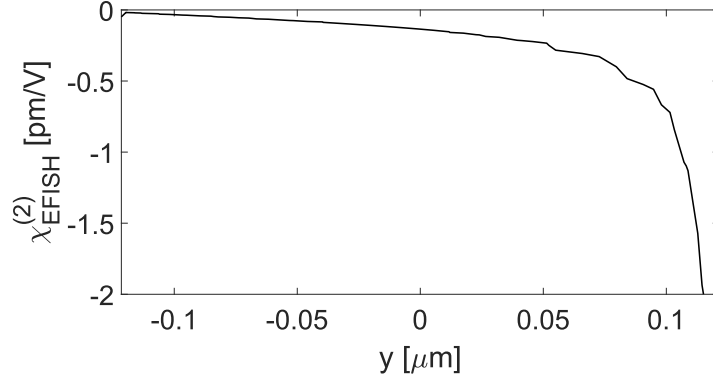


Fig. 7.9: $\chi_{\text{EFISH}}^{(2)}$ value evaluated along the black line reported in Fig. 7.8.

Tab. 7.1: Simulated values of $\langle |\chi_{\text{EFISH}}^{(2)}| \rangle$, $|\Gamma^{(2)}|$ and $\chi_{\text{eff}}^{(2)}$ for modal combinations where the SH signal is generated on TM modes.

Combination	w [μm]	$\langle \chi_{\text{EFISH}}^{(2)} \rangle$ [pm/V]	$ \Gamma^{(2)} $ [fm/V]	$\chi_{\text{eff}}^{(2)}$ [pm/V]
TE1-TM3	0.91	0.295	0.982	0.269
TE1-TM4	1.54	0.313	~ 0	-
TE1-TM5	2.10	0.322	0.156	0.274

waveguide width. From Fig. 7.7(b) it can be noted that the field $E_{DC,y}$ decreases close to the corner of the waveguide. Larger is the waveguide and smaller is this side effect, and so larger is the average value of $\chi_{\text{EFISH}}^{(2)}$ inside the waveguide.

Table 7.1 shows also the values of $|\Gamma^{(2)}|$ for all these modal combinations, evaluated according to the definition given in Eq. (4.11). The combinations where SH is generated on the TM3 and on the TM5 modes show a nonzero $|\Gamma^{(2)}|$ value, while $|\Gamma^{(2)}|$ is negligible for the combination where SH is generated on the TM4 mode. This is due to the symmetry of the $\chi_{\text{EFISH}}^{(2)}$ distribution with respect to the waveguide center while moving along the x direction. According to Eq. (4.32), $\chi_{\text{eff}}^{(2)}$ is also evaluated and shown in the table.

The results predicted by simulations for the TE1-TM3 and for the TE1-TM5 combinations are compared with the experimental results in Tab. 7.2. The error bars on the simulations result from the uncertainty on literature values. Considering the simplicity of the model, it can be concluded that the experimental and the simulation results are in good agreement.

Tab. 7.2: Comparison between the values of $|\Gamma^{(2)}|$ and $\chi_{\text{eff}}^{(2)}$ determined from the experiment and the values estimated from the simulation. The error bars on the simulations result from the uncertainty on literature values.

Combination	$ \Gamma^{(2)} $ [fm/V]		$\chi_{\text{eff}}^{(2)}$ [pm/V]	
	Experiment	Simulation	Experiment	Simulation
TE1-TM3	1.7 ± 0.2	1.0 ± 0.6	0.46 ± 0.06	0.3 ± 0.2
TE1-TM5	0.39 ± 0.06	0.16 ± 0.10	0.6 ± 0.1	0.27 ± 0.15

SH signal on the TE mode. Analogously to the situation treated before, if the SH mode is generated on a TE mode, one should write $\chi_{\text{EFISH}}^{(2)} = 3\chi_{xxxx}^{(3)}E_{DC,x}$. Figure 7.10 shows $\chi_{\text{EFISH}}^{(2)}$ evaluated in this way in a $1.08\ \mu\text{m}$ wide waveguide, where phase-matching is expected between the TE1 and the TE4 modes. The $\chi_{\text{EFISH}}^{(2)}$ distribution inside the waveguide along the x direction shows an anti-symmetric behavior with respect to the center of the waveguide. Therefore, the average value of $\chi_{\text{EFISH}}^{(2)}$ inside the waveguide is negligible. However, evaluating the average of the absolute value of $\chi_{\text{EFISH}}^{(2)}$, a value of $0.32\ \text{pm/V}$ is estimated.

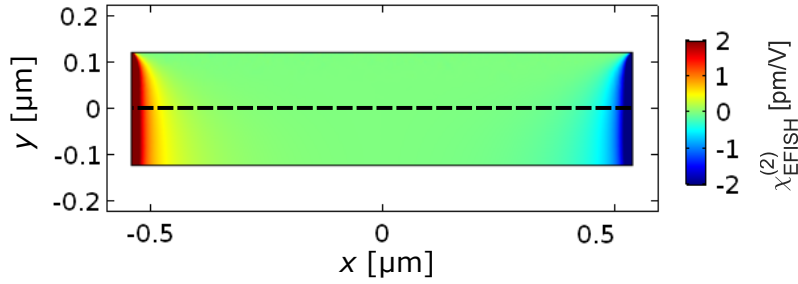


Fig. 7.10: $\chi_{\text{EFISH}}^{(2)}$ distribution in a $1.08\ \mu\text{m}$ wide waveguide, where phase-matching on the TE1-TM3 modal combination is expected.

In Fig. 7.11 $\chi_{\text{EFISH}}^{(2)}$ is evaluated on a cutline directed in the x direction and passing through the center of the waveguide: the value of $\chi_{\text{EFISH}}^{(2)}$ is high close to the lateral borders of the waveguide, rapidly decreasing while moving through the center of the waveguide.

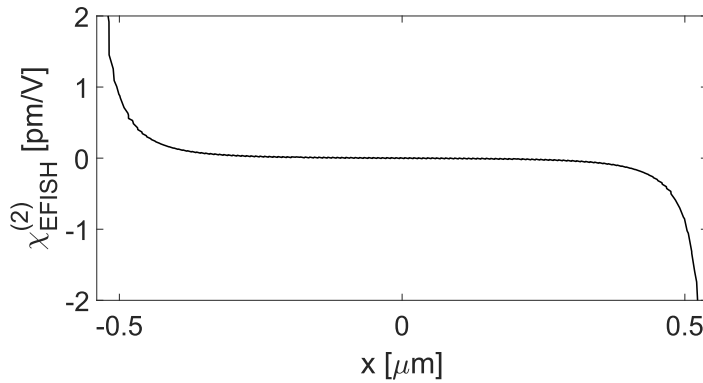


Fig. 7.11: $\chi_{\text{EFISH}}^{(2)}$ value evaluated along the black line reported in Fig. 7.10.

Table 7.3 shows the average of the absolute value of $\chi_{\text{EFISH}}^{(2)}$ in the waveguide for the combinations shown in Tab. 4.1 that predict SHG on TE modes. It can be noted that, larger is the waveguide, and smaller is the average value of $\chi_{\text{EFISH}}^{(2)}$. This is due to the fact that lateral borders have a dominant role, and so increasing the waveguide width their effect lowers. Table 7.3 reports also the values of $|\Gamma^{(2)}|$ for these modal combinations, evaluated according to the definition given in Eq. (4.11). Surprisingly, it can be noted that $|\Gamma^{(2)}|$ is negligible for combinations where the SH signal is generated on odd parity modes (TE5, TE7), while it is strong for combinations where

Tab. 7.3: Simulated values of $\langle |\chi_{\text{EFISH}}^{(2)}| \rangle$ and $|\Gamma^{(2)}|$ for modal combinations where the SH signal is generated on TE modes.

Combination	w [μm]	$\langle \chi_{\text{EFISH}}^{(2)} \rangle$ [pm/V]	$ \Gamma^{(2)} $ [fm/V]
TE1-TE4	1.08	0.320	0.357
TE1-TE5	1.44	0.246	~ 0
TE1-TE6	1.79	0.202	0.104
TE1-TE7	2.13	0.174	~ 0
TE1-TE8	2.46	0.154	0.043

the SH signal is generated on even parity modes (TE4, TE6, TE8). This fact has to be attributed to the anti-symmetric behavior of the $\chi_{\text{EFISH}}^{(2)}$ distribution with respect to the center of the waveguide along the x direction.

For these modal combination it is nonsense introducing the $\chi_{\text{eff}}^{(2)}$ value. In fact, according to its definition in Eq. (4.32), $\chi_{\text{eff}}^{(2)} = |\Gamma^{(2)}|/K$. However, for these combinations $K \sim 0$. This is not absurd, because $\chi_{\text{eff}}^{(2)}$ is defined as the equivalent spatially constant $\chi^{(2)}$ that would have given the same SHG efficiency. In this case, only an infinite spatially constant $\chi^{(2)}$ can give the same SHG efficiency, since these combinations require an anti-symmetric $\chi^{(2)}$ distribution to be efficient.

7.5 Conclusions and perspectives

The results shown in this chapter allows to conclude that charges play a crucial role in the measured SHG phenomenon. The measured second-order nonlinear susceptibility of about 0.5 pm/V can be totally ascribed to the EFISH process, induced by the charges trapped in the SiN cladding. The strain effect on $\chi^{(2)}$ is below the noise level, setting an upper limit of 0.05 pm/V to the strain-induced nonlinear coefficient. Interestingly, the upper limit to the measured strain-induced $\chi^{(2)}$ is comparable with the theoretical results of [115, 116]. In these works it was demonstrated that the deformation of the crystalline lattice, induced by the strain gradient, yields low values of $\chi^{(2)}$. Clearly, the results of this work hold by considering the strain values introduced by the silicon nitride layer. By applying larger amounts of strain, it is not possible to exclude that a measurable SHG signal can be obtained.

The outcomes of this work offer interesting perspectives, introducing a paradigmatic change in the development of these kinds of structures. Till now great effort was done towards increasing the amount of strain inside the waveguide. However, in this work it has been evidenced that the strain plays a secondary role, and large nonlinearities can be obtained by increasing the DC fields inside the waveguide. This can be done both by maximizing the amount of charges deposited on the waveguide sides, as well as by realizing thinner waveguides. This clearly has the drawback to increase the propagation losses, since charges cause the increase of the free carriers

inside the waveguide. Therefore, a trade-off condition must be found between the strength of the DC field and the absorption induced by the carriers.

Furthermore, this work shows that SHG efficiency can be controlled by applying UV irradiation. This offers interesting perspectives for the realization of quasi-phase matched (poled) waveguides. Applying a proper photolithographic mask and exposing it to UV light, periodically varying $\chi^{(2)}$ can be introduced along the waveguide propagation direction. Setting the proper poling period, the conversion between fundamental modes can be directly studied, measuring large conversion efficiencies due to the stronger mode overlap with respect to the intermodal approach.

A recent work already showed the possibility to exploit EFISH in silicon by applying DC fields via lateral p-n junctions [125]. This method allows to induce larger electric fields, and so larger values of $\chi_{\text{EFISH}}^{(2)}$. Therefore, in the following this method will be investigated in detail.

Part III

Second order nonlinearities in waveguides with static fields

The outcomes of Part II show that, even in strained waveguides, the measured SHG is due to static fields within the waveguide caused by trapped charges. This part aims at studying a more efficient way to introduce static electric fields in waveguides.

The first approach consists of using silicon waveguides with lateral p-n junctions. This geometry is characterized both theoretically and experimentally in **Chapter 8**. Considering racetrack resonators, the effect of the junction polarization on the resonator transmission spectra is studied.

Chapter 9 applies this configuration to the study of SHG. First, SHG theory is adapted to the new waveguide geometry, which also introduces the periodic poling as a method to satisfy phase-matching. Then, the waveguide engineering procedure is shown. This chapter considers also the possibility to perform the opposite process, namely the SPDC process.

The experimental characterization of SHG is shown in **Chapter 10**.

Using a similar approach, **Chapter 11** studies the possibility to perform SHG and SPDC in silicon oxynitride waveguides, applying the static field by means of metallic pads.

DC Kerr effect and plasma dispersion in silicon racetrack resonators

8.1	Lateral p-n junctions in microresonators	120
8.1.1	Effect on the material refractive index	120
8.1.2	Effect on the material absorption	121
8.2	Microresonator engineering	122
8.2.1	Single mode waveguides	122
8.2.2	Distance between the waveguide and metal	123
8.2.3	Curvature radius	125
8.2.4	Resonator coupling region	125
8.3	The realized devices	126
8.4	The effect of doping on waveguides	128
8.4.1	Modeling the system via transfer matrix methods	129
8.4.2	Characterization of devices without junctions	131
8.4.3	The effect of doping on microresonators	136
8.4.4	Modeling free-carrier absorption	136
8.5	Electrical characterization of waveguides	138
8.6	Electro-optic measurements	139
8.6.1	Modeling the electro-optic strength	140
8.6.2	Measurement of the electro-optic effect	142
8.7	Perspectives	145

In this work, lateral p-n junctions are used to introduce static fields within waveguides, which in turn enable field-induced second order nonlinearities. In this chapter, the effect of junctions on the propagation of optical modes is quantified. Doing, optical microresonators are considered. Laterally to the resonators waveguides, p-n junctions are formed. As it is introduced in Sec. 8.1, the junctions affect the resonator features, changing both the material refractive index and the absorption coefficient. The aim of this chapter is to measure these effects, and to model them for testing the simulation methods. Section 8.2 describes the engineering procedure used to design the microresonators. Images of the realized devices are shown in Sec. 8.3. In Sec. 8.4, microresonators are analyzed without applying any bias, in order to

quantify the effect of doping on the propagating modes. The measured results are also compared with simulations. In Sec. 8.5 the resonators junctions are biased and electrically analyzed. Finally, electro-optic measurements are performed in Sec. 8.6, showing a comparison with the simulations. The chapter is concluded in Sec. 8.7, where the main results are recovered and interesting perspectives are proposed. The experiments described in this chapter have been realized with Mr. R. Franchi. The theoretical model of the resonator has been realized with Mr. S. Biasi. The samples have been produced by Dr. M. Ghulinyan at Fondazione Bruno Kessler.

8.1 Lateral p-n junctions in microresonators

A sketch of the top view of one of the resonators described in this section is shown on the left of Fig. 8.1, while on the right the cross-section is shown. By applying the proper reverse bias to the junction, both the material refractive index as well as its absorption are affected. These two effects are treated separately in the following.

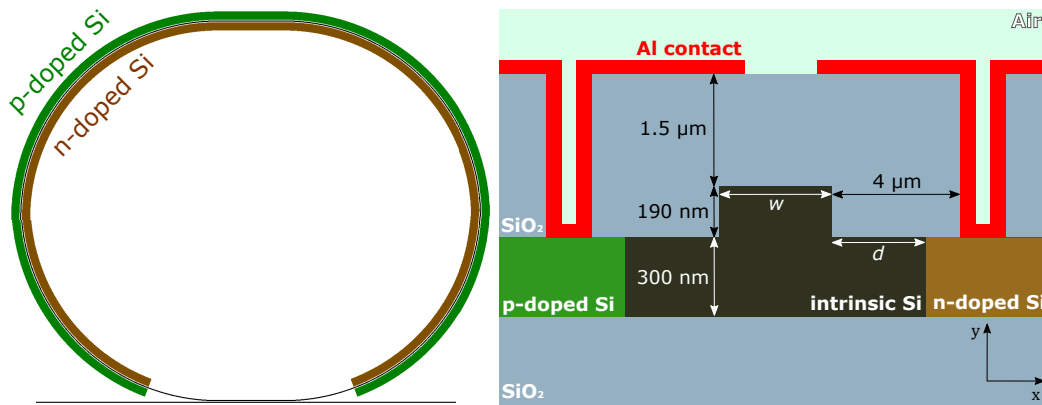


Fig. 8.1: Top-view and cross-section of one of the resonators described in this chapter.

8.1.1 Effect on the material refractive index

When a p-n junction is biased, the material refractive index is modified due to both plasma-dispersion effect and DC Kerr effect [125].

Plasma-dispersion is a linear optical effect caused by the variation of the free-carrier concentration in the material. If ΔN_e and ΔN_h are the variation of the electron and of the hole concentration, the material refractive index is modified by [160]:

$$\Delta n_{pd} = -p\Delta N_e^q - r\Delta N_h^s. \quad (8.1)$$

The coefficients p , q , r and s characterize each semiconductor, and depend on the wavelength. For silicon at the wavelength of 1550 nm these quantities are $p =$

$5.4 \times 10^{-22} \text{ cm}^3$, $q = 1.011$, $r = 1.53 \times 10^{-18} \text{ cm}^3$ and $s = 0.838$ [160].

DC Kerr effect is a third order nonlinear effect. It can be described starting from Eq. (1.8) and considering $\omega_3 = 0$ (one frequency is set to DC). In this case, additional phase-modulation terms appear in Eq. (1.8). Considering the wave propagating at frequency ω_1 , the nonlinear polarization vector takes the form:

$$\mathbf{P}^{(3)}(\mathbf{r}, t) = 3\varepsilon_0\chi^{(3)} [\mathbf{E}(\mathbf{r}, 0) + \mathbf{E}^*(\mathbf{r}, 0)]^2 \mathbf{E}_1(\mathbf{r}, \omega_1)e^{-i\omega_1 t} + c.c. \quad (8.2)$$

By introducing $\mathbf{E}_{DC} = \mathbf{E}(\mathbf{r}, 0) + c.c.$ and using $\mathbf{P} = \mathbf{P}_0 + \mathbf{P}^{(3)}$, it results that:

$$\mathbf{P}(\mathbf{r}, t) = \varepsilon_0 [\chi^{(1)} + 3\chi^{(3)}|\mathbf{E}_{DC}|^2] \mathbf{E}_1(\mathbf{r}, \omega_1)e^{-i\omega_1 t} + c.c. \quad (8.3)$$

So, DC Kerr effect introduces a susceptibility perturbation $\Delta\chi = 3\chi^{(3)}|\mathbf{E}_{DC}|^2$. Since $n^2 = \chi^{(1)} + 1$, the DC Kerr effect results in a index perturbation Δn_k given by:

$$\Delta n_k = \frac{3\chi^{(3)}|\mathbf{E}_{DC}|^2}{2n_0}, \quad (8.4)$$

being n_0 the unperturbed refractive index value.

Both DC Kerr effect and plasma dispersion cause a variation of the material refractive index $\Delta n = \Delta n_{pd} + \Delta n_k$. This results in an effective refractive index variation of the resonator mode Δn_{eff} , which in turn determines a shift $\Delta\lambda$ of the resonance wavelength. This quantity is related to Δn_{eff} by [120]:

$$\Delta\lambda = \varrho \frac{\lambda}{n_g} \Delta n_{\text{eff}}, \quad (8.5)$$

being λ the resonance wavelength, n_g the group index of the mode and ϱ the fraction of the resonator perimeter that undergoes the effective index variation Δn_{eff} (in the resonators analyzed in this work, the coupling region does not feel the index variation because the p-n junction is not present).

8.1.2 Effect on the material absorption

The presence of lateral p-n junctions does not affect only the effective refractive index of the propagating mode, but also its absorption. This can be due both to **defects** introduced during the implantation of the dopants, but also to **free-carrier-induced absorption**. In fact, the variations ΔN_e and ΔN_h of the electron and of the hole concentration induce a variation of the absorption coefficient $\Delta\alpha$ given by [160]:

$$\Delta\alpha = a\Delta N_e^b + c\Delta N_h^d, \quad (8.6)$$

where, for silicon at the wavelength of 1550 nm, $a = 8.88 \times 10^{-21} \text{ cm}^2$, $b = 1.167$, $c = 5.84 \times 10^{-20} \text{ cm}^2$ and $d = 1.109$ [160].

Variations of the material absorption can be measured by analyzing the spectral features of the resonator. In fact, according to Eq. (1.18), a variation of the resonator intrinsic losses determines a variation of the intrinsic quality factor. This, in turn, provides a variation of the resonator transmission spectrum.

8.2 Microresonator engineering

A cross-section of the resonator waveguide is sketched on the right of Fig. 8.1. It is formed by a 300 nm high slab, while the total height of the waveguide is 490 nm. The width of the waveguide is $w = 550$ nm. As it will be discussed later, this value is chosen to keep the single mode operation around the wavelength of 1550 nm. The doped regions are realized at a distance d from the waveguide borders. Different values of d are proposed in the design, respectively 200 nm, 500 nm and 800 nm. The smaller is d , and the larger is the electric field inside the waveguide for a given voltage. However, if d is smaller, the mode feels more the doped region, and so it suffers of larger losses, due both to the abundance of free-carriers in the doped region, as well as to the defects introduced by ion implantation. The electron concentration is $1 \times 10^{18} \text{ cm}^{-3}$ in the n-doped region, like the hole concentration in the p-doped region. Silicon inside the waveguide has a residual $1 \times 10^{15} \text{ cm}^{-3}$ p-type doping, corresponding to the doping level of the SOI wafer. An oxide cladding is deposited on the top of the waveguide. Vias are created within oxide to contact the doped regions with aluminum pads and to polarize the junction.

8.2.1 Single mode waveguides

As already introduced, the width of the resonator waveguide w is 550 nm. This value is chosen to keep the single mode operation of the waveguide around 1550 nm. To determine w , the effective refractive index of the guided modes is simulated as a function of w using the Electro-Magnetic module of the COMSOL Multiphysics® FEM software [56]. Figure 8.2(a) shows this quantity for the fundamental TE and TM modes, as well as of the second order TE mode, at the wavelength of 1550 nm. For large waveguides, the effective refractive indexes of all the modes vary with w . However, decreasing w , the effective refractive indexes become constant. This is because, decreasing w , the mode is less and less confined in the rib waveguide. After a certain point it becomes a slab mode, and thus it does not depend any more on w and remains constant. Therefore, in the single mode operation only the fundamental mode shows a dependence on w . In the case of this work, $w = 550$ nm satisfies this condition, and it is represented by a black vertical line in Fig. 8.2(a). The same check can be done by looking at Fig. 8.2(b), where the propagation losses of all the modes are reported as a function of w . For the slab modes the propagation losses are much

larger than for the rib modes, due to the fact that the mode is not well confined and it is absorbed by the boundary conditions used in the simulation. It is important to stress that, in this case, the losses are calculated without accounting for free-carriers, which in turn affect losses according to (8.6). Their effect is considered later on in this chapter. The aim of this study is just calculating the geometric parameters of a single-mode waveguide.

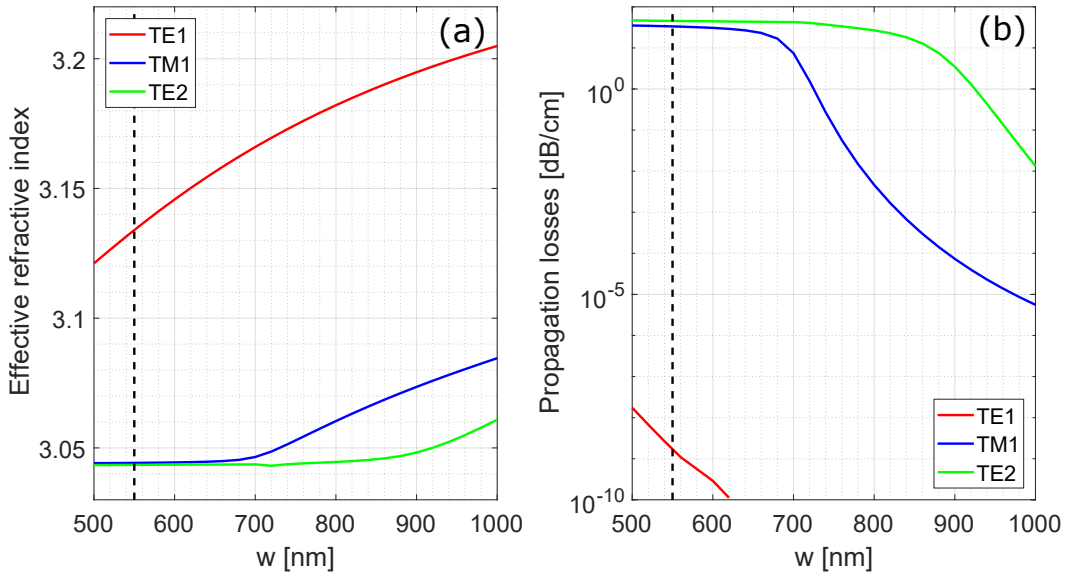


Fig. 8.2: Effective refractive index (a) and propagation losses (b) dependence on the waveguide width w for the TE1, TE2 and TM1 modes at the wavelength of 1550 nm. The vertical black lines refer to the selected single mode waveguide width of 550 nm.

8.2.2 Distance between the waveguide and metal

An important parameter to fix in the design of the structures is the distance between the waveguide and the metal, to avoid absorption of the optical mode. This requires to determine properly the height of the oxide cladding, as well as the distance between the waveguide and the hole used to contact the junctions.

To estimate the correct height of the oxide cladding, the propagation losses are evaluated as a function of the oxide layer height using a 2D FEM simulation. The sketch of the simulation domain is shown in the left hand side of Fig. 8.3. On the right hand side of Fig. 8.3 the result of the simulation are shown. The simulation refers to the wavelength of 1550 nm and to $w = 550$ nm. Propagation losses decrease as the oxide cladding height increases because the metallic layer is moved away from the waveguide. At a certain point, the propagation losses saturate because of the boundary conditions of the simulation, which become the main loss source. It should be stressed that this is not a physical reason. However, in the actual device there are other sources of loss that are not taken into account in this simulation (such as the waveguide surface roughness). The vertical black line reported in Fig. 8.3 refers to

the cladding height selected for the actual device, that is $1.5\ \mu\text{m}$. Using this cladding height, the metal-induced propagation losses are kept down to $1 \times 10^{-9}\ \text{dB/cm}$, orders of magnitude below the surface roughness losses.

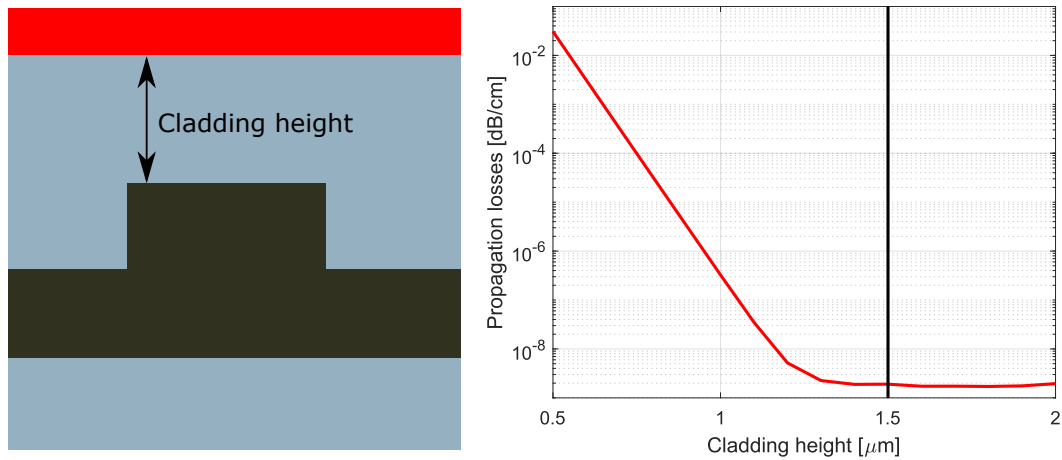


Fig. 8.3: Left: simulation domain used to estimate the proper oxide cladding layer height. Right: metal-induced propagation losses for the wavelength of $1550\ \text{nm}$ for $w = 550\ \text{nm}$. The black line refers to the value used for the design.

Another source of loss are lateral metallic contacts, that must be kept far away from the waveguide. The left side of Fig. 8.4 shows the simulation domain used to estimate these losses. The results are reported on the right side of the figure. Also in this case the minimum loss value depends on boundary conditions. For this reason, a distance larger than $4\ \mu\text{m}$ is used, keeping metal-induced losses below $1 \times 10^{-7}\ \text{dB/cm}$.

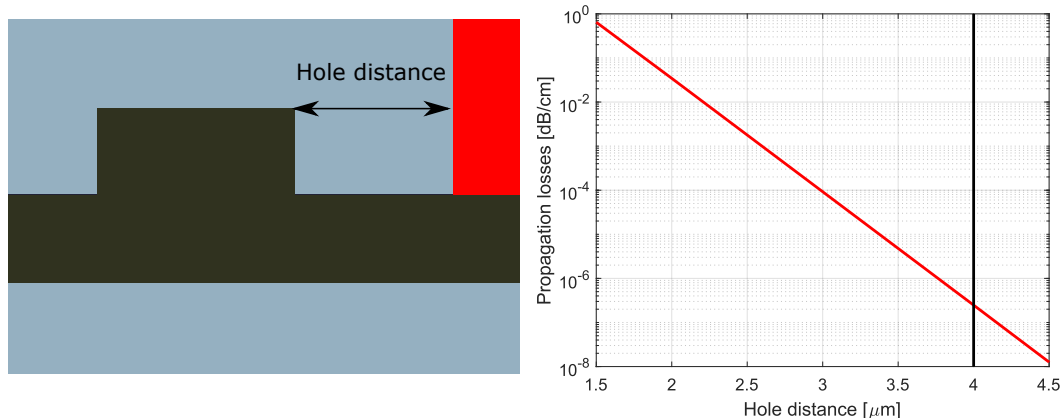


Fig. 8.4: Left: simulation domain used to estimate the distance between the waveguide and the lateral metal. Right: metal-induced propagation losses for the wavelength of $1550\ \text{nm}$ and $w = 550\ \text{nm}$. The black line reports the selected value.

8.2.3 Curvature radius

To estimate the proper resonator waveguide curvature, a 2D axisymmetric mode-solver is used. Using the wavelength of 1550 nm and $w = 550$ nm, the simulation is realized varying the curvature radius R . For each curvature radius, the modal effective radius R_{eff} is evaluated calculating the following integral:

$$R_{\text{eff}} = \frac{\int r |\mathbf{E}(r)|^2 dA}{\int |\mathbf{E}(r)|^2 dA}. \quad (8.7)$$

The integration is taken on all the domain, r is the distance from the rotation axis and $\mathbf{E}(r)$ the electric field. This quantity takes into account the mean radius where the propagating field is localized. This quantity must be compared with the actual radius of the curve. Smaller is the curvature radius, and less the propagating field is localized into the waveguide. So, the curvature radius R and the effective radius R_{eff} differ more. To this purpose, in Fig. 8.5 the ratio R_{eff}/R is shown as a function of R , referred to the waveguide width of 550 nm at a wavelength of 1550 nm. This quantity is important because it is related to the localization of the optical mode: less localized it is, and larger are the radiative losses. By taking a curvature radius of $150 \mu\text{m}$, which is sketched by the black vertical in the figure, R_{eff} and R differ by less than 0.02%. This is the actual value of R used in this work.

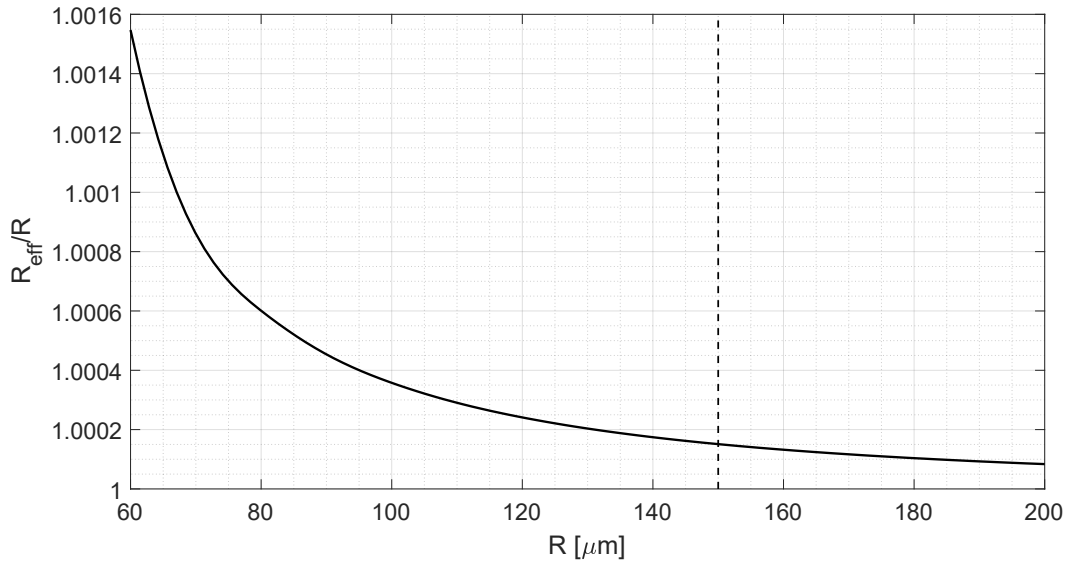


Fig. 8.5: Dependence of the ratio R_{eff}/R on the curvature radius at the wavelength of 1550 nm and $w = 550$ nm. The black lines shows the selected curvature radius.

8.2.4 Resonator coupling region

In the coupling region, the resonator and the bus waveguides are identical ($w = 550$ nm), and their separation is 600 nm. Different resonators have been realized,

each characterized by a different length L_s of the straight part of the coupling region. Figure 8.6 reports, as a function of L_s , the transmission coefficient t of the bus waveguide-resonator coupler (it is related to the coupling coefficient κ by $t^2 = 1 - \kappa^2$). The result refers to a wavelength of 1550 nm. This quantity accounts for the coupling both in the straight part of the resonator coupler, as well as for the coupling between the bus waveguide and the bent part of the resonator. Doing so, the waveguide-resonator coupler is divided in different domains, and the coupling is evaluated separately in each of these domains. This is done evaluating, for each domain, the even and the odd modes of the coupler system [164]. To achieve the critical coupling condition, the transmission coefficient t must match the roundtrip loss coefficient α . Since the latter depends on the quality of the realized resonator, it cannot be determined before realizing the device. Therefore, different values of L_s are proposed in the design (namely $L_s = 0 \mu\text{m}$, $10 \mu\text{m}$, $20 \mu\text{m}$, $30 \mu\text{m}$, $40 \mu\text{m}$, $50 \mu\text{m}$).

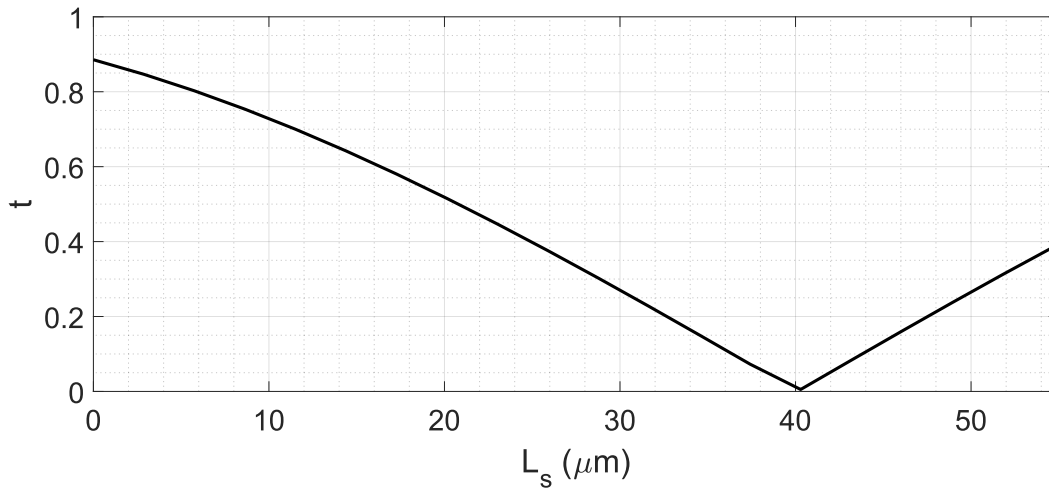


Fig. 8.6: Transmission coefficient t of the bus waveguide-resonator coupler as a function of the coupling region length L_s . The result refers to a wavelength of 1550 nm.

8.3 The realized devices

The waveguides described in this chapter are defined using a 365 nm UV lithography, and are realized by reactive ion etching. Figure 8.7 shows an optical image taken after the definition of the waveguides. Four resonators with different coupling region lengths are visible, each of which coupled to a bus waveguide. Straight reference waveguides are also visible.

After the definition of the optical waveguides, doped regions are realized close to the waveguide borders. Doing so, all the chip is covered, except the regions where ions are implanted to dope silicon. Figure 8.8 shows an optical image of the chip before the implantation of p-type ions (top) and n-type ions (bottom).

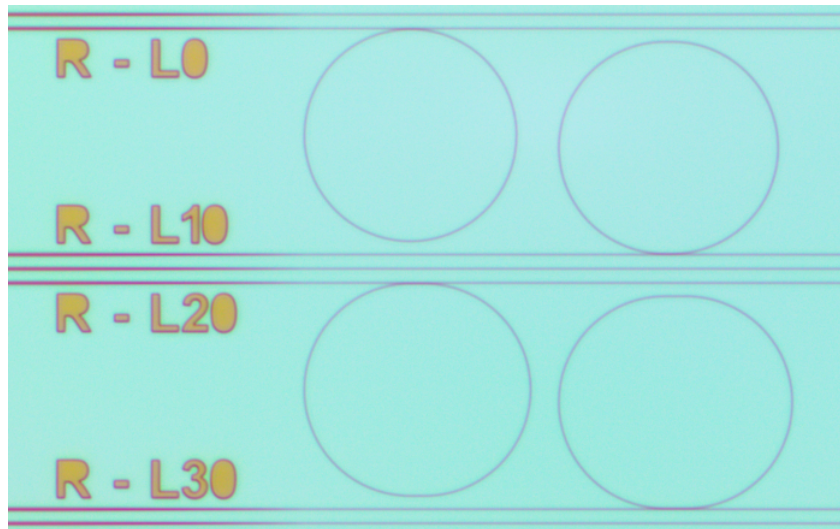


Fig. 8.7: Optical image of part of the realized sample taken after the definition of waveguides. Image courtesy of Dr. M. Ghulinyan.

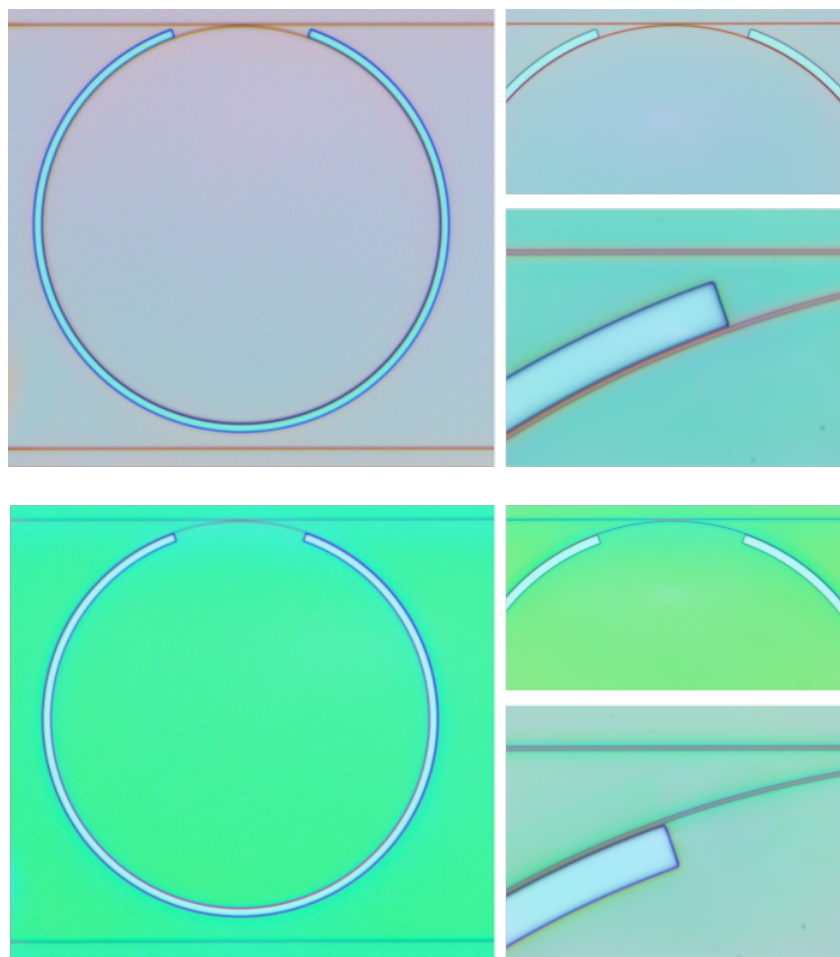


Fig. 8.8: Optical image of the chip before the implantation of p-type ions (top) and n-type ions (bottom). Image courtesy of Dr. M. Ghulinyan.

After the ionic implantation, oxide is grown on the top of the waveguide. After this process, holes are realized in the oxide layer in order to deposit metallic pads which can contact the doped regions. Figure 8.9 shows an optical image of the chip after the realization of the contact holes.



Fig. 8.9: Optical image of the chip after the realization of the contact holes. Image courtesy of Dr. M. Ghulinyan.

Finally, once that all the previous steps are processed, aluminum layers are deposited. An example of this is shown in Fig. 8.10. A large metallic layer is realized in the center of the resonator, to contact the n-type doped silicon layer. The p-type silicon is connected to a large pad, common to all the resonators, realized close to them.

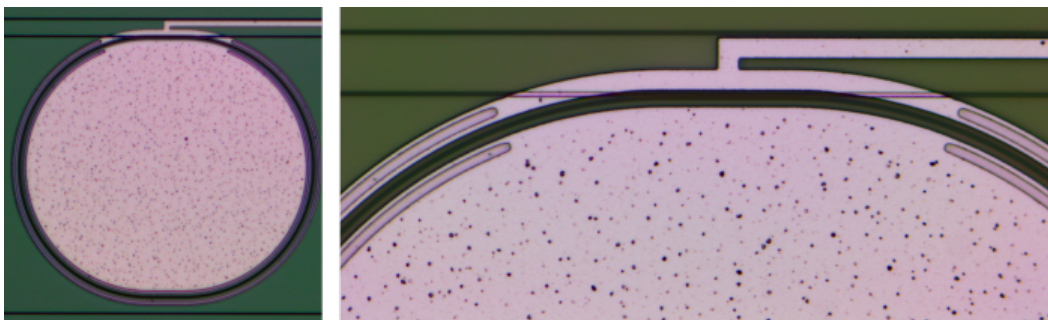


Fig. 8.10: Metallic layers deposited on the top. Image courtesy of Dr. M. Ghulinyan.

8.4 The effect of doping on waveguides

This section aims at quantifying the effect of doping on resonators in terms of losses. The purpose is to experimentally compare the transmission spectra of resonators where no doping is present with resonators having lateral p-n junctions, considering the three proposed configurations ($d = 200$ nm, 500 nm, 800 nm). Even if no bias is applied, doping is expected to increase the waveguide losses, due both to the abundance of free carriers and to the damages introduced by ion implantation. To extract losses from the resonator transmission spectra, a model to fit them is needed. This model is derived in Sec. 8.4.1. Then, it is applied to fit the transmission spectra of resonators without junctions (Sec. 8.4.2) and with lateral junctions (Sec. 8.4.3).

Finally, in Sec. 8.4.4 a FEM model able to quantify the effect of free-carriers on the absorption is described, comparing the results with the experiment.

8.4.1 Modeling the system via transfer matrix methods

The system analyzed in this section is formed by a resonator in the all-pass configuration. The transfer matrix of this system M_r is given by [165]:

$$M_r = \begin{bmatrix} \frac{1-t\alpha e^{i\phi}}{t-\alpha e^{i\phi}} & 0 \\ 0 & \frac{t-\alpha e^{i\phi}}{1-\alpha e^{i\phi}} \end{bmatrix}. \quad (8.8)$$

Here, t is the transmission coefficient of the bus waveguide-resonator coupler (it is related to the coupling coefficient κ by $t^2 = 1 - \kappa^2$), while α is the roundtrip loss coefficient in the resonator (it relates the power coupled into the resonator P_i with the power after one complete roundtrip P_o by $P_o = |\alpha|^2 P_i$). The coefficient $\phi = \beta L$ is the phase acquired in a complete roundtrip, being L the resonator length and $\beta = 2\pi n_{\text{eff}}/\lambda$ the propagation constant in the resonator waveguide.

However, this is not enough to describe the system analyzed in this work. In fact, light is coupled in and out from the bus waveguide via butt coupling. Due to the strong refractive index difference between the silicon waveguide and air, the input and the output facets are characterized by a strong reflectance. Therefore, the input and the output facets of the waveguide form a Fabry-Perot cavity, whose transmission spectrum is superimposed to the one of the resonator. So, also this effect has to be considered. Therefore, this system can be described like it is sketched in Fig. 8.11.

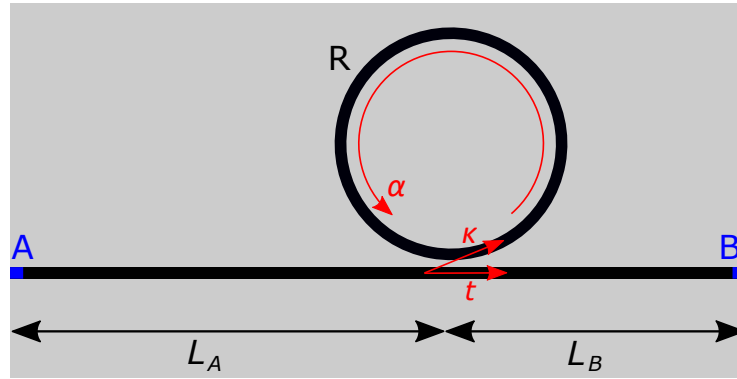


Fig. 8.11: Sketch of the model described here, which considers the coupling facets A and B, the bus waveguide (divided in sections of length L_A and L_B) and the resonator.

The transfer matrix of this system is:

$$M = M_{F,B} M_{L,B} M_r M_{L,A} M_{F,A}, \quad (8.9)$$

being $M_{F,A}$ and $M_{F,B}$ the transfer matrices of the input and of the output facets, while $M_{L,A}$ and $M_{L,B}$ are the transfer matrices describing the propagation in the

bus waveguide between the input facet and the resonator and between the resonator and the output facet.

The transfer matrices describing the input and of the output facets are [52]:

$$M_{F,A} = \frac{1}{\tau_A} \begin{bmatrix} 1 & ir_A \\ -ir_A & 1 \end{bmatrix} \quad M_{F,B} = \frac{1}{\tau_B} \begin{bmatrix} 1 & -ir_B \\ ir_B & 1 \end{bmatrix} \quad (8.10)$$

being τ_A and τ_B the transmission coefficients of the input and of the output facets, while r_A and r_B are the reflection coefficients of the same facets. These quantities are related by $r_A^2 + \tau_A^2 = 1$ and $r_B^2 + \tau_B^2 = 1$. The matrices $M_{F,A}$ and $M_{F,B}$ have opposite sign on the anti-diagonal terms because the interfaces are opposite.

The transfer matrices describing the propagation in the bus waveguides are [52]:

$$M_{L,A} = \begin{bmatrix} e^{-i\phi_A} & 0 \\ 0 & e^{i\phi_A} \end{bmatrix} \quad M_{L,B} = \begin{bmatrix} e^{-i\phi_B} & 0 \\ 0 & e^{i\phi_B} \end{bmatrix} \quad (8.11)$$

being ϕ_A and ϕ_B the phases acquired respectively between the input facet and the resonator and between the resonator and the output facet. In general, they are defined as $\phi_j = (\beta_j + i\alpha_j)L_j$, being β_j the propagation constant, α_j the absorption coefficient and L_j the waveguide length.

By multiplying the matrices, one gets the system transfer function T [52]:

$$T = \left| \frac{1}{M_{2,2}} \right|^2 = \left| \frac{\tau_A \tau_B}{\frac{1-t\alpha e^{i\phi}}{t-\alpha e^{i\phi}} e^{-i(\phi_A+\phi_B)} - r_A r_B \frac{t-\alpha e^{i\phi}}{1-\alpha e^{i\phi}} e^{i(\phi_A+\phi_B)}} \right|^2. \quad (8.12)$$

The experimental spectrum can be thus fitted by a function of the form T .

Compared to this model, some simplifications are introduced. Since the bus waveguide is short (around 2 mm), propagation losses in the bus waveguide are neglected ($\alpha_j = 0$). Moreover, being the cross-section of the input and of the output waveguides equal, it is introduced $r = r_A = r_B$. Moreover, one should consider that the effective refractive index of both the bus waveguide and the resonator waveguide modes are wavelength dependent. By Taylor expanding them at the first order around a wavelength λ_0 , the propagation constants can be written as:

$$\beta(\lambda) = \frac{2\pi}{\lambda} n_{\text{eff}}(\lambda) \sim \frac{2\pi}{\lambda} n_g(\lambda_0) + 2\pi \left. \frac{\partial n}{\partial \lambda} \right|_{\lambda_0}. \quad (8.13)$$

So, the propagation constants have a wavelength dependent term (related to the group index) and a constant term. Since the propagation constants enter into (8.12) through periodic functions, from the fit it is possible to uniquely determine the wavelength-dependent terms (and so the group indices), but not the constant terms. So, using this simplified model, the fitting parameters are the bus waveguide and the resonator group indices ($n_{g,r}$ and $n_{g,wg}$), the input/output waveguide reflectance r , the coupler transmission t and the resonator roundtrip loss α .

8.4.2 Characterization of devices without junctions

Figure 8.12 shows the transmission spectra of six different resonators. The measurements have been taken on an undoped wafer, i.e., after defining the waveguides, the cladding oxide layer is deposited. The transmission spectra are measured by using a tunable laser source at the input. After a polarizing stage, light is butt-coupled in the bus waveguide using a tapered lensed fiber. Another lensed fiber collects light at the output, which is analyzed by an InGaAs detector and by an oscilloscope.

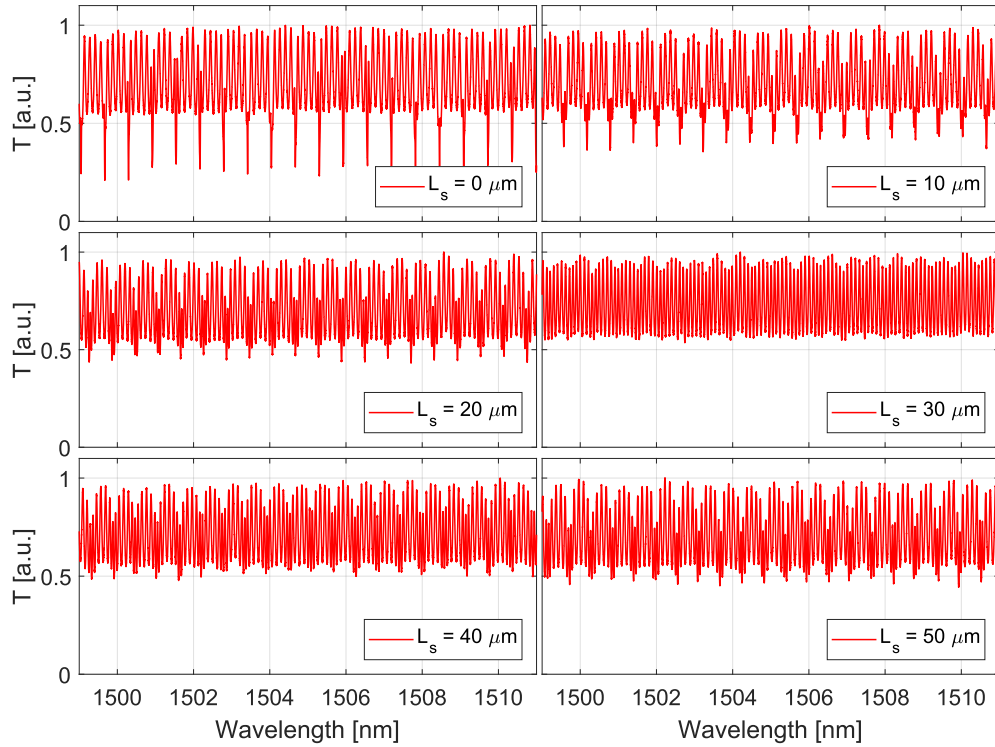


Fig. 8.12: Normalized transmission spectra of six different resonators, each characterized by L_s varying from $0\ \mu\text{m}$ to $50\ \mu\text{m}$.

The six panels of Fig. 8.12 refer to six resonators where the length of the coupling part L_s varies from $0\ \mu\text{m}$ to $50\ \mu\text{m}$. All the spectra are affected by a strong Fabry-Perot interference pattern. Some of the transmission spectra show resonance peaks due to the microresonator. Since the resonance peaks never go to zero, none of the resonators is in the critical coupling regime. The resonator showing the deepest resonances is the one with $L_s = 0\ \mu\text{m}$. Increasing L_s , the resonance becomes less deep. This means that at $L_s = 0\ \mu\text{m}$ the resonator is already in the overcoupling regime. The larger L_s , and the larger is the power coupled into the resonator, and the worst is the quality factor of the resonator. For $L_s = 30\ \mu\text{m}$, the quality factor is so bad that resonances are completely hidden under the Fabry-Perot interference. For larger L_s the coupling region grows so much that it overcomes the length where coupling is maximum, so the overall coupling is smaller and the resonances appear again. This means that, even at $L_s = 0\ \mu\text{m}$, the transmission coefficient t is too small

(or, equivalently, the coupling coefficient κ is too large). So, the coupling in the bent part of the coupler is too large and overcomes the roundtrip losses. To achieve critical coupling, one should have used larger gaps in the coupling region.

From now on, the attention of this work is devoted to the resonator $L_s = 0\ \mu\text{m}$, where resonances are more prominent. This work aims at fitting the spectra using Eq. (8.12) to derive the most important parameters of the resonator.

First, the group index of the resonator waveguide and of the bus waveguide and are roughly estimated according to Eq. (1.15) from the measured FSR and knowing the cavity length L . In the case of the microresonator $L = 2(\pi R + L_s)$, while in the case of the Fabry-Perot cavity the cavity length is twice the bus waveguide length $L_{\text{bus}} = 1.95\ \text{mm}$. To guess the facet reflectance r , the first fit is done on a reference bus waveguide that is not coupled to any resonator. The fit is performed using Eq. (8.12) with $t = 1$. The result of the fit is shown on the top of Fig. 8.13. The same function is then used to fit the resonator transmission spectrum, using the results of the previous fit as a starting point. The result of the fit is shown on the bottom of Fig. 8.13. This fit allows to roughly estimate r , which is then used as a starting point to fit the total resonator transmission spectrum.

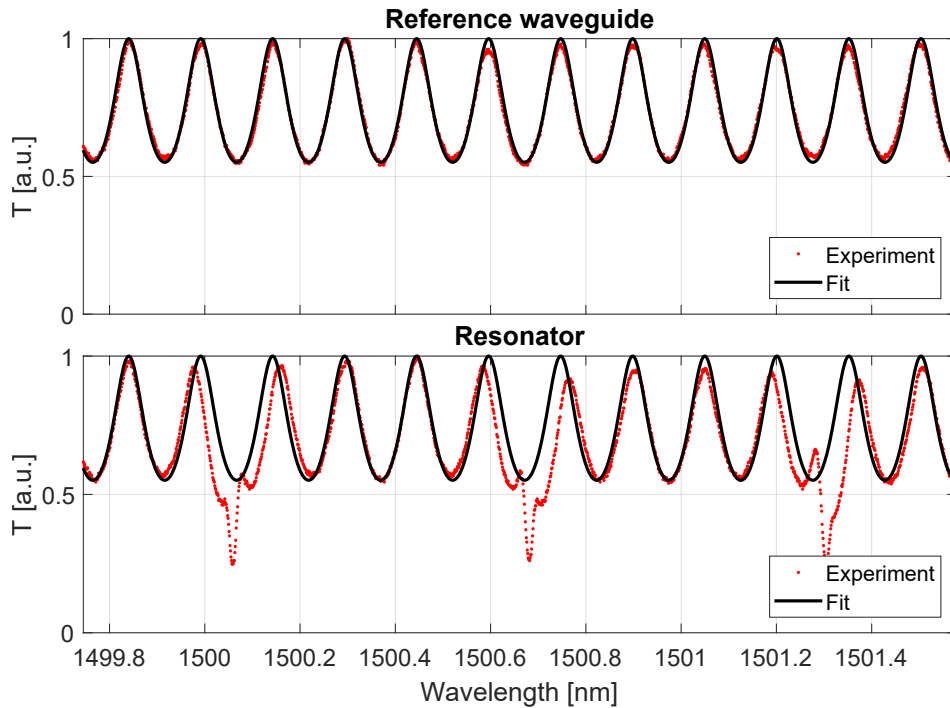


Fig. 8.13: Preliminary fitting procedures. Fit of the transmission spectrum of a reference bus waveguide (top) and of a resonator (bottom) with Eq. (8.12) and $t = 1$ (the coupling with the resonator is neglected).

Once that the group indexes n_g and the facet reflectance r are roughly estimated from preliminary fits, Eq. (8.12) is used to fit the resonator spectrum. The spectrum is divided in groups of two resonances each. Each group is fitted according to Eq. (8.12). The result of the fit is shown in Fig. 8.14. The top panel reports with

different colors the parts of the spectrum that are fitted separately. The continuous black line represents the fit function. On the bottom panel a couple of resonances are fitted, showing that the fit function well reproduces the experimental data.

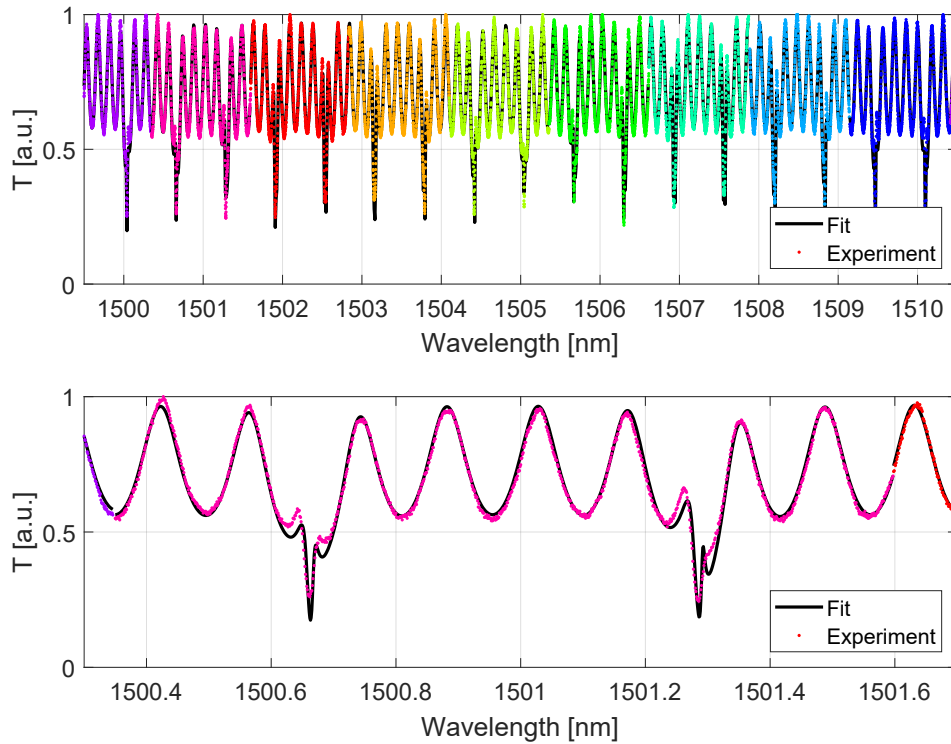


Fig. 8.14: On the top, the resonator transmission spectrum is fitted by Eq. (8.13). The transmission spectrum is divided in groups of two resonances each, represented by different colors in the figure. Each group is fitted separately. The black line represents the fit function. On the bottom, part of the fitted spectrum is zoomed.

Once that the fit is performed, the resulting parameters can be investigated. Figure 8.15 reports the value of the reflectance coefficient r as a function of wavelength. The three panels refer to measurements taken on three different chips. The first two chips belong to the same wafer, while the third chip belongs to a different wafer. On the same panel, the different colors represent measurements taken on different resonators with nominally identical parameters. Each of the scatter points results from the fit of a couple of resonances, as described previously. The solid lines come from a quadratic fit of the scatter points. The resulting values show that, as expected, r does not show any dependence on wavelength. Moreover, Fig. 8.15 shows that waveguides of wafer 2 have low reflectance values, with large variability between different waveguides. This agrees with observations done by optical microscope, which revealed that the cutting procedure resulted in bad and less uniform facets on wafer 2. On wafer 1 the facet reflectance is larger, demonstrating higher quality facets. The variability between different structures on the same chip is lower, demonstrating more uniform cuts.

Figure 8.16 reports the transmission coefficient t . In this case, t decreases with wavelength, demonstrating that larger the wavelength and larger is the power coupled

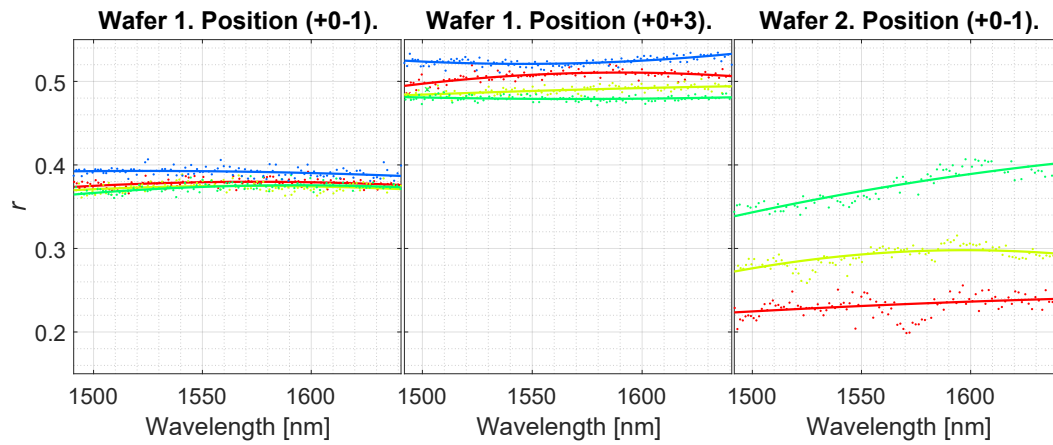


Fig. 8.15: Reflectance coefficient as a function of wavelength on three different chips (three panels). On the same panel, each color shows measurements taken on different resonators with nominally identical parameters. Each point comes from the fit of two resonances, while solid lines are quadratic fits of the scatter points.

into the resonator. This is reasonable, since the larger is the wavelength and the larger is the mode effective area, and so the strength of coupling with the resonator waveguide increases. In this case, the values assumed by t are almost similar on the different resonators, demonstrating geometrical uniformity. Wafer 2 shows a slightly larger t value if compared to wafer 1, which demonstrates a smaller coupling coefficient. This can derive from a larger gap between the bus waveguide and the resonator. The results reported here agree with that of the simulation shown in Fig. 8.6, which was referred to a wavelength of 1550 nm and showed a value of t slightly below 0.9 in the case $L_s = 0\mu\text{m}$. The fit results reported in Fig. 8.16 demonstrate that, in all the resonators analyzed in this work, t is in the range between 0.8 and 0.9 at the wavelength of 1550 nm.

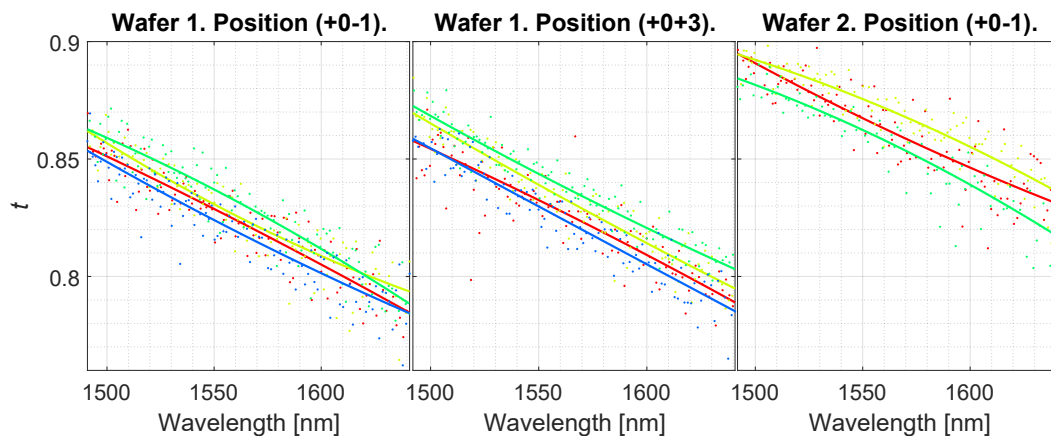


Fig. 8.16: Transmission coefficient of the bus waveguide-resonator coupling region as a function of wavelength on three different chips (three panels). On the same panel, each color shows measurements taken on different resonators with nominally identical parameters. Each point comes from the fit of two resonances, while solid lines are quadratic fits of the scatter points.

Analogously, Fig. 8.17 reports the roundtrip loss α . In this case, α slightly decreases

with wavelength, showing that larger losses are present for longer wavelengths, when the mode is less localized in the waveguide. Moreover, the figure shows that in wafer 2 the waveguides are less lossy than in wafer 1.

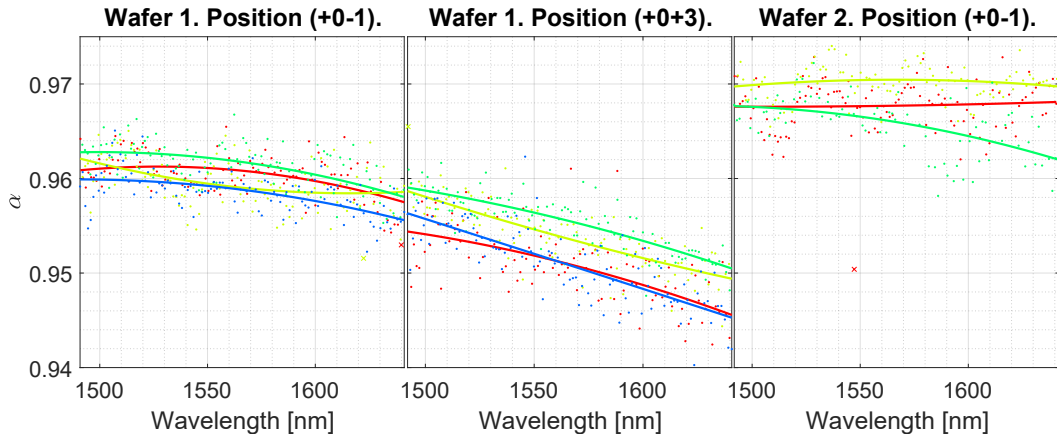


Fig. 8.17: Roundtrip loss coefficient as a function of wavelength on three different chips (three panels). On the same panel, each color shows measurements taken on different resonators with nominally identical parameters. Each point comes from the fit of two resonances, while solid lines are quadratic fits of the scatter points.

It is possible to introduce a propagation loss coefficient \mathcal{L} as follows:

$$\mathcal{L} = -\frac{1}{L} 10 \log_{10} |\alpha|^2, \quad (8.14)$$

being L the resonator waveguide length. This quantity is shown in Fig. 8.18. If radiative losses are negligible, the coefficient \mathcal{L} represents scattering losses due to surface roughness. From this result it is possible to quantify propagation losses of wafer 1 at about 4 dB/cm, while in wafer 2 losses are around 3 dB/cm.

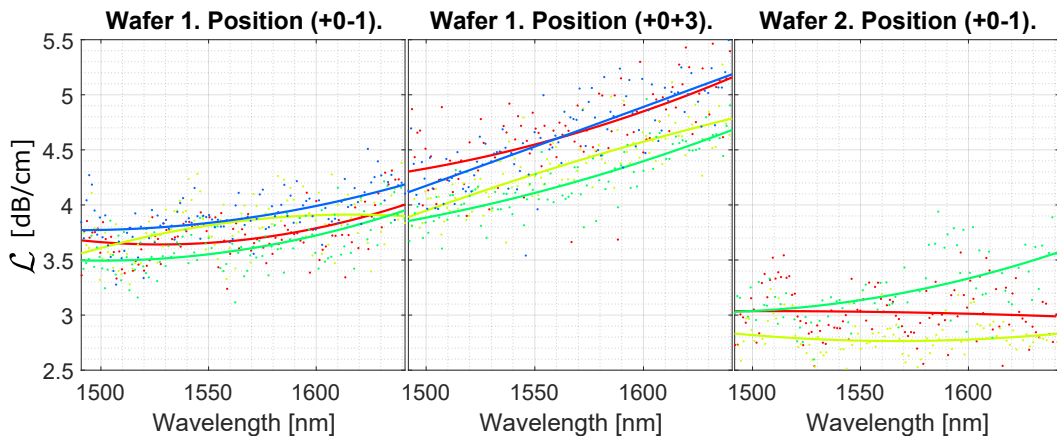


Fig. 8.18: Propagation loss coefficient as a function of wavelength on three different chips (three panels). On the same panel, each color shows measurements taken on different resonators with nominally identical parameters. Each point comes from the fit of two resonances, while solid lines are quadratic fits of the scatter points.

8.4.3 The effect of doping on microresonators

The results discussed so far are measured on chips realized without doping. Now, results on resonators with lateral doping are presented.

Four kinds of resonators are analyzed in detail. The first is a reference resonator, where no doping ions are implanted on the sides of the resonator waveguide. The other structures are characterized by three values of the distance d between the doped region and the waveguide borders (200 nm, 500 nm and 800 nm). For each structure, the transmission spectrum is measured without applying any bias.

The left panel of Fig. 8.19 reports as a function of d the loss coefficient \mathcal{L} , evaluated from the fit of the resonances. The plot reports also the value measured on the reference spectrum, shown in red and labeled by "R". The error-bars result from measurements repeated on four nominally identical resonators. Similarly, on the right panel of Fig. 8.19 the transmission coefficient of the waveguide-resonator coupler is shown as a function of d . The results of Fig. 8.19 are evaluated at the wavelength of 1550 nm. These results show that t does not vary with d , while \mathcal{L} strongly increases for small d . This confirms that doped regions increase losses. At the same time, as expected, doping does not affect the coupling between the bus waveguide and the resonator.

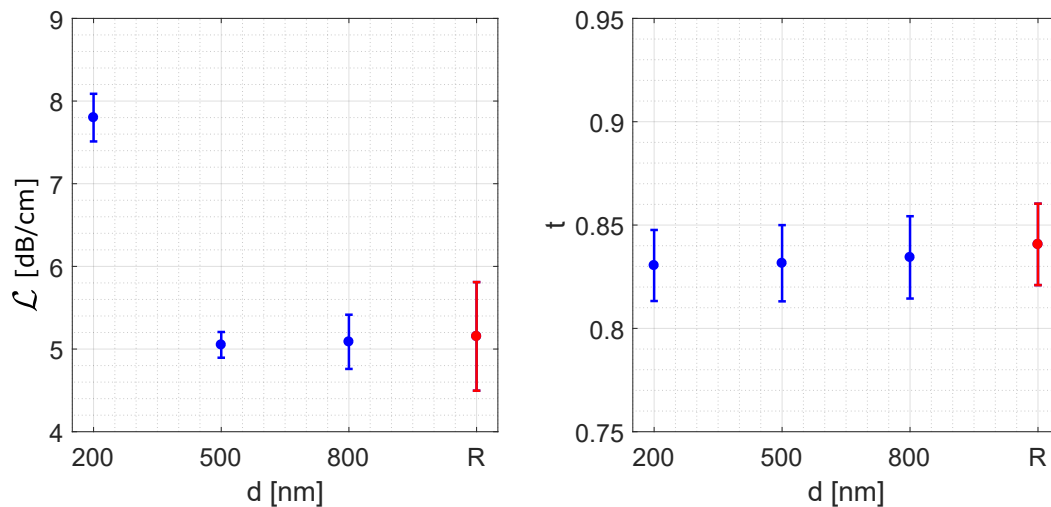


Fig. 8.19: Propagation loss coefficient (left) and transmission coefficient of the waveguide-resonator coupler (right) as a function of d . The error-bars result from measurement repeated on four nominally identical resonators, and are evaluated at the wavelength of 1550 nm. The reference resonator is shown in red and it is indicated by the label "R": here no doping is implanted.

8.4.4 Modeling free-carrier absorption

The results presented so far demonstrate that lateral junctions increase the waveguide propagation losses. This can be due to two effects, namely the carrier-induced

losses and the defects introduced by ion implantation. To clarify this point, FEM simulations are performed in order to quantify the carrier-induced losses. The result of the simulation, compared to the experimental value, can provide an estimation of the losses introduced by damages caused by ion implantation.

The simulation is performed using the Semiconductor Module of the COMSOL Multiphysics® software [56]. The simulation uses a $1 \times 10^{18} \text{ cm}^{-3}$ doping concentration both in the n-side and in the p-side of the junction, while it is $1 \times 10^{15} \text{ cm}^{-3}$ p-type doping in the waveguide. The results of Fig. 8.20 report the electron and hole density distribution inside the waveguide for $d = 200 \text{ nm}$, 500 nm and 800 nm .

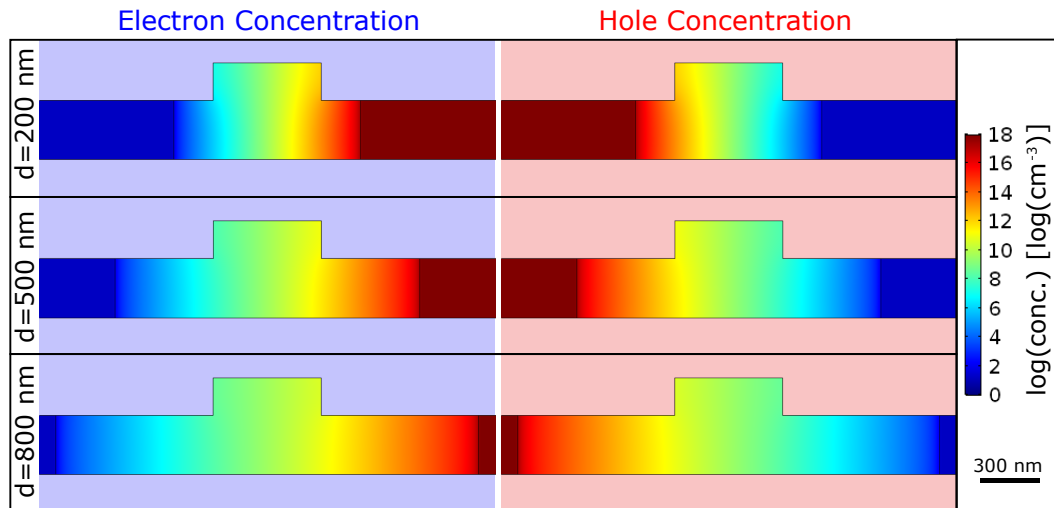


Fig. 8.20: Logarithm of the electron and hole density distribution within the considered structure, referred to $d = 200 \text{ nm}$, 500 nm and 800 nm .

Once that the carrier distribution map is known, the distribution of the carrier-induced absorption coefficient can be evaluated according to Eq. (8.6). The absorption coefficient map can be used then in a mode analysis FEM simulation, to evaluate the absorption coefficient of the optical mode propagation inside the waveguide. The resulting absorption coefficient is reported in Fig. 8.21 as a function of the parameter d . The propagation loss coefficient decreases as d increases, saturating at 0 dB/cm for large values of d . This value cannot be directly compared to the experimental value reported in Fig. 8.19, because in the experiment the absorption coefficient saturates to a nonzero value, determined by surface scattering of the waveguide. To this purpose, comparing the simulation with the experiment requires a normalization of the experimental value. For this reason, the values shown in Fig. 8.19 have been normalized with respect to the value measured on the reference device "R", and are superimposed to the simulated value in Fig. 8.21. The experiment and the simulation show a good agreement, demonstrating that the main source of losses introduced by the presence of the junctions is the free-carrier absorption. The losses introduced by defects caused by ion implantation are negligible.

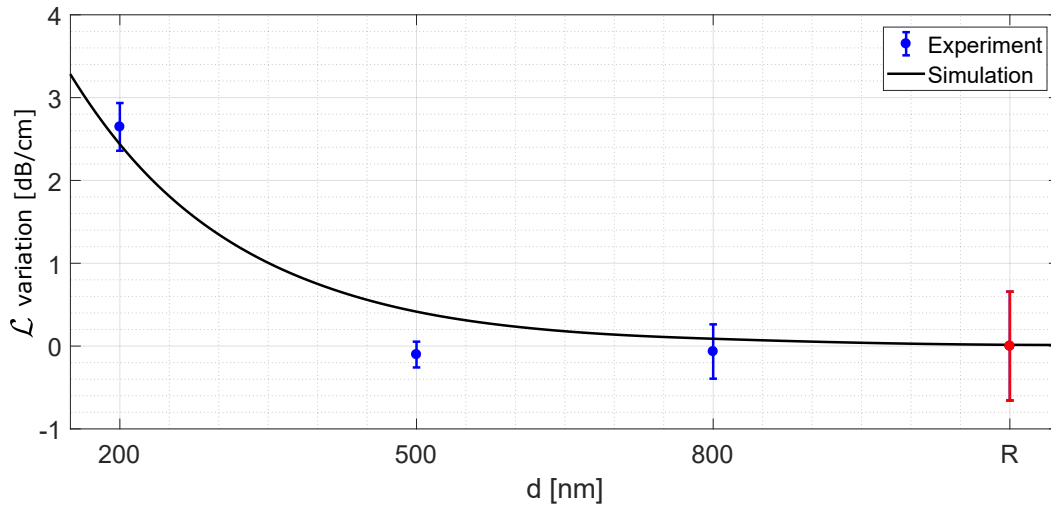


Fig. 8.21: Absorption coefficient variation introduced by the presence of the lateral p-n junction, reported as a function of d . The solid line is calculated from a FEM simulation. The experimental data are the same of Fig. 8.19, normalized over the value measured on the reference structure "R".

8.5 Electrical characterization of waveguides

Once that the structures have been passively analyzed, they need to be actively polarized in order to observe the effect on refractive index. Before that, they need to be electrically characterized to confirm that they work properly also from an electrical point of view. To this aim, tungsten tips are used to contact the aluminum electrodes that contact the junctions. Using a DC voltage generator, the junctions are properly biased. Using an amperometer, the current flowing in the circuit is monitored. Therefore, I-V curves of the structure under analysis are measured.

Figure 8.22 shows the typical I-V curve measured on the three analyzed structures, corresponding to the different values of d . When forward biased, the junction shows the typical exponential behavior. When reversely biased, a small current slightly above $0.1 \mu\text{A}$ flows in the diode. This holds until the breakdown, where a large current starts flowing. The breakdown voltage V_b changes depending on the value of d : it is about 24 V for $d = 200 \text{ nm}$, 40 V for $d = 500 \text{ nm}$ and 53 V for $d = 800 \text{ nm}$. The fact that V_b changes with d is not surprising. In fact, for the same applied voltage, the electric field inside the junction is larger if d is smaller. Therefore, the breakdown field of silicon is reached for smaller values of the applied voltage, and the value of V_b is smaller.

To confirm the experimental results, the polarized junction is simulated using the same FEM simulation described in Sec. 8.4.4. Figure 8.23 shows the distribution inside the structure of the electron and hole density, as well as the x component of the electric field, referred to different values of the applied reverse bias voltage. The simulations refer to the case $d = 200 \text{ nm}$. The field distribution at $V = 0 \text{ V}$ corresponds to the zero-bias field of the junction. When the bias increases, the

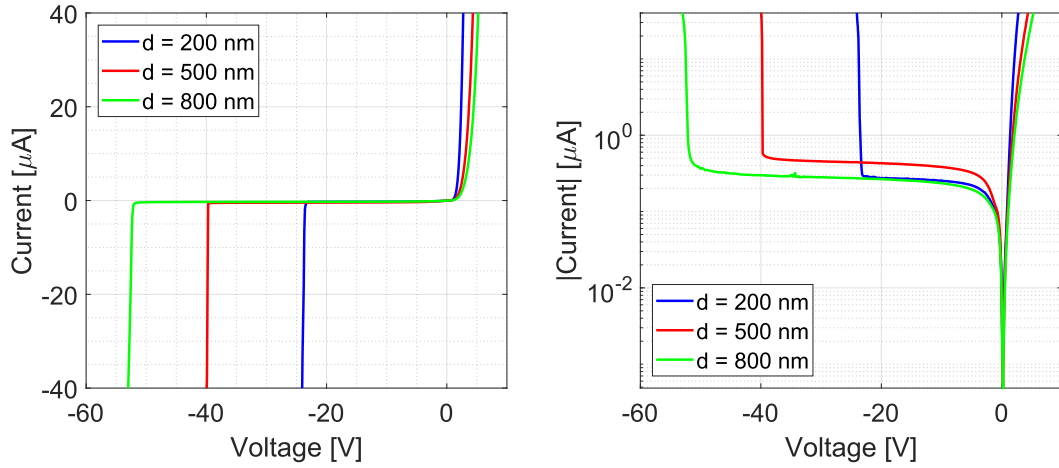


Fig. 8.22: On the left: I-V curves of the different structures analyzed in this work. On the right: the same quantities are reported by taking the absolute value of the current and by reporting it in log scale. This emphasizes the value of the leakage current in the diode when it is reversely polarized.

Tab. 8.1: Experimental and simulated values of the breakdown voltage V_b for the different values of d .

d nm	Experimental V_b [V]	Simulated V_b [V]
200	24 ± 2	24
500	40 ± 3	37
800	53 ± 4	47

junction is depleted from the carriers and the electric field inside the waveguide increases accordingly.

Figure 8.24 shows the electric field inside the waveguide referred to a reverse bias voltage of 20 V and calculated for the different values of d . As expected, for a given applied bias the electric field lowers as d increases.

The simulation described here is used to estimate the breakdown voltage V_b . To this purpose, the simulation is performed as a function of V and for the different d . For each situation, the maximum value of the electric field inside the waveguide E_{\max} is evaluated. E_{\max} is reported in Fig. 8.25 as a function of the applied reverse bias voltage for the different d . The breakdown field V_b can be estimated as the value of V providing E_{\max} larger than the breakdown field of silicon ($40 \text{ V}/\mu\text{m}$) [166]. The simulated results, compared with the experiment, are shown in Tab. 8.1. The agreement with the experiment ensures that the junction is properly modeled.

8.6 Electro-optic measurements

The final aim of this chapter is quantifying the effect of the applied voltage on the material refractive index, demonstrating that this determines a shift of the resonance

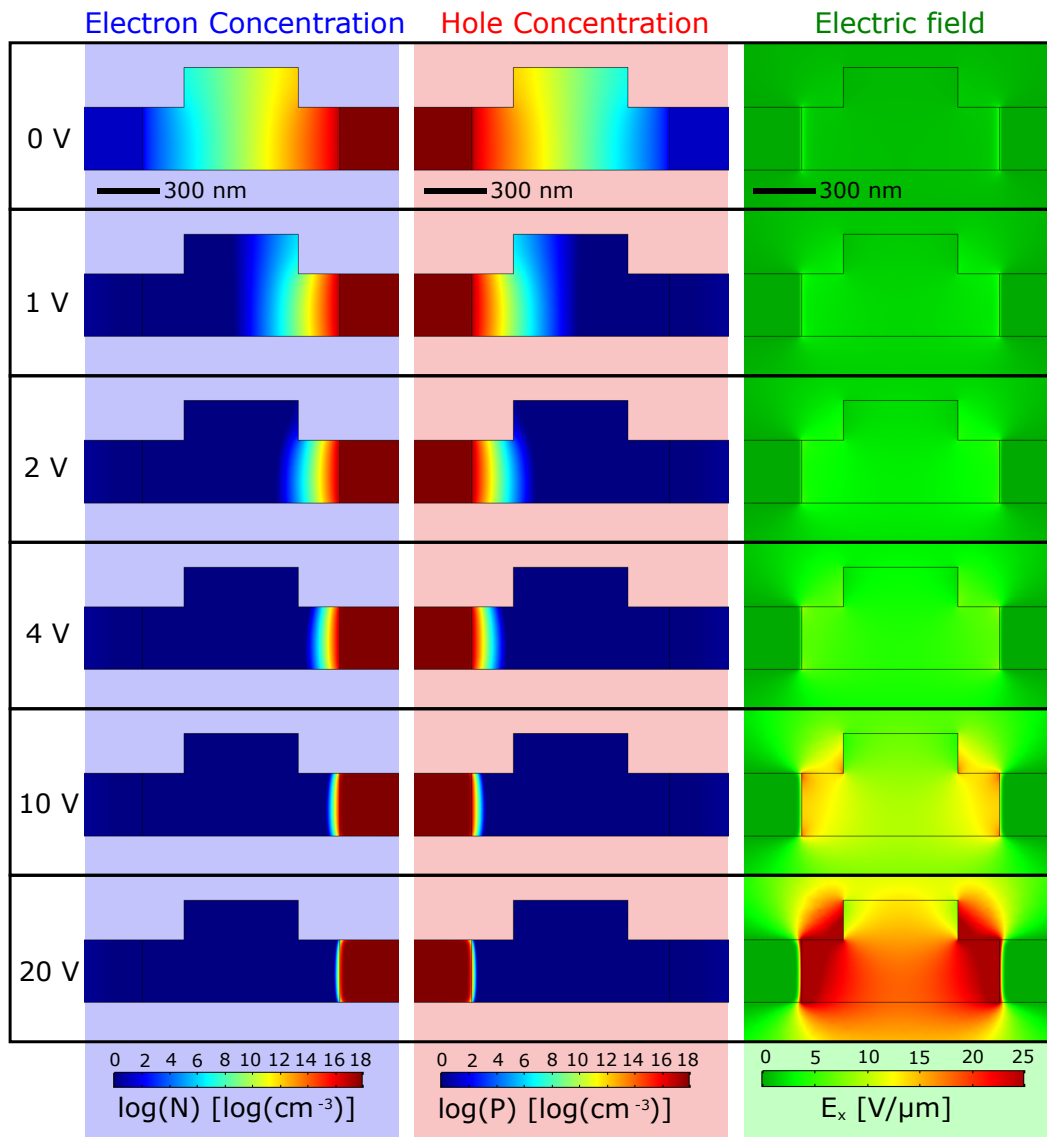


Fig. 8.23: Logarithm of the electron and hole density, as well as the electric field distribution inside the structure for different values of the applied reverse bias voltage. The simulation refers to the case $d = 200$ nm.

wavelength. In Sec. 8.6.1, this shift is first quantified by means of simulations. Then, in Sec. 8.6.2, the simulated results are compared with the experimental values.

8.6.1 Modeling the electro-optic strength

To quantify the strength of the electro-optic effect, simulations performed using the Semiconductor Module of COMSOL Multiphysics[®] are used.

Once that the carrier distribution is known, the plasma-dispersion-induced variation of the material refractive index is estimated according to Eq. (8.1). Once that the new material refractive index is known, the variation of the effective index of the mode is quantified using a mode analysis simulation. In Fig. 8.26 the effective index

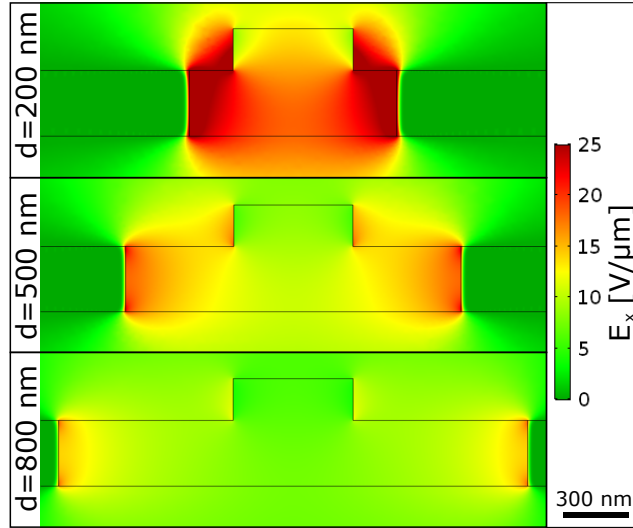


Fig. 8.24: Electric field inside the waveguide referred to a reverse bias voltage of 20 V and calculated for different values of d .

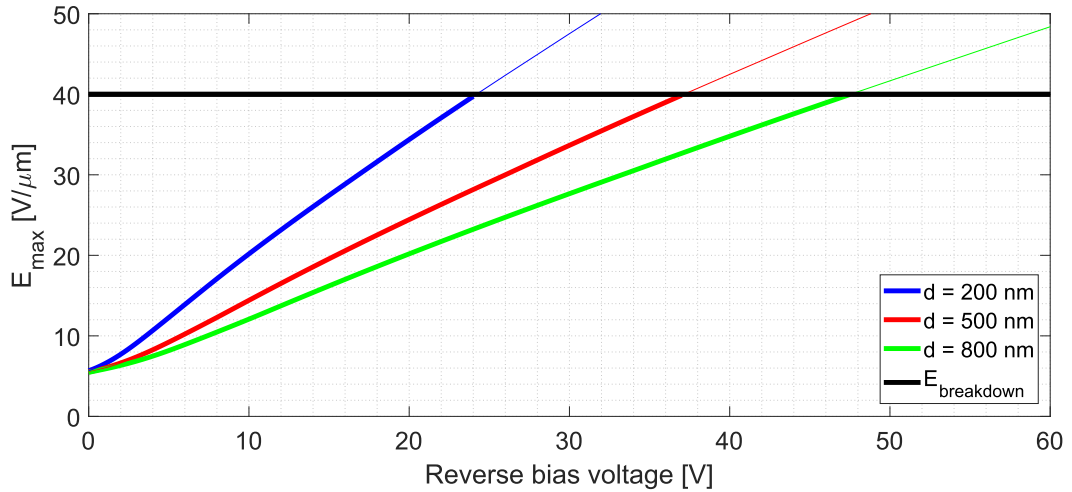


Fig. 8.25: Maximum value of the electric field inside the waveguide as a function of the applied reverse bias voltage for the different values of d . The black line reports the breakdown field of silicon, which is about $40 \text{ V}/\mu\text{m}$ [166].

variation induced by plasma dispersion is reported in blue as a function of the reverse bias voltage for $d = 200 \text{ nm}$, $d = 500 \text{ nm}$ and $d = 800 \text{ nm}$. On the right-hand axes, the corresponding shift of the resonance wavelength is shown, calculated according to Eq. (8.5). Doing so, the experimental group index has been used. Moreover, for the resonator with $L_s = 0 \mu\text{m}$, the fraction of the resonator perimeter between p-n junctions is $\rho = 0.9$. Figure 8.26 shows that plasma-dispersion effect is stronger for small d . In fact, for small d the optical mode feels more the variation of the carrier distribution, which mostly occurs close to the interface between the intrinsic and the doped region. For larger d , the carrier variation felt by the optical mode is lower, and so the shift of the resonance wavelength is smaller.

To estimate the strength of the DC Kerr effect, the same simulation is considered.

Once that the electric field distribution inside the waveguide is known, the corresponding refractive index variation due to the DC Kerr effect is calculated using Eq. (8.4). The new refractive index distribution is then used in a mode analysis simulation to quantify the variation of the effective refractive index of the optical mode. This quantity, as well as the corresponding resonance wavelength shift, is shown in red in Fig. 8.26 for the different values of d . In all the situations, DC Kerr effect is much stronger than plasma-dispersion.

The overall effective index variation is shown in black, considering both the plasma-dispersion and the DC Kerr effect.

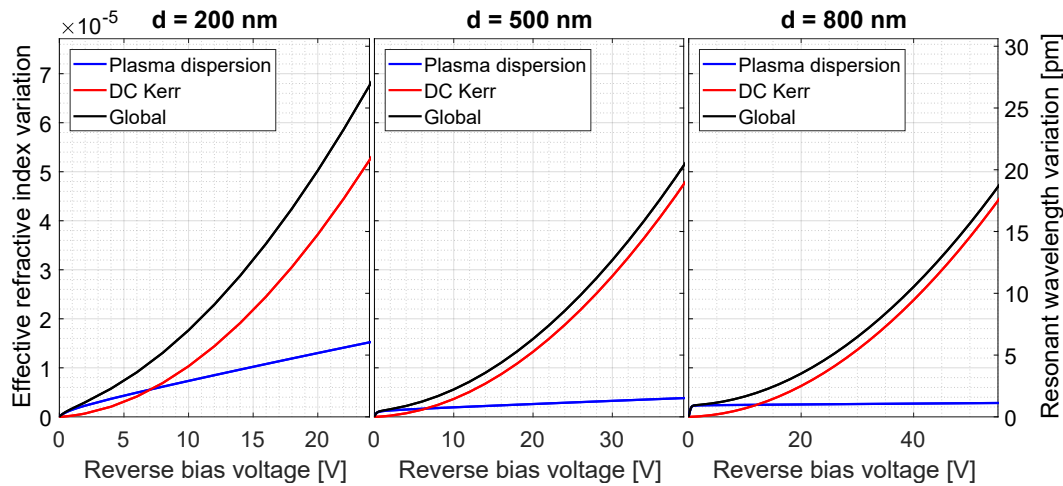


Fig. 8.26: On the left axes: effective refractive index variation as a function of the applied reverse bias voltage for $d = 200$ nm, 500 nm and 800 nm. The blue curve considers only the plasma dispersion, the red curve only the DC Kerr effect, while the black line considers both the effects. On the right axes, the corresponding shift of the resonant wavelength is reported.

The global result for all the values of d is shown in Fig. 8.27. Figure 8.27 shows that the largest electro-optic effect is expected for the smallest values of d .

8.6.2 Measurement of the electro-optic effect

The electro-optic effect is experimentally quantified by measuring the transmission spectra of resonators as a function of the reverse bias voltage. Figure 8.28 shows the transmission spectrum of a resonator considering three different reverse bias voltages, namely 0 V, 10 V and 20 V. By biasing the junction, the peak is shifted.

To quantify the shift, each resonance is fitted by a Lorentian function. The resonant wavelength shift is then calculated by taking the difference between the measured resonant wavelength and the one taken at zero bias. This shift is reported in Fig. 8.29 as a function of the reverse bias voltage for the different d . The errorbars are obtained from repeated measurements. The experimental results are compared with the theoretical expectations of Fig. 8.27. The experiment agrees with simulations, except for $d = 200$ nm. In this case, the electro-optic shift is larger than the simulated

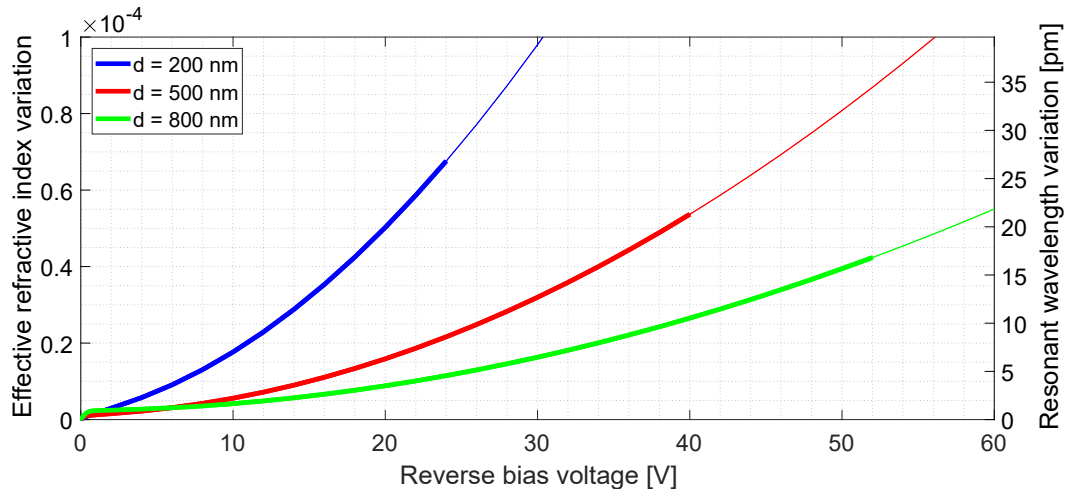


Fig. 8.27: Refractive index variation (left hand axis) and the corresponding resonant wavelength shift (right hand axis) for various d . The thicker lines emphasize the range of bias voltages that can be achieved before causing the junction breakdown, evaluated from the experiments described previously.

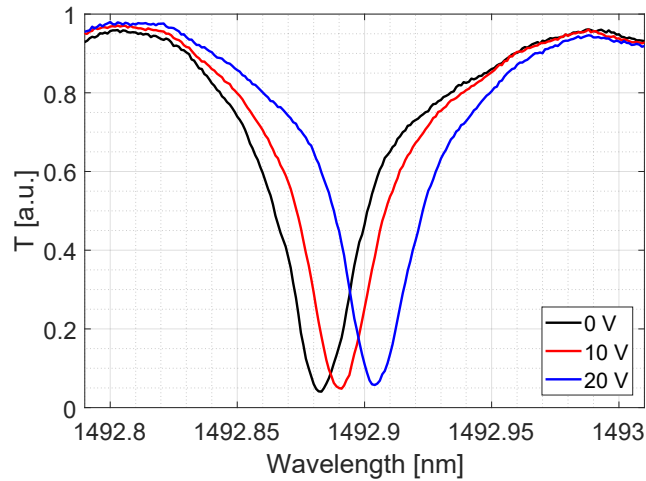


Fig. 8.28: Normalized transmission spectrum of a resonator with $d = 200$ nm measured at three different reverse bias voltages.

one. This can be due to a difference between the actual d and the designed one, e.g. because of the diffusion of ions after implantation. The actual value of d can be quantified by determining which value provides the best agreement with the experiment. In this case, the best agreement is obtained for $d = 136$ nm, which is reported as a dashed line in Fig. 8.27(a). This demonstrates that, in the realized devices, the value of d is about 64 nm smaller than the designed one. This fact is not visible in the measurements on devices with $d = 500$ nm and $d = 800$ nm. However, in these structures a variation of 64 nm determines a much smaller relative variation, which causes electro-optic variations below the experimental error.

To further confirm the model proposed here, Fig. 8.30 reports the variation of the loss coefficient as a function of the applied voltage. The experimental values are evaluated using the fitting procedure described previously. On the other hand, the

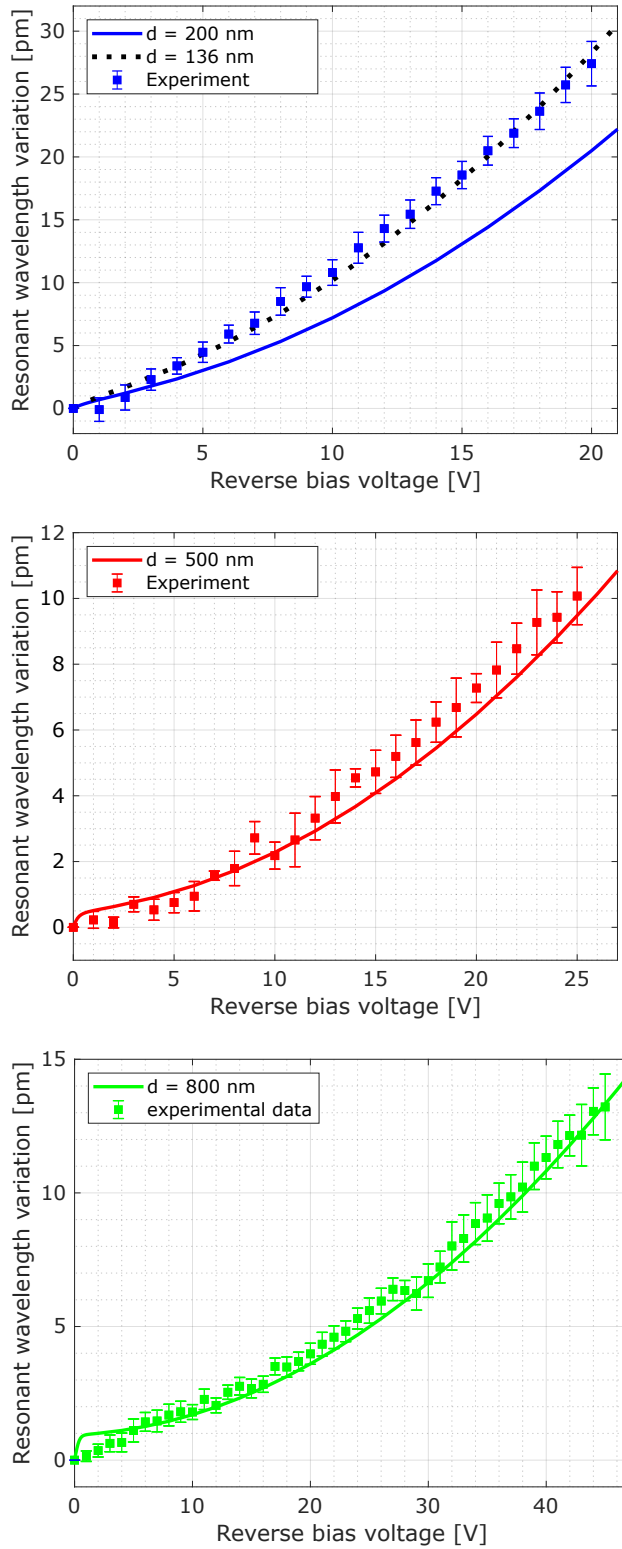


Fig. 8.29: Resonant wavelength shift as a function of the reverse bias voltage for the different d . Experimental results are compared with simulations.

simulated result are calculated using mode analysis simulations, knowing the carrier distribution inside the waveguide and, consequently, the carrier-induced absorption

given by Eq. (8.6). All the values reported in Fig. 8.30 are normalized to the result measured at zero bias. In the cases $d = 500$ nm and $d = 800$ nm, any variation of the absorption coefficient is below the experimental error. This agrees with the little variations predicted by simulations. For $d = 200$ nm, the variation of the absorption coefficient is larger than the one predicted by simulation. However, agreement can be found if the simulation is performed considering the value $d = 136$ nm that was evaluated from the analysis of the resonance wavelength shift. This fact confirms that the experiment is well reproduced by the simulation.

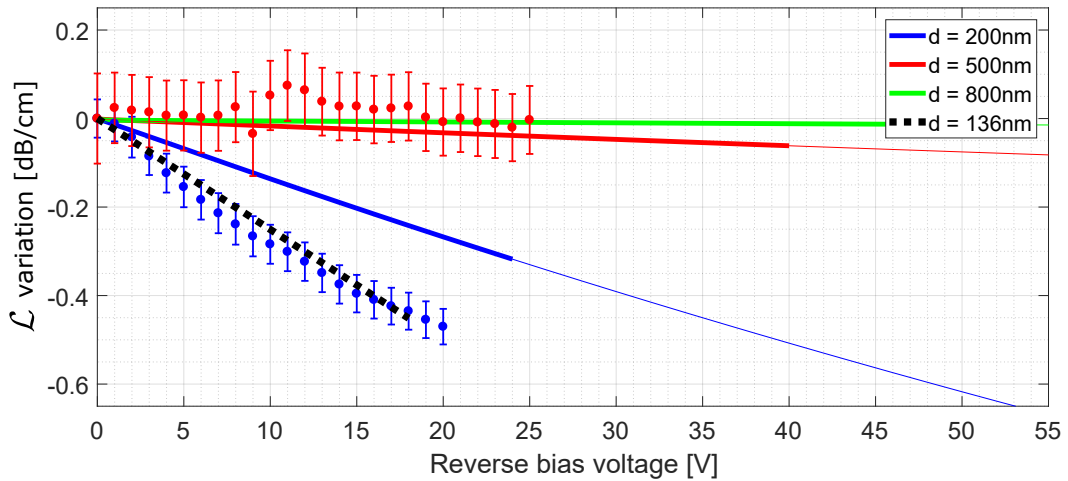


Fig. 8.30: Experimental and simulated loss coefficient variation as a function of the applied voltage. The errorbars on the experimental results come from repeated measurements. All the values are normalized to the result measured at zero bias. For clarity, the experimental result for $d = 800$ nm is not reported (it is very similar to the case $d = 500$ nm).

8.7 Perspectives

The results presented in this chapter show that FEM simulations are able to reproduce the experimental data. In rib waveguides with lateral p-n junctions, the model quantifies the refractive index variation due to both plasma-dispersion and DC Kerr effect, as well as the carrier-induced absorption coefficient variation. The model described here can be then used in the following chapters to quantify the strength of the field-induced nonlinearities in similar structures.

One of the most important outcomes of this chapter is also the confirmation that, as demonstrated in [125], rib waveguides with lateral doping induce electro-optic effects in silicon by means of both plasma-dispersion and DC Kerr effect. The role of plasma dispersion is, however, of less importance when moving to fast electro-optic modulation, since its modulation speed is limited by the carrier mobility. On the other hand, DC Kerr effect is of great interest due to the possibility to achieve fast electro-optic modulation. For this purpose, it is interesting to compare the electro-

optic capability of this platform with others. These are mainly based on second order nonlinearities, which provide a linear electro-optic modulation. So, it is interesting to estimate the strength of the equivalent second order nonlinear coefficient $\chi_{\text{eq}}^{(2)}$ that would provide an electro-optic modulation of the same strength. To do so, one should recall that the effective index variation Δn_{eff} caused by an electric field E in a waveguide characterized by a second-order nonlinear coefficient $\chi^{(2)}$ is [120]:

$$\Delta n_{\text{eff}} = \frac{\chi^{(2)} E n_g}{2n_0^2}, \quad (8.15)$$

being n_g the group index and n_0 the material refractive index. Consider for example Fig. 8.26, where it is shown that an effective index variation as large as 5×10^{-5} can be introduced for a reverse bias of 20 V in a waveguide with $d = 200$ nm. In this situation, Fig. 8.24 shows that an average electric field of 20 V/ μm is present in the waveguide. Considering that $n_g \sim 3.8$ and $n_0 \sim 3.47$, from Eq. (8.15) the equivalent second order nonlinear coefficient $\chi_{\text{eq}}^{(2)}$ is about 16 pm/V. It has to be recalled that the measured effect is a third order nonlinear effect, and so this estimation has to be only considered as a method to compare the strength of the measured effect with that of other platforms. The results show that the strength of the measured effect is comparable to that of materials with an intrinsic $\chi^{(2)}$, such as lithium niobate, whose $\chi^{(2)}$ is 39 pm/V (Tab. 1.2). This result is even much stronger than the most recent measurements of strain-induced Pockels effect in silicon, which quantified $\chi^{(2)}$ at about 1.8 pm/V [110]. Even larger effects could be obtained by efficiently engineering the waveguide cross section, by taking for example smaller values of d or by reducing the waveguide width and its height. For example, in [125] the waveguide height is much smaller, and the strength of the measured effect is larger than the one reported in this work. Therefore, the platform presented in this chapter can provide interesting perspectives in terms of the electro-optic capability.

SHG and SPDC in silicon waveguides with lateral doping

9.1	Description of nonlinearities in quasi-phase-matched waveguides	148
9.1.1	Second Harmonic Generation	148
9.1.2	Spontaneous Parametric Down Conversion	149
9.1.3	The shape of the poling function	150
9.2	Engineering poled waveguides	152
9.2.1	Setting the poling period	154
9.2.2	Estimating the generation efficiency	155
9.2.3	Coherence length of the process	156
9.2.4	Realized waveguide geometries	156
9.2.5	Tolerance to fabrication uncertainties	158
9.2.6	Geometry of the junction	160
9.3	Modeling the electric field in poled waveguides	162
9.3.1	Description of the FEM model	163
9.3.2	Field distribution and nonlinear strength	163
9.3.3	The poling function	168
9.3.4	The maximum achievable field	169
9.3.5	The maximum nonlinearity	171
9.4	Estimation of the SHG and SPDC efficiency	173

The results reported in the previous chapter show that p-n junctions can be used to generate high electric fields in waveguides. Moreover, these fields are well described by the simulation procedure based on FEM analysis. Therefore, this method can be used for waveguides where lateral junctions introduce field-induced second order nonlinearities. Like in [125], the DC field is applied in a periodic way. In this way the second order nonlinear coefficient varies periodically and introduces **Quasi-Phase-Matching** (QPM). The aim of this chapter is to model the system, and to engineer the most efficient waveguides enabling this process. The system is optimized to perform both **SHG** as well as the opposite process, namely **SPDC**. The theoretical framework of this study is introduced in Sec. 9.1. In Sec. 9.2, the waveguide engineering is introduced. Section 9.3 models the DC field in the system, Finally, in Sec. 9.4, the field-induced second order nonlinear strength is estimated.

9.1 Description of nonlinearities in quasi-phase-matched waveguides

This section theoretically describes SHG and SPDC in periodically poled waveguides. To avoid confusion, in this chapter the larger wavelength is named fundamental (and is labeled by f), while the shorter wavelength is named second-harmonic (labeled by sh). Therefore, SHG involves the conversion between the fundamental pump wave and the second-harmonic wave, while SPDC determines a conversion between the second-harmonic pump wave and the fundamental wave.

9.1.1 Second Harmonic Generation

SHG in presence of periodic poling. The propagation of optical pulses in waveguides in presence of SHG is described by Eq. (4.26). However, that formulation accounts for a constant $\chi^{(2)}$ along the propagation direction z . In the case of periodic poling, $\chi^{(2)}$ varies along z . Assume now that $\chi^{(2)}$ can be **factorized** as follows:

$$\chi^{(2)}(\mathbf{r}_\perp, z) = \chi^{(2)}(\mathbf{r}_\perp) s(z), \quad (9.1)$$

being $\chi^{(2)}(\mathbf{r}_\perp)$ the second order nonlinear coefficient in the waveguide cross-section plane, while $s(z)$ is named poling function, and expresses the $\chi^{(2)}$ modulation along z . In this case, it is possible to define the coefficient $\tilde{\Gamma}^{(2)}$ as follows:

$$\tilde{\Gamma}^{(2)} = \frac{\sqrt{A_0} \int \mathbf{e}(\mathbf{r}_\perp, \omega_f) \chi^{(2)}(\mathbf{r}_\perp) : \mathbf{e}^*(\mathbf{r}_\perp, \omega_{sh}) \mathbf{e}(\mathbf{r}_\perp, \omega_f) dA}{\left(\int n^2(\mathbf{r}_\perp, \omega_f) |\mathbf{e}(\mathbf{r}_\perp, \omega_f)|^2 dA \right) \left(\int n^2(\mathbf{r}_\perp, \omega_{sh}) |\mathbf{e}(\mathbf{r}_\perp, \omega_{sh})|^2 dA \right)^{1/2}}. \quad (9.2)$$

According to (4.11), one has that $\Gamma^{(2)} = s(z) \tilde{\Gamma}^{(2)}$. Analogously, $\tilde{\gamma}_i^{(2)}$ is defined by:

$$\tilde{\gamma}_i^{(2)} = \omega_i \frac{n_{G,f} \sqrt{n_{G,sh}}}{\sqrt{8A_0 \epsilon_0 c^3}} \tilde{\Gamma}^{(2)}. \quad (9.3)$$

So, according to Eq. (4.10), $\gamma_i^{(2)} = s(z) \tilde{\gamma}_i^{(2)}$. Therefore, Eq. (4.26) becomes:

$$\begin{cases} \frac{du_{sh}}{dz} + \sum_{m \geq 1} \frac{(i)^{m-1} \beta_{sh,m}}{m!} \frac{\partial^m u_{sh}}{\partial t^m} = \\ \quad = i \tilde{\gamma}_{sh}^{(2)} s(z) \frac{P_{0,f}}{\sqrt{P_{0,sh}}} u_f^2 e^{i\Delta\beta z} + 2i \gamma_{sh,f}^{(3)} P_{0,f} |u_f|^2 u_{sh} - \frac{\alpha_{sh}}{2} u_{sh}, \\ \frac{du_f}{dz} + \sum_{m \geq 1} \frac{(i)^{m-1} \beta_{f,m}}{m!} \frac{\partial^m u_f}{\partial t^m} = \\ \quad = 2i \tilde{\gamma}_f^{(2)*} s(z) \sqrt{P_{0,sh}} u_{sh} u_f^* e^{-i\Delta\beta z} + i \gamma_{f,f}^{(3)} P_{0,f} |u_f|^2 u_f - \frac{\alpha_f}{2} u_f. \end{cases} \quad (9.4)$$

Equation (9.4) is analogue to Eq. (4.26), with the difference that the term $s(z)$ here is factorized.

Undepleted pump and continuous wave. Similarly to Sec. 4.1.6, the case of undepleted pump is considered, so that $u_f(z) \sim \text{const.}$ A continuous wave pulse is assumed, where temporal derivatives can be neglected. Moreover, also third-order nonlinearities and losses are negligible. So, Eq. (9.4) becomes:

$$\frac{du_{sh}}{dz} = i\tilde{\gamma}_{sh}^{(2)} s(z) \frac{P_{0,f}}{\sqrt{P_{0,sh}}} u_f^2 e^{i\Delta\beta z}. \quad (9.5)$$

This equation can be analytically solved integrating on all the waveguide length L . In this case, the total SH power can be expressed as:

$$P_{sh} = P_f^2 \left| \tilde{\gamma}_{sh}^{(2)} \right|^2 L^2 S, \quad (9.6)$$

where the coefficient S is defined as:

$$S = \frac{1}{L^2} \left| \int_0^L s(z) e^{i\Delta\beta z} \right|^2. \quad (9.7)$$

This result matches the one reported in [167].

9.1.2 Spontaneous Parametric Down Conversion

Using the same notation used so far, in [167] the power generated by SPDC is calculated in the continuous wave undepleted pump approximation, and is given by:

$$P_{SPDC} = P_p \left| \tilde{\gamma}_{sh}^{(2)} \right|^2 L^2 \frac{\hbar\omega_f}{\tau}, \quad (9.8)$$

being in this case ω_f the generated photons frequency and τ is called the generation bandwidth time. The generation bandwidth time is given by:

$$\tau = \frac{2\pi}{\int_0^{\omega_{sh}/2} d\Omega \left[1 - \left(\frac{2\Omega}{\omega_{sh}} \right)^2 \right] S}, \quad (9.9)$$

where Ω is the positive detuning from the frequency $\omega_{sh}/2$. In the case of QPM, this expression can be further simplified by writing:

$$\tau \simeq \frac{6\pi}{\omega_{sh}} \frac{1}{S} \quad (9.10)$$

So, also in this case the generation efficiency is proportional to the factor $\left| \tilde{\gamma}_{sh}^{(2)} \right|^2 S$.

9.1.3 The shape of the poling function

The solution of the integral S shows interesting features of the generated signal in case of periodically poled structures. In the following, the integral is solved both analytically and numerically, in many different interesting situations.

Perfect phase-matching. When no periodic poling is applied, $s(z) = 1$. So, by solving the integral, $S = \text{sinc}^2(\Delta\beta L/2)$. In this case, Eq. (9.6) recovers the simple result of Eq. (4.28). If $\Delta\beta \sim 0$, one finds the perfect phase-matching condition.

Quasi-phase-matching with square-wave poling function. Consider now the case where $s(z)$ is a periodic function of period Λ . Each period is formed by two domains of length $\Lambda/2$. Passing from one domain to the successive, $s(z)$ changes from $+1$ to -1 , so that its value in the n -th domain can be expressed as $(-1)^n$. If N is the total number of periods, the integral of Eq. (9.7) can be analytically solved, and gives [168]:

$$S = \frac{\Lambda^2}{4L^2} \text{sinc}^2\left(\frac{\Delta\beta\Lambda}{4}\right) \left[\frac{1 - \cos(\Delta\beta\Lambda N)}{1 + \cos(\Delta\beta\Lambda/2)} \right], \quad (9.11)$$

In order to have a non-zero value of this expression, Λ has to be given by:

$$\Lambda = m \frac{2\pi}{\Delta\beta} = 2mL_{coh}, \quad (9.12)$$

where $L_{coh} = \pi/\Delta\beta$ is the coherence length of the non-linear process [1]. In this situation the expression for S becomes:

$$S = \begin{cases} 0 & m \text{ even} \\ \left(\frac{2}{\pi m}\right)^2 & m \text{ odd} \end{cases} \quad (9.13)$$

So, using QPM, an efficient process can be achieved by properly setting the poling period Λ as expressed by Eq. (9.12), and by using an odd m . The most efficient situation is provided by $m = 1$, where $S = (2/\pi)^2$. For larger values of odd m , the coefficient S scales as $(1/m)^2$.

The same fact can be observed by numerically solving Eq. (9.7). Figure 9.1 shows the quantity SL^2 (which is proportional to the generation efficiency) as a function of the waveguide length L . For clarity, L is normalized to the coherence length L_{coh} . Results are reported for the perfect phase-matching situation (black) and for the QPM with different values of m . The dashed lines report the results of the analytic solution reported in Eq. (9.13). Figure 9.1 shows that, to have an efficient process, the sign of $s(z)$ has to change after an odd multiple of the coherence length L_{coh} . The results reported so far are valid if the length l^+ over which $s(z) = +1$ is equal to the length l^- over which $s(z) = -1$. Consider now the situation $l^+ \neq l^-$, but still

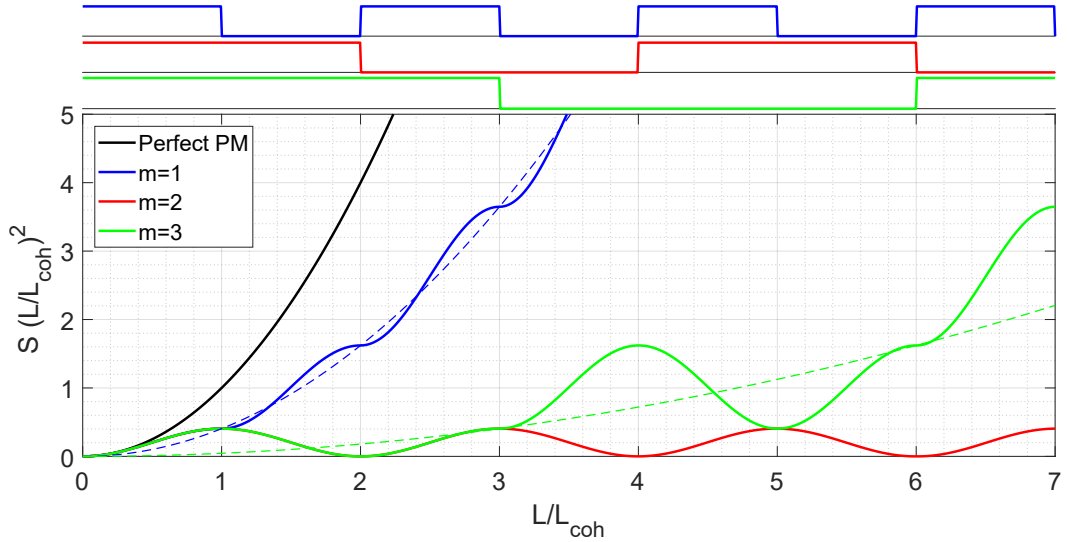


Fig. 9.1: Dependence of the quantity SL^2 (which is proportional to the generation efficiency) on the waveguide length L . L is normalized to the coherence length L_{coh} . The solid lines are evaluated from the numeric solution of Eq. (9.7), while the dashed lines refer to the analytic solution reported in Eq. (9.13). The black line refers to the perfect phase-matching solution, while the colored lines refer to the QPM case with different values of m . On the top of the figure, the behavior of $s(z)$ is shown for the different cases of QPM.

holds the condition $l^+ + l^- = \Lambda$. In this case, it is usual to define the duty cycle $\mathcal{D} = l^+/\Lambda$ [169, 170]. This quantity defines the fraction of the poling period Λ over which $s(z) = +1$. Figure 9.2 reports the same quantities of Fig. 9.1, but considering $\mathcal{D} = 0.25$. In this case the generation efficiency is non-zero even for $m = 2$, in contrast with the result of Fig. 9.1 referred to $\mathcal{D} = 0.5$. This means that, with the proper \mathcal{D} , the generation efficiency can be non-zero also for even values of m .

To clarify the role of the duty cycle, Figure 9.3 reports S as a function of \mathcal{D} . Figure 9.3 shows that, for odd m , the most efficient duty cycle is $\mathcal{D} = 0.5$. On the other hand, if m is even, efficiency is zero for $\mathcal{D} = 0.5$. However, considering $m = 2$, efficient generation is obtained for $\mathcal{D} = 0.25$ (or, equivalently, $\mathcal{D} = 0.75$).

Quasi-phase-matching with sinusoidal poling function. Figure 9.4 reports the quantity SL^2 as a function of L for a sinusoidal $s(z)$ of period $\Lambda = 2mL_{coh}$. This results shows that, in this case, the generation is nonzero only for $m = 1$.

Quasi-phase-matching with arbitrary periodic poling function. The last case is true only if $s(z)$ is truly sinusoidal. If $s(z)$ is distorted but remains periodic, the process can be efficient even for $m > 1$. In this framework, Fig. 9.5 shows the case of a sinusoidal $s(z)$ with $m = 1$ and $m = 2$, as well as for an arbitrary periodic function with $m = 2$. This last function provides a non-zero efficiency even if $m = 2$.

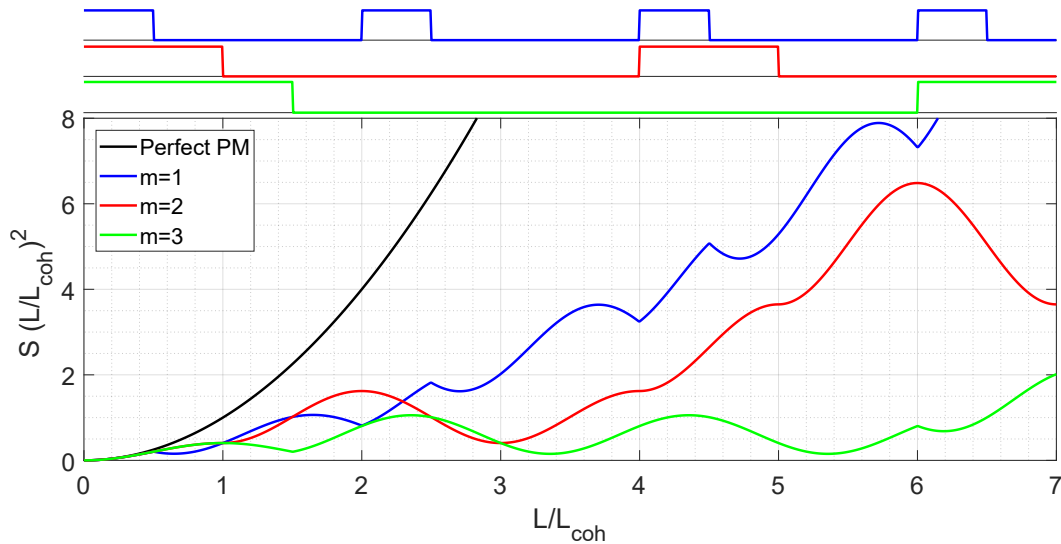


Fig. 9.2: Dependence of the quantity SL^2 (which is proportional to the generation efficiency) on the waveguide length L . The black line refers to the perfect phase-matching solution, while the colored lines refer to the QPM case with different values of m and for a duty cycle $\mathcal{D} = 0.25$. On the top of the figure, the behavior of $s(z)$ is shown for the different values of m .

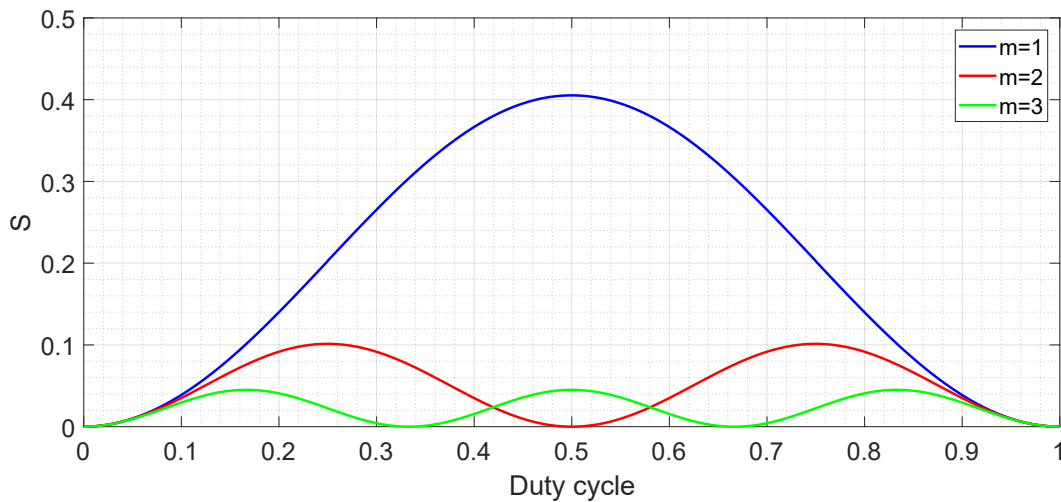


Fig. 9.3: Dependence of the coefficient S on the duty cycle \mathcal{D} for different values of m .

9.2 Engineering poled waveguides

The waveguides have the same cross-section of the ones sketched in Fig. 8.1. The waveguide width w is determined to maximize the generation efficiency. The SHG experiment aims at pumping at wavelengths λ_f above 2250 nm, generating photons at halved wavelength λ_{sh} . In this way, the SH wave is still guided in silicon, while the pump wave does not suffer TPA effect. For the SPDC process, the pump and the generated wavelengths are swapped. Different waveguide widths and poling periods are proposed, in order to phase-match different wavelengths.

Being the junction placed at the sides of the waveguide, the conversion between

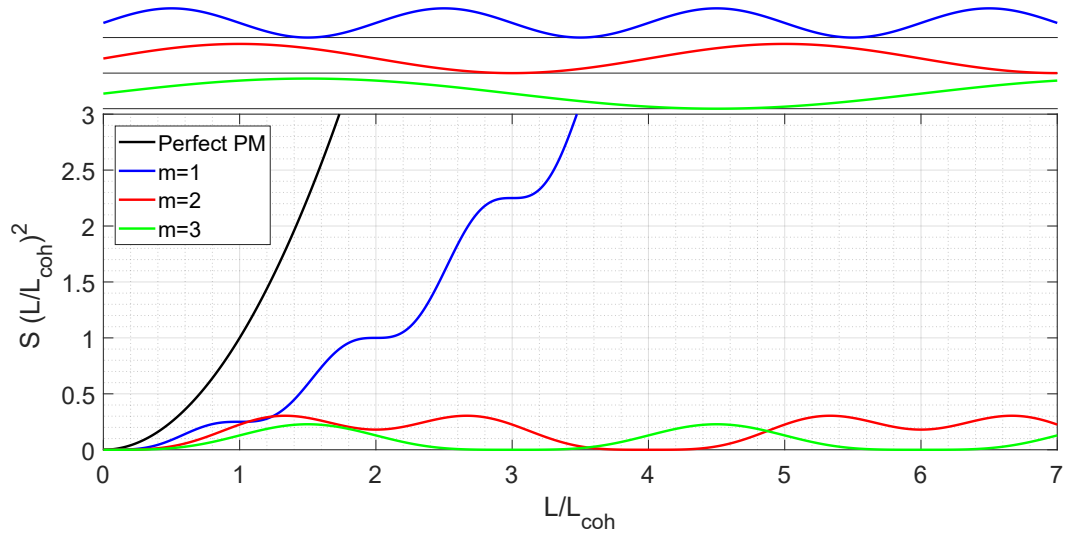


Fig. 9.4: Dependence of the quantity SL^2 on L for a sinusoidal $s(z)$ with different values of m . The behavior of $s(z)$ is shown on the top.

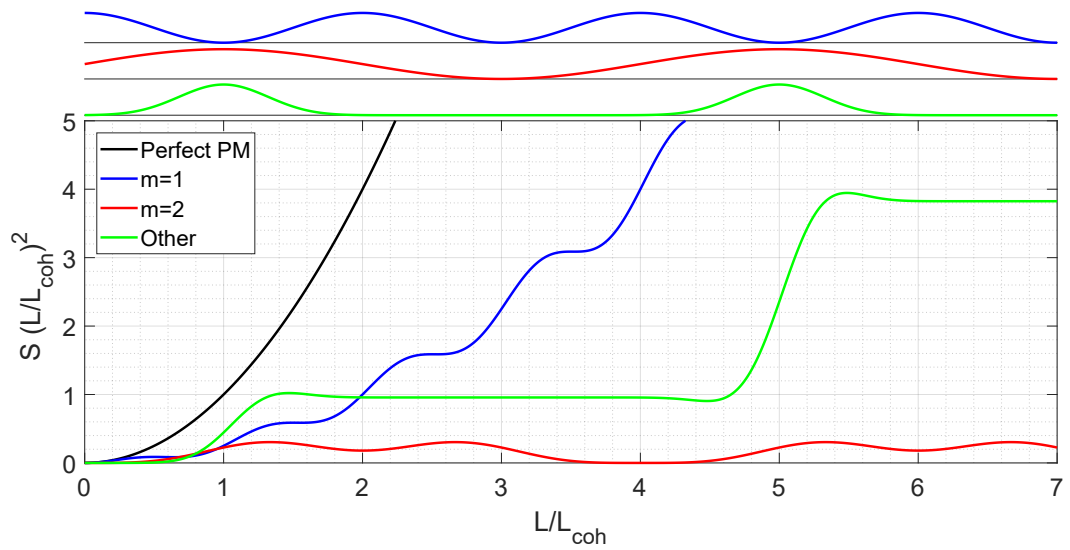


Fig. 9.5: Dependence of the quantity SL^2 on L for a sinusoidal $s(z)$ with different values of $m = 1$ and $m = 2$, as well as for an arbitrary periodic function with $m = 2$.

TE polarized modes is enabled. Since the phase mismatch is corrected here by the use of periodically poling, there is no reason to use high order modes, and thus the fundamental TE modes are used both for the pump and the generated waves.

9.2.1 Setting the poling period

Both the SHG and the SPDC processes are performed between the fundamental TE modes. The poling period Λ must be fixed in order to satisfy Eq. (9.12). In this case, one can redefine the phase mismatch coefficient $\Delta\beta$ as:

$$\Delta\beta = 2\beta_{\omega_f} - \beta_{\omega_{sh}} + \frac{2\pi m}{\Lambda}. \quad (9.14)$$

Considering that $\lambda_f = 2\lambda_{sh}$, the phase-matching condition $\Delta\beta = 0$ is satisfied if the following condition holds:

$$\Lambda = m \frac{\lambda_{sh}}{n_{\text{eff},sh} - n_{\text{eff},f}}. \quad (9.15)$$

The evaluation of the required poling period is performed using a 2D mode solver. The poling period dependence on w is shown in Fig. 9.6, considering $m = 1$. The calculations are done for a conversion process between $\lambda_f = 2300$ nm and $\lambda_{sh} = 1150$ nm. Figure 9.6 shows that larger the waveguide and larger is the required Λ . This can be understood looking at Eq. (9.15) and considering that the larger the waveguide and the closer are the effective refractive indexes of the two modes. The choice of w is based on the estimation of the generation efficiency, which is shown in the following. Once that w is chosen, the proper Λ is evaluated as it is described in this section.

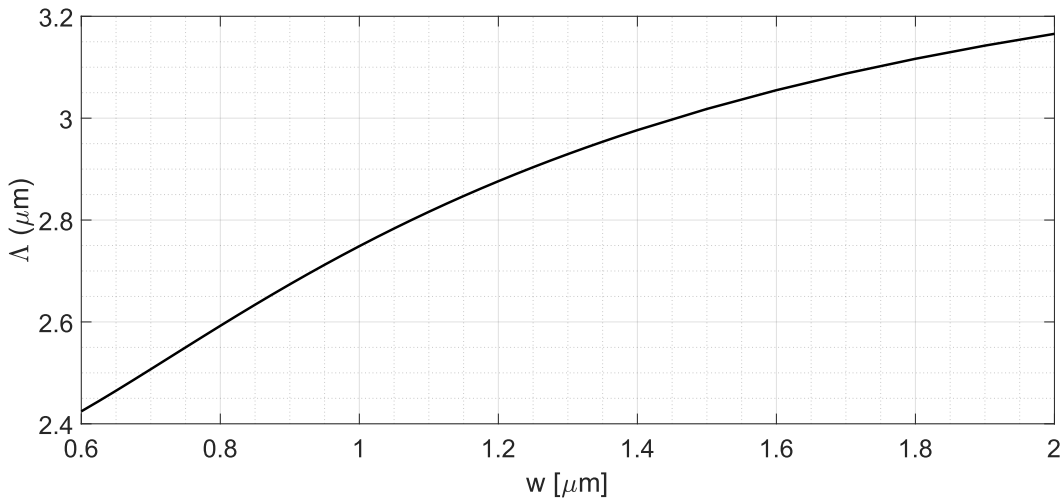


Fig. 9.6: Dependence of the poling period on the waveguide width. The simulation is performed for a conversion process between $\lambda_f = 2300$ nm and $\lambda_{sh} = 1150$ nm.

9.2.2 Estimating the generation efficiency

The waveguide width w is determined by evaluating a parameter that is proportional to the generation efficiency for the two processes of interest. Equations (9.6) and (9.8) show that, for both SHG and SPDC processes, the generated power is proportional to $|\tilde{\gamma}_{sh}^{(2)}|^2$. This coefficient clearly depends on the $\chi^{(2)}$ distribution inside the waveguide. In this study, $\chi^{(2)}$ is introduced by an external field applied with lateral junctions. So, the $\chi^{(2)}$ inside the waveguide depends on many parameters, such as the distance of the doped region from the waveguide, but also on w . However, for simplicity, the dependence of $|\tilde{\gamma}_{sh}^{(2)}|^2$ on w is evaluated here assuming to introduce a spatially constant $\chi^{(2)}$ with a strength independent on w . In this way, $\chi^{(2)}$ can be factorized out from the coefficient $|\tilde{\gamma}_{sh}^{(2)}|^2$.

Figure 9.7 reports the dependence of $|\tilde{\gamma}_{sh}^{(2)}|^2$ on w . This quantity is normalized with respect to its maximum value. The simulation refers to a conversion process between $\lambda_f = 2300$ nm and $\lambda_{sh} = 1150$ nm. The coefficient $|\tilde{\gamma}_{sh}^{(2)}|^2$ increases with w for small w , while it decreases for large w . The reason of this comes from the definition of $\tilde{\gamma}_{sh}^{(2)}$ in Eq. (9.3), which shows that it depends on the group indexes of the modes (that grow with w) and on $\tilde{\Gamma}^{(2)}$ (that decreases with w because the modes are less localized). Therefore, one can find an optimum value of w to maximize $|\tilde{\gamma}_{sh}^{(2)}|^2$.

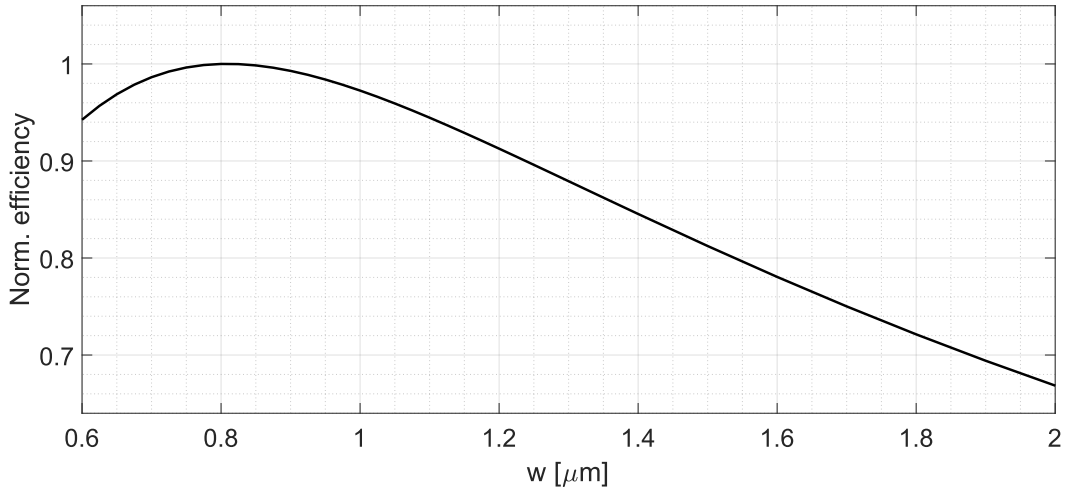


Fig. 9.7: Normalized efficiency of the generation process, evaluated as the factor $|\tilde{\gamma}_{sh}^{(2)}|^2$, as a function of the waveguide width w . The simulation refers to a frequency conversion process between $\lambda_f = 2300$ nm and $\lambda_{sh} = 1150$ nm.

Figure 9.8 shows on a color map again the normalized $|\tilde{\gamma}_{sh}^{(2)}|^2$ as a function of w and λ_f . This figure shows that, as λ_f increases, also the value of w providing the maximum efficiency increases. The white line represents the waveguide width w that, for each λ_f , provides the maximum achievable efficiency. The red and the black lines represent (respectively) waveguide width w that, for each λ_f , provides the 90% and the 70% of the maximum efficiency.

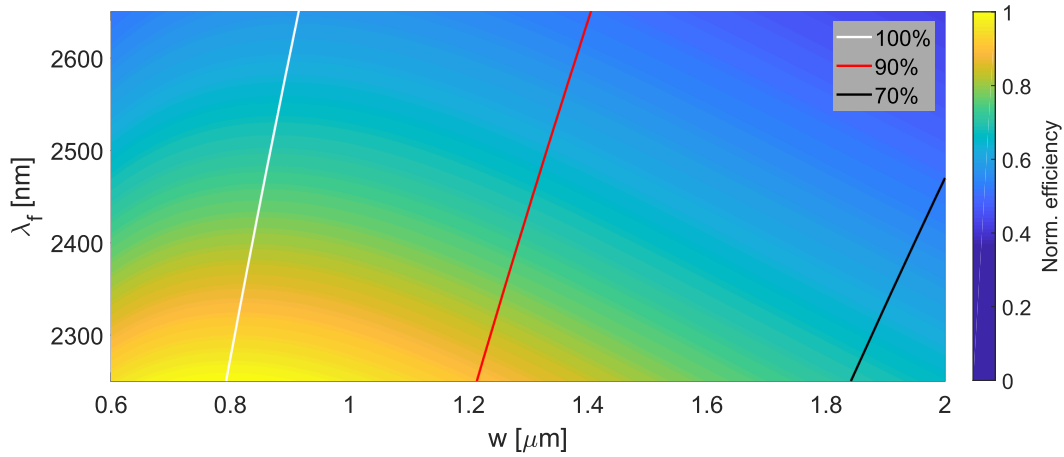


Fig. 9.8: Normalized efficiency of the generation process, evaluated as the factor $|\tilde{\gamma}_{sh}^{(2)}|^2$, as a function of the waveguide width w and the wavelength λ_f .

9.2.3 Coherence length of the process

Figure 9.9 reports the coherence length as a function of λ_f , referred to the waveguide providing phase-matching at $\lambda_f = 2300$ nm. The coherence length exceeds 1 cm over a bandwidth slightly below 2 nm. This means that, for a sample length of 1 cm, λ_f can be modified less than 2 nm to maintain an efficient generation.

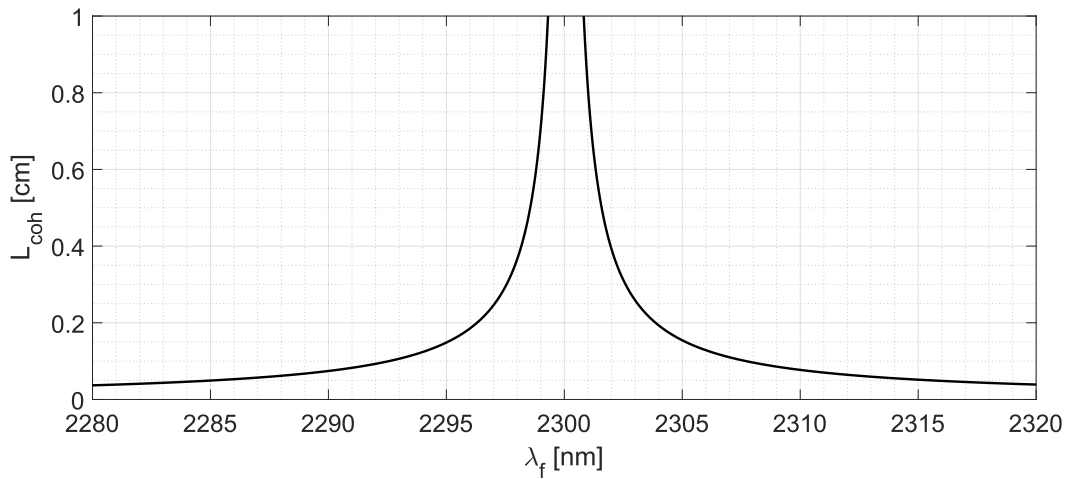


Fig. 9.9: Coherence length as a function of the pump wavelength. The values of w and Λ are selected for having phase-matching at a wavelength $\lambda_f = 2300$ nm.

9.2.4 Realized waveguide geometries

Table 9.1 reports the parameters of the realized waveguides.

Tab. 9.1: Geometric parameters and corresponding wavelengths for the proposed waveguides. The generation efficiency is calculated from the $|\tilde{\gamma}_{sh}^{(2)}|^2$ parameter, and is normalized on the maximum achievable efficiency at that wavelength.

	λ_f [μm]	Norm. efficiency	Waveguide width w [μm]	Poling period Λ [μm]	Poling order m
1	2.25	100%	0.794	2.564	1
2	2.3	100%	0.809	2.600	1
3	2.3	90%	1.238	2.897	1
4	2.3	70%	1.878	3.137	1
5	2.3	100%	0.809	5.200	2
6	2.3	100%	0.809	7.800	3
7	2.3	100%	0.809	10.400	4
8	2.35	100%	0.824	2.634	1
9	2.4	100%	0.839	2.667	1
10	2.4	90%	1.285	2.974	1
11	2.4	70%	1.949	3.222	1
12	2.45	100%	0.854	2.698	1
13	2.55	100%	0.885	2.756	1
14	2.6	100%	0.900	2.784	1
15	2.65	100%	0.916	2.811	1
16	3.09	100%	1.066	3.018	1

- The first geometries are selected to work with λ_f between $2.25\mu\text{m}$ and $2.45\mu\text{m}$. This is the wavelength range available with the laser source described in chapter 5. For this wavelength range, the corresponding Λ have been selected. These waveguides are identified by numbers 1, 2, 8, 9 and 12 in Tab. 9.1.
- For the waveguides designed to work at $\lambda_f = 2.3\mu\text{m}$ and $\lambda_f = 2.4\mu\text{m}$, three configurations are proposed. The first one maximizes the generation efficiency. The two additional configurations provide the 90% and the 70% of the maximum achievable efficiency at that wavelength. These configurations are less efficient, but use larger waveguides. So, they should be affected by smaller propagation losses and they should be less affected by fabrication uncertainties. These waveguides are identified by numbers 2, 3, 4 and 9, 10, 11 in Tab. 9.1.
- For the case $\lambda_f = 2.3\mu\text{m}$ three alternative designs are proposed, where higher order poling periods are used. These are identified by numbers 5, 6 and 7, and refer to poling orders $m = 2, 3$ and 4 . As already discussed in Sec. 9.1.3, no generation is expected on high order poling if $s(z)$ is sinusoidal. If $s(z)$ is a square-wave function, generation is expected only for odd m . If none of these is the real situation, generation is expected for all the values of m . So, these structures can be used to understand the shape of $s(z)$, and so the variation of the nonlinear coefficient along the waveguide propagation direction.

- Some configurations are selected to work at longer wavelengths (λ_f is in the range between $2.55\ \mu\text{m}$ and $2.65\ \mu\text{m}$). These combinations are proposed for the SPDC process. This is motivated by the abundance of laser diodes at wavelengths around $1.3\ \mu\text{m}$. These waveguides are identified by numbers 13, 14, 15 in the table.
- The last combination works in the conversion between $1.545\ \mu\text{m}$ and $3.09\ \mu\text{m}$. This combination is proposed because of the abundance of sources around $1.545\ \mu\text{m}$. These waveguide is identified by number 16 in the table.

9.2.5 Tolerance to fabrication uncertainties

Due to the uncertainty of fabrication, it may happen that the realized devices differ from the design. So, it is important to understand how to manage this situation. So far, the aim of the design was to find the waveguide geometry providing the maximum efficiency at a given wavelength. Now, the aim is to find the experimental conditions that can provide an efficient experiment if the actual geometry differs from the design. To this purpose, Fig. 9.10 reports the fundamental and the SH wavelengths that provide phase-matching as a function of both the waveguide width w and the poling period Λ . The central point of the figure represents the design geometry ($w = 0.824\ \mu\text{m}$ and $\Lambda = 2.634\ \mu\text{m}$), which provides phase-matching between $\lambda_f = 2350\ \text{nm}$ and $\lambda_{sh} = 1175\ \text{nm}$. This corresponds to the configuration labeled by number 8 in Tab. 9.1. Figure 9.10 shows that, if w and Λ differ from the design, the phase-matching moves to different wavelengths. To emphasize this, the black lines represent a variation of $10\ \text{nm}$ on w and Λ . Therefore, both in the SHG and in the SPDC process, the pump wavelengths can be properly changed to recover an efficient conversion at wavelengths different from the designed ones.

While in the SHG process the only way to overcome the fabrication error is changing the pump wavelength, in the SPDC process one can take advantage from an additional degree of freedom, which is the possibility to have a non-degenerate process. In fact, in SPDC the pump photon at frequency ω_{sh} can generate two photons at two different frequencies $\omega_{f,1}$ and $\omega_{f,2}$, which have to satisfy the energy conservation relationship $\omega_{f,1} + \omega_{f,2} = \omega_{sh}$. In this case, the phase-mismatch coefficient $\Delta\beta$ is:

$$\Delta\beta = \beta_{\omega_{f,1}} + \beta_{\omega_{f,2}} - \beta_{\omega_{sh}} + \frac{2\pi m}{\Lambda}. \quad (9.16)$$

Therefore, even if the realized geometry differs from the design and it cannot provide SPDC at frequency $\omega_f = \omega_{sh}/2$, it may occur that two other frequencies $\omega_{f,1}$ and $\omega_{f,2}$ satisfy phase-matching and provide an efficient conversion.

In this framework, Fig. 9.11 reports $|\Delta\beta|$ as a function of the pump wavelength λ_{sh} and of the wavelength of one generated photon $\lambda_{f,1}$. Once that λ_{sh} and $\lambda_{f,1}$ are

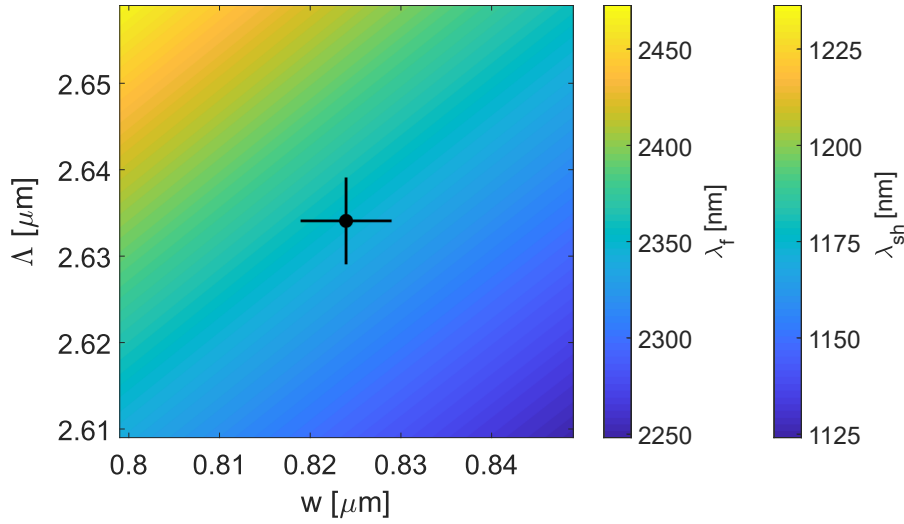


Fig. 9.10: Fundamental and SH wavelengths that provide phase-matching as a function of w and Λ . The black point represents the designed geometry, while the black lines represent variations of 10 nm on w and Λ .

determined, the wavelength $\lambda_{f,2}$ of the other photon is fixed by energy conservation. The simulation is performed using the geometry number 8 in Tab. 9.1 ($w = 0.824 \mu\text{m}$ and $\Lambda = 2.634 \mu\text{m}$). When $|\Delta\beta| = 0$, phase-matching is satisfied and the conversion process is efficient. This condition is satisfied for $\lambda_{sh} \sim 1175 \text{ nm}$ and $\lambda_f \sim 2350 \text{ nm}$, which corresponds to the degenerate process used in the design, and shown in Tab. 9.1. This process is indicated by the white lines in the figure. However, Fig. 9.11 shows that phase-matching can be satisfied also by using lower pump wavelengths, which provide the generation of photons at different wavelengths $\lambda_{f,1}$ and $\lambda_{f,2}$.

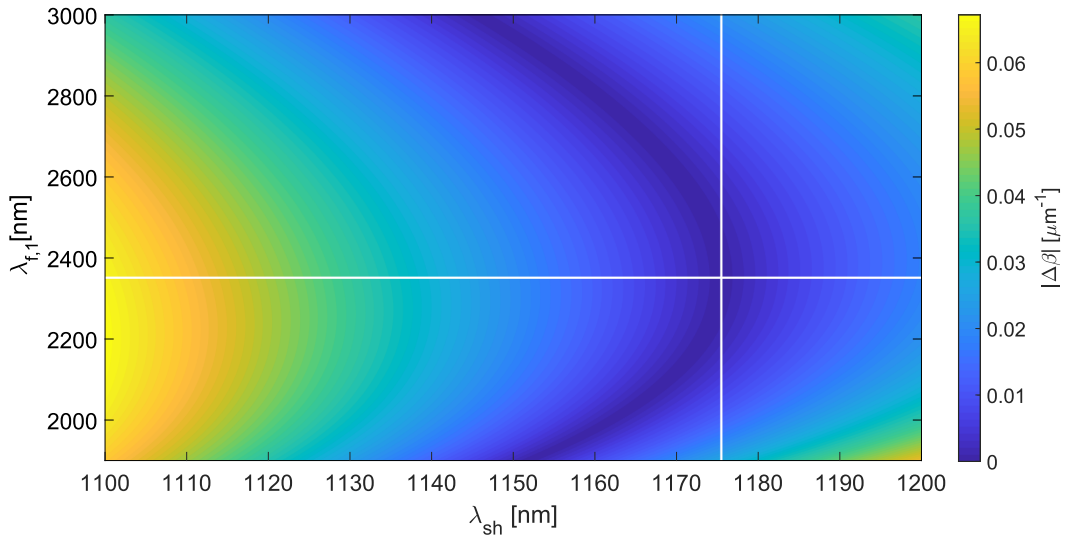


Fig. 9.11: Color map reporting $|\Delta\beta|$ as a function of λ_{sh} and $\lambda_{f,1}$ ($\lambda_{f,2}$ can be easily determined by energy conservation). The uses the configuration number 8 in Tab. 9.1. The white lines individuate the degenerate process.

Consider now the red curves shown in Fig. 9.12. These represent the values of $\lambda_{f,1}$ and $\lambda_{f,2}$ which provide phase matching as a function of λ_{sh} , referred to the same

geometry of Fig. 9.11. From this plot, one can see the same behavior described previously. Figure 9.12 represents also in green the same quantities referred to Λ increased by 10 nm. By keeping the original pump wavelength $\lambda_{sh} \sim 1175$ nm, the SPDC process is still possible, but the generated photons are no more degenerate in energy (they are generated at about 2750 nm and 2050 nm). On the other hand, the blue curves of Fig. 9.12 refer to the case of Λ reduced by 10 nm. In this case, SPDC process is no more possible using $\lambda_{sh} \sim 1175$ nm.

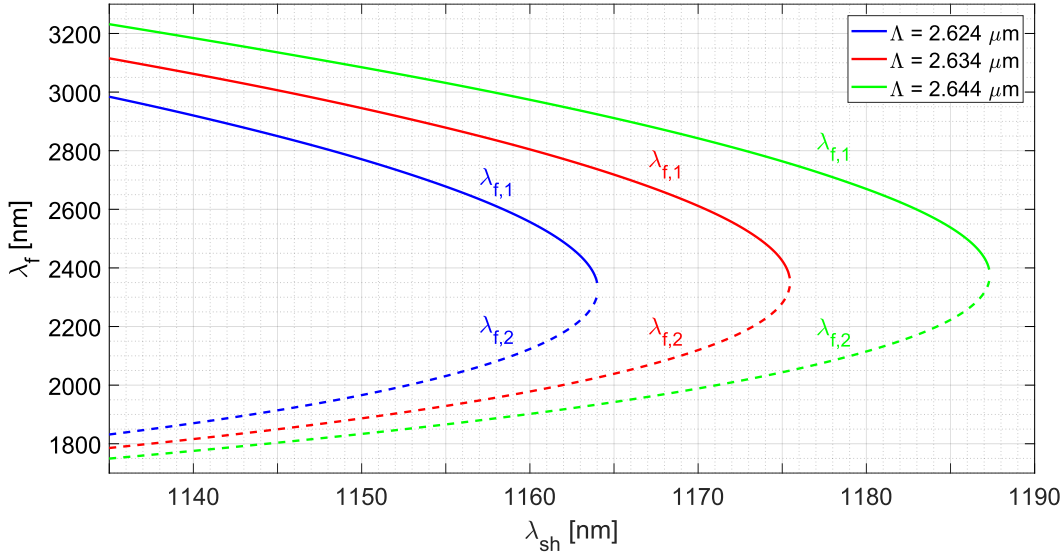


Fig. 9.12: Values of $\lambda_{f,1}$ and $\lambda_{f,2}$ which provide phase matching as a function of the pump wavelength λ_{sh} in the SPDC process, using the configuration number 8 of Tab. 9.1. The red curve considers the nominal value of Λ , while in the blue (resp. green) curve the values of Λ are decreased (resp. increased) by 10 nm.

A similar effect happens also if one considers variations of w . However, in this situation a larger w determines a smaller value of λ_{sh} for the degenerate process. Conversely, a smaller w determines a larger λ_{sh} for the degenerate process. Therefore, by considering non-degenerate conversion, in some situations the SPDC is still possible by using the designed pump wavelength even if the geometry of the realized device differs from the design.

9.2.6 Geometry of the junction

Figure 9.13 shows the top view of the waveguides analyzed in this chapter. Two different configurations of the lateral p-n junctions are proposed.

The configuration shown on the left of Fig. 9.13 is similar to the one used in [125]. It consists of doped regions of width δ , each of which separated from the successive by a distance $\Delta = \Lambda - \delta$. In this configuration, one type of doping is realized on each side of the waveguide. In this way, the DC field inside the waveguide is always directed in the same direction. This configuration is named **simple** configuration.

The configuration shown on the right of Fig. 9.13 consists of doped regions of

alternating type. Each of these regions has a width δ , and successive regions are separated by Δ , in a way such that $2(\delta + \Delta) = \Lambda$. This configuration represents the best choice, because it allows a transition from negative to positive values of the field inside the waveguide. This configuration is named **interdigitated** configuration.

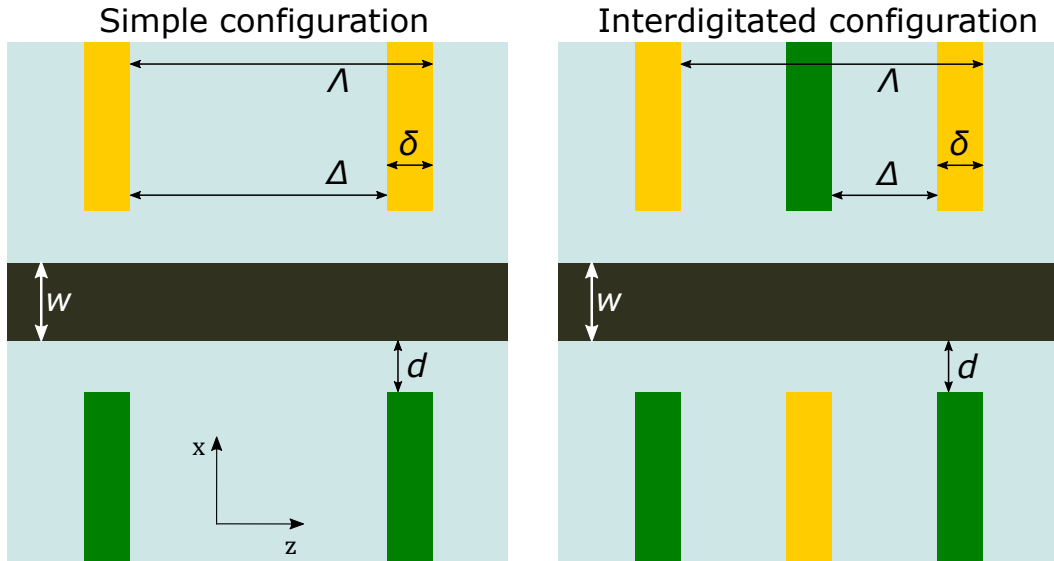


Fig. 9.13: Top view sketch of the waveguides analyzed in this work: the simple configuration (left) and the interdigitated configuration (right). The black color represents the waveguide, while the green and the yellow bars represent the p-type and the n-type doped regions. Three values of d are realized (respectively 200 nm, 500 nm and 800 nm). The parameter δ is 500 nm in all the configurations. The values of w and Λ are chosen differently for each of the situations described in Tab. 9.1. Once that Λ is fixed, Δ is quantified accordingly.

As already discussed in chapter 8, an important parameter that must be set properly is the separation d between the waveguide border and the doped region. The ideal situation consists of $d = 0$ nm, because it provides the maximum field inside the waveguide. However, this makes the waveguide lossy. Therefore, following the procedure of chapter 8, three values of d are proposed, namely $d = 200$ nm, $d = 500$ nm and $d = 800$ nm. The first is the best in terms of the DC field amplitude introduced in the waveguide, but it also affects more the waveguide performance in terms of losses. The last one affects less the propagating mode, but it also provides a smaller DC field inside the waveguide.

The size of each doped region, δ , is 500 nm. In this situation, once that Λ is set, the value of Δ is determined accordingly. The value $\delta = 500$ nm is a compromise between a value unaffected by the lithographic resolution (so a large δ), and a large Δ to avoid breakdown between successive doped regions (so a small δ).

Therefore, for each waveguide, six different configurations are proposed: three replicas of the interdigitated configuration, and three replicas of the simple configuration, considering respectively $d = 200$ nm, $d = 500$ nm and $d = 800$ nm.

An example of the realized structures (in the simple and in the interdigitated form) is shown in Fig. 9.14. The different colors represent the six different photolithographic

processes required to realize them. The first lithographic process is used to define the rib waveguide, and is shown in black in Fig. 9.14. Then there are two lithographies required to define the doped regions, represented in green and yellow. The fourth one is used to deposit a 200 nm high oxide layer on the top of some doped region, in order to prevent contacting the junction in the wrong place. This level is present only for the interdigitated situation, and it is sketched in light blue in Fig. 9.14. The fifth level is used to realize holes in the oxide cladding to contact the junctions with the metallic pads. Holes are sketched in blue in the Fig. 9.14. The last level, used to realize the metallic contacts, is reported in red.

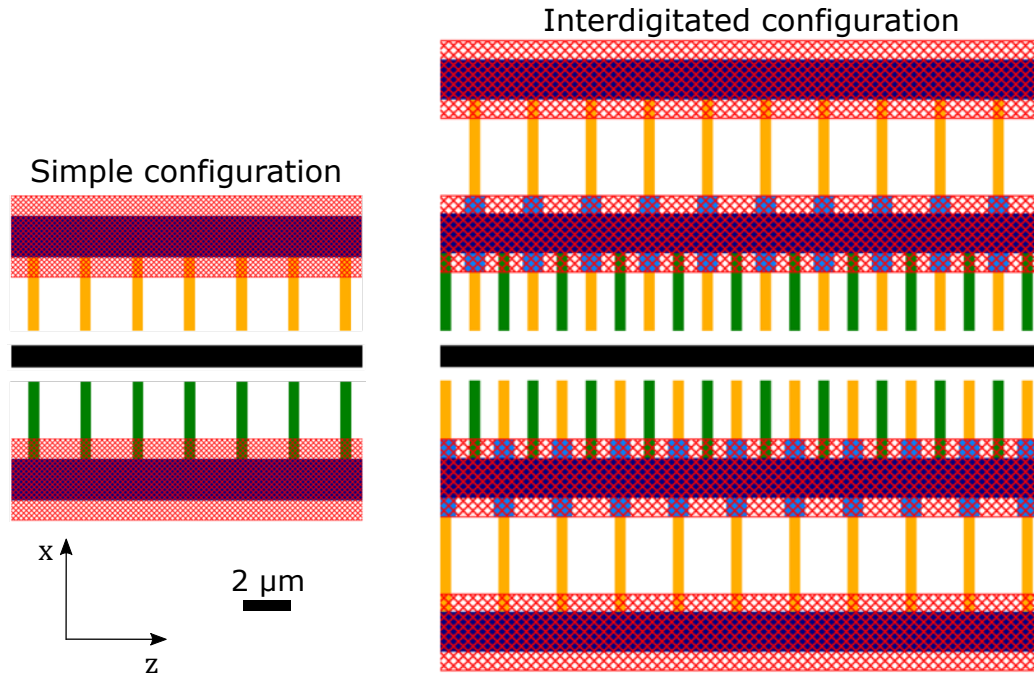


Fig. 9.14: Top view of the realized structures. On the left, the simple configuration is shown. The black line is the rib silicon waveguide, the green and the yellow rectangles are the p-type and the n-type doped regions, the blue part is the hole in the oxide cladding to access the doped region, while the red corresponds to the metal to contact the junctions. On the right it is sketched the interdigitated configuration. The color legend is the same of the other case, but here an additional level is present, represented in light-blue, corresponding to a 200 nm high oxide layer introduced to avoid the metallic strip to contact the wrong junction.

9.3 Modeling the electric field in poled waveguides

In this section, the DC field inside the waveguide is modeled, with the aim of estimating the nonlinear strength that can be obtained inside the waveguide.

9.3.1 Description of the FEM model

To estimate the DC field inside the waveguide, the system is modeled by a 3D simulation using the semiconductor module of COMSOL Multiphysics® software [56]. The use of a 3D model is necessary because it allows taking into account the effect of adjacent junctions. The geometry of the system is reported in Fig. 9.15. Both the n -type and the p -type doped regions are modeled by a $1 \times 10^{18} \text{ cm}^{-3}$ doping concentration, while intrinsic doping is assumed in the rest of the silicon layer. This is not the real case, because a $1 \times 10^{15} \text{ cm}^{-3}$ p -type doping is present in the real devices. However, introducing this kind of doping gives problems for the convergence of the 3D simulation. Therefore, simulations are performed assuming intrinsic doping. As a first order approximation, this simulation models well the system. For reasons of computational power, the 3D simulations are not as refined as the 2D ones. So, also for this reason, the simulation works as a first order approximation.

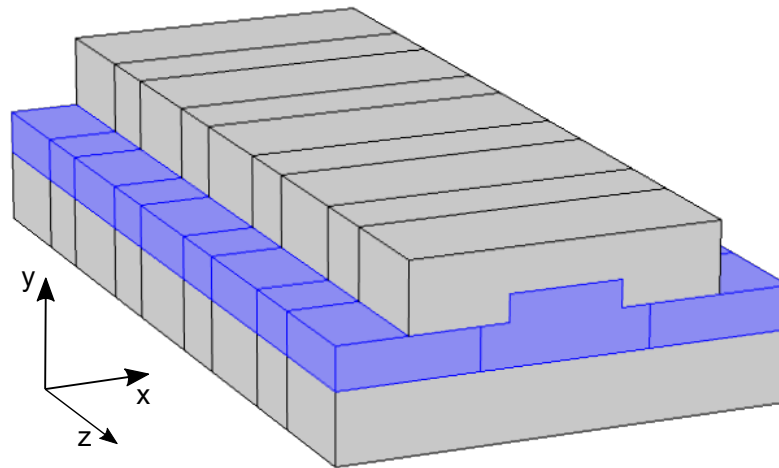


Fig. 9.15: Geometry of the model used to estimate the DC field inside the waveguide. The blue domains represent the silicon layer, while the grey part represents the oxide. On the xy -plane one can see the boundaries between the core of the waveguide and the lateral doped regions. Along z , the periodicity of the junctions is shown. The FEM software does not allow to apply periodic conditions, so the simulation is performed considering a number of periods such that the central regions is not affected by the introduction of new periods at the boundaries.

9.3.2 Field distribution and nonlinear strength

An example of the results of the model described here is shown in Fig. 9.16. The figure reports on a color scale the x component of the DC field E_{DC} evaluated in the middle of a junction. The simulation is performed considering the waveguide geometry reported in the first line of Tab. 9.1 with $d = 200 \text{ nm}$. The left hand side panel refers to the simple configuration, while the right hand side panel reports

the case of the interdigitated configuration. Both the simulations refer to a reverse bias voltage of 20 V. They show similar field distributions. Compared to the simple situation, the interdigitated geometry shows a larger electric field close to the doped region, while the field is smaller in the center of the waveguide. This is due to the presence of adjacent doped region with opposite polarization along z . Figure 9.16 shows also a second color axis, reporting the distribution of the corresponding field-induced second order nonlinear coefficient $\chi_{\text{EFISH}}^{(2)} = 3\chi_{xxxx}^{(3)}E_{DC,x}$. As already discussed in chapter 7, literature values for $\chi_{xxxx}^{(3)}$ are ambiguous and range from $0.94 \times 10^{-19} \text{ m}^2/\text{V}^2$ to $4.24 \times 10^{-19} \text{ m}^2/\text{V}^2$ [81, 162, 163]. Thus, an average value of $\chi_{xxxx}^{(3)} = 2.6 \times 10^{-19} \text{ m}^2/\text{V}^2$ is used. Due to the large applied electric fields, $\chi_{\text{EFISH}}^{(2)}$ is larger than the one determined by trapped charges in chapter 7.

Figure 9.17 reports $E_{DC,x}$ and $\chi_{\text{EFISH}}^{(2)}$ in the xz -plane in the middle of the slab waveguide. The results are evaluated for $d = 200 \text{ nm}$ and a reverse bias voltage of 20 V. The field distribution, as well as the field-induced nonlinearity, varies along the waveguide. In the simple situation the electric field varies its strength, but it keeps always the same sign. As expected, in the interdigitated situation the sign of the field as well as of $\chi_{\text{EFISH}}^{(2)}$ change.

The same can be observed from Fig. 9.18, where $E_{DC,x}$ and $\chi_{\text{EFISH}}^{(2)}$ are evaluated in the middle of the waveguide along the waveguide propagation direction z . In the interdigitated configuration, $\chi_{\text{EFISH}}^{(2)}$ changes sign, while in the simple configuration $\chi_{\text{EFISH}}^{(2)}$ varies but it keeps the same sign. The maximum value reached by the interdigitated configuration is smaller, due to adjacent junctions with opposite polarization.

Figure 9.19 reports $E_{DC,x}$ and $\chi_{\text{EFISH}}^{(2)}$ in the xz -plane in the middle of the waveguide, comparing $d = 200 \text{ nm}$, $d = 500 \text{ nm}$ and $d = 800 \text{ nm}$ in the interdigitated configuration. All the simulations refer to a reverse bias voltage of 20 V. It is not surprising that, when d becomes larger, $\chi_{\text{EFISH}}^{(2)}$ still changes sign. However, the value assumed in the middle of the waveguide is smaller, due to the larger separation between the junctions.

Similarly, Fig. 9.20 reports $E_{DC,x}$ and $\chi_{\text{EFISH}}^{(2)}$ in the central point of the waveguide

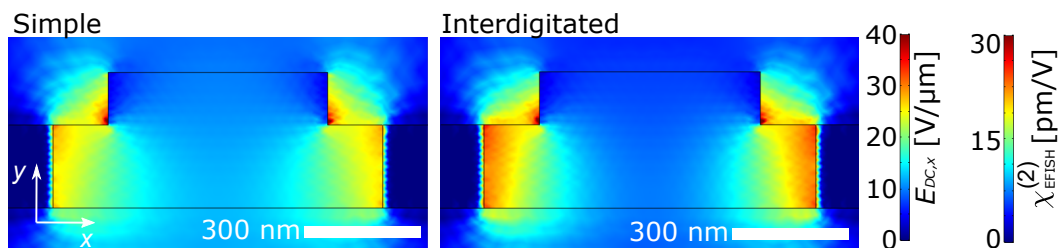


Fig. 9.16: Color scale representation of both the x component of the DC field E_{DC} and the field-induced second order nonlinear coefficient $\chi_{\text{EFISH}}^{(2)}$. The result is evaluated in the xy -plane in the middle of a junction. It refers to the geometry of the first line of Tab. 9.1 with $d = 200 \text{ nm}$, considering both the simple and the interdigitated configurations with an applied reverse bias voltage of 20 V.

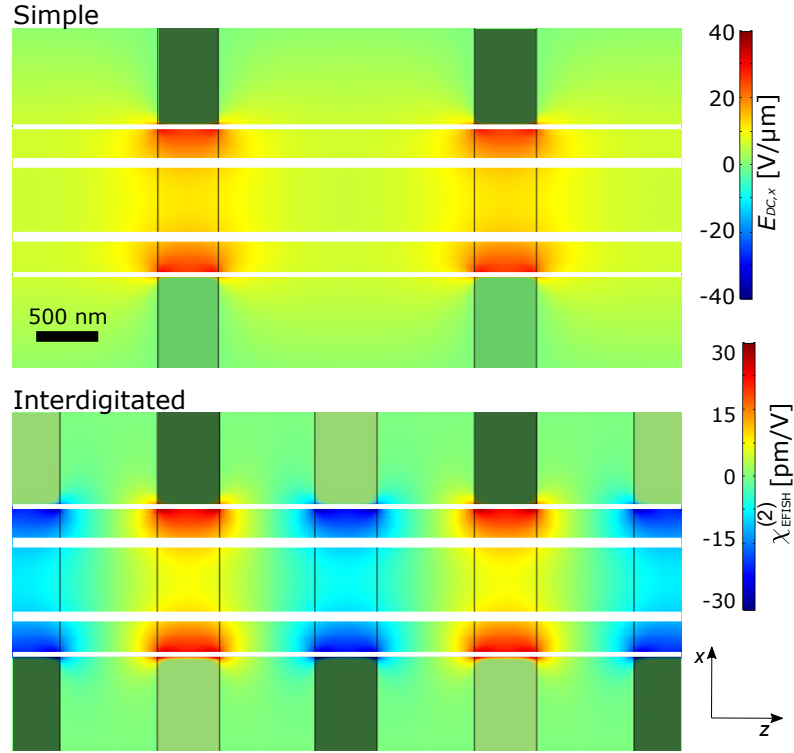


Fig. 9.17: Distribution of $E_{DC,x}$ and $\chi_{EFISH}^{(2)}$ in the xz -plane in the middle of the waveguide. The simulation is performed considering the waveguide geometry reported in the first line of Tab. 9.1, with $d = 200$ nm and with an applied reverse bias voltage of 20 V. The narrow white lines represent the position where the doping begins, while the thicker ones represent the limits of the rib waveguide. To emphasize their position, the doped regions are represented using darker colors.

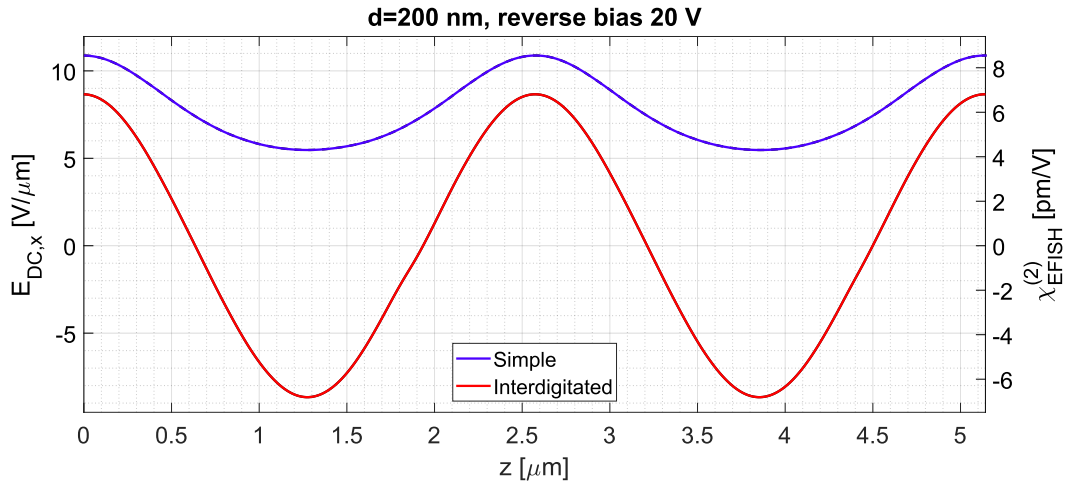


Fig. 9.18: $E_{DC,x}$ and $\chi_{EFISH}^{(2)}$ evaluated in the middle of the waveguide along the waveguide propagation direction z for the simple and the interdigitated configurations. The simulations are performed considering the waveguide geometry reported in the first line of Tab. 9.1 with $d = 200$ nm and a reverse bias voltage of 20 V.

along the waveguide propagation z for the configurations $d = 200$ nm, $d = 500$ nm and $d = 800$ nm in the simple and the interdigitated geometry.

All the situations described so far refer to a reverse bias voltage of 20 V. Clearly,

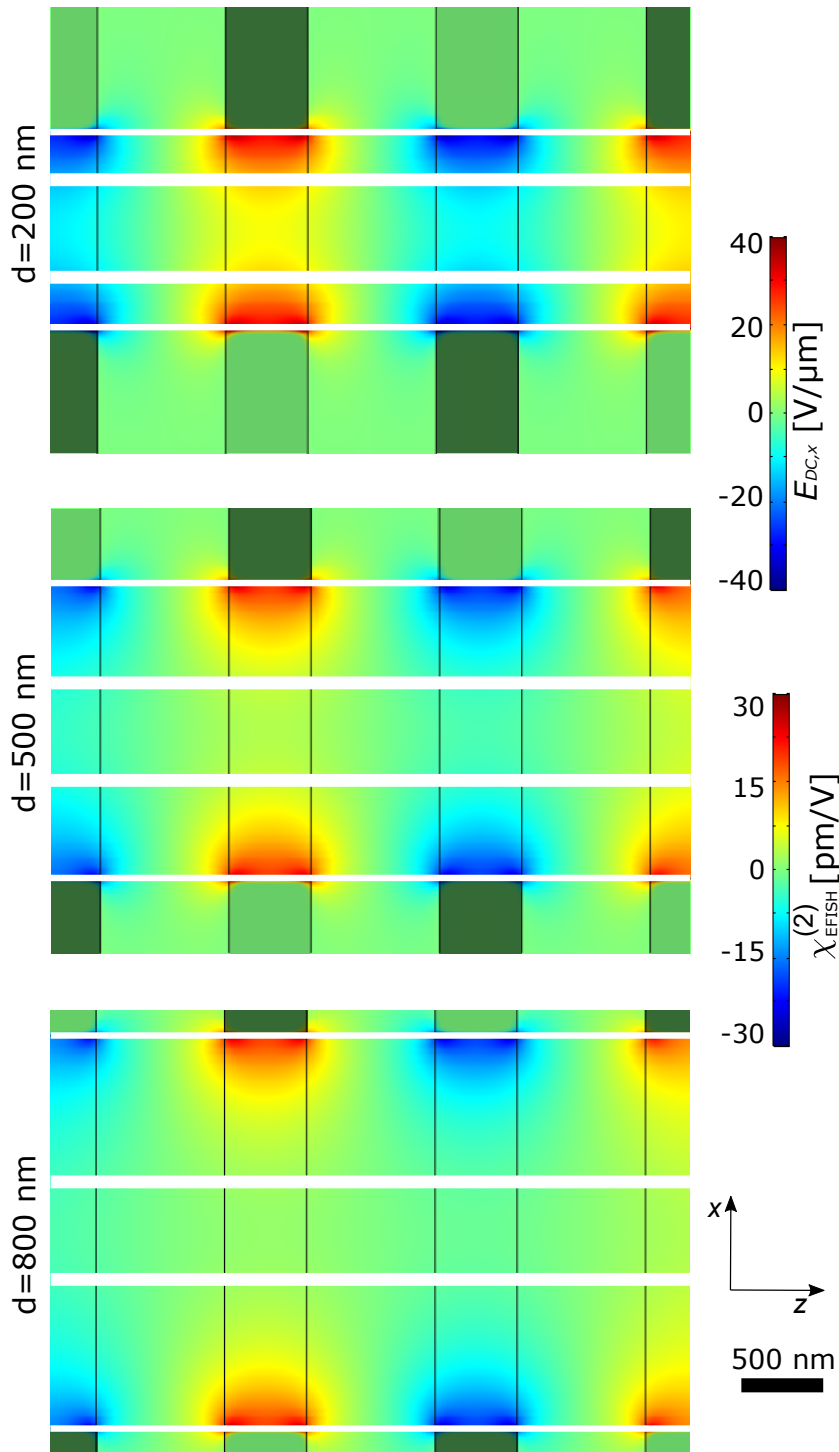


Fig. 9.19: $E_{DC,x}$ and $\chi_{EFISH}^{(2)}$ in the xz -plane in the middle of the waveguide, considering $d = 200$ nm, $d = 500$ nm and $d = 800$ nm in the interdigitated configuration. All the simulations refer to the waveguide geometry reported in the first line of Tab. 9.1, with a reverse bias voltage of 20 V.

by changing the bias voltage the DC field strength changes, and consequently the value of $\chi_{EFISH}^{(2)}$ is modified. In the top panel of Fig. 9.21 $E_{DC,x}$ and $\chi_{EFISH}^{(2)}$ are evaluated in the center of the waveguide along the waveguide propagation direction

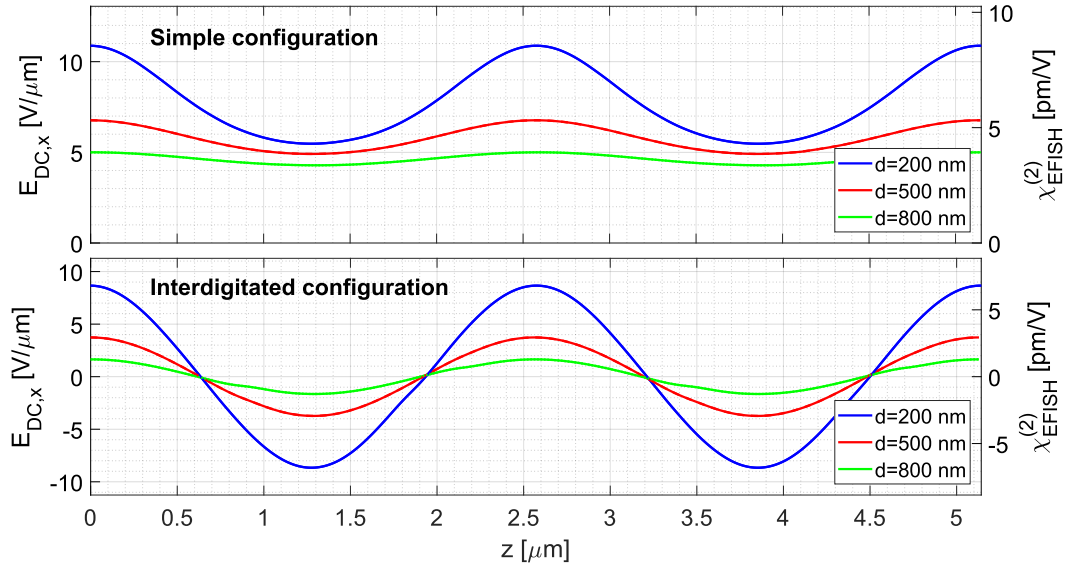


Fig. 9.20: $E_{DC,x}$ and $\chi_{EFISH}^{(2)}$ in center of the waveguide along z for different d and a reverse bias of 20 V. The simulations refer to the geometry of the first line of Tab. 9.1.

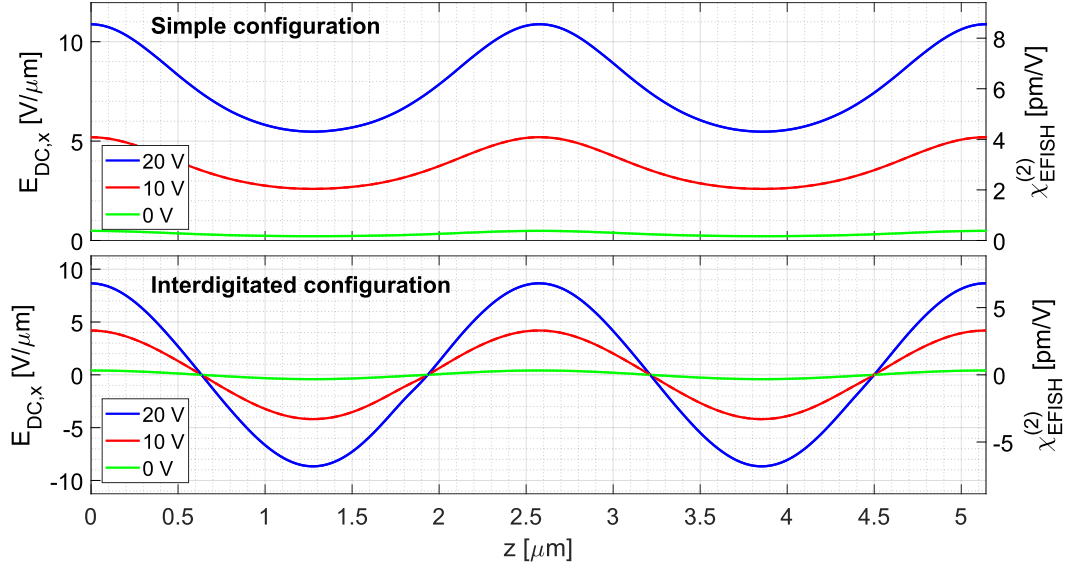


Fig. 9.21: $E_{DC,x}$ and $\chi_{EFISH}^{(2)}$ in the center of the waveguide along z for $d = 200$ nm and different biases. The simulations refer to the geometry at first line of Tab. 9.1.

z . The simulations refer to the simple configuration with $d = 200$ nm, when reverse bias voltages of 0 V, 10 V and 20 V are applied. In the bottom panel of Fig. 9.21 the same quantities are shown referred to the interdigitated configuration. In both the situations if the applied voltage decreases also the strength of $\chi_{EFISH}^{(2)}$ decreases. Also when no bias voltage is applied (0 V) $\chi_{EFISH}^{(2)}$ is non-zero. This is due to the presence of the doped regions, which determines the equilibrium condition for a nonzero potential across the junction (the so called built-in potential). This potential introduces a non-zero electric field even if the junction is not polarized, which in turn determines a non-zero $\chi_{EFISH}^{(2)}$.

9.3.3 The poling function

The results of these simulations allow to determine the distribution of the nonlinear coefficient inside the waveguide. To use the theoretical description of Sec. 9.1, one should verify the possibility of rewriting $\chi_{\text{EFISH}}^{(2)}$ as expressed by Eq. (9.1).

Doing that, the interdigitated configuration is considered first. In the top panel of Fig. 9.22 the quantity $E_{DC,x}$ is evaluated along z in different positions of the waveguide, sketched in the inset of the same figure. The corresponding $\chi_{\text{EFISH}}^{(2)}$ is shown on the right axis. The situation refers to a reverse bias of 20 V and $d = 200$ nm. The blue curve, evaluated in the center of the waveguide, is the same curve already reported in the previous figures. Moving closer to the waveguide border, the strength of $\chi_{\text{EFISH}}^{(2)}$ becomes larger, as in Fig. 9.16. Moreover, the shape of $\chi_{\text{EFISH}}^{(2)}$ becomes more "squared". On the other hand, moving closer to the top of the rib waveguide $\chi_{\text{EFISH}}^{(2)}$ becomes smaller. At this point, one can normalize each curve shown in Fig. 9.22 with respect to its maximum value. If the factorization expressed by Eq. (9.1) can be done, the resulting curve should be the same independently on the waveguide position where it is evaluated. If this is true, the resulting curve is the poling function $s(z)$. In the case analyzed here, this is reported in the bottom panel of Fig. 9.22, referred to the same positions represented on the top side panel. All the curves show a similar shape: only the ones evaluated close to the border present slight variations. This confirms that the approximation expressed by Eq. (9.1) is valid in this case. The curve evaluated in the center of the waveguide is fitted by a sinusoidal function, shown by the black dashed line in Fig. 9.22. Therefore, in the interdigitated configuration, the factorization expressed by Eq. (9.1) can be done. The function $\chi^{(2)}(\mathbf{r}_{\perp})$ is given by the spatial distribution of $\chi_{\text{EFISH}}^{(2)}$ in the waveguide cross-section in the middle of the junction (where the nonlinear strength is maximum), while $s(z)$ is a sinusoidal function with the period of the poling.

Consider now the case of the simple configuration. In the top panel of Fig. 9.23, the quantities $E_{DC,x}$ and $\chi_{\text{EFISH}}^{(2)}$ are evaluated along z in different positions of the waveguide, sketched in the inset of the figure. The situation refers to a reverse bias of 20 V and $d = 200$ nm. Also in this case, on the bottom of Fig. 9.23 the value of $\chi_{\text{EFISH}}^{(2)}$ is normalized on its maximum. Clearly, in this case the shape of $s(z)$ shows an offset, due to the fact that $\chi_{\text{EFISH}}^{(2)}$ does not change sign every poling period. Moreover, in this case the shape of $s(z)$ differs strongly depending on the position where it is evaluated. It is quite well approximated by a sinusoidal function in the center of the waveguide, as it is shown by the fit represented by the black dashed line. However, the shape of $s(z)$ strongly differs from the sinusoidal behavior close to the waveguide border. Due to this reason, in the case of the simple configuration the factorization expressed by Eq. (9.1) is not generally valid. However, as a first order approximation, that approximation is considered in this work.

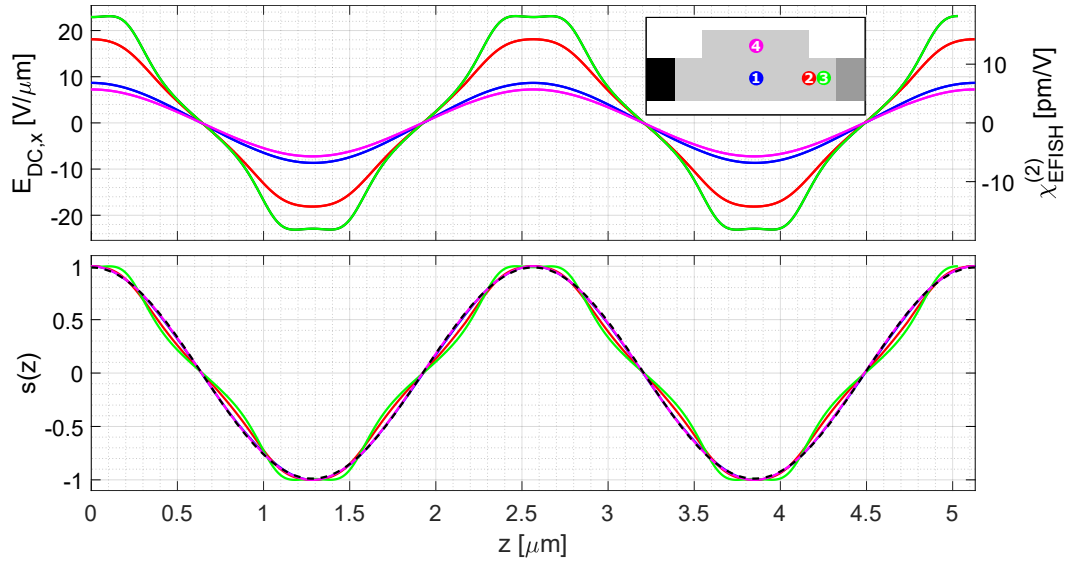


Fig. 9.22: On the top: $E_{DC,x}$ and $\chi_{EFISH}^{(2)}$ values evaluated along the waveguide propagation direction z in different positions of the waveguide, sketched with colors in the inset. The simulation refers to the waveguide geometry reported in the first line of Tab. 9.1 in the interdigitated configuration with $d = 200$ nm and a reverse bias voltage of 20 V. On the bottom: shape of the poling function, evaluated by normalizing the $\chi_{EFISH}^{(2)}$ distribution on its maximum value. The black dashed line is a sinusoidal fit of the function in the center of the waveguide.

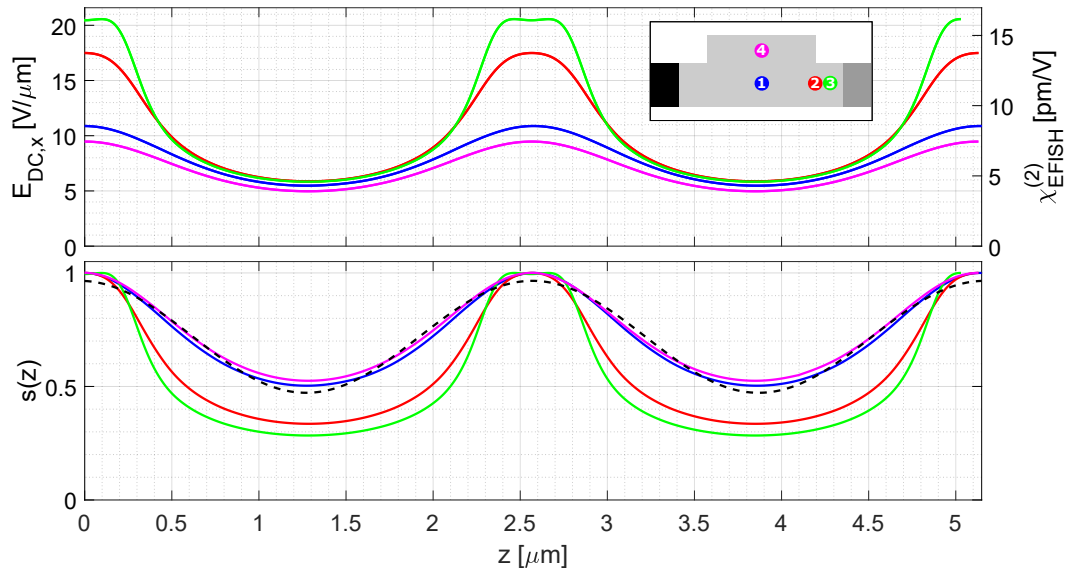


Fig. 9.23: On the top: $E_{DC,x}$ and $\chi_{EFISH}^{(2)}$ values evaluated along the waveguide propagation direction z in different positions of the waveguide, sketched with colors in the inset. The simulation refers to the waveguide geometry reported in the first line of Tab. 9.1 in the simple configuration with $d = 200$ nm and a reverse bias voltage of 20 V. On the bottom: shape of the poling function, evaluated by normalizing $\chi_{EFISH}^{(2)}$ on its maximum value. The black dashed line is a sinusoidal fit of the function in the center of the waveguide.

9.3.4 The maximum achievable field

The maximum reverse bias voltage that can be applied to the system is limited by the breakdown field of silicon. Consider for example the results shown in Fig.

9.24, which reports the distribution of $|E_{DC}|$ in the xz -plane in the middle of the waveguide, referred to $d = 200$ nm for both the simple and the interdigitated configurations. The plot shows that the field between adjacent junctions is strong in the case of the interdigitated situation, while it is almost zero for the simple configuration. This is caused by the different polarization of adjacent junctions in the interdigitated case. The figure shows also that the largest $|E_{DC}|$ is achieved in both the cases close to the edge of the doped region. This fact can be attributed to the sharp edge formed by the doped region, which determines a large electric field close to it.

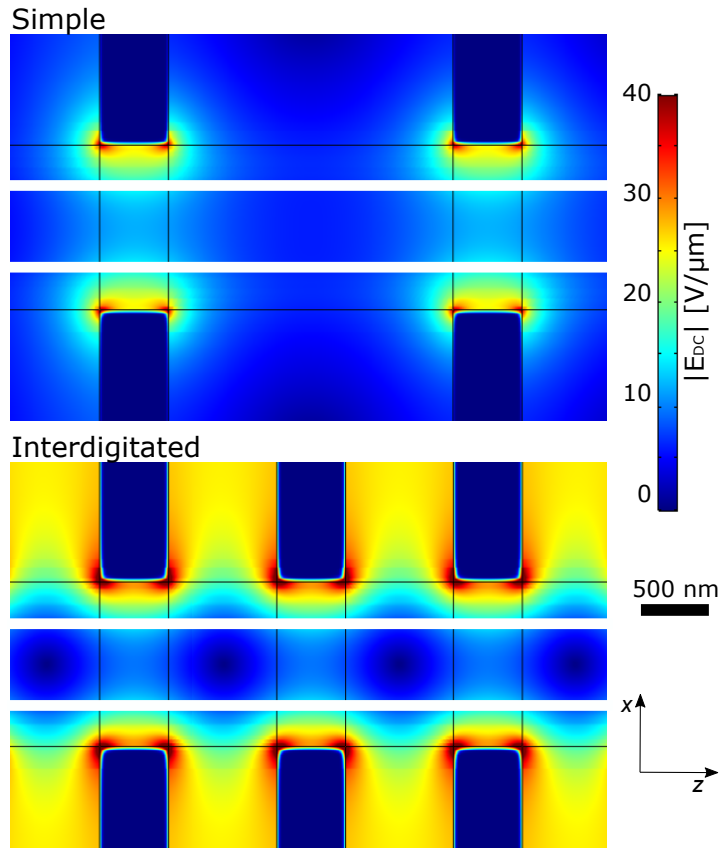


Fig. 9.24: Distribution of $|E_{DC}|$ in the xz -plane in the middle of the waveguide, referred to $d = 200$ nm for both the simple and the interdigitated configuration. The simulations refer to the waveguide geometry reported in the first line of Tab. 9.1 with a reverse bias voltage of 20 V.

To quantify the maximum reverse bias voltage that can be applied, the maximum value of the electric field within the silicon layer is evaluated as a function of the applied bias. Figure 9.25 reports this value for all the values of d described in this work, for both the simple and the interdigitated configuration. The maximum $|E_{DC}|$ increases with the bias. This value is compared with the breakdown field of silicon, set to 40 V/ μm [166]. In this way, it is possible to quantify the maximum bias, which is represented by the vertical dashed lines in Fig. 9.25. In the case of the simple configuration, this value increases with d . This is reasonable, because the larger d

and the larger is the distance between regions with opposite polarization, and so the smaller is the electric field. On the contrary, in the case of the interdigitated situation the maximum voltage that can be applied is almost the same. This is due to the presence of adjacent junctions with opposite polarizations, whose distance Δ is the same independently on d . For this reason, the maximum value of $|E_{DC}|$ is not affected by d . Note that the slight difference between the results with different d reported in Fig. 9.25 can be due to the approximations done in the simulations and to the assumption of sharp edge dopings. However, in the realized devices the edges can be less sharp, due to both the lithographic resolution and the diffusion of doping ions. Therefore, the maximum field that can be obtained in the real devices can be larger than the one shown here, and the voltage limit calculated in this section can be considered as a lower bound.

Summarizing, Fig. 9.25 shows that in the simple configuration larger biases can be applied than in the interdigitated configuration. Moreover, while in the interdigitated configuration the larger amount of bias voltage is almost independent on d , for the simple configuration larger voltages can be applied with larger values of d . However, independently on the required bias voltage, what really matters is the strength of the nonlinear parameter that can be induced inside the waveguide.

It can be noted that, for all the interdigitated geometries and for the simple geometry with $d = 200$ nm, the maximum voltage is below 20 V, which is the value used in most of the simulations presented so far. However, as already remarked, it is expected that in the real experiment the actual bias voltage that can be applied is larger than the one shown here. Moreover, the simulations shown previously were presented just for remarking the main parameters that act on the field distribution inside the waveguide. In the following, when SHG and SPDC efficiencies are estimated, calculations are done using bias voltages below the limits predicted by the simulation shown in Fig. 9.25.

9.3.5 The maximum nonlinearity

In Sec. 9.3.2, the values of $\chi_{\text{EFISH}}^{(2)}$ obtained in the different structures have been calculated. In Sec. 9.3.4 the maximum bias voltage that can be applied to the different junctions is evaluated. By combining the results of these sections, it is possible to estimate the maximum value of $\chi_{\text{EFISH}}^{(2)}$ that can be obtained.

On the left hand side axes of Fig. 9.26 it is reported the maximum value of $\chi_{\text{EFISH}}^{(2)}$ evaluated in the center of the waveguide along z . In other words, it consists of the maximum value of the curves reported in the Fig. 9.20. The maximum $\chi_{\text{EFISH}}^{(2)}$ grows linearly with the applied reverse bias voltage. The vertical dashed lines represent the maximum achievable reverse bias voltage, that is obtained from results reported in the previous section. The results of Fig. 9.26 show that the maximum $\chi_{\text{EFISH}}^{(2)}$ is smaller for larger values of d . Moreover, the maximum $\chi_{\text{EFISH}}^{(2)}$ is smaller for the

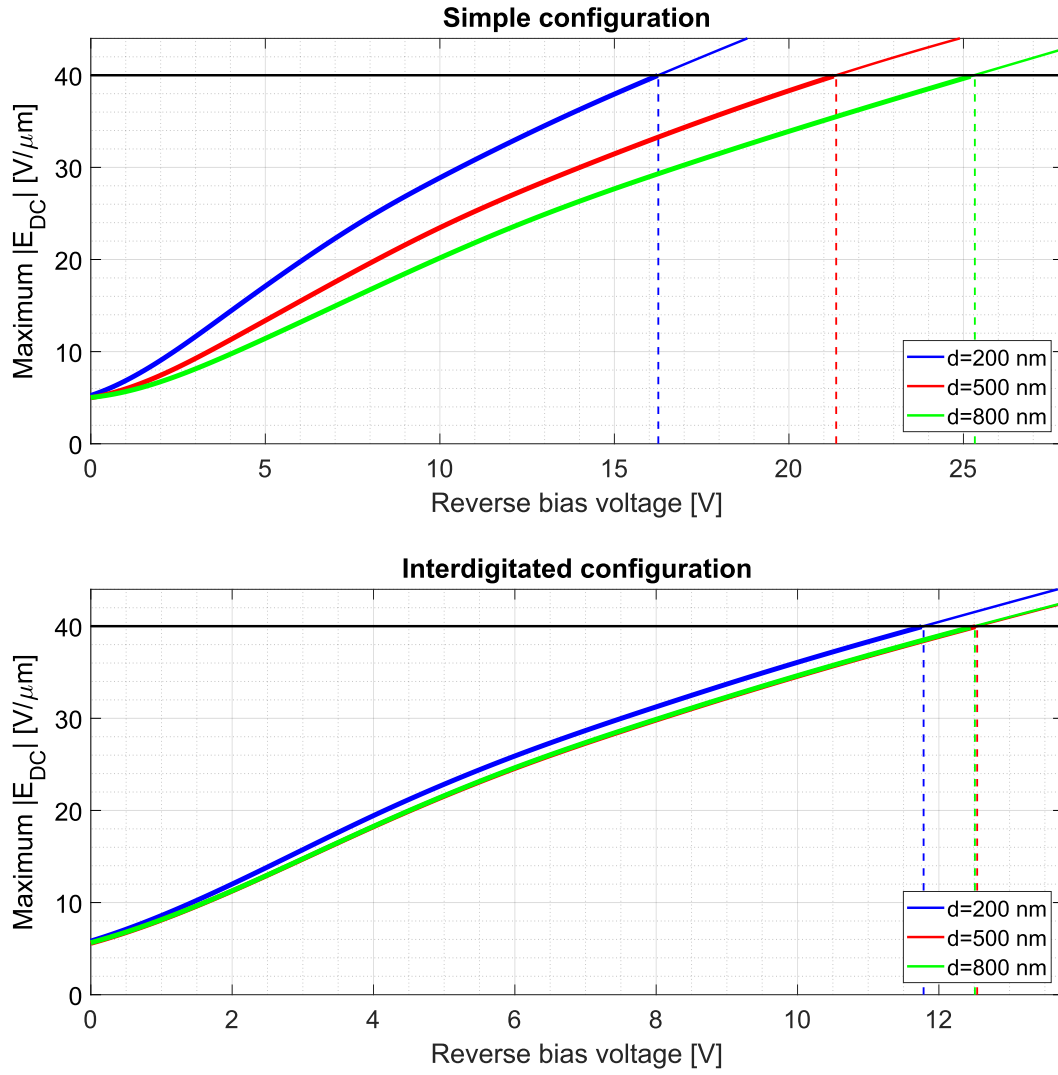


Fig. 9.25: Maximum value of $|E_{DC}|$ within the silicon layer as a function of the applied reverse bias voltage for both the simple and the interdigitated configuration and for all the values of d . The simulations refer to the waveguide geometry reported in the first line of Tab. 9.1. The black line represents the silicon breakdown voltage. The vertical dashed lines indicate the reverse bias voltage providing the maximum $|E_{DC}|$ equal to the breakdown field.

interdigitated configuration than for the simple configuration. However, what really matters is not the absolute value of $\chi_{\text{EFISH}}^{(2)}$, but the strength of its variation along z , which enables the QPM mechanism. To this purpose, the amplitude of the $\chi_{\text{EFISH}}^{(2)}$ variation along z in the center of the waveguide (referred as $\Delta\chi_{\text{EFISH}}^{(2)}$) is reported on the right hand-side of the plots of Fig. 9.26. $\Delta\chi_{\text{EFISH}}^{(2)}$ is evaluated as the difference between the maximum and the minimum value of $\chi_{\text{EFISH}}^{(2)}$ along z in the center of the waveguide. In the case of the interdigitated configuration, $\Delta\chi_{\text{EFISH}}^{(2)}$ is clearly 2 times the maximum value of $\chi_{\text{EFISH}}^{(2)}$. In the case of the simple configuration, $\Delta\chi_{\text{EFISH}}^{(2)}$ is not straightforward. Comparing these results, one can note that $\Delta\chi_{\text{EFISH}}^{(2)}$ decreases with d . Moreover, one can see that the interdigitated configuration is always more efficient than the simple one.

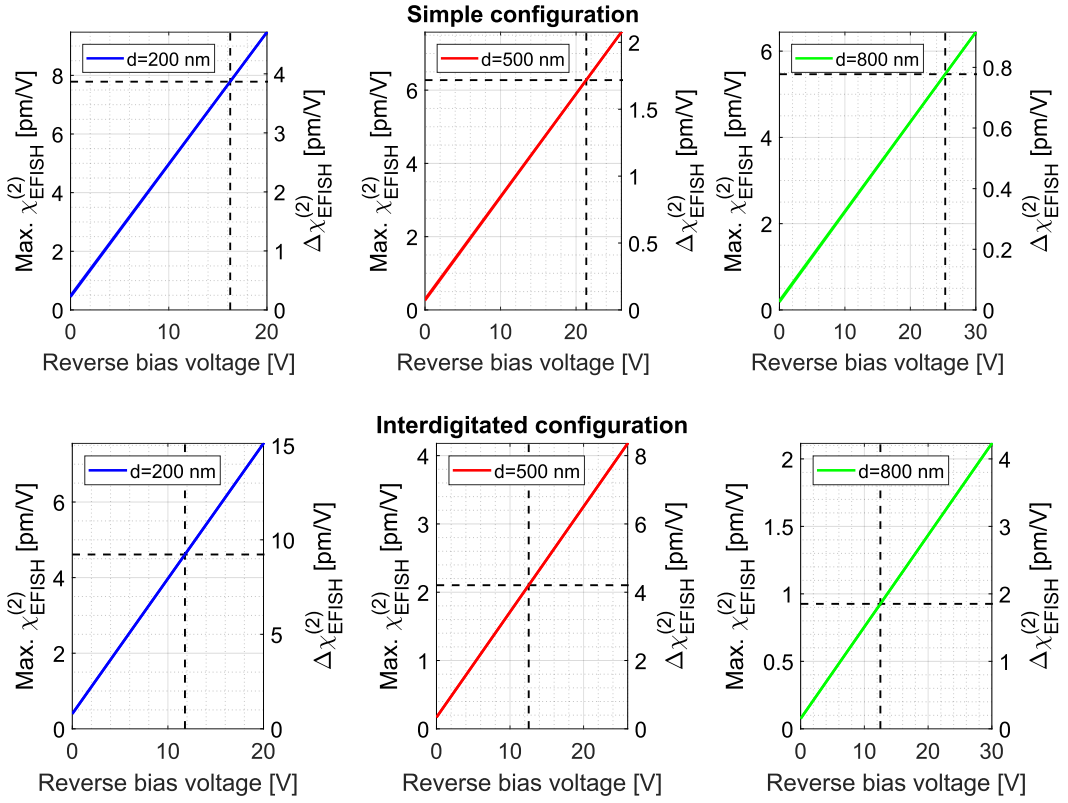


Fig. 9.26: Maximum value of $\chi_{\text{EFISH}}^{(2)}$ and $\Delta\chi_{\text{EFISH}}^{(2)}$ evaluated in the center of the waveguide along the z direction for both the simple and the interdigitated situations and for all the d values. The simulations refer to the waveguide geometry reported in the first line of Tab. 9.1.

9.4 Estimation of the SHG and SPDC efficiency

In the previous section, the strength of $\chi_{\text{EFISH}}^{(2)}$ has been evaluated along z . Now, these results can be used to quantify the conversion efficiencies of both the SHG and the SPDC process. For simplicity, in this case the distribution of $\chi_{\text{EFISH}}^{(2)}$ within the waveguide cross-section is assumed constant, and equal to the value in the center. As it is visible from Fig. 9.16, this is not really true. However, this approximation is done for simplicity, to give a first order approximation of the powers that can be obtained from such a geometry. Moreover, it is assumed that the factorization expressed by Eq. (9.1) is valid, and a sinusoidal shape is taken for $s(z)$. Following the discussions of the previous sections, this is really true only for the interdigitated configuration. However, this is considered valid also for the simple configuration. Within this framework, the second order nonlinear coefficient can be factorized out from the integral of Eq. (9.2). Moreover, the integral of Eq. (9.7) simply results $1/4$. By taking a continuous wave pump and by considering the undepleted pump approximation, the SHG and the SPDC generated powers can be evaluated using Eq. (9.6) and Eq. (9.8). The main results are shown in Tab. 9.2 and in Tab. 9.3, referring (respectively) to the cases of an unpolarized junction and to the case of the

maximum reverse bias voltage. In both the tables, the waveguide length L is 1 cm, with 1 mW pump power for both the SHG and the SPDC processes. The results refer to the configuration shown in the first line of Tab. 9.1.

Tab. 9.2: SHG and SPDC power evaluated for the different configurations and referred to unbiased junctions. The results refer to a 1 cm long waveguide and to a pump power of 1 mW, for the waveguide geometry of the first line of Tab. 9.1.

Config.	Rev. bias voltage [V]	$\chi_{\text{EFISH}}^{(2)}$ maximum [pm/V]	$\Delta\chi_{\text{EFISH}}^{(2)}$ [pm/V]	P_{sh} [pW]	P_{SPDC} [fW]
i-200	0	0.40	0.79	217	1700
s-200	0	0.44	0.24	20	157
i-500	0	0.17	0.34	40	315
s-500	0	0.26	0.08	2	17
i-800	0	0.08	0.15	8	61
s-800	0	0.18	0.03	0.3	2

Tab. 9.3: SHG and SPDC power evaluated for different junction configurations. The results refer to the maximum reverse bias voltage that can be applied before reaching the breakdown field in silicon, which is reported in the second column of the table. The results refer to a 1 cm long waveguide and to a pump power of 1 mW, considering the waveguide geometry reported in the first line of Tab. 9.1.

Config.	Rev. bias voltage [V]	$\chi_{\text{EFISH}}^{(2)}$ maximum [pm/V]	$\Delta\chi_{\text{EFISH}}^{(2)}$ [pm/V]	P_{sh} [nW]	P_{SPDC} [pW]
i-200	11.8	4.61	9.22	29.6	231
s-200	16.3	7.78	3.87	5.2	40.8
i-500	12.5	2.10	4.21	6.1	48.3
s-500	21.3	6.27	1.72	1.0	8.1
i-800	12.5	0.93	1.85	1.2	9.3
s-800	25.3	5.46	0.78	0.2	1.7

Table 9.2 shows that a measurable generated signal is possible also for the unbiased situation, for both SHG and SPDC. Considering the geometry of the system and the experimental configurations analyzed here, SHG conversion efficiency is almost two orders of magnitude larger than SPDC. Clearly, the conversion efficiency is lower in the case of the simple configuration, as well as for large values of d .

A similar trend is visible from Tab. 9.3. In this case, the applied reverse bias is the one that provides the breakdown field within silicon, as estimated in Sec. 9.3.4. In both the cases, the conversion efficiency is much stronger for the polarized junction than for the unbiased one. In fact, as it is shown in Fig. 9.26, the second order nonlinearity linearly changes with bias. Considering that both the SHG and the SPDC conversion efficiencies depend quadratically on the second order nonlinearity, the generated power is expected to grow quadratically with bias.

Demonstration of SHG in silicon waveguides with lateral doping

10.1	The realized devices	175
10.2	Electrical characterization	177
10.3	Experimental characterization of SHG	178
10.3.1	Dependence on the pump wavelength	178
10.3.2	Dependence on the pump power	179
10.3.3	Dependence on the waveguide length	179
10.3.4	Dependence on the applied voltage	181
10.4	Comparison between the experiment and simulations	182
10.4.1	Phase-matching wavelength	183
10.4.2	SH power	184
10.5	Conclusions and perspectives	186

This chapter reports on the experimental characterization of SHG in the silicon waveguides with lateral doping engineered in the previous chapter. The same experimental setup described in chapter 5 is used. First, in Sec. 10.1, images of the realized structures are shown. In Sec. 10.2, the lateral junctions are electrically characterized. Then, in Sec. 10.3, the SHG process is characterized. In Sec. 10.4 the experimental results are compared with simulations. Finally, in Sec. 10.5 the main results of this chapter are summarized, showing also perspectives for future developments, aimed both at showing a better characterization of the SHG process and to perform SPDC measurements.

The experiments described in this chapter have been realized with Mr. R. Franchi. The samples have been produced by Dr. M. Ghulinyan at Fondazione Bruno Kessler.

10.1 The realized devices

Like the structures of chapter 8, the waveguides described in this chapter are defined using a 365 nm UV lithography, and are realized by reactive ion etching. Figure 10.1 shows an optical image of the chip before the implantation of n-type ions. The figure shows different geometries of the waveguide. The one on the left is an interdigitated waveguide. The one in the middle, refers to an interdigitated waveguide with higher

order poling. The one on the right shows waveguides in the simple configuration (n-type doping is present only on one side of the waveguide).

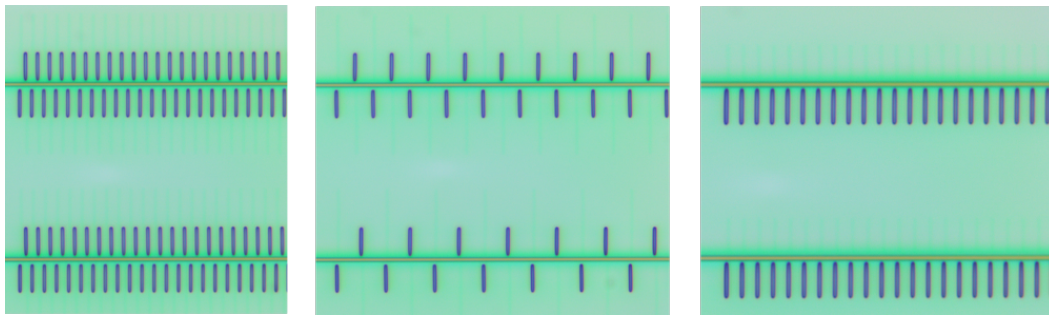


Fig. 10.1: Optical image of the chip before the implantation of n-type ions, showing different geometries of the waveguide: interdigitated configuration (left), interdigitated waveguide with higher order poling (center) and simple configuration (right). Image courtesy of Dr. M. Ghulinyan.

After realizing the doped regions, a 200 nm high oxide layer was deposited on the top of some doped region, to prevent contacting the junction in the wrong place. Then, a $1.5\mu\text{m}$ thick oxide layer is deposited everywhere. Finally, contact holes are realized to access the doped regions. Figure 10.2 shows part of the chip after realizing these holes. The vertical bars visible in some holes are the oxide layers realized to prevent contact.

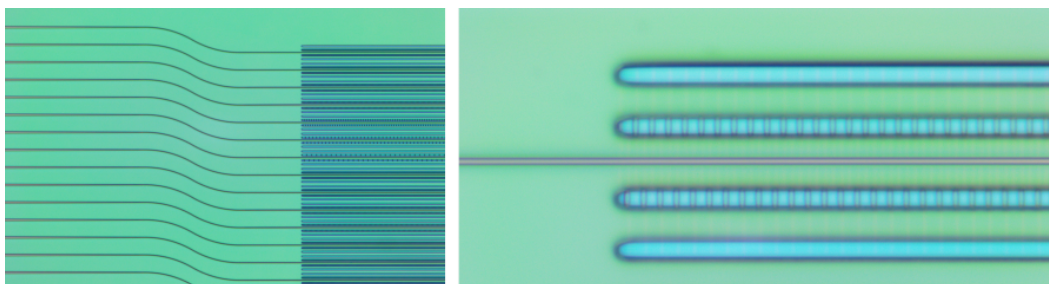


Fig. 10.2: Chip after the realization of the contact holes. Image courtesy of Dr. M. Ghulinyan.

Finally, aluminum layers are deposited. An example of this is shown in Fig. 10.3.

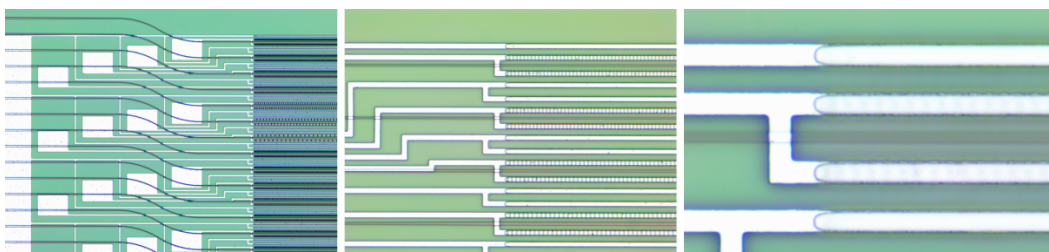


Fig. 10.3: Metallic layers deposited on the top. Image courtesy of Dr. M. Ghulinyan.

10.2 Electrical characterization

Before dealing with the optical characterization, the waveguides designed to perform SHG and SPDC are electrically analyzed. To this purpose, I-V curves are measured, considering both the simple and the interdigitated configurations.

Figure 10.4 shows the I-V curves measured on waveguides in the simple configuration, referred to the three values of d . When inversely polarized, a current in the range $10\ \mu\text{A}$ to $20\ \mu\text{A}$ flows in the junction. This value is much larger than the one measured in Sec. 8.5 on racetrack resonators, which was below $1\ \mu\text{A}$. However, in this case the size of the junction is much larger, since it corresponds to the waveguide length (about 17 mm), while in the previous situation it was given by the resonator perimeter (less than 1 mm).

Figure 10.4 shows also the breakdown region for all the junction geometries. The breakdown voltage V_b is about 37 V for the junction $d = 200\ \text{nm}$, 43 V for $d = 500\ \text{nm}$ and 47 V for $d = 800\ \text{nm}$. These values are larger than the ones reported in Sec. 9.3.4, which were respectively 16 V, 21 V and 25 V. They were estimated from a 3D simulation of the junction. This approach worked properly in the case of the resonator with lateral junctions reported in Sec. 8.5. However, in Sec. 9.3.4 it was already reported that the estimation should have been considered as a lower bound of V_b . In fact, the maximum electric field causing breakdown was determined by the sharp edge formed by the doped regions. However, in the realized devices the edges can be less sharp. Therefore, it is reasonable that the experimental breakdown voltage V_b is larger than the one estimated in Sec. 9.3.4.

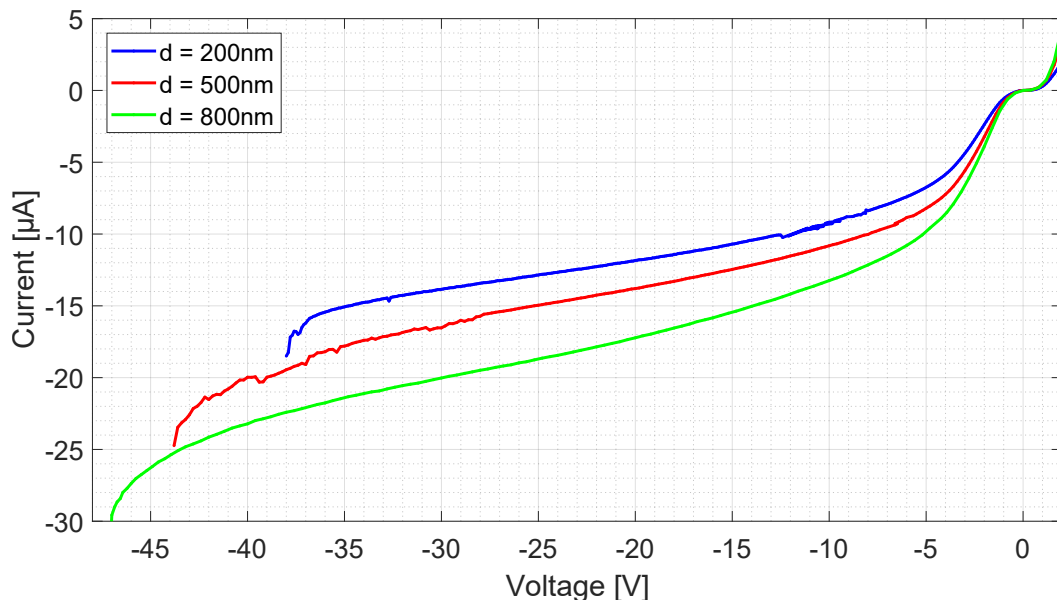


Fig. 10.4: I-V curves measured on three waveguides in the simple configuration referred to different d . The measurements are performed on waveguide number 7 of Tab. 9.1.

Figure 10.5 reports the same measurement of Fig. 10.4, but referred to the interdigitated configuration with $d = 200$ nm. The two measurements refer to two nominally identical waveguides realized separately on two different wafers. In the forward bias, the two devices show a reasonable behavior. However, the structures show a strange behavior when reversely biased. In fact, a large current flows in the circuit, even if it is a little bit smaller than in the case of the forward bias. In one of the two devices, for small reverse bias voltages, it is possible to recognize the plateau that typically characterizes reversely polarized junctions. However, as soon as the voltage is increased, also the current increases enormously. This seems to indicate that, besides the junction, other channels where current can flow are present.

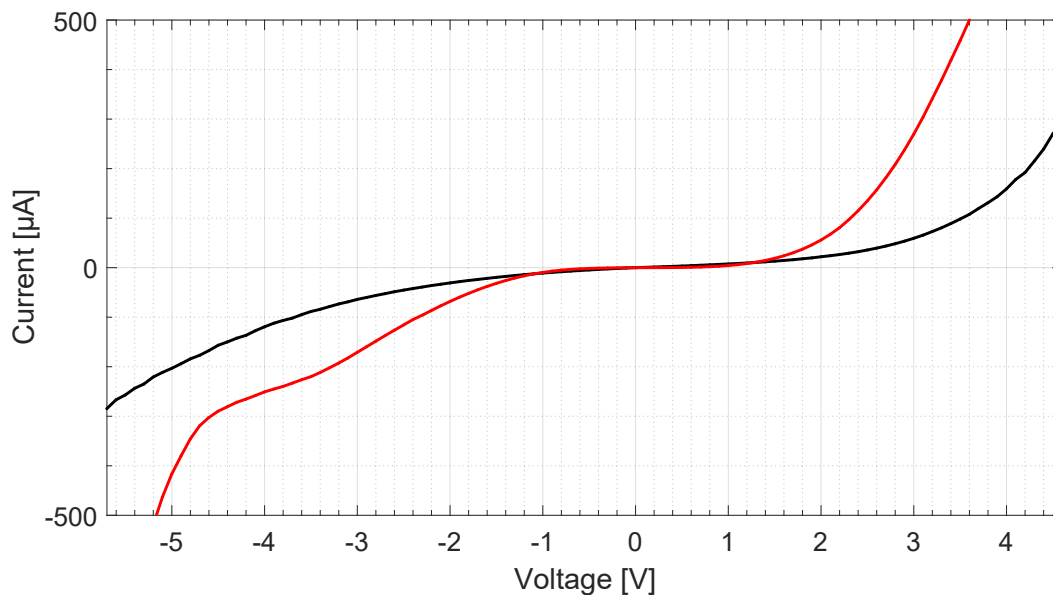


Fig. 10.5: I-V curves measured on two nominally identical waveguides with $d = 200$ nm realized on two different wafers. The measurements refer to the waveguide number 7 of Tab. 9.1.

10.3 Experimental characterization of SHG

The characterization of SHG is performed using the same setup of chapter 5.

10.3.1 Dependence on the pump wavelength

Figure 10.6 reports the experimental dependence of the average SH power on the pump wavelength λ_f . The measurement is performed on a 15.7 mm long waveguide, whose geometry is identified by number 4 in Tab. 9.1. The waveguide presents lateral doping in the simple configuration and $d = 200$ nm, with no applied bias

voltage. The clear peak present for $\lambda_f \sim 2291$ nm demonstrates the satisfaction of the phase-matching.

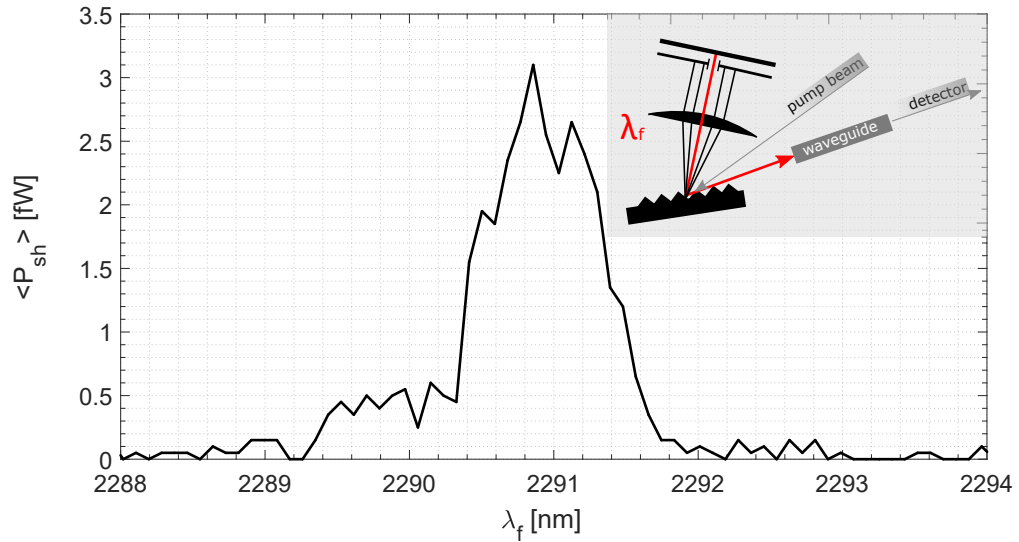


Fig. 10.6: On-chip average SH power as a function of the pump wavelength λ_f . The inset shows a sketch of the experimental apparatus used to perform this measurement. The measurement refers to a 15.7 mm long waveguide, whose geometry is identified by number 4 in Tab. 9.1. The waveguide presents lateral doping in the simple configuration, $d = 200$ nm and no applied bias voltage.

10.3.2 Dependence on the pump power

Figure 10.7 reports the on-chip average SH power $\langle P_{sh} \rangle$ as a function of the average pump power $\langle P_f \rangle$ in a log-log scale. The linear fit provides a slope of 1.8 ± 0.2 , which matches the value of 2 predicted by theory. The measurement refers to a 1.68 mm long waveguide, whose geometry is identified by number 1 in Tab. 9.1. The waveguide is in the simple configuration with $d = 200$ nm and no applied bias.

10.3.3 Dependence on the waveguide length

SHG theory predicts that, in absence of losses, the generation efficiency should grow quadratically with the waveguide length L . The model shown in Sec. 4.3, which describes the propagation of optical pulses in waveguides under the effect of SHG, shows that the presence of large propagation losses strongly affects this behavior. In the situation of chapter 5 propagation losses were about 8 dB/cm, providing a non-trivial dependence of the SHG efficiency on L . Moreover, the presence of such a large amount of losses prevented to collect detectable signals at the output of long waveguides. In the experiment shown in this chapter, propagation losses are much smaller (about 2.4 dB/cm estimated via cut-back method). Therefore, this allows

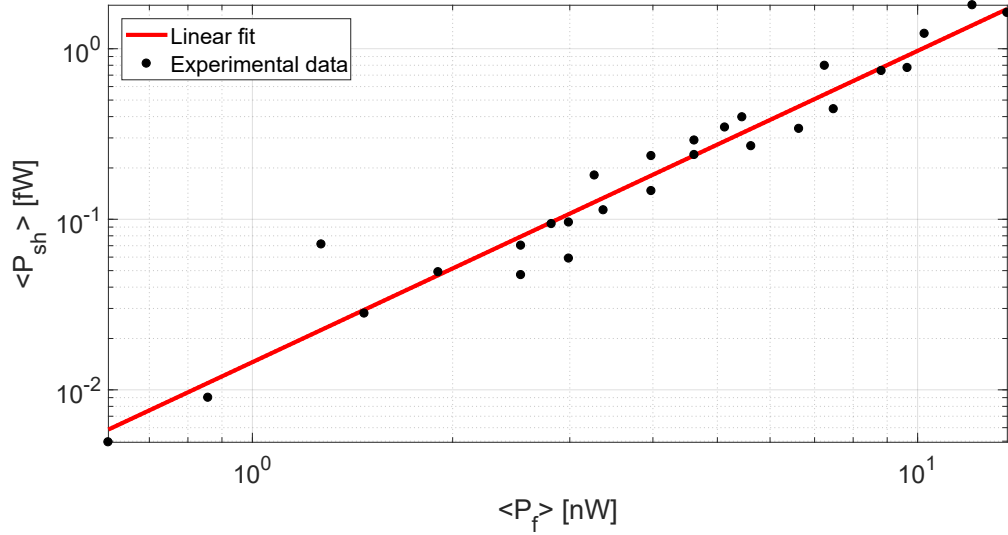


Fig. 10.7: On-chip SH power as a function of the on-chip pump power. Results are reported in a log-log scale and are fitted by a straight line. The measurement is performed on a 1.68 mm long waveguide in the simple configuration with $d = 200$ nm, whose geometry is identified by number 1 in Tab. 9.1, with no applied bias.

testing longer waveguides, enabling to recover the quadratic dependence of the SH power on L .

Due to the small dynamic range of the SPAD detector, the measurements taken during this experiment refer often to different pump powers. To compare different measurements, it is then necessary to normalize them over the pump power. Since the SH power is expected to grow quadratically with the pump power, it is useful defining the peak conversion efficiency η and the average conversion efficiency η_{av} as:

$$\eta = \frac{P_{sh}}{P_f^2} \quad \eta_{av} = \frac{\langle P_{sh} \rangle}{\langle P_f \rangle^2} \quad (10.1)$$

Figure 10.8 reports both η and η_{av} as a function of L . The measurements are referred to the waveguide number 1 of Tab. 9.1 in the simple configuration, with $d = 200$ nm, without applying any bias voltage. The experimental data are fitted by a quadratic curve.

A similar result is shown in Fig. 10.9, referred to the same waveguide but to the interdigitated configuration.

One can note also that SHG process in the interdigitated configuration is more efficient than in the simple configuration. Comparing Fig. 10.9 with Fig. 10.8, almost one order of magnitude larger efficiency is estimated in the interdigitated configuration than in the simple configuration. This fact is well predicted by the simulations of chapter 9. In fact, Tab. 9.2 shows that in the interdigitated configuration the $\chi_{EFISH}^{(2)}$ amplitude is almost 3 times larger than in the simple configuration for $d = 200$ nm. Since the SHG efficiency depends quadratically on the $\chi_{EFISH}^{(2)}$ amplitude, it is reasonable that in the interdigitated configuration the SHG efficiency is almost

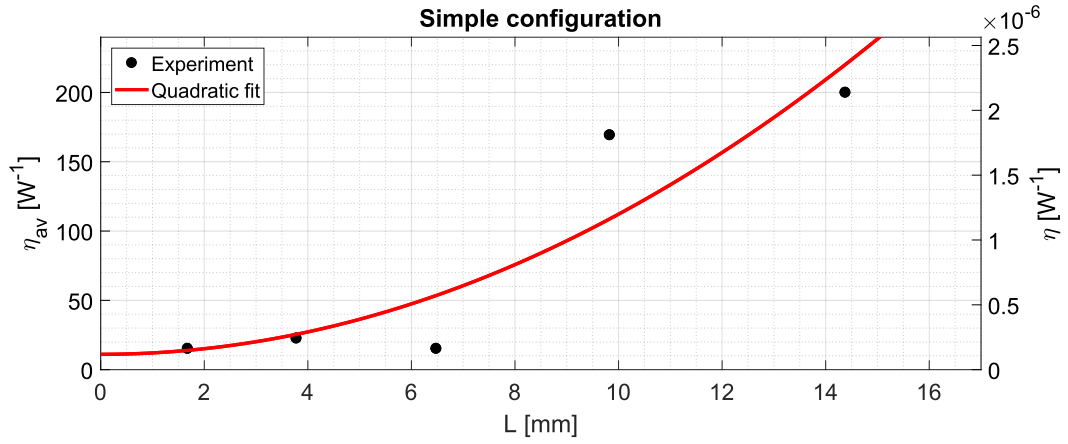


Fig. 10.8: Conversion efficiencies η and η_{av} as a function of the waveguide length L , referred to the waveguide number 1 of Tab. 9.1 in the simple configuration with $d = 200$ nm, without applying any bias voltage to the junction.

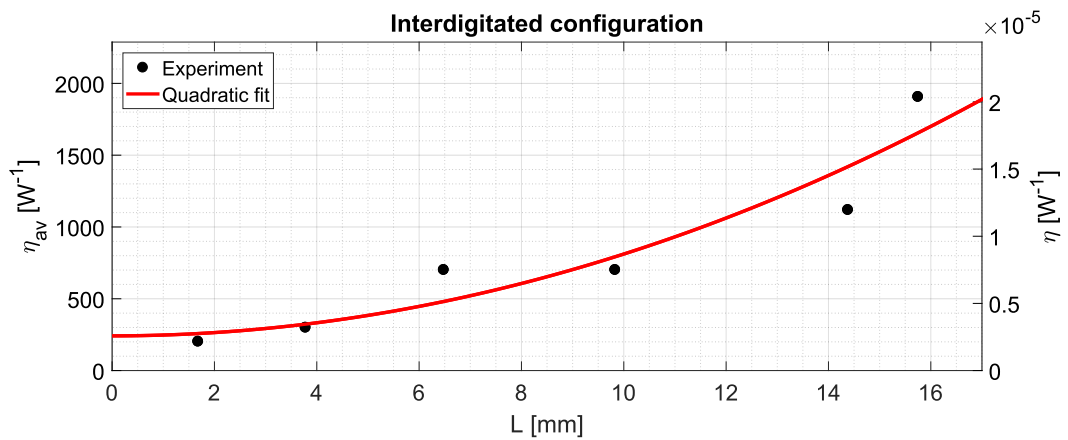


Fig. 10.9: Conversion efficiency η as a function of the waveguide length, referred to the waveguide number 1 of Tab. 9.1 in the interdigitated configuration with $d = 200$ nm, without applying any bias voltage to the junction.

one order of magnitude larger than in the simple configuration.

The results of Fig. 10.9 demonstrate that the waveguides work well also in the interdigitated configuration. Even if the current flowing in the circuit when the junction is reversely polarized is surprisingly high, the unbiased junctions seems to be unaffected by this problem.

10.3.4 Dependence on the applied voltage

The measurements reported so far refer to situations where no bias is applied to the junctions. Therefore, the generation is due to the field induced by the built-in potential of the junction. However, the generation is expected to increase a lot if the field within the junction is increased. In particular, the results of simulations reported in Fig. 9.26 show that the amplitude of the nonlinear coefficient $\chi_{EFISH}^{(2)}$ varies linearly with the applied reverse bias voltage. Therefore, since the generation

efficiency grows quadratically with $\chi_{\text{EFISH}}^{(2)}$, the SH power is expected to grow quadratically also with the applied reverse bias voltage. Figure 10.10 shows the SH power as a function of the reverse bias voltage applied to the waveguide number 1 of Tab. 9.1 in the simple configuration with $d = 200$ nm. The experimental results are well fitted by a quadratic curve.

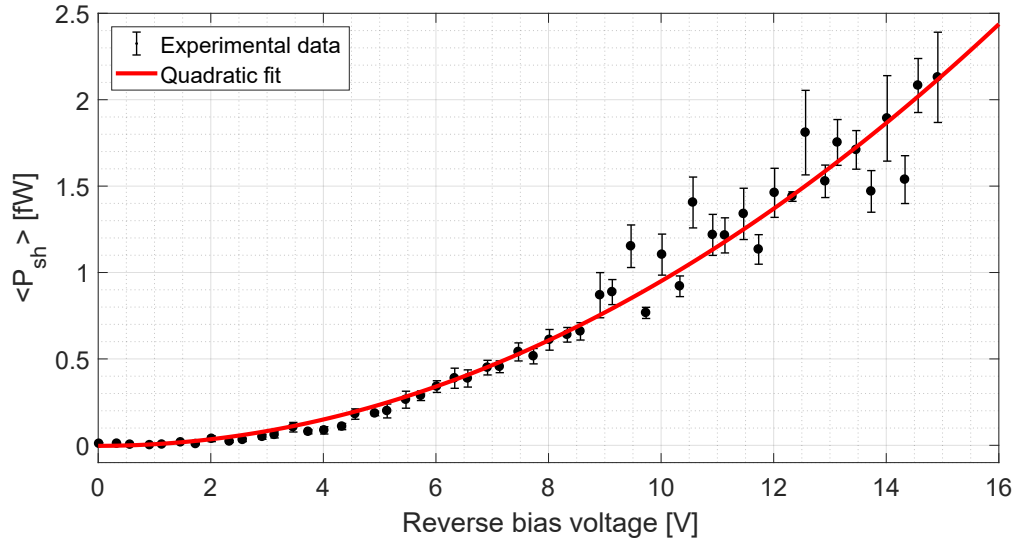


Fig. 10.10: SH power as a function of the applied reverse bias voltage for the waveguide number 1 of Tab. 9.1 in the simple configuration with $d = 200$ nm. Errorbars result from repeated measurements.

A similar result is shown in Fig. 10.11, referred to the interdigitated configuration. The applied bias voltage is kept below 3.5 V because of the large current flowing in the system when polarizing it. However, good agreement with a quadratic fit is shown also in this case. This demonstrates that, when the circuit is polarized, the p-n junction is reversely biased in the proper way. Therefore, the large current does not flow through the junction, but on a different channel. This is confirmed also by the fact that, when biasing the junction, the amount of propagation losses does not vary significantly. If the current was flowing in the waveguide, this would have strongly affected the carrier density, and so the propagation losses.

10.4 Comparison between the experiment and simulations

In this section, the experimental results are compared with the ones resulting from simulations. First, the comparison is done considering the phase-matching wavelength. Then, the experimental and the simulated SHG efficiencies are compared.

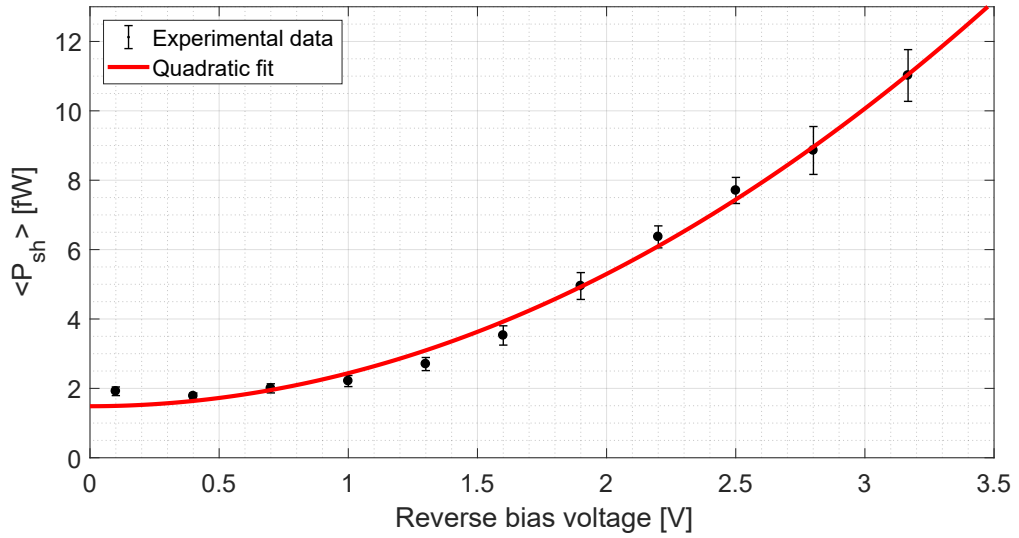


Fig. 10.11: SH power as a function of the applied reverse bias voltage for the waveguide number 1 of Tab. 9.1 in the interdigitated configuration with $d = 200$ nm. Errorbars result from repeated measurements.

10.4.1 Phase-matching wavelength

Figure 10.12 reports the experimental phase-matching wavelengths $\lambda_{f,exp}$ as a function of the phase-matching wavelength predicted by simulations $\lambda_{f,th}$. The different points refer to the different waveguide configurations analyzed in this work. The numbers in the plot indicate the corresponding configuration number shown in Tab. 9.1. The black dashed line represents the ideal value (so, $\lambda_{f,exp} = \lambda_{f,th}$).

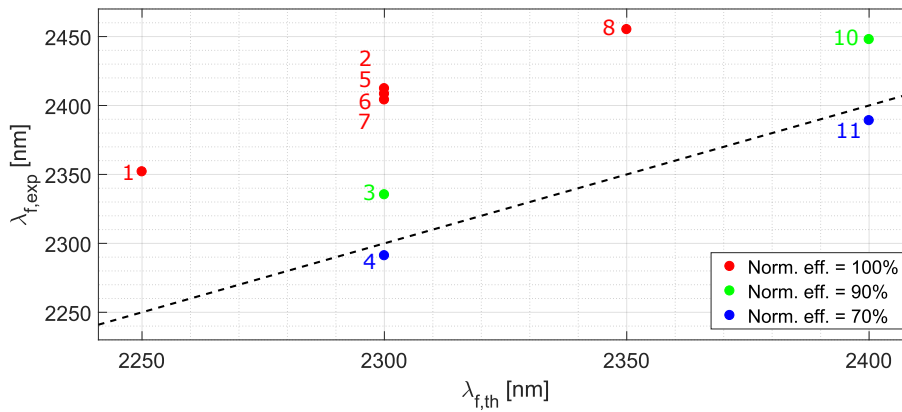


Fig. 10.12: Experimental phase-matching wavelengths $\lambda_{f,exp}$ as a function of the simulated phase-matching wavelength $\lambda_{f,th}$. The different points refer to the different waveguide configurations analyzed in this work. The numbers indicate the configuration number shown in Tab. 9.1. The black line represents the ideal value.

Consider first the configurations number 1, 2 and 8 (red dots). These are the standard configurations, designed to provide conversion efficiencies at the wavelengths of 2250 nm, 2300 nm and 2350 nm. Figure 10.12 shows that the experimental phase-

matching wavelength is shifted of almost 100 nm towards longer wavelengths with respect to simulations. This can be caused by fabrication inaccuracies. In fact, in Sec. 9.2 it has already been shown that, if the geometry of the realized devices differs from the design, this causes a shift of the phase-matching wavelength.

Consider now the configurations 3 and 4 (or, analogously, 10 and 11). These waveguides should provide the 90% and the 70% of the maximum achievable efficiency, but they work on larger waveguides. So, they should be less affected by fabrication uncertainties. This is confirmed by the experiment, which shows that in these waveguides the phase-matching wavelength is closer to simulation.

Consider now the configurations 2, 5, 6 and 7. In these cases, the waveguide geometry is the same, but the poling order m varies. The experimental results show that the phase-matching wavelength does not change with m . This allows to conclude that the variability of the phase-matching wavelength does not depend on variations of the poling period (and so of the poling order), but is mostly due to variations of the waveguide geometry.

Figure 10.13 reports the simulated phase-matching wavelength as a function of the waveguide width w and the poling period Λ . The black point shows the geometry represented by number 8 in Tab. 9.1, which provides phase-matching for a pump wavelength of 2350 nm. The black lines represent variations of 50 nm on both w and Λ . The red line represents the value measured experimentally, namely 2455 nm. The figure shows that the measured value can be ascribed to a reduction of w of about 50 nm, or to an enlargement of Λ of about 40 nm, or to a combinations of these effects. Also other effects can cause a similar modification, such as differences between the actual refractive indexes and the ones used in the simulation, or variations of both the rib and the slab waveguide height. However, it is not possible to disentangle variations on height and width since they both cause a modification of the mode effective index, and so a modification of the phase-matching wavelength. Since fabrication uncertainties affect mainly the waveguide width rather than the height, for simplicity height variations have not been considered here.

Figure 10.14 reports the same quantities of Fig. 10.13, referred to the geometries represented by numbers 2, 3 and 4 in Tab. 9.1. The figure reports the theoretical results for all the configurations, while the red contour lines show the experimental values. The theoretical results and the experiment show good agreement, especially for larger values of w .

10.4.2 SH power

The analytic evaluation of the SHG efficiency requires to solve Eq. (9.4). Like in Sec. 4.3, this can be done by using the split-step method.

The model uses parameters that come both from FEM simulations (propagation constants, group indices, modal profiles) and from experimental measurements

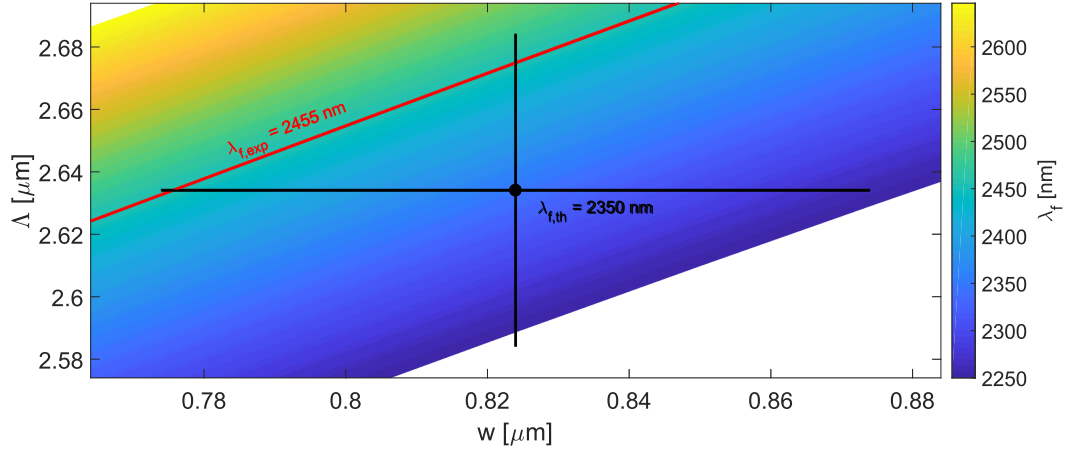


Fig. 10.13: Simulated phase-matching wavelength as a function of w and Δ . The black point represents the nominal geometry (number 8 in Tab. 9.1), while the black lines represent variations of 50 nm on both w and Δ . The red line corresponds to the value measured experimentally.

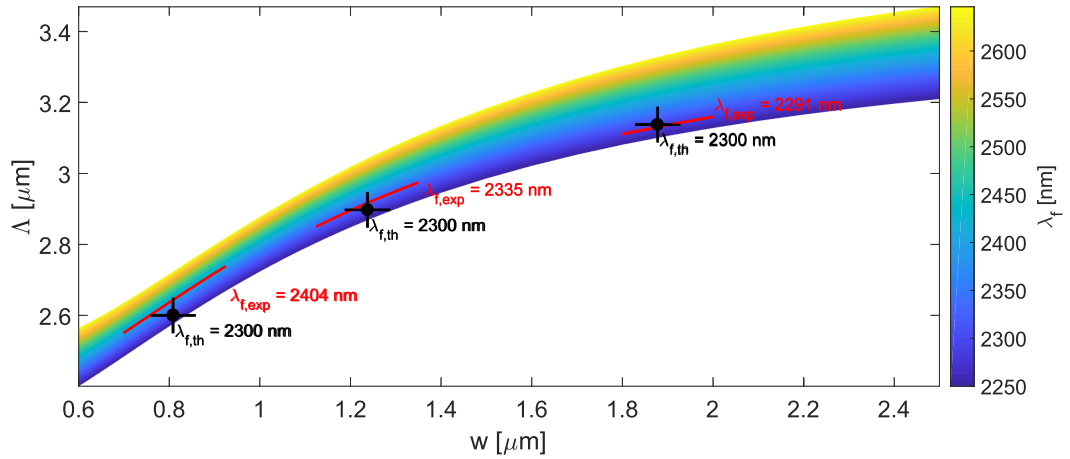


Fig. 10.14: Simulated phase-matching wavelength as a function of w and Δ . The black points represent the geometries represented by numbers 2, 3 and 4 in Tab. 9.1, while the black lines represent variations of 50 nm on both w and Δ . The red lines are the contour lines corresponding to the values measured experimentally.

(refractive indexes, propagation losses). The pump loss coefficient is estimated by cut-back method, and is about 2.4 dB/cm. For simplicity, the SH loss coefficient is taken equal to the pump loss coefficient.

The equations (9.4) contain the coefficient $\tilde{\gamma}_i^{(2)}$. Equation (9.3) shows that $\tilde{\gamma}_i^{(2)}$ is proportional to $\tilde{\Gamma}^{(2)}$, which is defined by Eq. (9.2). The term at the numerator of the coefficient $\tilde{\Gamma}^{(2)}$ contains an overlap integral between the optical modes and $\chi^{(2)}(\mathbf{r}_\perp)$, namely the distribution of the second order nonlinear coefficient in the waveguide cross-section plane. As already discussed in Sec. 9.3, this quantity is evaluated starting from a 3D electric FEM simulation of the waveguide. The amplitude of the modulation of $\chi^{(2)}$ in the middle of the waveguide is taken as an approximation of $\chi^{(2)}(\mathbf{r}_\perp)$. Moreover, the poling function $s(z)$ is taken sinusoidal with the period of the poling. As already discussed in Sec. 9.3, this is a good approximation in the

case of the interdigitated situation. To evaluate $\chi^{(2)}$, the DC field distribution $E_{DC,x}$ is first evaluated. Then, $\chi^{(2)}$ is evaluated as $3\chi_{xxxx}^{(3)}E_{DC,x}$. However, as already discussed, the values of $\chi_{xxxx}^{(3)}$ reported in literature are ambiguous and show a big spread, showing values in the range $0.94 \times 10^{-19} \text{ m}^2/\text{V}^2$ to $4.24 \times 10^{-19} \text{ m}^2/\text{V}^2$ [81, 162, 163]. The calculations performed in chapter 9 consider a mean value of these quantities. In this case, the simulations are performed taking both these quantities, in order to find an interval of admitted SHG efficiencies.

Figure 10.15 reports a comparison between the simulated and the experimental SHG efficiencies as a function of the waveguide length L . The results are referred to both the simple and the interdigitated configurations. The results are referred to the waveguide number 1 in Tab. 9.1 with $d = 200 \text{ nm}$, without applying any bias. The solid lines represent the SHG efficiencies evaluated using the upper and the lower bound of the values of $\chi_{xxxx}^{(3)}$ reported in literature. The results show that the experimental data follow the same behavior predicted by simulations. The experimental data and the simulated ones are comparable by taking the smallest $\chi_{xxxx}^{(3)}$ value reported in literature.

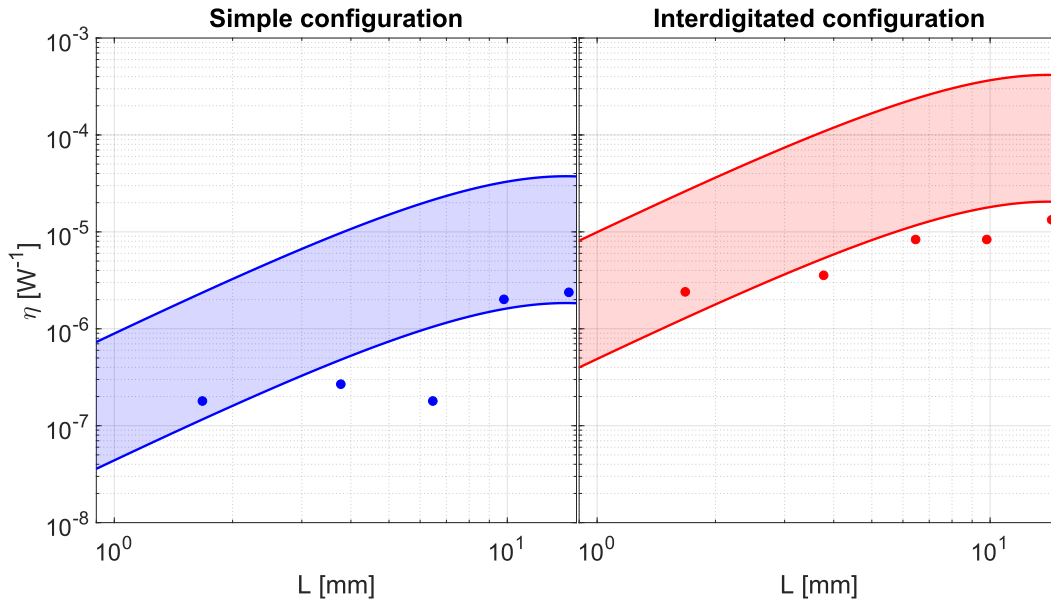


Fig. 10.15: Comparison between the simulated (solid) and the experimental (scatter) SHG efficiencies as a function of the waveguide length L , for the waveguide number 1 in Tab. 9.1 with $d = 200 \text{ nm}$, without applying any bias voltage to the junction. The solid lines represent the SHG efficiencies evaluated using the upper and the lower bound of the values of $\chi_{xxxx}^{(3)}$ reported in literature.

10.5 Conclusions and perspectives

In this chapter, the experimental characterization of SHG in silicon waveguides with lateral p-n junctions has been shown. The reported results demonstrate the expected

quadratic behavior with the pump power, with the applied reverse bias voltage and with the waveguide length. The main experimental outcomes of this chapter are reported in Tab. 10.1, with the comparison to the results reported in [125]. In [125], the authors use waveguides in the simple configuration. One can see that the experimental efficiencies measured in this thesis are smaller than the one reported in [125]. This discrepancy can be partially attributed to the different waveguide geometry. In particular, in [125] the total waveguide height is 220 nm, while in the case of this thesis it is 490 nm. This determines a smaller modal confinement and, in turn, a smaller conversion efficiency. However, this geometric difference is not enough to justify such a large discrepancy. In [125], the authors model the SHG process assuming that the poling function varies abruptly along the waveguide propagation direction, passing from its maximum value (in between the junction) to 0 (when there is no junction). The 3D FEM simulation shown in this thesis demonstrates that this is not the case: the transition is not abrupt (it shows a sinusoidal shape) and the poling function is not 0 where there is no junction. Using a more reasonable poling function, the simulated conversion efficiencies are much smaller than the ones experimentally measured in [125]. Moreover, even if they use a poling function which overestimates the SHG conversion efficiency, in [125] the authors need to use the largest $\chi^{(3)}$ value reported in the literature to reproduce their experimental data. In the end, using the simulation tool proposed in this thesis, the SHG efficiency experimentally demonstrated in [125] is too large for being totally attributed to the EFISH caused by the junctions. On the contrary, by using the smallest $\chi^{(3)}$ value reported in literature, the model reproduces well the experimental data reported in this thesis. It can be noted that the efficiency improvement from the 0 V to the 20 V case in both measurements is almost the same (three orders of magnitude).

Tab. 10.1: Main experimental outcomes of this chapter regarding SHG in silicon waveguides with lateral p-n junctions. Results are compared to the ones of [125].

Config.	L [mm]	Rev. bias [V]	η [W ⁻¹]	$\Delta\chi_{\text{EFISH}}^{(2)}$ [pm/V]
s-200	4	0	4×10^{-7}	0.08
s-200	4	20	5×10^{-4}	2.7
i-200	4	0	4×10^{-6}	0.28
i-200	4	3	1.6×10^{-5}	0.56
[125]	1	0	5×10^{-4}	2.5
[125]	1	21	0.13	41

Table 10.2 reports the main results of chapter 5 on the measurement of SHG in strained silicon waveguides. In the case of waveguides with lateral p-n junctions, the SHG efficiency is much larger, even considering the simple configuration and no applied bias. This has to be attributed to the use of intermodal phase-matching in the strained waveguides. This determines a small mode overlap and, in the end, a smaller conversion efficiency. Comparing the $\chi^{(2)}$ values, with a 20 V bias voltage

the poled waveguide in the simple configuration shows a nonlinear coefficient about 5 times larger than the strained silicon waveguide. Using the interdigitated configuration, 3 V are enough to have the same $\chi^{(2)}$ value demonstrated in strained silicon.

Tab. 10.2: Main experimental outcomes of results of chapter 5, referred to the measurement of SHG in strained silicon waveguides. Even if $\chi_{\text{eff}}^{(2)}$ is comparable in the two cases, η is smaller for the combination involving generation on the higher order mode due to the worst mode overlap with the pump.

Config.	L [mm]	η [W ⁻¹]	$\chi_{\text{eff}}^{(2)}$ [pm/V]
TE1-TM3	4	2×10^{-7}	0.46 ± 0.06
TE1-TM5	4	2×10^{-8}	0.6 ± 0.1

To characterize better the SHG process in waveguides with lateral p-n junctions, the possibility of using a continuous-wave pump source should be considered. On the one hand, this would offer a more stable and simpler experimental setup. On the other hand, this would provide a narrow linewidth, which would allow to investigate the SHG bandwidth. Even if a continuous-wave laser would provide a smaller peak power, the simulation results reported in Tab. 9.2 and 9.3 show that a detectable signal should be generated. Using a more stable and simple setup will allow also studying the dependence of the SH signal on the poling order m and on the distance d between the waveguide and the junction.

In this chapter, SHG has been demonstrated using both the simple and the interdigitated configurations. However, increasing the reverse bias voltage, a large current flows in the interdigitated waveguide system. This large current flow does not affect the optical properties of the waveguide, and the SHG intensity varies correctly with the applied bias. However, to properly demonstrate the potential of this system, the origin of this large current flow should be understood and possibly limited.

The structures demonstrated in this chapter use a periodic poling of the p-n junctions to introduce QPM. This determines a large conversion efficiency, because it involves the conversion between fundamental modes. However, this system has also some drawbacks. One derives from the use of rectangular doped regions with sharp edges. The simulations of Sec. 9.3 show that this determines a large electric field close to the edges, resulting in a smaller breakdown voltage of the system. To prevent this, one could use continuous doped regions with variable distance. In this way, the applied DC field varies along the waveguide propagation direction, being smaller where the distance is larger and larger when the distance is smaller. Another drawback derives from the fact that, in the QPM approach, the usable nonlinearity is the amplitude of the $\chi^{(2)}$ variation along the waveguide propagation direction. Especially in the simple configuration, the average $\chi^{(2)}$ is large, but its amplitude variation is weaker. This limits strongly nonlinear conversion. This fact would benefit from the use of an intermodal approach. In this case, even if the mode overlap determines a smaller conversion efficiency, one can take advantage of the entire $\chi^{(2)}$ strength.

Finally, other interesting perspectives are offered by the use of microresonators. In microresonators the nonlinear interaction is increased by the field enhancement inside these structures. In [127], the authors propose a design of a resonator that uses a periodic distribution of p-n junctions, and demonstrate that SHG efficiency can be enhanced from 4 to 50 times with respect to the straight waveguide configuration depending on the microresonator geometry. This approach can have interesting application for the realization of resonator-based nonlinear processes, like the frequency comb mediated by $\chi^{(2)}$ [171].

SHG and SPDC in silicon oxynitride waveguides

11.1 Waveguide cross-section	191
11.2 The DC field inside the waveguide	193
11.3 The required poling period	194
11.4 Conversion efficiency	198

In the previous chapters, lateral p-n junctions have been demonstrated as a technology able to introduce second order nonlinearities in silicon. In this chapter, other structures are proposed to introduce the same effect in waveguides on a CMOS platform. In this case, waveguides are done not by silicon, but by **silicon oxynitride** (SiON) [70]. This material is **transparent in the visible**. This allows performing SHG processes using a pump at about 1550 nm, generating the SH signal at about 775 nm. SiON offers also the advantage of being **free from two photon absorption**, which typically limits the power coupled in silicon waveguides. However, also two big drawbacks affect the performances of this material. The first one is the **small third order nonlinear coefficient** of SiON, about two orders of magnitude below than that of silicon [70]. Moreover, since SiON is not a semiconductor, p-n junctions cannot be used to induce the DC field. Therefore, the DC field is introduced by **metallic pads** realized on the top of the waveguide cladding.

Section 11.1 describes the cross section of the waveguides. Section 11.2 describes the way used to estimate the DC field induced within the waveguide. Then, in Sec. 11.3 the method used to evaluate the poling period is described. Finally, in Sec. 11.4 the conversion efficiencies of both SHG and SPDC are evaluated.

11.1 Waveguide cross-section

The cross-section of the waveguides analyzed in this chapter is shown in Fig. 11.1. It is formed by a 550 nm-high SiON waveguide, whose cladding is formed by a 950 nm-high BPSG layer and a 1500 nm-high layer of oxide PECVD. The waveguide width w is optimized to optimize the conversion process. On the top of the system, the metallic layer is formed by TiN. The metallic strips can be disposed to introduce a DC field E_{DC} in the waveguide along both the x and y directions. So, SHG and

SPDC processes can be induced considering both TE and TM polarizations.

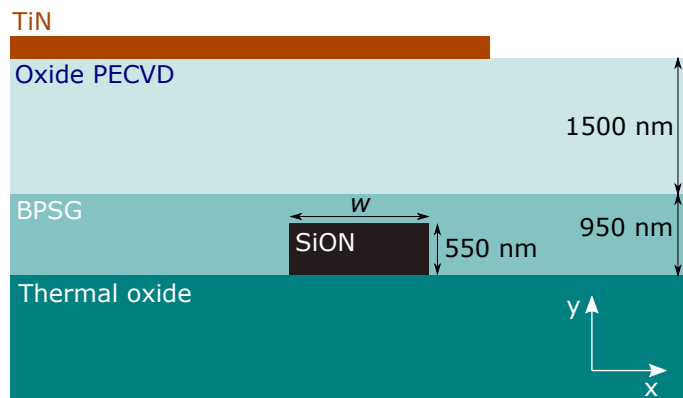


Fig. 11.1: Off-scale cross-section of the waveguides described in this chapter.

A first configuration is shown from a top-view perspective on the left side of Fig. 11.2. The green and yellow rectangles represent the metallic strips, while the black rectangle shows the SiON waveguide. The metallic strips induce a DC field in the waveguide along the y direction. This configuration is designed to achieve frequency conversion between TM-polarized modes. On the right side of Fig. 11.2 the other waveguide configuration is shown. In this case, the metallic strips induce a DC field in the x direction, and so conversion between TE-polarized modes.

In both configurations, the poling period Λ is determined by optical simulations, as discussed in the following. The distance between different metallic strips is 700 nm to match fabrication constraints.

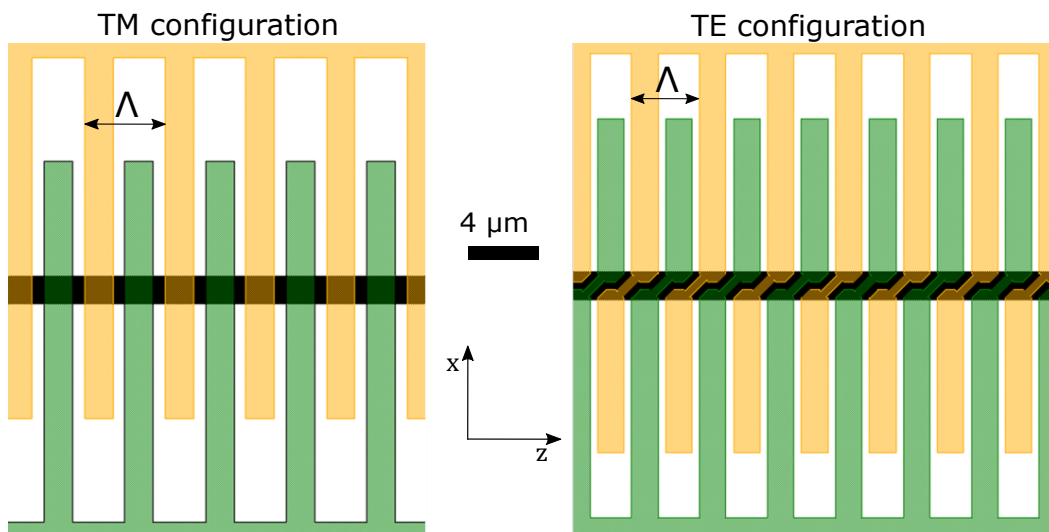


Fig. 11.2: Top view of the realized waveguides. On the left, it is shown the device realized to induce a DC field along the y direction, and so to realize frequency conversion between TM-polarized modes. The green and yellow rectangles represent the metallic strips, while the black rectangle shows the SiON waveguide. On the right, it is shown the device realized to induce a DC field along the x direction, and so frequency conversion between TE-polarized modes.

11.2 The DC field inside the waveguide

The DC field in the waveguide is evaluated using the Electrostatics module of the COMSOL Multiphysics® software [56] through a 3D simulation. The simulation domains used for the two configurations are shown in Fig. 11.3. The simulations refer to an arbitrary poling period $\Lambda = 5\ \mu\text{m}$ and a waveguide width $w = 3\ \mu\text{m}$. The simulations are realized using periodic boundary conditions.

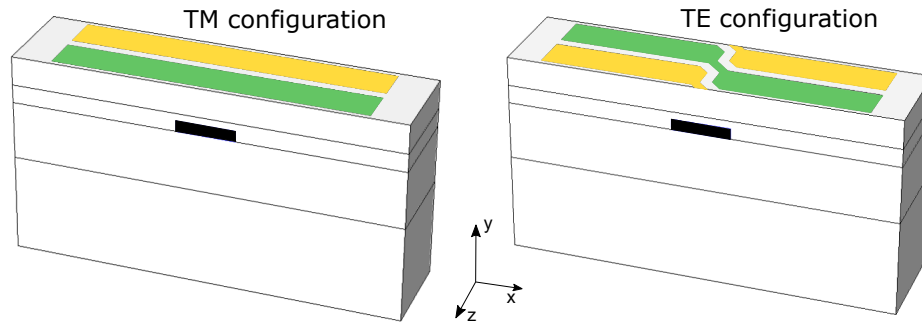


Fig. 11.3: Simulation domain used to compute the field distribution in the waveguide, referred to the waveguide designed for the conversion between TM modes (left) and between TE modes (right). Periodic boundary conditions are applied.

The left side of Fig. 11.4 shows on a color map the y component of the DC field E_{DC} in the xz - plane in the middle of the waveguide. The simulation refers to the structure designed to support conversion between TM-polarized modes, when a bias of 100 V is applied. $E_{DC,y}$ shows a periodic behavior along z , as expected from the design. A similar result is shown on the right side of Fig. 11.4, which shows the x component of the DC field E_{DC} in the case of the structure designed to support conversion between TE polarized modes. Also in this case, the applied bias is 100 V.

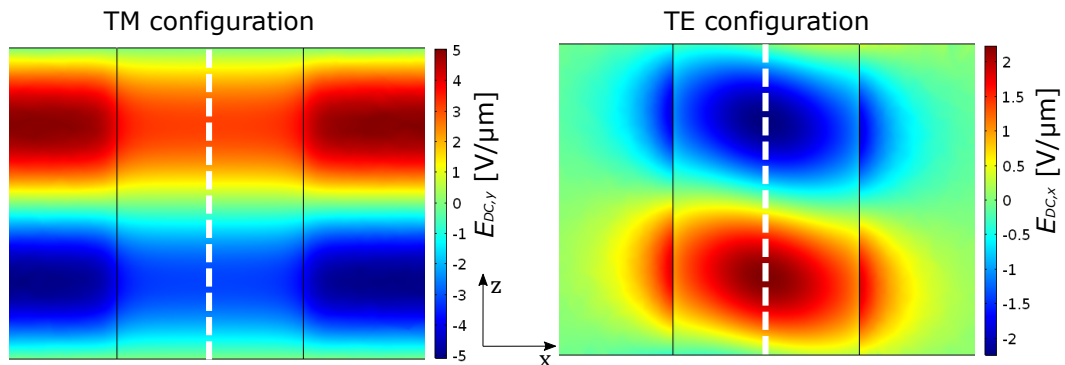


Fig. 11.4: Color map representation of $E_{DC,y}$ (left) and $E_{DC,x}$ (right) in the xz - plane in the middle of the waveguide. The plots are referred to the structure designed for conversion between TM (left) and TE (right) polarized modes. In the simulations $\Lambda = 5\ \mu\text{m}$ and $w = 3\ \mu\text{m}$, while the applied bias is 100 V. The white lines show the position of the center of the waveguide.

To emphasize this fact, Fig. 11.5 reports $E_{DC,y}$ evaluated in the middle of the waveguide along z (the black line of Fig. 11.4). The simulation refers to the TM

configuration with a bias voltage of 100 V. The field has an amplitude of about $3 \text{ V}/\mu\text{m}$. Compared to the results of chapter 9, even if the applied voltage is much larger, the resulting electric field is smaller. This is due to the distance between the metallic pads, which is longer than in the case of p-n junctions. The result of Fig. 11.5 is well fitted by a sinusoidal curve. On the right axis of Fig. 11.5, the corresponding $\chi_{\text{EFISH}}^{(2)}$ is evaluated, using the $\chi^{(3)}$ reported in [70]. The corresponding values are around $0.01 \text{ pm}/\text{V}$, much smaller than the ones estimated for silicon p-n junctions in chapter 9. This is due to both the smaller DC field achieved, but also to the small $\chi^{(3)}$ of SiON, which is 2 orders of magnitude smaller than that of silicon.

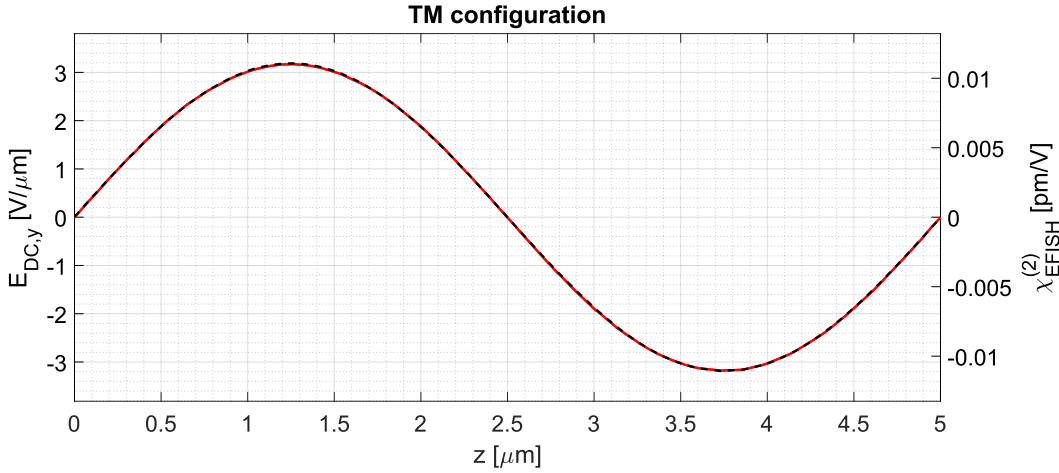


Fig. 11.5: $E_{DC,y}$ in the middle of the waveguide along the waveguide propagation direction z , referred to the TM configuration and to an applied bias of 100 V. The simulations refers to an arbitrary poling period $\Lambda = 5 \mu\text{m}$ and a waveguide width $w = 3 \mu\text{m}$.

In a similar way, Fig. 11.6 reports the case of the TE configuration. Again, the simulation considers an applied bias voltage of 100 V. In this case, the field amplitude is about $2 \text{ V}/\mu\text{m}$, providing a $\chi_{\text{EFISH}}^{(2)}$ amplitude below $0.01 \text{ pm}/\text{V}$.

11.3 The required poling period

The required poling period Λ can be evaluated using the same approach of Sec. 9.2.1. Figure 11.7 shows the Λ dependence on the waveguide width w . The calculations are done for a conversion process between $\lambda_f = 1550 \text{ nm}$ and $\lambda_{sh} = 775 \text{ nm}$. Also in this case, larger is w and larger is the required Λ . Moreover, for the TM combinations the required Λ is shorter than for the TE combinations.

The conversion efficiency is proportional to the factor $|\tilde{\gamma}_{sh}^{(2)}|^2$ for both SHG and SPDC processes. Assume for a while that the $\chi_{\text{EFISH}}^{(2)}$ introduced in the waveguide is the same, independently on w and the corresponding Λ . In this way, $|\tilde{\gamma}_{sh}^{(2)}|^2$ can be evaluated based only on optical simulations, and it is reported in normalized units in Fig. 11.8. The figure shows that the maximum efficiency is reached with two

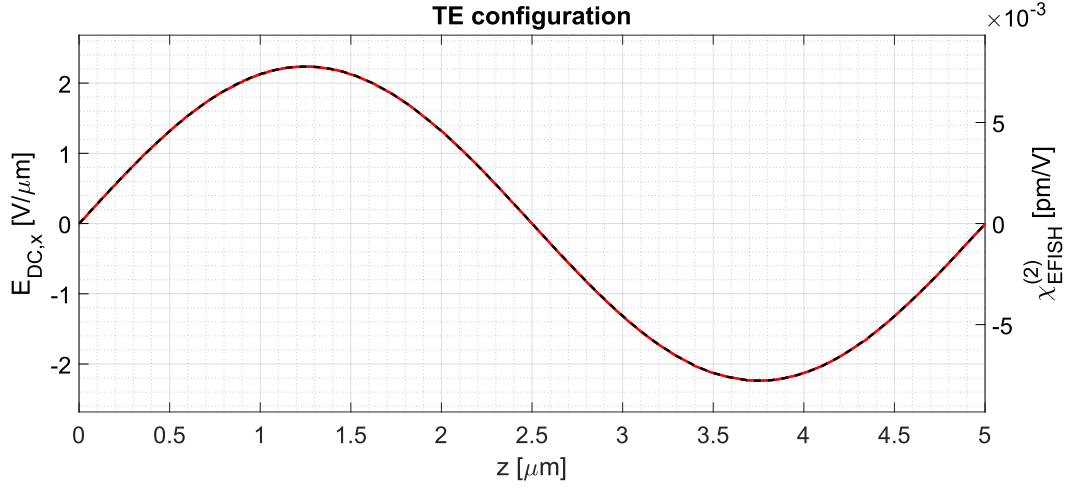


Fig. 11.6: $E_{DC,x}$ in the middle of the waveguide along the waveguide propagation direction z , referred to the TE configuration and an applied bias of 100 V. The simulations refers to an arbitrary poling period $\Lambda = 5 \mu\text{m}$ and a waveguide width $w = 3 \mu\text{m}$.

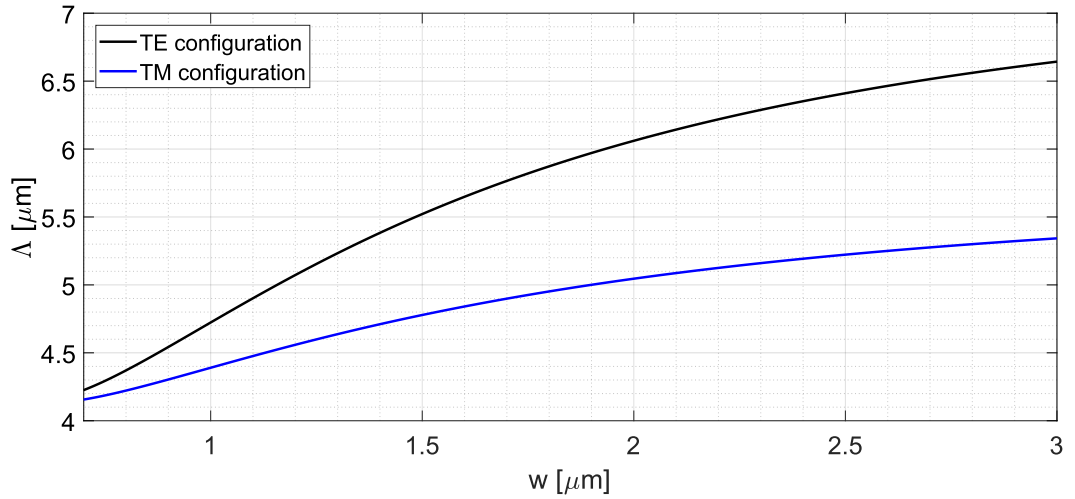


Fig. 11.7: Poling period dependence on waveguide width. Black line refers to the TE configuration, while blue line refers to the TM configuration.

different waveguide widths w for the TE and the TM combinations. The poling period Λ corresponding to these w can be evaluated using the result reported in Fig. 11.7.

So far, the simulation referred to the conversion between $\lambda_f = 1550 \text{ nm}$ and $\lambda_{sh} = 775 \text{ nm}$. However, also additional structures have been proposed, aimed at working between $\lambda_f = 1500 \text{ nm}$ and $\lambda_{sh} = 750 \text{ nm}$, as well as between $\lambda_f = 1600 \text{ nm}$ and $\lambda_{sh} = 800 \text{ nm}$. A summary of the selected waveguides is shown in Tab. 11.1.

The situation presented so far is, however, too simplified. The factor $|\tilde{\gamma}_{sh}^{(2)}|^2$ depends in fact on the second order nonlinear coefficient, which in turn depends on the DC field induced inside the waveguide. The electrostatic simulations described in the previous section can therefore be used to predict the strength of the DC field inside the waveguide, and the $\chi_{EFISH}^{(2)}$ connected to it. Once that this is known, the factor

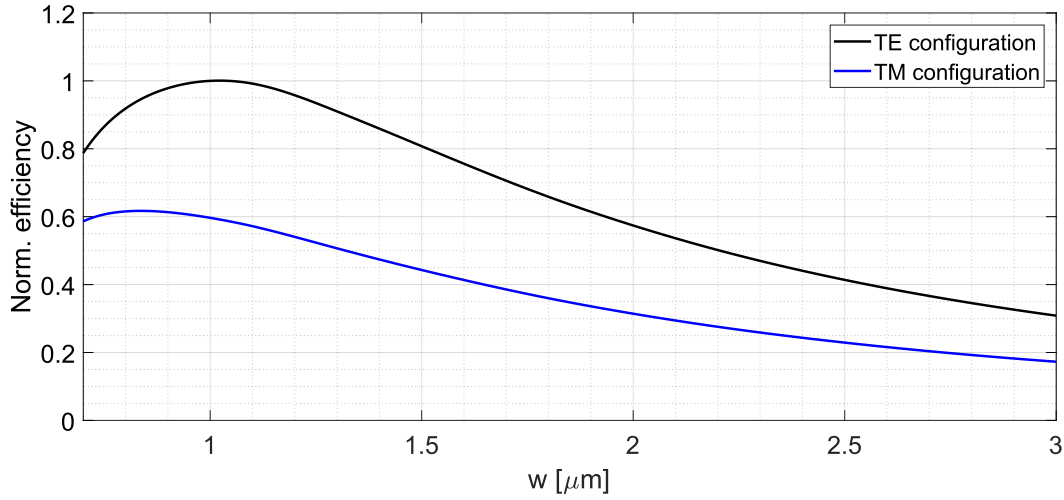


Fig. 11.8: Normalized efficiency of the generation process, evaluated as the factor $|\tilde{\gamma}_{sh}^{(2)}|^2$. The simulation refers to a frequency conversion process between $\lambda_f = 1550$ nm and $\lambda_{sh} = 775$ nm. Black line refers to TE combinations, while blue line refers to TM combinations. This factor is evaluated based only on optical simulations, assuming that the second order nonlinearity introduced in the waveguide is the same independently on the waveguide width and the corresponding poling period.

Tab. 11.1: Geometric parameters of the selected waveguides. In this case, calculations are performed based on only optical simulations, assuming that the same nonlinear strength can be introduced in the waveguide independently on the waveguide width and the corresponding poling period.

Pol.	λ_f [nm]	Waveguide width w [μm]	Poling period Λ [μm]
TE	1500	1	4.571
TE	1550	1	4.723
TE	1600	1	4.876
TM	1500	0.8	4.086
TM	1550	0.8	4.222
TM	1600	0.8	4.358

$|\tilde{\gamma}_{sh}^{(2)}|^2$ can be newly evaluated.

To this purpose, Fig. 11.9 reports the amplitude of both the DC field E_{DC} and the corresponding $\chi_{\text{EFISH}}^{(2)}$ evaluated in the center of the waveguide as a function of the waveguide width w . The amplitude of E_{DC} and $\chi_{\text{EFISH}}^{(2)}$ are evaluated by taking their shape along z in the center of the waveguide and by fitting it with a sinusoidal function. Therefore, the amplitude is considered as one half of the difference between the maximum and the minimum value assumed along z . Figure 11.9 shows that $\chi_{\text{EFISH}}^{(2)}$ increases with w . This is due to the fact that, as w increases, also the corresponding poling period Λ increases. Consequently, the screening effect caused by adjacent metallic stripes also reduces.

Therefore, the factor $|\tilde{\gamma}_{sh}^{(2)}|^2$ can be newly evaluated for each w by considering the proper DC field that can be introduced inside the waveguide. The corrected version

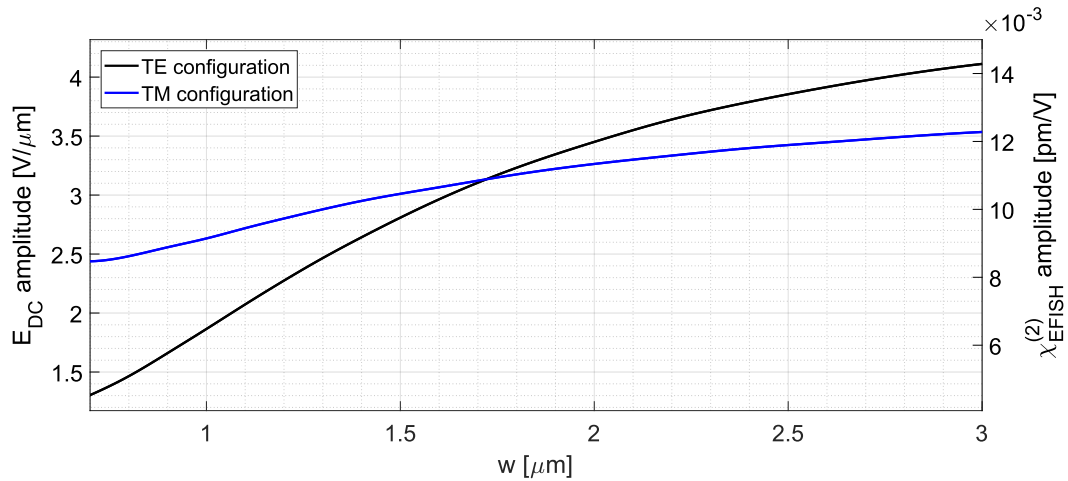


Fig. 11.9: Amplitude of the DC field E_{DC} (left hand side axis) and of $\chi_{\text{EFISH}}^{(2)}$ (right hand side axis) evaluated as a function of the waveguide width w . The amplitude is taken by fitting these quantities in the center of the waveguide along the waveguide propagation direction z . Black line refers to the TE configuration, while blue line refers to the TM configuration.

of the $|\tilde{\gamma}_{sh}^{(2)}|^2$ factor is now reported, as a function of the waveguide width, in Fig. 11.10.

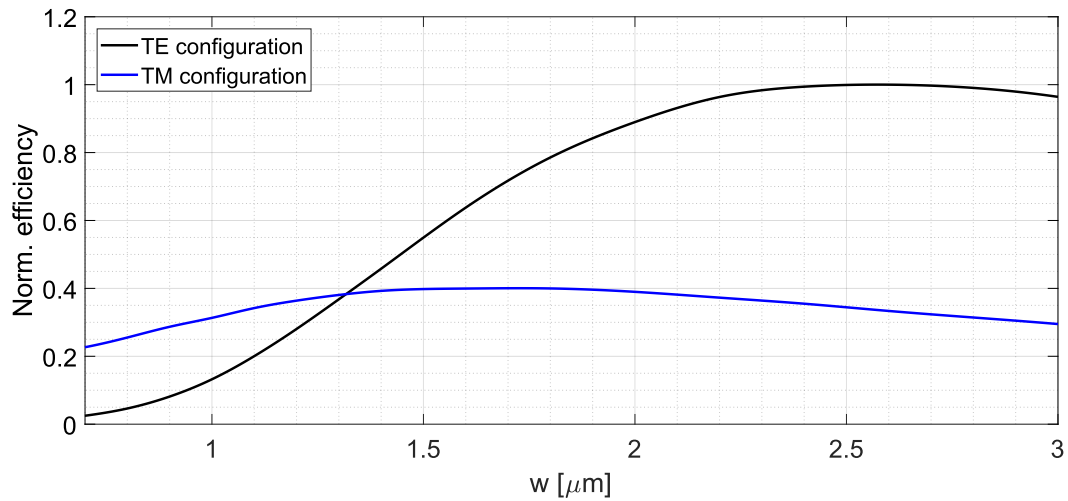


Fig. 11.10: Normalized efficiency of the generation process, evaluated as the factor $|\tilde{\gamma}_{sh}^{(2)}|^2$ and considering also the strength of the DC field that can be obtained inside the waveguide. The simulation refers to a frequency conversion process between $\lambda_f = 1550$ nm and $\lambda_{sh} = 775$ nm. Black line refers to TE combinations, while blue line refers to TM combinations.

Comparing the results of Fig. 11.10 with the ones of Fig. 11.8, it is clear that the optimal configuration changes a lot. The new optimal parameters, evaluated considering this new method, are shown in Tab. 11.2.

Tab. 11.2: Geometric parameters of the waveguides selected for being realized. In this case, the DC field that can be introduced in the waveguide is taken into account in the evaluation of the most efficient combination.

Pol.	λ_f [nm]	Waveguide width w [μm]	Poling period Λ [μm]
TE	1500	2.6	6.256
TE	1550	2.6	6.465
TE	1600	2.6	6.673
TM	1500	1.6	4.685
TM	1550	1.6	4.841
TM	1600	1.6	4.997

11.4 Conversion efficiency

In the final design, both the structures belonging to Tab. 11.1 and Tab. 11.2 have been proposed. The most efficient ones should be those of Tab. 11.2. For some combinations, the SHG and SPDC conversion efficiencies are finally calculated, and are reported in Tab. 11.3. For these combinations, a CW pump power of about 10 mW is considered. The waveguide length is set to 16.5 mm, corresponding to the length of the waveguide actually realized. The applied voltage is 100 V.

Tab. 11.3: Generation efficiency for some of the combinations proposed here. For these combinations, a CW pump power of about 10 mW and a waveguide length of 16.5 mm are considered. The applied voltage is 100 V.

Pol.	λ_f [nm]	Waveguide width w [μm]	Poling period Λ [μm]	P_{sh} [pW]	P_{SPDC} [fW]
TE	1550	2.6	6.465	358	296
TM	1550	1.6	4.841	225	186

The simulations proposed in this section show that both SHG and SPDC are possible in SiON waveguides with the proper design. However, the efficiency of the process described here is much lower than the one shown in chapter 9 and related to the study of silicon waveguides with lateral junctions. In this case, the simulations reported in Tab. 11.3 are obtained by considering a CW pump power of 10 mW and a waveguide length of 16.5 mm, which are values much larger than the ones used in the simulations of chapter 9. Therefore, even if the experimental configuration that can be used to measure SHG and SPDC in SiON waveguides is much simpler, the efficiency is much lower than in the case of silicon waveguides with lateral doping. This makes this approach less attractive than the one based on the use of p-n junctions in silicon.

Conclusions

In Part I, the effect of strain on integrated optical structures has been studied in detail. In Chapter 2 the experimental characterization of a set of silicon racetrack resonators under the effect of an external mechanical load was shown. In Chapter 3, this effect was modeled, accounting for the waveguide deformation and the photoelastic effect, and showed good agreement with the experiment. Both the theoretical model and the experiment confirmed that the strain-induced resonance wavelength shift can vary from positive to negative values when changing the resonator orientation angle. The possibility of **tuning the resonance shift** value by changing the resonator orientation offers interesting applications in the field of strain sensors, since the presence of many resonators with different orientations on the same sample can provide information on the strain direction. Moreover, the resonator orientation angle can be tuned in order to realize **strain-insensitive** resonators, offering interesting applications for flexible photonics.

Part II was dedicated to the study of SHG in **strained silicon waveguides**. Chapter 4 introduced the theoretical framework of SHG in waveguides. The technical details of the SHG experiment were then described in Chapter 5, estimating a second-order nonlinear susceptibility of about 0.5 pm/V . Chapter 6 investigated the SHG process under the effect of an external mechanical load: even if theoretical models predicted a strain-induced variation of the SHG efficiency of more than 50%, the experimental efficiency did not vary significantly. Chapter 7 studied the effects on SHG of the charges trapped at the waveguide edges, which introduce a static electric field in the waveguide that enables the EFISH process. UV treatment was applied in order to remove these charges, demonstrating a complete suppression of the SHG signal and thus highlighting the main role of charges on SHG. The strain effect on $\chi^{(2)}$ was below the noise level, setting an upper limit of 0.05 pm/V to the strain-induced nonlinear coefficient.

Part III studied more efficient ways to induce static fields inside waveguides. The first consisted of using **silicon rib waveguides with lateral p-n junctions**. In this way, by polarizing the junction, a static field was introduced. In Chapter 8 this kind of geometry was characterized by considering silicon racetrack resonators with lateral junctions. An **electro-optic effect** was measured, relying both on plasma-dispersion and DC Kerr effect. In Chapter 9 the use of lateral junctions was applied to the study

of **SHG and SPDC**. By using FEM simulations, the nonlinear strength was predicted, and both the SHG and SPDC efficiencies were estimated. The SHG process was experimentally characterized in Chapter 10, and was well reproduced by the model. Chapter 11 studied the possibility to perform SHG and SPDC in **silicon oxynitride waveguides**. This platform is less efficient in terms of the nonlinear strength, but it can offer interesting experimental advantages.

The first important outcome of my thesis is the clear answer to the debated question on the origin of SHG in strained silicon waveguides. The complete suppression of the SHG signal after the UV treatment demonstrates the fundamental role of trapped charges, and the importance of the EFISH process. This introduces a paradigmatic change in the development of these kinds of structures. Till now great effort was done towards increasing the amount of strain inside the waveguide. However, my work evidences that strain plays a secondary role, and large nonlinearities can be obtained by increasing the DC fields inside the waveguide. This can be done both by maximizing the amount of charges deposited on the waveguide edges, as well as by realizing thinner waveguides. However, this has the drawback to increase the propagation losses caused by the increase of the free carriers inside the waveguide. Moreover, applying a proper photolithographic mask and exposing it to UV light, a periodically varying $\chi^{(2)}$ can be introduced along the waveguide propagation direction, which allows getting SHG between fundamental modes.

My work demonstrates also that SHG can be induced by applying a DC field within the waveguide via lateral p-n junctions. By properly biasing the junctions, $\chi^{(2)}$ coefficients much larger than the ones measured in the strained silicon waveguides are demonstrated. By using an interdigitated junction configuration, a $\chi^{(2)}$ of the same order of magnitude of the one measured in strained silicon is estimated even without bias, due to the built-in potential of the junction. The junctions are arranged in a periodic way to exploit QPM technique. In this way, the conversion between fundamental modes is studied. This yields a conversion efficiency much larger than the one of strained silicon.

In this framework, the use of the waveguide with lateral junctions offers interesting perspectives for the achievement of the SPDC process. The simulations reported in Chapter 9 show that a SPDC signal in the pW range could be generated by using reasonable experimental configurations. This kind of sensitivity could be achieved by using single photon counting techniques based on up-conversion modules [172] or on superconducting nanowires [173].

Using the same silicon platform with lateral p-n junctions, electro-optic effects have been demonstrated in racetrack resonators. The electro-optic capability of this platform is compared to the ones most commonly used nowadays, which are based

on second order nonlinearities. Doing so, the strength of the equivalent second order nonlinear coefficient $\chi_{\text{eq}}^{(2)}$ that would have provided an electro-optic modulation of the same strength is estimated. A value of about 16 pm/V is demonstrated. This value is comparable with the one of $\chi^{(2)}$ materials (such as lithium niobate) and at least one order of magnitude stronger than the most recent measurements of strain-induced Pockels effect in silicon [110]. This result demonstrates that lateral p-n junctions can provide extensive opportunities for fast electro-optic modulation in silicon.

In conclusion, the silicon platform with lateral p-n junctions offers interesting perspectives for the integration of both SPDC photon sources as well as fast electro-optic modulators. This can enable fascinating perspectives in the field of integrated quantum photonics. In one of the most recent and advanced integrated quantum photonic experiments, multidimensional entanglement was demonstrated in a silicon chip [50]. Entangled photon states were generated by means of spontaneous FWM, and thermo-optic phase-shifters were used to manipulate the generated states. Using silicon waveguides with lateral p-n junctions, entangled photons could be generated using SPDC process. This would make tremendously simpler the pump filtering procedure, since the generated photons are spectrally far away from the pump signal. Moreover, the use of phase-shifters based on DC Kerr effect would offer a much faster response than the ones based on thermo-optic effect, whose response time is in the microsecond timescale [67].

Bibliography

- ¹ G. New, *Introduction to Nonlinear Optics* (Cambridge University Press, Apr. 7, 2011), 275 pp. (cit. on pp. 1, 5, 6, 64, 150).
- ² J. Kerr, “A new relation between electricity and light: Dielectrified media birefringent”, *The London, Edinburgh, and Dublin Philosophical Magazine and Journal of Science* **50**, 337–348 (1875) (cit. on p. 1).
- ³ F. Pockels, “Über den Einfluss des elektrostatischen Feldes auf das optische Verhalten piezoelektrischer Krystalle”, *Dieterichsche Verlags-Buchhandlung* **39** (1894) (cit. on p. 1).
- ⁴ M. F. L’Annunziata, *Radioactivity: Introduction and History, From the Quantum to Quarks* (Elsevier, May 13, 2016), 934 pp. (cit. on p. 1).
- ⁵ J. Hecht, “How the Laser Launched Nonlinear Optics”, *Optics and Photonics News* **21**, 34–40 (2010) (cit. on pp. 1–3).
- ⁶ B. O’Brien, “A Story of Science in Night Warfare”, (cit. on p. 2).
- ⁷ R. W. Boyd, “History of Research in Nonlinear Optics at The Institute of Optics”, (cit. on p. 2).
- ⁸ T. H. Maiman, “Stimulated Optical Radiation in Ruby”, *Nature* **187**, 493–494 (1960) (cit. on p. 2).
- ⁹ P. A. Franken, A. E. Hill, C. W. Peters, and G. Weinreich, “Generation of Optical Harmonics”, *Physical Review Letters* **7**, 118–119 (1961) (cit. on pp. 2, 7).
- ¹⁰ J. A. Giordmaine, “Mixing of Light Beams in Crystals”, *Physical Review Letters* **8**, 19–20 (1962) (cit. on pp. 2, 10).
- ¹¹ P. D. Maker, R. W. Terhune, M. Nisenoff, and C. M. Savage, “Effects of Dispersion and Focusing on the Production of Optical Harmonics”, *Physical Review Letters* **8**, 21–22 (1962) (cit. on pp. 2, 10).
- ¹² J. A. Armstrong, N. Bloembergen, J. Ducuing, and P. S. Pershan, “Interactions between Light Waves in a Nonlinear Dielectric”, *Physical Review* **127**, 1918–1939 (1962) (cit. on pp. 3, 4).
- ¹³ N. Bloembergen and J. Ducuing, “Experimental verification of optical laws of non-linear reflection”, *Physics Letters* **6**, 5–6 (1963) (cit. on p. 3).

- ¹⁴ R. L. Carman, R. Y. Chiao, and P. L. Kelley, “Observation of Degenerate Stimulated Four-Photon Interaction and Four-Wave Parametric Amplification”, *Physical Review Letters* **17**, 1281–1283 (1966) (cit. on p. 3).
- ¹⁵ R. Y. Chiao, E. Garmire, and C. H. Townes, “Self-Trapping of Optical Beams”, *Physical Review Letters* **13**, 479–482 (1964) (cit. on p. 3).
- ¹⁶ F. Shimizu, “Frequency Broadening in Liquids by a Short Light Pulse”, *Physical Review Letters* **19**, 1097–1100 (1967) (cit. on p. 3).
- ¹⁷ G. Eckhardt, R. W. Hellwarth, F. J. McClung, et al., “Stimulated Raman Scattering From Organic Liquids”, *Physical Review Letters* **9**, 455–457 (1962) (cit. on p. 3).
- ¹⁸ R. Y. Chiao, C. H. Townes, and B. P. Stoicheff, “Stimulated Brillouin Scattering and Coherent Generation of Intense Hypersonic Waves”, *Physical Review Letters* **12**, 592–595 (1964) (cit. on p. 3).
- ¹⁹ S. A. Akhmanov, A. I. Kovrigin, A. S. Piskarskas, V. V. Fadeev, and R. V. Khokhlov, “Observation of parametric amplification in the optical range”, *Jetp Lett* **2**, 191 (1965) (cit. on p. 3).
- ²⁰ J. A. Giordmaine and R. C. Miller, “Tunable Coherent Parametric Oscillation in LiNbO₃ at Optical Frequencies”, *Physical Review Letters* **14**, 973–976 (1965) (cit. on p. 3).
- ²¹ C. Li, *Nonlinear Optics: Principles and Applications* (Springer, Aug. 26, 2016), 399 pp. (cit. on p. 3).
- ²² H. M. Gibbs, S. L. McCall, and T. N. C. Venkatesan, “Differential Gain and Bistability Using a Sodium-Filled Fabry-Perot Interferometer”, *Physical Review Letters* **36**, 1135–1138 (1976) (cit. on p. 3).
- ²³ L. F. Mollenauer, R. H. Stolen, and J. P. Gordon, “Experimental Observation of Picosecond Pulse Narrowing and Solitons in Optical Fibers”, *Physical Review Letters* **45**, 1095–1098 (1980) (cit. on pp. 3, 11).
- ²⁴ E. J. Lim, M. M. Fejer, R. L. Byer, and W. J. Kozlovsky, “Blue light generation by frequency doubling in periodically poled lithium niobate channel waveguide”, *Electronics Letters* **25**, 731–732 (1989) (cit. on p. 4).
- ²⁵ F. Calegari, G. Sansone, S. Stagira, C. Vozzi, and M. Nisoli, “Advances in attosecond science”, *Journal of Physics B: Atomic, Molecular and Optical Physics* **49**, 062001 (2016) (cit. on p. 4).
- ²⁶ M. M. Fejer, “Nonlinear Optical Frequency Conversion”, *Physics Today* **47**, 25 (2008) (cit. on p. 4).
- ²⁷ E. Garmire, “Nonlinear optics in daily life”, *Optics Express* **21**, 30532–30544 (2013) (cit. on p. 4).
- ²⁸ S. Wabnitz and B. J. Eggleton, *All-Optical Signal Processing: Data Communication and Storage Applications* (Springer, Apr. 11, 2015), 525 pp. (cit. on p. 4).
- ²⁹ G. Agrawal, *Nonlinear Fiber Optics* (Academic Press, Oct. 10, 2012), 653 pp. (cit. on pp. 4, 11, 72).
- ³⁰ M. Deubel, G. von Freymann, M. Wegener, et al., “Direct laser writing of three-dimensional photonic-crystal templates for telecommunications”, *Nature Materials* **3**, 444–447 (2004) (cit. on p. 4).

- ³¹ R. W. Boyd, *Nonlinear Optics* (Elsevier, Jan. 7, 2003), 596 pp. (cit. on pp. 5–7, 10, 64).
- ³² L. Caspani, C. Xiong, B. J. Eggleton, et al., “Integrated sources of photon quantum states based on nonlinear optics”, *Light: Science & Applications* **6**, e17100 (2017) (cit. on pp. 8, 9).
- ³³ J. Leuthold, C. Koos, and W. Freude, “Nonlinear silicon photonics”, *Nature Photonics* **4**, 535–544 (2010) (cit. on p. 9).
- ³⁴ R. M. Osgood, N. C. Panoiu, J. I. Dadap, et al., “Engineering nonlinearities in nanoscale optical systems: physics and applications in dispersion-engineered silicon nanophotonic wires”, *Advances in Optics and Photonics* **1**, 162–235 (2009) (cit. on pp. 9, 58).
- ³⁵ S. Signorini, M. Mancinelli, M. Borghi, et al., “Intermodal four-wave mixing in silicon waveguides”, *Photonics Research* **6**, 805–814 (2018) (cit. on pp. 10, 20, 66, 89).
- ³⁶ M. Yamada, N. Nada, M. Saitoh, and K. Watanabe, “First-order quasi-phase matched LiNbO₃ waveguide periodically poled by applying an external field for efficient blue second-harmonic generation”, *Applied Physics Letters* **62**, 435–436 (1993) (cit. on pp. 10, 20).
- ³⁷ P. S. Kuo and G. S. Solomon, “On- and off-resonance second-harmonic generation in GaAs microdisks”, *Optics Express* **19**, 16898–16918 (2011) (cit. on p. 11).
- ³⁸ M. A. Foster, A. C. Turner, M. Lipson, and A. L. Gaeta, “Nonlinear optics in photonic nanowires”, *Optics Express* **16**, 1300–1320 (2008) (cit. on p. 11).
- ³⁹ R. H. Stolen, E. P. Ippen, and A. R. Tynes, “Raman Oscillation in Glass Optical Waveguide”, *Applied Physics Letters* **20**, 62–64 (1972) (cit. on p. 11).
- ⁴⁰ E. Ippen and R. Stolen, “Stimulated Brillouin scattering in optical fibers”, *Applied Physics Letters* **21**, 539–541 (1972) (cit. on p. 11).
- ⁴¹ R. H. Stolen, J. E. Bjorkholm, and A. Ashkin, “Phase-matched three-wave mixing in silica fiber optical waveguides”, *Applied Physics Letters* **24**, 308–310 (1974) (cit. on p. 11).
- ⁴² R. Stolen, “Phase-matched-stimulated four-photon mixing in silica-fiber waveguides”, *IEEE Journal of Quantum Electronics* **11**, 100–103 (1975) (cit. on p. 11).
- ⁴³ R. H. Stolen and C. Lin, “Self-phase-modulation in silica optical fibers”, *Physical Review A* **17**, 1448–1453 (1978) (cit. on p. 11).
- ⁴⁴ H. Nakatsuka, D. Grischkowsky, and A. C. Balant, “Nonlinear Picosecond-Pulse Propagation through Optical Fibers with Positive Group Velocity Dispersion”, *Physical Review Letters* **47**, 910–913 (1981) (cit. on p. 11).
- ⁴⁵ B. Nikolaus and D. Grischkowsky, “12× pulse compression using optical fibers”, *Applied Physics Letters* **42**, 1–2 (1983) (cit. on p. 11).
- ⁴⁶ M. C. Farries and D. N. Payne, “Optical fiber switch employing a Sagnac interferometer”, *Applied Physics Letters* **55**, 25–26 (1989) (cit. on p. 11).
- ⁴⁷ C. Headley and G. Agrawal, *Raman Amplification in Fiber Optical Communication Systems* (Elsevier, Jan. 20, 2005), 389 pp. (cit. on p. 11).
- ⁴⁸ M. E. Marhic, *Fiber Optical Parametric Amplifiers, Oscillators and Related Devices* (Cambridge University Press, Nov. 15, 2007), 379 pp. (cit. on p. 11).

- ⁴⁹ C. Pollock and M. Lipson, *Integrated Photonics* (Springer Science & Business Media, Nov. 30, 2003), 400 pp. (cit. on p. 11).
- ⁵⁰ J. Wang, S. Paesani, Y. Ding, et al., “Multidimensional quantum entanglement with large-scale integrated optics”, *Science*, eaar7053 (2018) (cit. on pp. 12, 201).
- ⁵¹ S. M. Hendrickson, A. C. Foster, R. M. Camacho, and B. D. Clader, “Integrated nonlinear photonics: emerging applications and ongoing challenges [Invited]”, *JOSA B* **31**, 3193–3203 (2014) (cit. on p. 12).
- ⁵² B. E. A. Saleh and M. C. Teich, *Fundamentals of Photonics* (Wiley, Feb. 5, 2013), 1 p. (cit. on pp. 12, 13, 130).
- ⁵³ J. Broeng, D. Mogilevstev, S. E. Barkou, and A. Bjarklev, “Photonic Crystal Fibers: A New Class of Optical Waveguides”, *Optical Fiber Technology* **5**, 305–330 (1999) (cit. on p. 12).
- ⁵⁴ A. V. Krasavin and A. V. Zayats, “Silicon-based plasmonic waveguides”, *Optics Express* **18**, 11791–11799 (2010) (cit. on p. 12).
- ⁵⁵ M. Borghi, “Linear, nonlinear and quantum optics in Silicon Photonics”, phd (University of Trento, Mar. 21, 2016), 227 pp. (cit. on p. 13).
- ⁵⁶ *COMSOL Multiphysics® v. 5.3a*, www.comsol.com. COMSOL AB, Stockholm, Sweden. (Cit. on pp. 13, 38, 66, 70, 122, 137, 163, 193).
- ⁵⁷ C. D. Salzberg and J. J. Villa, “Infrared Refractive Indexes of Silicon Germanium and Modified Selenium Glass*”, *JOSA* **47**, 244–246 (1957) (cit. on p. 13).
- ⁵⁸ I. H. Malitson, “Interspecimen Comparison of the Refractive Index of Fused Silica*,†”, *JOSA* **55**, 1205–1209 (1965) (cit. on p. 13).
- ⁵⁹ F. Turri, “Experiments and modelling of vertically coupled Microresonators”, phd (University of Trento, July 24, 2017), 138 pp. (cit. on pp. 14, 16, 17).
- ⁶⁰ A. C. Turner, C. Manolatou, B. S. Schmidt, et al., “Tailored anomalous group-velocity dispersion in silicon channel waveguides”, *Optics Express* **14**, 4357–4362 (2006) (cit. on p. 15).
- ⁶¹ W. Bogaerts, P. D. Heyn, T. V. Vaerenbergh, et al., “Silicon microring resonators”, *Laser & Photonics Reviews* **6**, 47–73 (2012) (cit. on p. 15).
- ⁶² J. Heebner, R. Grover, T. Ibrahim, and T. A. Ibrahim, *Optical Microresonators: Theory, Fabrication, and Applications* (Springer Science & Business Media, 2008), 275 pp. (cit. on p. 15).
- ⁶³ C. Grivas, C. Li, P. Andreakou, et al., “Single-mode tunable laser emission in the single-exciton regime from colloidal nanocrystals”, *Nature Communications* **4**, 2376 (2013) (cit. on p. 15).
- ⁶⁴ D. K. Armani, T. J. Kippenberg, S. M. Spillane, and K. J. Vahala, “Ultra-high-Q toroid microcavity on a chip”, *Nature* **421**, 925–928 (2003) (cit. on p. 15).
- ⁶⁵ J. S. Levy, A. Gondarenko, M. A. Foster, et al., “CMOS-compatible multiple-wavelength oscillator for on-chip optical interconnects”, *Nature Photonics* **4**, 37–40 (2010) (cit. on pp. 15, 19).

- ⁶⁶ A. M. Prabhu, A. Tsay, Z. Han, and V. Van, “Extreme Miniaturization of Silicon Add–Drop Microring Filters for VLSI Photonics Applications”, *IEEE Photonics Journal* **2**, 436–444 (2010) (cit. on p. 15).
- ⁶⁷ M. Borghi, C. Castellan, S. Signorini, A. Trenti, and L. Pavesi, “Nonlinear silicon photonics”, *Journal of Optics* **19**, 093002 (2017) (cit. on pp. 16, 19, 20, 24, 33, 58, 201, 215).
- ⁶⁸ M. Bernard, “Lightwave circuits for integrated Silicon Photonics”, phd (University of Trento, Apr. 27, 2017), 222 pp. (cit. on p. 16).
- ⁶⁹ D. J. Moss, R. Morandotti, A. L. Gaeta, and M. Lipson, “New CMOS-compatible platforms based on silicon nitride and Hydex for nonlinear optics”, *Nature Photonics* **7**, 597–607 (2013) (cit. on p. 18).
- ⁷⁰ A. Trenti, M. Borghi, S. Biasi, et al., “Thermo-optic coefficient and nonlinear refractive index of silicon oxynitride waveguides”, *AIP Advances* **8**, 025311 (2018) (cit. on pp. 18, 191, 194).
- ⁷¹ K. Ikeda, R. E. Saperstein, N. Alic, and Y. Fainman, “Thermal and Kerr nonlinear properties of plasma-deposited silicon nitride/silicon dioxide waveguides”, *Optics Express* **16**, 12987–12994 (2008) (cit. on p. 18).
- ⁷² B. J. Eggleton, T. D. Vo, R. Pant, et al., “Photonic chip based ultrafast optical processing based on high nonlinearity dispersion engineered chalcogenide waveguides”, *Laser & Photonics Reviews* **6**, 97–114 (2012) (cit. on pp. 18, 19).
- ⁷³ S. Serna, H. Lin, C. Alonso-Ramos, et al., “Nonlinear optical properties of integrated GeSbS chalcogenide waveguides”, *Photonics Research* **6**, B37–B42 (2018) (cit. on pp. 18, 19).
- ⁷⁴ F. Xu, Z.-x. Wu, and Y.-q. Lu, “Nonlinear optics in optical-fiber nanowires and their applications”, *Progress in Quantum Electronics* **55**, 35–51 (2017) (cit. on p. 18).
- ⁷⁵ T. Lee, Y. Jung, C. A. Codemard, et al., “Broadband third harmonic generation in tapered silica fibres”, *Optics Express* **20**, 8503–8511 (2012) (cit. on p. 18).
- ⁷⁶ M. I.M. A. Khudus, F. D. Lucia, C. Corbari, et al., “Phase matched parametric amplification via four-wave mixing in optical microfibers”, *Optics Letters* **41**, 761–764 (2016) (cit. on p. 18).
- ⁷⁷ M. Liao, W. Gao, T. Cheng, et al., “Flat and broadband supercontinuum generation by four-wave mixing in a highly nonlinear tapered microstructured fiber”, *Optics Express* **20**, B574–B580 (2012) (cit. on p. 18).
- ⁷⁸ C. Markos, J. C. Travers, A. Abdolvand, B. J. Eggleton, and O. Bang, “Hybrid photonic-crystal fiber”, *Reviews of Modern Physics* **89**, 045003 (2017) (cit. on p. 18).
- ⁷⁹ L. Razzari, D. Duchesne, M. Ferrera, et al., “CMOS-compatible integrated optical hyper-parametric oscillator”, *Nature Photonics* **4**, 41–45 (2010) (cit. on p. 19).
- ⁸⁰ D. Duchesne, M. Ferrera, L. Razzari, et al., “Hydex Glass: a CMOS Compatible Platform for Integrated Waveguide Structures for Nonlinear Optics”, (2015) (cit. on p. 19).
- ⁸¹ A. D. Bristow, N. Rotenberg, and H. M. van Driel, “Two-photon absorption and Kerr coefficients of silicon for 850–2200nm”, *Applied Physics Letters* **90**, 191104 (2007) (cit. on pp. 19, 66, 73, 112, 164, 186).

- ⁸² D. Dimitropoulos, R. Jhaveri, R. Claps, J. C. S. Woo, and B. Jalali, “Lifetime of photo-generated carriers in silicon-on-insulator rib waveguides”, *Applied Physics Letters* **86**, 071115 (2005) (cit. on p. 19).
- ⁸³ M. A. Foster, A. C. Turner, J. E. Sharping, et al., “Broad-band optical parametric gain on a silicon photonic chip”, *Nature* **441**, 960–963 (2006) (cit. on p. 20).
- ⁸⁴ X. Liu, B. Kuyken, G. Roelkens, et al., “Bridging the mid-infrared-to-telecom gap with silicon nanophotonic spectral translation”, *Nature Photonics* **6**, 667–671 (2012) (cit. on p. 20).
- ⁸⁵ S. Sederberg and A. Y. Elezzabi, “Coherent Visible-Light-Generation Enhancement in Silicon-Based Nanoplasmonic Waveguides via Third-Harmonic Conversion”, *Physical Review Letters* **114**, 227401 (2015) (cit. on p. 20).
- ⁸⁶ B. Kuyken, X. Liu, G. Roelkens, et al., “50 dB parametric on-chip gain in silicon photonic wires”, *Optics Letters* **36**, 4401–4403 (2011) (cit. on p. 20).
- ⁸⁷ X. Liu, R. M. O. Jr, Y. A. Vlasov, and W. M. J. Green, “Mid-infrared optical parametric amplifier using silicon nanophotonic waveguides”, *Nature Photonics* **4**, 557–560 (2010) (cit. on p. 20).
- ⁸⁸ F. Leo, S.-P. Gorza, J. Safioui, et al., “Dispersive wave emission and supercontinuum generation in a silicon wire waveguide pumped around the 1550 nm telecommunication wavelength”, *Optics Letters* **39**, 3623–3626 (2014) (cit. on p. 20).
- ⁸⁹ J. W. Silverstone, D. Bonneau, J. L. O’Brien, and M. G. Thompson, “Silicon Quantum Photonics”, *IEEE Journal of Selected Topics in Quantum Electronics* **22**, 390–402 (2016) (cit. on p. 20).
- ⁹⁰ I. Shoji, T. Kondo, A. Kitamoto, M. Shirane, and R. Ito, “Absolute scale of second-order nonlinear-optical coefficients”, *JOSA B* **14**, 2268–2294 (1997) (cit. on p. 21).
- ⁹¹ W. H. P. Pernice, C. Xiong, C. Schuck, and H. X. Tang, “Second harmonic generation in phase matched aluminum nitride waveguides and micro-ring resonators”, *Applied Physics Letters* **100**, 223501 (2012) (cit. on pp. 21, 22).
- ⁹² H. Jin, F. M. Liu, P. Xu, et al., “On-Chip Generation and Manipulation of Entangled Photons Based on Reconfigurable Lithium-Niobate Waveguide Circuits”, *Physical Review Letters* **113**, 103601 (2014) (cit. on pp. 20, 21).
- ⁹³ S. Tanzilli, H. D. Riedmatten, H. Tittel, et al., “Highly efficient photon-pair source using periodically poled lithium niobate waveguide”, *Electronics Letters* **37**, 26–28 (2001) (cit. on p. 21).
- ⁹⁴ S. Fathpour, “Heterogeneous Nonlinear Integrated Photonics”, *IEEE Journal of Quantum Electronics* **54**, 1–16 (2018) (cit. on p. 22).
- ⁹⁵ A. Rao and S. Fathpour, “Compact Lithium Niobate Electrooptic Modulators”, *IEEE Journal of Selected Topics in Quantum Electronics* **24**, 1–14 (2018) (cit. on p. 22).
- ⁹⁶ A. Rao, A. Patil, M. Malinowski, et al., “Electro-optic and second-order nonlinear effects in thin film lithium niobate on silicon”, in 2017 IEEE Photonics Society Summer Topical Meeting Series (SUM) (July 2017), pp. 151–152 (cit. on p. 22).
- ⁹⁷ A. Rao, J. Chiles, S. Khan, et al., “Second-harmonic generation in single-mode integrated waveguides based on mode-shape modulation”, *Applied Physics Letters* **110**, 111109 (2017) (cit. on p. 22).

- ⁹⁸ C. Wang, Z. Li, M.-H. Kim, et al., “Metasurface-assisted phase-matching-free second harmonic generation in lithium niobate waveguides”, *Nature Communications* **8**, 2098 (2017) (cit. on p. 22).
- ⁹⁹ A. Rao, N. Nader, M. J. Stevens, et al., “Photon Pair Generation on a Silicon Chip Using Nanophotonic Periodically-Poled Lithium Niobate Waveguides”, in *Conference on Lasers and Electro-Optics* (2018), paper JTh3C.2 (May 13, 2018), JTh3C.2 (cit. on p. 22).
- ¹⁰⁰ X. Guo, C.-l. Zou, C. Schuck, et al., “Parametric down-conversion photon-pair source on a nanophotonic chip”, *Light: Science & Applications* **6**, e16249 (2017) (cit. on p. 22).
- ¹⁰¹ L. Chang, A. Boes, X. Guo, et al., “Heterogeneously Integrated GaAs Waveguides on Insulator for Efficient Frequency Conversion”, *Laser & Photonics Reviews* **12**, 1800149 (2018) (cit. on p. 23).
- ¹⁰² P. S. Kuo, J. Bravo-Abad, and G. S. Solomon, “Second-harmonic generation using -quasi-phases matching in a GaAs whispering-gallery-mode microcavity”, *Nature Communications* **5**, 3109 (2014) (cit. on p. 23).
- ¹⁰³ N. Morais, I. Roland, M. Ravaro, et al., “Directionally induced quasi-phase matching in homogeneous AlGaAs waveguides”, *Optics Letters* **42**, 4287–4290 (2017) (cit. on p. 23).
- ¹⁰⁴ D. J. Wilson, K. Schneider, S. Hoehl, et al., “Integrated gallium phosphide nonlinear photonics”, (2018) (cit. on p. 23).
- ¹⁰⁵ P. Guillemé, Y. Dumeige, J. Stodolna, et al., “Second harmonic generation in gallium phosphide microdisks on silicon: from strict to random quasi-phase matching”, *Semiconductor Science and Technology* **32**, 065004 (2017) (cit. on p. 23).
- ¹⁰⁶ M. A. Gouveia, T. Lee, R. Ismael, et al., “Second harmonic generation and enhancement in microfibers and loop resonators”, *Applied Physics Letters* **102**, 201120 (2013) (cit. on p. 23).
- ¹⁰⁷ J. S. Levy, M. A. Foster, A. L. Gaeta, and M. Lipson, “Harmonic generation in silicon nitride ring resonators”, *Optics Express* **19**, 11415–11421 (2011) (cit. on p. 23).
- ¹⁰⁸ M. W. Puckett, R. Sharma, H.-H. Lin, et al., “Observation of second-harmonic generation in silicon nitride waveguides through bulk nonlinearities”, *Optics Express* **24**, 16923–16933 (2016) (cit. on p. 23).
- ¹⁰⁹ R. S. Jacobsen, K. N. Andersen, P. I. Borel, et al., “Strained silicon as a new electro-optic material”, *Nature* **441**, 199–202 (2006) (cit. on pp. 24, 25).
- ¹¹⁰ M. Berciano, G. Marcaud, P. Damas, et al., “Fast linear electro-optic effect in a centrosymmetric semiconductor”, *Communications Physics* **1**, 64 (2018) (cit. on pp. 25, 27, 70, 71, 74, 100, 101, 146, 201).
- ¹¹¹ M. Borghi, M. Mancinelli, F. Merget, et al., “High-frequency electro-optic measurement of strained silicon racetrack resonators”, *Optics Letters* **40**, 5287–5290 (2015) (cit. on pp. 25, 26, 34, 95).
- ¹¹² B. Chmielak, M. Waldow, C. Matheisen, et al., “Pockels effect based fully integrated, strained silicon electro-optic modulator”, *Optics Express* **19**, 17212–17219 (2011) (cit. on p. 25).
- ¹¹³ B. Chmielak, C. Matheisen, C. Ripperda, et al., “Investigation of local strain distribution and linear electro-optic effect in strained silicon waveguides”, *Optics Express* **21**, 25324–25332 (2013) (cit. on p. 25).

- ¹¹⁴ P. Damas, X. L. Roux, D. L. Bourdais, et al., “Wavelength dependence of Pockels effect in strained silicon waveguides”, *Optics Express* **22**, 22095–22100 (2014) (cit. on p. 25).
- ¹¹⁵ N. K. Hon, K. K. Tsia, D. R. Solli, B. Jalali, and J. B. Khurgin, “Stress-induced $\chi^{(2)}$ in silicon — Comparison between theoretical and experimental values”, in 2009 6th IEEE International Conference on Group IV Photonics (Sept. 2009), pp. 232–234 (cit. on pp. 26, 115).
- ¹¹⁶ J. B. Khurgin, T. H. Stievater, M. W. Pruessner, and W. S. Rabinovich, “On the origin of the second-order nonlinearity in strained Si-SiN structures”, *JOSA B* **32**, 2494–2499 (2015) (cit. on pp. 26, 115).
- ¹¹⁷ C. L. Manganelli, P. Pintus, and C. Bonati, “Modeling of strain-induced Pockels effect in Silicon”, *Optics Express* **23**, 28649–28666 (2015) (cit. on pp. 26, 35).
- ¹¹⁸ P. Damas, D. Marris-Morini, E. Cassan, and L. Vivien, “Bond orbital description of the strain-induced second-order optical susceptibility in silicon”, *Physical Review B* **93**, 165208 (2016) (cit. on pp. 26, 27, 70, 71, 100, 101).
- ¹¹⁹ S. S. Azadeh, F. Merget, M. P. Nezhad, and J. Witzens, “On the measurement of the Pockels effect in strained silicon”, *Optics Letters* **40**, 1877–1880 (2015) (cit. on p. 26).
- ¹²⁰ M. Borghi, M. Mancinelli, M. Bernard, et al., “Homodyne Detection of Free Carrier Induced Electro-Optic Modulation in Strained Silicon Resonators”, *Journal of Lightwave Technology* **34**, 5657–5668 (2016) (cit. on pp. 27, 121, 146).
- ¹²¹ I. Olivares, T. Angelova, and P. Sanchis, “On the influence of interface charging dynamics and stressing conditions in strained silicon devices”, *Scientific Reports* **7**, 7241 (2017) (cit. on p. 27).
- ¹²² C. Matheisen, M. Waldow, B. Chmielak, et al., “Electro-optic light modulation and THz generation in locally plasma-activated silicon nanophotonic devices”, *Optics Express* **22**, 5252–5259 (2014) (cit. on p. 27).
- ¹²³ S. Abel, F. Eltes, J. E. Ortmann, et al., “Large Pockels effect in micro- and nanostructured barium titanate integrated on silicon”, *Nature Materials* **18**, 42 (2019) (cit. on p. 27).
- ¹²⁴ M. Cazzanelli, F. Bianco, E. Borga, et al., “Second-harmonic generation in silicon waveguides strained by silicon nitride”, *Nature Materials* **11**, 148–154 (2012) (cit. on pp. 27, 28).
- ¹²⁵ E. Timurdogan, C. V. Poulton, M. J. Byrd, and M. R. Watts, “Electric field-induced second-order nonlinear optical effects in silicon waveguides”, *Nature Photonics* **11**, 200–206 (2017) (cit. on pp. 28, 29, 116, 120, 145–147, 160, 187).
- ¹²⁶ C. Schriever, F. Bianco, M. Cazzanelli, et al., “Second-Order Optical Nonlinearity in Silicon Waveguides: Inhomogeneous Stress and Interfaces”, *Advanced Optical Materials* **3**, 129–136 (cit. on pp. 28, 104, 106).
- ¹²⁷ F. D. Leonardis, R. A. Soref, and V. M. N. Passaro, “Investigation of Electric Field Induced Mixing in Silicon Micro Ring Resonators”, *Scientific Reports* **7**, 3401 (2017) (cit. on pp. 29, 189).
- ¹²⁸ *Siquro project (Bando grandi progetti, Provincia Autonoma di Trento, 2012)*, <https://event.unitn.it/siquro/> (cit. on p. 29).
- ¹²⁹ *NEMO project (PRIN 2015KEZNYM supported by MIUR)*, <https://sites.google.com/view/prin-nemo/home> (cit. on p. 29).

- ¹³⁰ Y. Chen, H. Li, and M. Li, “Flexible and tunable silicon photonic circuits on plastic substrates”, *Scientific Reports* **2**, 622 (2012) (cit. on p. 33).
- ¹³¹ W. J. Westerveld, S. M. Leinders, P. M. Mulwijk, et al., “Characterization of Integrated Optical Strain Sensors Based on Silicon Waveguides”, *IEEE Journal of Selected Topics in Quantum Electronics* **20**, 101–110 (2014) (cit. on pp. 33, 45, 46).
- ¹³² L. Fan, L. T. Varghese, Y. Xuan, et al., “Direct fabrication of silicon photonic devices on a flexible platform and its application for strain sensing”, *Optics Express* **20**, 20564–20575 (2012) (cit. on p. 33).
- ¹³³ S. M. Leinders, W. J. Westerveld, J. Pozo, et al., “A sensitive optical micro-machined ultrasound sensor (OMUS) based on a silicon photonic ring resonator on an acoustical membrane”, *Scientific Reports* **5**, 14328 (2015) (cit. on p. 33).
- ¹³⁴ D. Dai, L. Liu, S. Gao, D.-X. Xu, and S. He, “Polarization management for silicon photonic integrated circuits”, *Laser & Photonics Reviews* **7**, 303–328 (cit. on p. 33).
- ¹³⁵ C. Castellan, A. Chalyan, M. Mancinelli, et al., “Tuning the strain-induced resonance shift in silicon racetrack resonators by their orientation”, *Optics Express* **26**, 4204–4218 (2018) (cit. on pp. 33, 45, 95, 97, 98, 215).
- ¹³⁶ P. A.L.d. S. Damas, “Pockels effect in strained silicon waveguides”, PhD thesis (Université Paris-Saclay, July 19, 2016) (cit. on pp. 35, 36, 104).
- ¹³⁷ P. Segall, *Earthquake and Volcano Deformation* (Princeton University Press, Jan. 4, 2010), 465 pp. (cit. on pp. 35, 36).
- ¹³⁸ M. A. Hopcroft, W. D. Nix, and T. W. Kenny, “What is the Young’s Modulus of Silicon?”, *Journal of Microelectromechanical Systems* **19**, 229–238 (2010) (cit. on pp. 36–38, 49).
- ¹³⁹ J. J. Wortman and R. A. Evans, “Young’s Modulus, Shear Modulus, and Poisson’s Ratio in Silicon and Germanium”, *Journal of Applied Physics* **36**, 153–156 (1965) (cit. on pp. 37, 38, 49).
- ¹⁴⁰ M. Huang, “Stress effects on the performance of optical waveguides”, *International Journal of Solids and Structures* **40**, 1615–1632 (2003) (cit. on pp. 37, 38, 50).
- ¹⁴¹ W. N. Ye, D. X. Xu, S. Janz, et al., “Birefringence control using stress engineering in silicon-on-insulator (SOI) waveguides”, *Journal of Lightwave Technology* **23**, 1308–1318 (2005) (cit. on pp. 38, 50).
- ¹⁴² R. L. Edwards, G. Coles, and W. N. Sharpe, “Comparison of tensile and bulge tests for thin-film silicon nitride”, *Experimental Mechanics* **44**, 49–54 (2004) (cit. on p. 38).
- ¹⁴³ Y. Amemiya, Y. Tanushi, T. Tokunaga, and S. Yokoyama, “Photoelastic Effect in Silicon Ring Resonators”, *Japanese Journal of Applied Physics* **47**, 2910 (2008) (cit. on pp. 39, 45).
- ¹⁴⁴ F. P. Beer, E. R. Johnston, and J. T. DeWolf, *Mechanics of Materials* (McGraw-Hill Higher Education, 2006), 824 pp. (cit. on p. 47).
- ¹⁴⁵ C. Castellan, A. Trenti, C. Vecchi, et al., “On the origin of second harmonic generation in silicon waveguides with silicon nitride cladding”, *Scientific Reports* **9**, 1088 (2019) (cit. on pp. 58, 83, 95, 103, 215).

- ¹⁴⁶ C. Castellan, A. Trenti, M. Mancinelli, et al., “From SHG to mid-infrared SPDC generation in strained silicon waveguides”, in *Quantum Photonic Devices*, Vol. 10358 (Aug. 29, 2017), p. 1035804 (cit. on pp. 65, 83, 216).
- ¹⁴⁷ A. Weiner, *Ultrafast Optics* (John Wiley & Sons, Sept. 20, 2011), 733 pp. (cit. on p. 72).
- ¹⁴⁸ K. Rottwitt and P. Tidemand-Lichtenberg, *Nonlinear Optics: Principles and Applications* (CRC Press, Dec. 11, 2014), 345 pp. (cit. on pp. 73, 112).
- ¹⁴⁹ A. Trenti, M. Mancinelli, A. Marchesini, C. Castellan, and M. G. L. Pavesi, “Towards MIR SPDC generation in strained silicon waveguides”, in 2017 Conference on Lasers and Electro-Optics Europe European Quantum Electronics Conference (CLEO/Europe-EQEC) (June 2017), pp. 1–1 (cit. on pp. 83, 216).
- ¹⁵⁰ A. Trenti, “Generation, manipulation and detection of NIR and MIR entangled photon pairs”, phd (University of Trento, Apr. 20, 2018), 223 pp. (cit. on p. 83).
- ¹⁵¹ J.-C. Diels and W. Rudolph, “8 - Pulse Shaping”, in *Ultrashort Laser Pulse Phenomena (Second Edition)*, edited by J.-C. Diels and W. Rudolph (Academic Press, Burlington, Jan. 1, 2006), pp. 433–456 (cit. on p. 85).
- ¹⁵² G. Reed and A. Knights, *Silicon Photonics: An Introduction* (Wiley, 2004) (cit. on p. 91).
- ¹⁵³ J. Robertson and M. J. Powell, “Gap states in silicon nitride”, *Applied Physics Letters* **44**, 415–417 (1984) (cit. on p. 104).
- ¹⁵⁴ J. Robertson, W. L. Warren, and J. Kanicki, “Nature of the Si and N dangling bonds in silicon nitride”, *Journal of Non-Crystalline Solids, Amorphous Insulating Thin Films II* **187**, 297–300 (1995) (cit. on p. 104).
- ¹⁵⁵ W. L. Warren, J. Robertson, and J. Kanicki, “Si and N dangling bond creation in silicon nitride thin films”, *Applied Physics Letters* **63**, 2685–2687 (1993) (cit. on pp. 104, 105).
- ¹⁵⁶ G. Piccoli, M. Bernard, and M. Ghulinyan, “Permanent mitigation of loss in ultrathin silicon-on-insulator high-Q resonators using ultraviolet light”, *Optica* **5**, 1271–1278 (2018) (cit. on pp. 105–108, 110).
- ¹⁵⁷ S. M. Sze and K. K. Ng, *Physics of Semiconductor Devices* (John Wiley & Sons, Nov. 3, 2006), 828 pp. (cit. on p. 105).
- ¹⁵⁸ G. Pfanner, C. Freysoldt, J. Neugebauer, and U. Gerstmann, “Ab initio EPR parameters for dangling-bond defect complexes in silicon: Effect of Jahn-Teller distortion”, *Physical Review B* **85**, 195202 (2012) (cit. on pp. 109, 110).
- ¹⁵⁹ P. Damas, M. Berciano, G. Marcaud, et al., “Comprehensive description of the electro-optic effects in strained silicon waveguides”, *Journal of Applied Physics* **122**, 153105 (2017) (cit. on p. 110).
- ¹⁶⁰ M. Nedeljkovic, R. Soref, and G. Z. Mashanovich, “Free-Carrier Electrorefraction and Electroabsorption Modulation Predictions for Silicon Over the 1–14- μm Infrared Wavelength Range”, *IEEE Photonics Journal* **3**, 1171–1180 (2011) (cit. on pp. 111, 120, 121).
- ¹⁶¹ J. Zhang, Q. Lin, G. Piredda, et al., “Anisotropic nonlinear response of silicon in the near-infrared region”, *Applied Physics Letters* **91**, 071113 (2007) (cit. on p. 112).
- ¹⁶² N. K. Hon, R. Soref, and B. Jalali, “The third-order nonlinear optical coefficients of Si, Ge, and Si $1-x$ Ge x in the midwave and longwave infrared”, *Journal of Applied Physics* **110**, 011301 (2011) (cit. on pp. 112, 164, 186).

- ¹⁶³ Q. Lin, J. Zhang, G. Piredda, et al., “Dispersion of silicon nonlinearities in the near infrared region”, *Applied Physics Letters* **91**, 021111 (2007) (cit. on pp. 112, 164, 186).
- ¹⁶⁴ M. M. Mancinelli, “Linear and non linear coupling effects in sequence of microresonators”, phd (University of Trento, Mar. 25, 2013), 236 pp. (cit. on p. 126).
- ¹⁶⁵ A. Yariv, “Critical coupling and its control in optical waveguide-ring resonator systems”, *IEEE Photonics Technology Letters* **14**, 483–485 (2002) (cit. on p. 129).
- ¹⁶⁶ R. Soref and B. Bennett, “Electrooptical effects in silicon”, *IEEE Journal of Quantum Electronics* **23**, 123–129 (1987) (cit. on pp. 139, 141, 170).
- ¹⁶⁷ L. G. Helt, M. Liscidini, and J. E. Sipe, “How does it scale? Comparing quantum and classical nonlinear optical processes in integrated devices”, *JOSA B* **29**, 2199–2212 (2012) (cit. on p. 149).
- ¹⁶⁸ *Quasi-phase-matching*, in *Wikipedia* () (cit. on p. 150).
- ¹⁶⁹ N.-E. Yu, J.-H. Ro, H.-K. Kim, et al., “High Order Quasi-Phase-Matched Second Harmonic Generations in Periodically Poled Lithium Niobate”, *Journal of the Korean Physical Society* **35**, 1384 (1999) (cit. on p. 151).
- ¹⁷⁰ N. E. Yu, S. Kurimura, and K. Kitamura, “Higher-order quasi-phase matched second harmonic generation in periodically poled MgO-doped stoichiometric LiTaO₃”, *Journal of the Korean Physical Society* **47**, 636–639 (2005) (cit. on p. 151).
- ¹⁷¹ I. Ricciardi, S. Mosca, M. Parisi, et al., “Frequency comb generation in quadratic nonlinear media”, *Physical Review A* **91** (2015) 10.1103/PhysRevA.91.063839 (cit. on p. 189).
- ¹⁷² J. S. Dam, P. Tidemand-Lichtenberg, and C. Pedersen, “Room-temperature mid-infrared single-photon spectral imaging”, *Nature Photonics* **6**, 788–793 (2012) (cit. on p. 200).
- ¹⁷³ G. Schön, “Quantum engineering: Superconducting nanowires”, *Nature* **404**, 948–949 (2000) (cit. on p. 200).
- ¹⁷⁴ C. Castellan, S. Tondini, M. Mancinelli, C. Kopp, and L. Pavesi, “Reflectance Reduction in a Whiskered SOI Star Coupler”, *IEEE Photonics Technology Letters* **28**, 1870–1873 (2016) (cit. on p. 215).
- ¹⁷⁵ F. Testa, C. J. Oton, C. Kopp, et al., “Design and Implementation of an Integrated Reconfigurable Silicon Photonics Switch Matrix in IRIS Project”, *IEEE Journal of Selected Topics in Quantum Electronics* **22**, 155–168 (2016) (cit. on p. 215).
- ¹⁷⁶ S. Tondini, C. Castellan, M. Mancinelli, C. Kopp, and L. Pavesi, “Methods for Low Crosstalk and Wavelength Tunability in Arrayed-Waveguide Grating for On-Silicon Optical Network”, *Journal of Lightwave Technology* **35**, 5134–5141 (2017) (cit. on p. 215).
- ¹⁷⁷ C. Castellan, R. Franchi, P. Guilleme, et al., “Field-induced nonlinearities in silicon waveguides embedded in lateral p-n junctions”, In preparation for *Frontiers in Physics* (2019) (cit. on p. 215).
- ¹⁷⁸ S. Tondini, C. Castellan, M. Manuel Alesandro, and P. Lorenzo, “Automatic initialization methods for photonic components on a silicon-based optical switch”, In preparation for *Applied Sciences* (2019) (cit. on p. 215).
- ¹⁷⁹ S. Tondini, C. Castellan, M. Mancinelli, and L. Pavesi, “Modeling and validation of high-performance and athermal AWGs for the silicon photonics platform”, in *Silicon Photonics and Photonic Integrated Circuits V*, Vol. 9891 (May 13, 2016), p. 98910C (cit. on p. 216).

- ¹⁸⁰ P. Pintus, C. Manganelli, S. Tondini, et al., “Silicon photonic toolkit for integrated switching matrices”, in 18th Italian National Conference on Photonic Technologies (Fotonica 2016) (June 2016), pp. 1–4 (cit. on p. 216).
- ¹⁸¹ C. J. Oton, C. J. Oton, P. Pintus, et al., “Silicon Photonics for Matrix Switching Applications: Ingredients and Recipes”, in Advanced Photonics 2016 (IPR, NOMA, Sensors, Networks, SPPCom, SOF) (2016), paper ITu3B.6 (July 18, 2016), ITu3B.6 (cit. on p. 216).
- ¹⁸² S. Tondini, C. Castellan, M. Mancinelli, and L. Pavesi, “Modeling and validation of high-performance and athermal AWGs for the silicon photonics platform”, in 2016 18th International Conference on Transparent Optical Networks (ICTON) (July 2016), pp. 1–4 (cit. on p. 216).
- ¹⁸³ C. Castellan, S. Tondini, M. Mancinelli, C. Kopp, and L. Pavesi, “Low crosstalk silicon arrayed waveguide gratings for on-chip optical multiplexing”, in Silicon Photonics: From Fundamental Research to Manufacturing, Vol. 10686 (May 21, 2018), p. 106860V (cit. on p. 216).

Publications

Peer-reviewed papers

- C. Castellan et al., “Reflectance Reduction in a Whiskered SOI Star Coupler”, IEEE Photonics Technology Letters **28**, 1870–1873 (2016)
- F. Testa et al., “Design and Implementation of an Integrated Reconfigurable Silicon Photonics Switch Matrix in IRIS Project”, IEEE Journal of Selected Topics in Quantum Electronics **22**, 155–168 (2016)
- M Borghi et al., “Nonlinear silicon photonics”, Journal of Optics **19**, 093002 (2017)
- S. Tondini et al., “Methods for Low Crosstalk and Wavelength Tunability in Arrayed-Waveguide Grating for On-Silicon Optical Network”, Journal of Lightwave Technology **35**, 5134–5141 (2017)
- C. Castellan et al., “Tuning the strain-induced resonance shift in silicon race-track resonators by their orientation”, Optics Express **26**, 4204–4218 (2018)
- C. Castellan et al., “On the origin of second harmonic generation in silicon waveguides with silicon nitride cladding”, Scientific Reports **9**, 1088 (2019)

In preparation

- C. Castellan et al., “Field-induced nonlinearities in silicon waveguides embedded in lateral p-n junctions”, In preparation for Frontiers in Physics (2019)
- S. Tondini et al., “Automatic initialization methods for photonic components on a silicon-based optical switch”, In preparation for Applied Sciences (2019)

Proceedings

- S. Tondini et al., “Modeling and validation of high-performance and athermal AWGs for the silicon photonics platform”, in *Silicon Photonics and Photonic Integrated Circuits V*, Vol. 9891 (May 13, 2016), p. 98910C
- P. Pintus et al., “Silicon photonic toolkit for integrated switching matrices”, in *18th Italian National Conference on Photonic Technologies (Fotonica 2016)* (June 2016), pp. 1–4
- C. J. Oton et al., “Silicon Photonics for Matrix Switching Applications: Ingredients and Recipes”, in *Advanced Photonics 2016 (IPR, NOMA, Sensors, Networks, SPPCom, SOF)* (2016), paper ITu3B.6 (July 18, 2016), ITu3B.6
- S. Tondini et al., “Modeling and validation of high-performance and athermal AWGs for the silicon photonics platform”, in *2016 18th International Conference on Transparent Optical Networks (ICTON)* (July 2016), pp. 1–4
- M. Bertolla, C. Castellan and D. Roilo "Proceedings of the event Industrial Problem Solving with Physics 2016. Trento, 2016." <http://events.unitn.it/en/ipsp2016>
- A. Trenti et al., “Towards MIR SPDC generation in strained silicon waveguides”, in *2017 Conference on Lasers and Electro-Optics Europe European Quantum Electronics Conference (CLEO/Europe-EQEC)* (June 2017), pp. 1–1
- C. Castellan et al., “From SHG to mid-infrared SPDC generation in strained silicon waveguides”, in *Quantum Photonic Devices*, Vol. 10358 (Aug. 29, 2017), p. 1035804
- C. Castellan et al., “Low crosstalk silicon arrayed waveguide gratings for on-chip optical multiplexing”, in *Silicon Photonics: From Fundamental Research to Manufacturing*, Vol. 10686 (May 21, 2018), p. 106860V

Conference presentations

Personally presented

- 9th Optoelectronics and Photonics Winter School: Integrated Quantum Photonics, 26 March-1 April 2017. Folgaria, Italy. Poster presentation on "Second Harmonic Generation generation in strained silicon waveguides: results and perspectives".
- FOTONICA 2017 - 19th italian conference on photonic technologies, 3-5 May 2017, Padova, Italy. Oral presentation on "High-performance SOI AWG for optical network applications".
- SPIE Optics + Photonics, 6-10 August 2017, San Diego, California, USA. Oral presentation on "From SHG to mid-infrared SPDC generation in strained silicon waveguides".
- Congresso Nazionale della Società Italiana di Fisica (SIF), 11-15 September 2017, Trento, Italy. Oral presentation on "High-performance integrated silicon AWG for optical network applications".
- 6th International Symposium on Optics and its Applications (OPTICS-2018), 17-20 February 2018, Trento, Italy. Organizer and member of the Scientific Committee. Oral presentation on "Second Harmonic Generation in strained silicon".
- SPIE Photonics Europe 2018, 22 - 26 April 2018, Strasbourg, France. Oral presentation on "Low crosstalk silicon arrayed waveguide gratings for on-chip optical multiplexing".
- SPIE Photonics Europe 2018, 22 - 26 April 2018, Strasbourg, France. Oral presentation on "Automatic alignment of photonic components of massive optical switch to ITU channels".
- 20th European Conference on Integrated Optics (ECIO-2018), 30 May - 1 June 2018, Valencia, Spain. Poster presentation on "Investigating the origin of second order nonlinearities in silicon waveguides strained by silicon nitride".
- IONS Yerevan 2018, 30 August - 2 September 2018, Yerevan, Armenia. Oral presentation on "What is the role of trapped charges on the second harmonic generation in strained silicon waveguides?".

- 10th Optoelectronics and Photonics Winter School: Nonlinear Photonics, 20-26 January 2019. Andalo, Italy. Poster presentation on "Investigating the origin of second order nonlinearities in silicon waveguides strained by silicon nitride".
- 10th Optoelectronics and Photonics Winter School: Nonlinear Photonics, 20-26 January 2019. Andalo, Italy. Poster presentation on "Field-induced second harmonic generation in silicon waveguides with lateral doping".

Co-authored

- OSA Congress Advanced Photonics 2016, 18-21 July 2016, Vancouver, Canada. Oral presentation on "Silicon Photonics for Matrix Switching Applications: Ingredients and Recipes" (presented by C. Oton).
- FOTONICA 2016 - 18th italian conference on photonic technologies, 6-8 June 2016, Rome, Italy. Oral presentation on "Silicon Photonic Toolkit for Integrated Switching Matrices" (presented by P. Pintus).
- SPIE Photonics Europe 2016, 22 - 26 April 2018, Bruxelles, Belgium. Poster presentation on "Modeling and validation of high-performance and athermal AWGs for the silicon photonics platform" (presented by S. Tondini).
- ICTON 2016, 10-14 July 2016, Trento, Italy. Poster presentation on "Modeling and validation of high-performance and athermal AWGs for the silicon photonics platform" (presented by S. Tondini).
- FOTONICA 2017 - 19th italian conference on photonic technologies, 3-5 May 2017, Padova, Italy. Oral presentation on "Second Harmonic Generation in Strained Silicon Waveguides" (presented by A. Marchesini).
- Conference on Lasers and Electro-Optics/Europe (CLEO), 25-29 June 2017, Munich, Germany. Oral presentation on "Towards MIR SPDC generation in strained silicon waveguides" (presented by A. Trenti).
- FOTONICA 2018 - 20th italian conference on photonic technologies, 23-25 May 2018, Lecce, Italy. Oral presentation on "Studying the origin of second harmonic generation in strained silicon waveguides" (presented by C. Vecchi).
- SPIE Photonics West, 2-7 February 2019, San Francisco, California, USA. Oral presentation on "Second order nonlinearities in silicon waveguides: from the physics to new applications" (presented by C. Vecchi).

- 10th Optoelectronics and Photonics Winter School: Nonlinear Photonics, 20-26 January 2019. Andalo, Italy. Poster presentation on "Field induced non linear effects in silicon waveguides" (presented by R. Franchi).

Schools and Workshops

- Nanoscience Laboratory Kick-Off meeting, Trento, 20 June 2015. Oral presentation on "Test and modeling of array waveguide multiplexers on a silicon photonics platform".
- Course on Experimental Quantum Optics, 10-11 March 2016, Zurich, Switzerland.
- Workshop on Integrated Non Linear and Quantum Photonics, 21 March 2016, Trento, Italy.
- Workshop on Networks Dynamics and Complexity, 20 May 2016, Trento, Italy.
- Industrial Problem Solving with Physics 2016, 18-23 July 2016, Trento, Italy. Organizer, member of the Scientific Committee, and editor of the proceedings.
- Course on Cryptography, 01-02 September 2016, Trento, Italy.
- SiQuero General Assembly, 16 September 2016, Trento, Italy. Oral presentation on "Phase matched second harmonic generation in silicon waveguides strained by silicon nitride".
- Nanoscience Laboratory Kick-Off meeting, 25 November 2016, Trento, Italy. Oral presentation on "Second harmonic generation in silicon waveguides strained by silicon nitride".
- PhD Workshop, 30 November 2016, Trento, Italy. Oral presentation on "Silicon photonics and optical communications: the IRIS project".
- General Assembly of the Società Italiana di Ottica e Fotonica (SIOF), 13 December 2016, Genova, Italy. Oral presentation on "Silicon photonics and optical communications: the IRIS project".
- 9th Optoelectronics and Photonics Winter School: Integrated Quantum Photonics, 26 March-1 April 2017. Folgaria, Italy.

- Photonics as a key enabling technology, 17 November 2017, Trento, Italy.
- Nanoscience Laboratory Kick-Off meeting, 24 November 2017, Trento, Italy. Oral presentation on "Second harmonic generation in silicon waveguides".
- PhD Workshop, 30 November 2017, Trento, Italy. Poster presentation on "Second Harmonic Generation in strained silicon waveguides: results and perspectives".
- Photonics as a key enabling technology, 15 November 2018, Trento, Italy.
- PhD Workshop, 28 November 2018, Trento, Italy. Poster presentation on "Investigating the origin of second order nonlinearities in silicon waveguides strained by silicon nitride".
- Nanoscience Laboratory Kick-Off meeting, 14 December 2018, Trento, Italy. Oral presentation on "Field-induced second harmonic generation in silicon waveguides".
- 10th Optoelectronics and Photonics Winter School: Nonlinear Photonics, 20-26 January 2019. Andalo, Italy.

Colophon

This thesis was typeset with $\text{\LaTeX}2_{\epsilon}$. It uses the *Clean Thesis* style developed by Ricardo Langner. The design of the *Clean Thesis* style is inspired by user guide documents from Apple Inc.

Download the *Clean Thesis* style at <http://cleanthesis.der-ric.de/>.

Acknowledgements

Arrived at the end of this long journey, it is time to thank all the people that made this possible.

First of all, sincere thanks to professor Pavesi, who gave me the opportunity of realizing this work. I thank him for his guidance and for his precious advices, which made me growing and becoming more mature.

After him, I thank all the past and current members of the Nanoscience Laboratory that I was honored to meet during these years. From each of them I learned something precious. It has been a great pleasure for me being part of this family, and I am sure that I will always miss the good time spent together.

I particularly thank Stefano S., for all the adventures we share in-n-out of the laboratory. I acknowledge the two Alessandro for their precious help in the laboratory, but also for the good discussions we had despite of the troubles with the “Kraken”. I thank Mattia, for introducing me in the world of nonlinear optics and for the enthusiasm that he is able to spread, and Riccardo, for the great help he gave me in making possible the last part of this thesis. I thank Stefano T. and Manuel, with which I worked on a project that is not part of this thesis, but who gave me many satisfactions.

A special thank to my favorite Armenian girl, Tatev, for her availability and for the good time we spend together in all our travels. Shnorhakalut’yun! Thanks also for starting the adventure of our SPIE Chapter, which gave us big satisfactions. I thank also Sara, who accepted the challenge to continue this adventure. I am sure that with her passion she will succeed, thanks also to the help of the disruptive team made by Chiara V., Nicolò, Davide and Clara.

I acknowledge Chiara P., faithful office mate and good friend. I want to give special thanks also to Maddalena, with which I share lot of adventures since the beginning of the university, and David. I will always remember the time spent together in the organization of the IPSP as one of the most funny and satisfactory periods of my PhD.

I also thank Stefano B., Massimo, Pierre, Paolo, Fernando, Zahra, Fabio and Ast: for each of them I should spend many words, recalling the good moments we spent together. I also thank Tania, for her precious help and advices, but also for the fun we had in the organization of the last winter school.

Finally, I acknowledge Mher: this work wouldn't have been realized without his intuitions and its ambition for realizing "good samples".

To conclude, I thank my family and all my friends. Even if it is sometimes difficult trying to explain in what consists my work, their presence and their continuous support have been fundamental for me. Thank you!

Claudio